

ELECTROCHEMISTRY OF NICOTINAMIDE ADENINE DINUCLEOTIDE MIMETICS

By

Chase Bruggeman

A DISSERTATION

Submitted to
Michigan State University
in partial fulfillment of the requirements
for the degree of

Chemical Engineering – Doctor of Philosophy

2024

ABSTRACT

Nicotinamide adenine dinucleotide (NAD^+) is a biological redox mediator responsible for a large number of chemical reactions necessary for life. About 15% of documented enzymes rely on NAD^+ or the related nicotinamide adenine dinucleotide phosphate (NADP^+). Both cofactors have a redox-active nicotinamide site, which can undergo a net two-electron-one-proton reduction to form a high-energy 1,4-dihydropyridine, NAD(P)H . This dihydropyridine can reduce a substrate of interest through a net hydride transfer, regenerating NAD(P)^+ in the process. As the chemical industry looks increasingly to bioderived compounds, the ability to control reactions involving NAD(P)H is a potential market opportunity, not only for their ability to transform biological feedstocks, but also for their safety (operating at or near room temperature) and their selectivity (reacting with high regio- and stereoselectivity). However, the cost of these cofactors – tens to hundreds of thousands of dollars per mole – is prohibitively high. Researchers have explored ways to regenerate NAD(P)H from NAD(P)^+ , which would make the cofactor more accessible for industry by enabling a catalytic amount to be used. An appealing way to regenerate NAD(P)H is by electrochemical reduction of NAD(P)^+ ; however, the reduction is often intercepted after the first electron transfer to give an enzymatically-inactive $(\text{NAD(P)})_2$ dimer. The ability to design systems for regenerable NADH is hindered by a lack of understanding of which structural features correlate with dimerization, and which features correlate with reduction to NAD(P)H . Cofactor mimetics (mNAD^+), which retain the redox active nicotinamide site but have variable molecular structures, have been explored as a platform for understanding the structure-function relationships governing the redox behavior of these cofactors.

The purpose of the present thesis is to explore the electrochemistry of mNAD^+ , to understand which structural features correlate with dimerization, and how systems can be designed to favor reduction to mNADH over mNAD dimer. There are four chapters in this thesis. The first chapter is a literature review of the electrochemistry of NAD^+ and mNAD^+ , with a special emphasis on methods of quantifying dimerization rates. The second chapter explores the effect of supporting electrolyte on the electrochemical reduction of mNAD^+ , and it is shown that sodium pyruvate favors the reduction of mNAD^+ to a new product that has the same electrochemical oxidation signature as a sample of chemically-prepared mNADH . The third chapter explores the effect of both the molecular structure and the counterion of mNAD^+ on the dimerization rate. It is shown that dimerization is faster at lower reduction potentials and, counterintuitively, when sterics at the 1-

position are larger. This last trend suggests dimerization takes place preferentially at the 4-position, and that large 1-substituents favor arrangements in solution that place these redox-active sites close to each other. The electrochemistry data suggest that the reduction is more likely of mNAD^+X^- ion pairs than of lone mNAD^+ ions, and NMR data reveal ionic interactions between mNAD^+ and X^- that are localized at the pyridinium 2- and 4-positions. The fourth chapter explores the mechanism of interaction between mNAD^+ and pyruvate when they are reduced together. Evidence is provided in support of a mechanism whereby the intermediate mNAD radical mediates electron transfer to pyruvate, and that a pyruvate radical interacts with an mNAD radical to form mNADH in a non-catalytic way. Efforts to characterize the desired mNADH were unsuccessful, although NMR data show the appearance of a new CH_2 unit with nonequivalent protons when mNAD^+ and N,N-dimethylpyruvamide (DMP) are reduced together compared to when they are reduced separately. The major product of mNAD^+ reduction without DMP is the 4,4'-dimer, consistent with the findings of Chapter 3. However, mNADH could not be conclusively identified by NMR. It is suggested that bulk electrolysis conditions mirror cyclic voltammetry conditions in every way possible to maximize mNADH formation.

ACKNOWLEDGEMENTS

Many people contributed to the success of this PhD dissertation. Thanks in the first place goes to my advisor, Dr. David Hickey, for introducing me to electrochemistry and for encouraging my growth as an independent scientist and as a communicator while a PhD student. Thanks also goes to the rest of my guidance committee, Drs. Woldring, Barton, and Jackson, for their instruction, insight, and willingness to support my applications for fellowships in and beyond graduate school. Thanks also goes to the Hickey Lab members, past and present, for their friendship and many discussions over the years: Lincoln, Sunanda, Sharmila, Nunzio, Emmanuel, Annabelle, Tyler, Karissa, Dominik, Jana, Abdullah, Macy, and Laina. I wish to thank the instructors I had at MSU, particularly Dr. Lira in ChEMS, and Drs. Wulff and Borhan in Chemistry, for combining classroom rigor with fair grading in a manner worthy of emulation. Thanks also goes to Dan Holmes for his guidance interpreting and envisioning NMR experiments, to Richard Staples for his quick turnaround on crystal structures, and to James Siegenthaler for his availability to help with boron doped diamond electrode studies. Thanks to current and former graduate students in the Chemistry department, especially Thomas Oleskey and Evan Savelson, for starting and continuing the tradition of mech night. Thanks to Dr. Stefanie Baier and the rest of the Graduate Educator Advancement and Teaching Office (GREAT) for offering friendship and opportunities to train the incoming cohorts of graduate teaching assistants over the years. Thanks to Declan McClintock for connecting me with the MSU Swing Dance group, where I learned how to dance and cultivated many friendships. Thanks goes to my friends, including Joey Wijffels, Samuel Wakeman, Timothy Szocinski, Paul Cantu, and many others, for being there for me during the highs and the lows of the PhD journey. Thanks to the chairs of the Electrochemistry Gordon Research Conference and Seminar, especially Frank Zambrini, for covering the cost of the trip for me. Thanks to Dr. Johna Leddy at Iowa State for attempting to tackle the second harmonic alternating current voltammetry equation with me, and to the mathematics graduate student Keshav Sutrave at MSU, who was able to rearrange the coupled differential equations into a form that looked, according to him, “less coupled-ish”. Thanks of course also goes to my family for being there with me and listening to my stories throughout graduate school. I wish to thank Johann Tauler for teaching me at MSU about the spiritual life, Fr. Michael Cassar for encouraging me in it, and Jesus Christ for modeling it. Finally, thank you to Samara Chamoun for listening to it all, for supporting me, and for sticking it out in graduate school together. I love you very much.

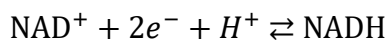
TABLE OF CONTENTS

CHAPTER 1: BACKGROUND	1
INTRODUCTION	1
NADH REGENERATION METHODS	3
STUDIES OF ELECTROCHEMICAL mNAD DIMERIZATION	6
FOCUS OF THE PRESENT THESIS	9
CHAPTER 2: DIMERIZATION RATE CONSTANTS OF NAD ⁺ MIMETICS: ALTERNATING CURRENT VOLTAMMETRY AS AN ELECTROANALYTICAL TOOL ..	13
ABSTRACT	13
INTRODUCTION	13
RESULTS AND DISCUSSION	15
CONCLUSION	28
CHAPTER 3: IMPACT OF SODIUM PYRUVATE ON THE ELECTROCHEMICAL REDUCTION OF NAD ⁺ ANALOGUES	29
ABSTRACT	29
INTRODUCTION	29
RESULTS AND DISCUSSION	31
CONCLUSION	40
CHAPTER 4: MECHANISTIC INSIGHTS INTO THE CO-REDUCTION OF NAD ⁺ MIMETICS WITH PYRUVATE DERIVATIVES	43
ABSTRACT	43
INTRODUCTION	43
RESULTS AND DISCUSSION	44
CONCLUSION	63
CHAPTER 5: SUGGESTIONS FOR FUTURE WORK	64
REFERENCES	67
APPENDIX FOR CHAPTER 2	76
APPENDIX FOR CHAPTER 3	146
APPENDIX FOR CHAPTER 4	155

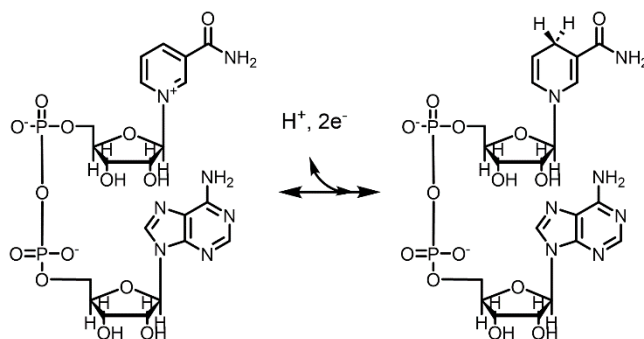
CHAPTER 1: BACKGROUND

INTRODUCTION

Nicotinamide adenine dinucleotide (phosphate) (NAD(P)^+) is a ubiquitous enzymatic cofactor, necessary for fundamental biological reactions like DNA replication and protein synthesis.¹ It is known for its redox behavior, acting as a net hydride donor/acceptor^a according to the following reaction (Scheme 1):



The equilibrium for this reaction lies strongly on the side of the oxidized NAD(P)^+ , which is about 60 kJ/mol lower in energy than NAD(P)H at pH 7 (the reduction reaction has a formal reduction potential $E^{0'}$ of -0.31 V at this pH).² As a result, NAD(P)H is unstable, and it seeks to give its hydride away to a suitable substrate, so that it may return to NAD(P)^+ .



Scheme 1.1. Reduction of NAD^+ (left) to NADH (right) involves the transfer of two electrons and one proton. NADPH has a phosphate group in place of the bottom-right -OH group.

Fortunately, substrates abound. Indeed, the $\text{NAD(P)}^+/\text{NAD(P)H}$ redox couple is used by roughly 15% of documented enzymes, with a substrate scope including ketones, alkenes, arenes, amines, organic halides, inorganic anions, and even transition metals.¹ A couple example reactions include the oxidation of 2-hydroxybiphenyl to 2,3-dihydroxybiphenyl with hydroxybiphenyl monooxygenase,³ and the stereoselective hydrogenation of activated alkenes with enoate reductase.⁴ The large diversity of substrates, combined with the inherent specificity of enzymatic reactions, make NAD(P)H an appealing target for industrial chemistry: if this redox cofactor can be harnessed, it opens up a large fraction of nature's chemical toolkit, and these reactions have an added safety benefit because they occur near ambient temperature and pressure. The chemical

^a Experimental data suggest the hydride transfer may be concerted in some reactions and sequential (one electron followed by one H atom) in others.^{58,91,92}

industry is looking increasingly toward biorenewable chemicals,⁵ and cofactors like NAD(P)H will become more relevant to transform natural feedstocks into value-added products.^b However, the cost of the cofactor obstructs its immediate scale-up. At the time of this writing (Jan 2024), from Sigma Aldrich, NAD⁺ is \$28,000/mol (\$1010/25g, #N0632), and its cousin NADP⁺ is \$318,000/mol (\$2020/5g, #NADP-RO). Oakwood Chemical offers NADP⁺ at a slightly lower price, \$280,000/mol (\$95/250mg, #103189); clearly, though, the price of the cofactor is very high.

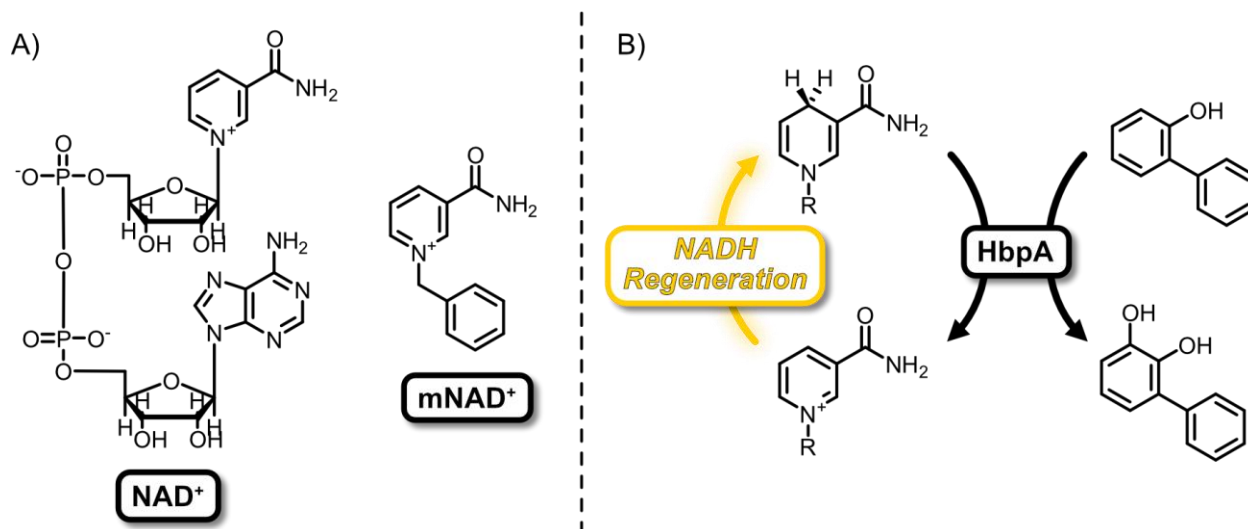
There are two main areas of research to circumvent the cost barrier. One method is to use low-cost NAD⁺ mimetics (mNAD⁺) instead of NAD⁺ itself. Particular attention is being given to structurally simple mNAD⁺, such as 1-benzyl pyridinium-3-carboxamide (Scheme 1.2A),^{4,6-8} which are cheap^c and which can demonstrate enzymatic activity on par with NADH.^{4,9} These mimetics retain the redox-active nicotinamide site while replacing the complex adenine dinucleotide group with a simpler 1-substituent, such as benzyl. However, such dramatic structural changes can render the cofactor inactive with many enzymes, and it is still not possible to predict in general which mimetics will be compatible with which enzymes. While some trends are known – for example, changes to the redox-active site are likely to lower activity, and the diphosphate group can help NADH bind to enzyme active sites¹⁰ – there is still a need for structure-activity relationships to inform the design of low-cost mNADH, so that the list of active mimetic-enzyme matches can be further expanded.

Another way to circumvent the cost barrier is to regenerate NADH from NAD⁺, which would allow a catalytic amount of NADH to drive a reaction, rather than a stoichiometric amount. An example reaction that can be driven in this way is the selective *ortho*-hydroxylation of 2-hydroxybiphenyl, catalyzed by hydroxybiphenyl monooxygenase (HbpA)³ (Scheme 1.2B). The cost may be lowered still further by regenerating mNADH, for example using the 1-benzyl mimetic in place of NADH itself.¹¹ A few NADH regeneration methods are chemical,¹²⁻¹⁵ photochemical,^{16,17} and electrochemical^{3,18-20} regeneration. These will be described here, and the electrochemical regeneration section will be used to introduce a more general discussion of the electrochemistry of mNAD⁺. The reader is directed to a review by Shi and colleagues for a more

^b The flavor industry is one example, customers will pay a premium for flavors derived from fermentation instead of from petrochemicals, and the industry is responding accordingly.

^c By comparison with the costs for NAD(P)⁺ above, the materials required to make 1-benzyl nicotinamide bromide cost \$35/mol from Sigma Aldrich (nicotinamide: \$14.4g/mol, \$118/kg, #N3376; benzyl bromide: \$20.7/mol, \$302/2.5kg, #B17905) (Accessed 15 Jan 2024).

comprehensive review of other NADH regeneration methods.^{21d} After describing the behavior of the mNAD⁺/mNADH redox couple, experimental methods for studying electrochemical mNAD⁺ reduction will be described, and then an overview will be given of the remaining chapters in this thesis.



Scheme 1.2. A) Structures of NAD⁺ and of 1-benzyl nicotinamide, a representative mNAD⁺. B) Schematic of an NADH-promoted reaction, the 3-hydroxylation of 2-hydroxybiphenyl, catalyzed by hydroxybiphenyl monooxygenase (HbpA). Molecular oxygen (not shown) is consumed in the reaction.

NADH REGENERATION METHODS

One of the oldest reagents used to reduce NAD⁺ to NADH is hexose monophosphate (presumably glucose-6-phosphate).¹² This reaction is fast, however it requires an enzymatic catalyst. An alternative is to use sodium dithionite, which can reduce NAD⁺ to NADH without an enzyme. The mechanism for this reaction appears to involve a sulfinate adduct at the pyridine 4-position, which hydrolyzes to release the 1,4-dihydropyridine and one equivalent of sulfite.¹³ Sodium borohydride may be used instead of sodium dithionite, at the cost of reaction selectivity, forming a mixture of *ortho*- and *para*-dihydropyridines.¹³ Other 1,4-dihydropyridines may also be used to reduce NAD⁺ to NADH, for example, 1-benzyl-1,4-dihydropyridine can regenerate NADH during the reduction of cyclohexanone, with modest yields.¹⁴ Of the chemical reduction methods, dithionite is preferred for its availability, simplicity, and selectivity; the main disadvantage is the

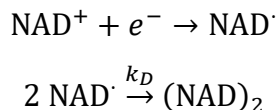
^d Of course, the reaction may be driven in the opposite direction, where NAD⁺ is regenerated from NADH. This latter reaction is energetically downhill, and may find applications in biofuel cells.^{89,93}

need to introduce stoichiometric amounts of reducing agent, which can interfere with enzyme function.¹⁵

Light is another reagent that can regenerate mNADH from mNAD⁺. Kalyanasundaram and colleagues found that a family of 1-alkyl mNADH could be prepared from mNAD⁺ with ruthenium and rhodium hydride transfer catalysts, with triethanolamine as the terminal electron donor.¹⁶ Wienkamp and Steckhan used the same triethanolamine-ruthenium-rhodium system to reduce NAD⁺ itself to NADH.¹⁷ Although the idea of visible light as a free energy source is appealing for NADH generation, the photochemical method cannot be recommended for industrial use, due to low quantum yields (~0.002), slow conversion (10-15 $\mu\text{mol/h}$), instability (NADH itself degrades under visible light^e), and the need for super-stoichiometric amounts of amine waste.

In electrochemical NAD⁺ reduction, the stoichiometric reducing agent is no longer an amine or an inorganic salt; instead, only electrons are used, delivered through an electrode. These electrons may flow to the substrate indirectly through a mediator, or directly from the electrode to the substrate. Steckhan and colleagues used mediated electron transfer for the oxidation of 2-hydroxybiphenyl, with a rhodium hydride-transfer catalyst similar to the one used in photochemical reduction of NAD⁺;³ however, the reaction is slow (~2 $\mu\text{mol min}^{-1}$), and the enzyme tended to be deactivated by adsorption onto the electrode surface. The authors suggested protecting the enzyme by immobilizing it onto a solid matrix at the electrode, a method which has been realized with dehydrogenase enzymes in the bioelectrocatalytic oxidation of methanol to CO₂.²²

In contrast to mediated NAD⁺ reduction, direct electrochemical reduction is appealing for its operational simplicity (does not require a mediator). However, it often fails to proceed to NADH; instead, the electrons are transferred one at a time, and two singly-reduced NAD radicals may dimerize according to the following reaction^f:

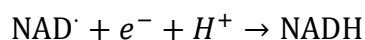


^e Kalyanasundaram and colleagues used this instability to their advantage, reducing methyl viologen and a Zn-porphyrin by illuminating mNADH with visible light.¹⁶

^f Evidence has repeatedly favored the dimerization of pyridyl radicals,^{24,26-28,94} disfavoring alternative mechanisms such as radical-cation or anion-cation dimerization.²⁹

where k_D is the dimerization rate constant.^g The dispersion force that attracts pyridine radicals together is very strong, strong enough even to overpower the coulombic repulsion between like charges. For example, non-covalent dimers, coined “pimers”, have been observed between viologen radical cations.²³ The attractive force is independent of both sterics and electronics of either member of the pair.

In order to regenerate NADH from NAD^+ with direct electrochemical reduction, a second electron and a proton must be transferred to the NAD^\bullet radical, according to the following reaction:



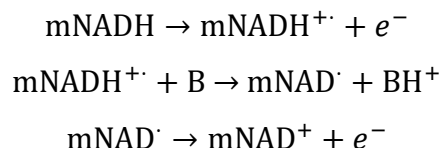
Evidence for a sequential two-electron reduction comes from Burnett and Underwood, who reduced 1-methyl nicotinamide to its dimer at -1.2 V vs SCE, and to its dihydropyridine at -1.8 V vs SCE. The participation of a proton in the second step was deduced from a shift of -27 mV per pH unit in the reduction event (theoretical -29.5 mV per pH unit for a 2 electron/1 proton process).²⁴

While the reduction of NAD^+ to NADH may be coerced at low applied potentials, dimer is frequently formed alongside the desired NADH. Higher selectivity may be obtained at more modest potentials by altering the electrode surface. For example, Omanovic and colleagues recovered 100% yield of NADH after reduction of NAD^+ on a glassy carbon electrode patterned with either Pt or Ni nanoparticles, with an optimum yield near -1.2 V vs SCE.¹⁸ They also found a 96% yield of NADH on a bare Ti electrode near -1.0 V vs SCE.¹⁹ Rashid-Nadimi and colleagues showed that electrode morphology also affected NADH yields; by switching from copper foil to copper foam, they increased NADH recovery from 54% to 80% near -1.1 V vs SCE.²⁰ In all cases, the yields depended on the applied potential; however, no general relationships between electrode structure and yield were extracted which could inform industrial design.

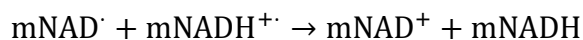
A discussion of the electrochemical reduction of mNAD^+ would be incomplete without also addressing the oxidation of mNADH. Briefly, the direct electrochemical oxidation of 1,4-dihydropyridines follows a sequential electron-proton-electron pathway, similar to the pathway for reduction. Haas and Blaedel observed two one-electron oxidation events by CV for mNADH in

^g The dimerization rate constant k_D is here defined by the equation $\frac{\partial}{\partial t}[\text{NAD}] = -k_D[\text{NAD}]^2$, where $[\text{NAD}]$ is the concentration of radical. An alternative definition is based on the appearance of dimer, $\frac{\partial}{\partial t}[(\text{NAD})_2] = k'_D[\text{NAD}]^2$. The radical disappears twice as fast as the dimer appears, so $k_D = 2k'_D$. It is not always clear in the literature which convention is used.

unbuffered acetonitrile, which afforded mNAD⁺ in 40% yield. In basic acetonitrile a single two-electron wave was observed, with quantitative mNAD⁺ regeneration.²⁵ They proposed the following mechanism:



where B is a base. The lower yield of mNAD⁺ without base was attributed to an acid-promoted decomposition of mNADH (which takes the place of B in the second reaction above). Savéant and colleagues deduced an alternative second oxidation step for 10-methylacridan in buffered acetonitrile. Based upon double potential step chronoamperometry data, they inferred that the intermediate mNAD[·] radical is oxidized in solution by mNADH⁺, rather than by the electrode surface, according to the following reaction:²⁶



The chemical reactions associated with mNADH oxidation and mNAD⁺ reduction are very rapid. The following section will describe some of the experimental methods researchers have used to find the chemical reaction rates that accompany electrochemical mNAD⁺ reduction.

STUDIES OF ELECTROCHEMICAL mNAD DIMERIZATION

Although there have been several studies of mNAD⁺ electrochemical reduction and dimerization, comparatively few rate constants have been determined precisely in the literature. One method of determining rate constants is cyclic voltammetry (CV), where the voltage is swept from high to low to form the radical, and then from low to high to re-oxidize the radical. If the potential is swept too slowly, no radical oxidation peak will be observed, but as the sweep rate becomes faster both reduction and oxidation events will become visible. Elving and colleagues used this method to determine a dimerization rate constant of $5 \times 10^6 \text{ M}^{-1} \text{ s}^{-1}$ for 1-methyl nicotinamide in pH 9 carbonate buffer.²⁷ Savéant and colleagues also used this method in a study of 10-methylacridinium reduction, reporting a dimerization rate constant of $3 \times 10^7 \text{ M}^{-1} \text{ s}^{-1}$ in acetonitrile.²⁶ Besides the ratio of oxidizing current to reducing current, another observable in CV is the shift in potential at peak current as a function of scan rate: slower scan rates will shift the reduction event to more positive potentials, but at fast scan rates the potential at which reduction occurs will remain constant. If both regions can be accessed, CV will provide both the reduction potential and the dimerization rate constant, but if only the slow region can be accessed, one of

these parameters will need to be determined from a different experiment. Elving and colleagues used the peak potential method to complement the peak current ratio method in a study of NAD^+ reduction, and both afforded k_D near $3 \times 10^7 \text{ M}^{-1} \text{ s}^{-1}$.²⁸

An alternative experimental method is rapid potential step chronoamperometry, where the potential is held at a reducing potential for a short time t (on the order of μs) and then immediately switched to an oxidizing potential. The current is measured at times $2t$ and t , and the ratio of these values is used to identify the chemical reaction mechanism and rate constant. The procedure requires very large potential jumps, so that any effects of electron transfer kinetics or ohmic resistance can be neglected. Savéant and colleagues used double potential step chronoamperometry to complement their CV studies of 10-methylacridinium reduction, mentioned in the previous paragraph. Hermolin and colleagues used a related technique, reverse-pulse voltammetry, to study the reduction of 1-alkyl-4-*t*-butyl pyridinium ions in acetonitrile. In this method, an initial reducing potential E_{in} is pulsed to an oxidizing potential E_p , and a range of oxidizing potentials E_p is swept. Similar to the previously mentioned study, fitting the current afforded both the mechanism for reduction and the reaction rate constant. A radical-radical coupling $m\cdot + m\cdot \rightarrow m_2$ was favored over radical-cation $m\cdot + m^+ \rightarrow m_2^+$ and anion-cation $m^- + m^+ \rightarrow m_2$ coupling mechanisms. The dimerization rate constant k_D was measured between 1×10^5 and $6 \times 10^6 \text{ M}^{-1} \text{ s}^{-1}$, depending on the pyridinium 1-substituent.^{29,h}

A third experimental method is electrochemical impedance spectroscopy (EIS), which measures the alternating current response to a sinusoidal alternating potential input. At small alternating potential magnitudes, there is a single alternating current response at the same frequency as the alternating potential (larger potential amplitudes may induce current responses at integer multiples of the applied frequency for a faradaic process). The difference in time between the two sine waves is measured as a phase angle, and the amplitude of the current sine wave is measured as a magnitude. The phase angle offers a wealth of information about the system under study: if the redox event is reversible, the current and voltage will be offset in time, but if some resistance is introduced (perhaps through a chemical reaction or through slow charge transfer), the current and voltage will be more closely aligned in time. Numerical simulations often accompany

^h Incidentally, Savéant and colleagues reported the same dimerization rate constant as Hermolin and colleagues for 1-methyl-4-*t*-butyl pyridinium, $6 \times 10^6 \text{ M}^{-1} \text{ s}^{-1}$, in dimethylformamide, by using double potential step chronoamperometry.³⁵ However, their k_D value is defined by the appearance of dimer, while the value of k_D reported previously in acetonitrile appears to be defined by the disappearance of radical.

such experiments to solve the nonlinear equations that describe dimerizing systems. Rueda and colleagues used EIS to study the reduction and subsequent dimerization of methyl viologen dications, reporting a dimerization rate constant of $10^4 \text{ M}^{-1} \text{ s}^{-1}$ in water.³⁰ Using only the phase angle, Pospíšil and colleagues reported a dimerization rate constant of $9 \times 10^5 \text{ M}^{-1} \text{ s}^{-1}$ for 1-dodecylpyridinium in acetonitrile.³¹ While these latter results are doubtful because the concentration of the pyridinium starting material was used in the equations in place of the concentration of neutral radical, the paper still offers a valuable insight that the data historically obtained from numerical simulations can in fact be derived from experimental data.

The potential input signals for each of the above experimental methods are illustrated schematically in Figure 1.1, along with the potential input for alternating current voltammetry (described below).

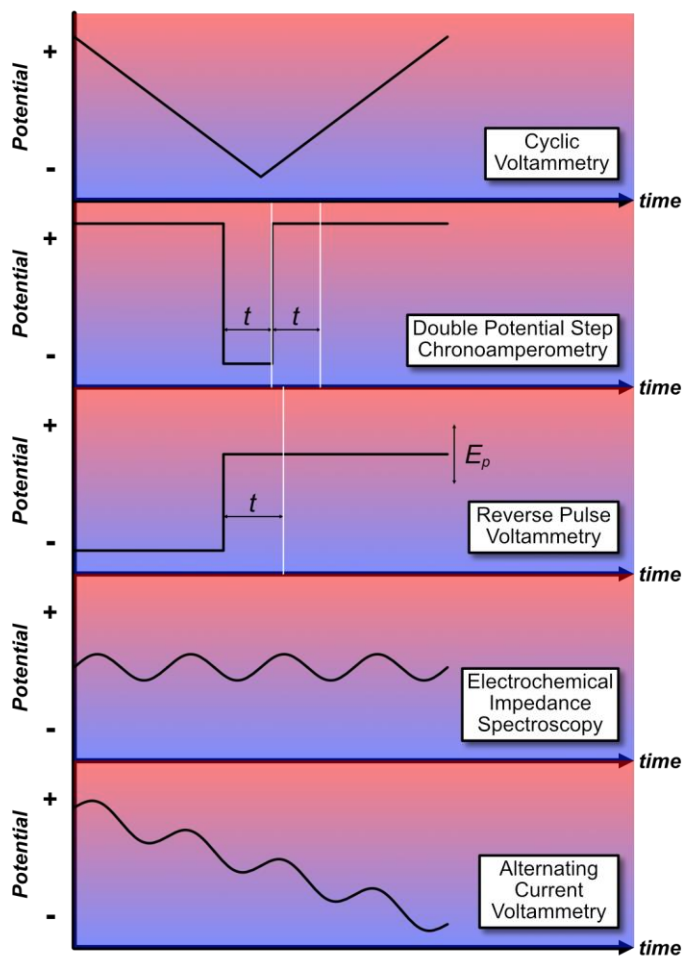


Figure 1.1. Schematic illustration of the potential waveforms for several electrochemistry experiments used for studying systems with rapid dimerization rates (not to scale).

FOCUS OF THE PRESENT THESIS

The focus of the present thesis is twofold. First, which factors influence the dimerization rates of mNAD⁺? Second, how can systems be designed for regenerable mNADH? The studies here that attempt to answer these questions rely heavily on NAD⁺ mimetics. Not only are mNAD⁺ low-cost (and occasionally enzymatically active), but they are easy to make, easy to purify, and stable for years at ambient conditions. They also offer a platform from which a variety of structural features can be investigated, to understand which interactions govern the electrochemical reduction mechanism. Additionally, emphasis in this thesis is placed on direct electrochemical reduction of mNAD⁺ over mediated electrochemical reduction, primarily because the former is easier to model.

Regarding the question of dimerization rates, the major hurdle to studying dimerization of nicotinamide-based radicals is simply that they react too quickly to be observed with conventional electrochemistry techniques. As seen in the previous section, dimerization rate constants are on the order of $10^7 \text{ M}^{-1} \text{ s}^{-1}$; by comparison, dimerization rate constants can only be resolved up to $\sim 10^6 \text{ L mol}^{-1} \text{ s}^{-1}$ with a CV sweep rate near 500 V s^{-1} (the limit of the potentiostat in the present writer's laboratory).³² Resolution improves with fast-scan CV,^{26,33,34} which can reach scan rates beyond 100 kV s^{-1} . However, it can cost tens of thousands of dollars to add a fast-scan potential generator to an existing potentiostat,ⁱ and the technique can suffer from a low signal/noise ratio. The rapid potential pulse techniques also described above can theoretically discern dimerization rate constants on the order of $10^8 \text{ L mol}^{-1} \text{ s}^{-1}$,³⁵ but these techniques can also have a low signal/noise ratio, and can require several scans at different concentrations and even differently-sized electrodes. The fast-scan CV and pulse techniques operate on the principle that, in order to access shorter timescales, the potential needs to change more quickly, but this principle does not apply uniformly to all experimental techniques.

The alternating current methods described above operate on a different principle, namely that measurement of a new dimension of data (in this case the phase angle) increases the kinetic resolution at slow scan rates.^j In EIS, the alternating potential is added to a constant applied

ⁱ One can circumvent the sticker price by making a rapid-scan setup at home, for a few hundred dollars.³⁴

^j No advantage comes without a cost, and alternating current techniques are no exception. The major price tag of obtaining rapid kinetic data at slow scan rates is theoretical complexity. The theory of ACV, admirably developed by D. E. Smith,⁴⁵ can yield equations which require a full page simply to write out, and data representation implicitly relies upon complex numbers. If a scientist is not comfortable with the math used to derive the solution (a process

potential, although the alternating potential may instead be added to a linear sweep potential, as is the case with alternating current voltammetry (ACV). The theoretical foundations of the two experiments are similar, but EIS generally operates under steady-state conditions, whereas ACV is an inherently transient experiment, like CV. The transient nature of ACV keeps experiments short, which not only saves time but also allows the assumption of 1-D semiinfinite diffusion to remain valid, so that techniques like convolution voltammetry (described in the appendix to Chapter 3) may be used to find concentrations of redox-active substrates (the method proposed by Pospíšil and colleagues).³¹

Chapter 2 of this thesis describes a study of twelve different mNAD^+X^- in acetonitrile, using ACV for its ability to resolve kinetic parameters at slow scan rates, and for its ability to predict alternating current data from direct current data. In response to the question about which structural features of mNAD^+X^- control its electrochemical reduction behavior, it is shown that dimerization is faster when the reduction potential is lower and, counterintuitively, also when out-of-plane sterics at the 1-position are more pronounced. These results suggest that the true species being reduced is a cluster of mNAD^+X^- ion pairs, rather than lone mNAD^+ ions, and that sterics at the 1-position favor an arrangement that allows dimerization at the 4-position. The conclusion of ionic aggregation is consistent with an observed drop in the reduction potential when $\text{X} = \text{Br}$ is replaced with $\text{X} = \text{Cl}$, and with concentration-dependent NMR data, which show that two disparate sites on mNAD^+ interact with X^- , and that this interaction is stronger with Cl^- than with Br^- . The takeaway is that electrochemical reduction of mNAD^+X^- should be considered from the standpoint of ionic aggregates rather than lone mNAD^+ ions.

Regarding the question of regenerable mNADH systems, a major challenge is the sensitivity of mNADH regeneration yield to experimental conditions like the applied potential and the amount of additive. In the electrode studies mentioned above, potentials either lower or higher than the optimal caused the yield of NADH to drop; this sensitivity can pose challenges for large-scale electrolyses, where currents of several amperes can cause errors in the measured potential to exceed the tolerance for optimal potential control. In this thesis, a method of NADH regeneration

which took multiple years for the author of this thesis), there can be a strong preference to avoid it altogether, instead relying on more familiar techniques which, if experimentally more tedious, are at least more easily grasped. It is the author's wish that ACV become an everyday electrochemistry experiment, although before this can happen the theory will need to be disseminated in a more accessible form to a broader audience than is done at present. It is hoped that the present thesis accomplishes this to a small extent.

was sought that was less sensitive to variations in experimental conditions. To this end, several supporting electrolytes were tested for their ability to alter the mNAD^+ reduction pathway.

In Chapter 3, sodium pyruvate is shown to promote the formation of a new oxidation event from mNAD^+ reduction, with an optimum yield around 50% from mNAD^+ . The oxidation event ($\text{ox}2$), characterized by CV, appeared at the same potential as the oxidation of a chemically prepared sample of 1,4-dihydro mNADH . The generation of $\text{ox}2$ is observed with a range of mimetics, and with NADH itself. No interaction between pyruvate and mNAD^+ was visible by NMR or by UV-Vis, consistent with an interaction between the two species that takes place only when one or both of the species are electrochemically reduced. In fact, the yield of $\text{ox}2$ formation appears to depend on the extent of overlap of the reduction events of sodium pyruvate and mNAD^+ . Without pyruvate, the oxidation of mNAD dimer was accompanied by a second oxidation event at acidic pH or at low potentials, although this other oxidation event was much weaker and could be an aggregate of multiple oxidation events.

In Chapter 4, the question from Chapter 3 is extended: by what mechanism does sodium pyruvate enable reduction to the 1,4-dihydropyridine? The ability to generate $\text{ox}2$ is apparently shared by a variety of vicinal dicarbonyls, including methyl pyruvate and several pyruvamides, so long as their electrochemical reduction overlaps with the reduction event of mNAD^+ . Diacetyl is a notable exception, being electrochemically active in the region of interest but having a negligible influence on mNAD^+ reduction. Kinetic isotope studies show negligible effect of the solvent (H_2O or D_2O) on the ratio of $\text{ox}1$ to $\text{ox}2$. Concentration studies show a first-order dependence of $\text{ox}2$ formation on both mNAD^+ and pyruvate, although attempts to find any catalytic behavior of pyruvate, whereby pyruvate regenerates itself after forming mNADH , were unsuccessful. Convolution voltammetry shows that the product distribution is nearly statistical (1:1:1 ratio of mNADH to mNAD dimer to pyruvate reduction product) below the potential where both mNAD^+ and pyruvate are being reduced. ACV studies show that electron transfer to pyruvate becomes much faster in the presence of 5 mol % mNAD^+ , suggesting that mNAD^\bullet may act as a mediator for electron transfer to pyruvate. Such a conclusion would be consistent with the data observed in Chapter 2, where 2 mol% of mNAD^+ greatly increases the rate of sodium pyruvate reduction, especially at acidic pH. Bulk electrolysis experiments show that $\text{ox}2$ is more likely attributable to oxidation of a heterodimer between mNAD and pyruvate, rather than to oxidation of 1,4-dihydro

mNADH, for which no spectroscopic evidence could be found. Electrochemistry data in this thesis are interpreted in light of heterodimer formation.

Chapter 5 is a brief summary of the findings of the present thesis, with several suggestions for avenues of future research.

CHAPTER 2: DIMERIZATION RATE CONSTANTS OF NAD⁺ MIMETICS:

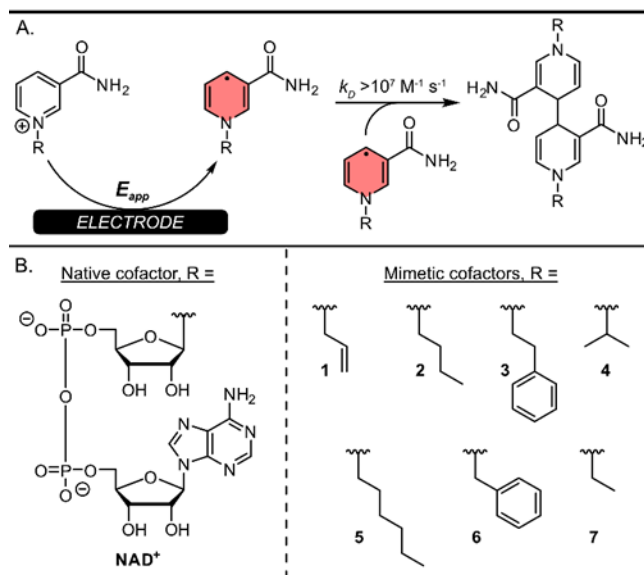
ALTERNATING CURRENT VOLTAMMETRY AS AN ELECTROANALYTICAL TOOL ABSTRACT

Electrochemical structure-activity relationships of NAD⁺ mimetics (mNAD⁺) are uncommon due to dimerization rates that are beyond the limit of resolution of many analytical techniques. Here, we demonstrate the ability of alternating current voltammetry (ACV) to shed light on these kinetically challenging systems. Plotting the current in polar form allows straightforward background corrections and order-of-magnitude estimates for kinetic parameters upon visual inspection. Best-fit ranges of kinetic parameters are found with a refined ACV theory that accounts for the dependence of electroactive species concentrations on position. We validate the method by replicating literature results for a model compound, and we use the method to study a family of mNAD⁺X⁻ (X = Br, Cl) in acetonitrile. Combining ACV with quantum mechanical computations shows that the dimerization rate constants are faster at lower reduction potentials and, counterintuitively, with larger out-of-plane sterics at the pyridinium 1-position. The trend suggests that mNAD⁺X⁻ may aggregate into ion pairs in solution, with bulky 1-substituents favoring arrangements that facilitate dimerization at the pyridinium 4-position. The results shed light on the structure-activity relationships of mNAD⁺, and they demonstrate the utility of ACV for investigating kinetically challenging systems.

INTRODUCTION

Oxidoreductase enzymes catalyze oxidation and reduction reactions in several important biological pathways and are gaining growing attention for use in large scale chemical synthesis.¹⁰ Furthermore, approximately half of oxidoreductase enzymes rely on the cofactor nicotinamide adenine dinucleotide (NAD⁺/NADH) and its phosphorylated analogue (NADP⁺/NADPH).³⁶ As the commodity chemical industry shifts towards biorenewable feedstocks,⁵ the broad range of enzyme-catalyzed reactions involving NADH makes it a desirable chemical redox agent for transforming biomass into value-added products.³⁷⁻³⁹ Despite the promise of NADH, high costs limit its present utilization at an industrial scale.²¹ Electrochemical reduction of NAD⁺ to NADH is an attractive way to make NADH more cost-effective by regenerating a catalytic amount of the cofactor while avoiding the buildup of chemical reductants. In practice, however, the two-electron-one-proton reduction is often intercepted after the first electron transfer to yield an enzymatically inactive dimer (Scheme 2.1A).^{24,28} The design of regenerable cofactor systems is hindered by the

lack of understanding about how different structural features of NAD^+ influence its reduction and subsequent dimerization.



Scheme 2.1. (A) Reaction diagram of the radical dimerization that occurs upon electrochemical reduction of NAD^+ (and its analogues). (B) Structures of 1-substituents for the native cofactor, NAD^+ (left) and the mimetic cofactors studied in this work (right).

Recently, low-cost NADH mimetics (mNADH) have gathered attention as a platform for studying the relationship between cofactor structure and redox behavior. Many of these mNADH – which include variable 1-substituents attached to the redox-active nicotinamide site (Scheme 2.1B) – display enzymatic activity up to or exceeding that of native NADH.^{4,8} However, there is no general way to predict the redox behavior of mNADH due to a lack of known structure-function relationships. In particular, precise electrochemical measurements of mNAD dimerization are scarce because the dimerization rate constants ($k_D > 10^7 \text{ M}^{-1} \text{ s}^{-1}$) are too fast to be discerned with traditional experiments like cyclic voltammetry (CV).²⁹ A common approach to increase kinetic resolution in voltammetry experiments is to increase the potential sweep rate, but the fast scan and rapid pulse experiments that adhere to this paradigm suffer from low signal/noise due to small electrode sizes and high charging currents. By contrast, alternating current voltammetry (ACV) obtains high kinetic resolution at slow scan rates by tracking the difference in time between voltage and current throughout an experiment. Based on this capability, we envisioned a way to utilize ACV to make precise kinetic studies of biologically relevant mNAD^+ more accessible.

Although ACV has been used to study dimerizing systems before, widespread adoption of the technique has been hindered by a few practical difficulties. One difficulty was the subtraction

of background current, called “a challenging operation” in a seminal publication.^{13,14} Another difficulty was the reliance on external simulations to find best-fit parameters, adding an unnecessary step to the fitting process. A third difficulty was an incomplete theoretical framework; for example, the concentration of neutral radical was assumed constant with respect to position, and it was not always differentiated from the concentration of oxidized substrate.^{31,40} We hypothesized that ACV implementation would be faster and more reliable if background subtractions were straightforward, if data fitting were self-contained, and if the theoretical framework were refined to include the dependence of the radical concentration on position. Herein, we synthesize a family of mNAD⁺ to test this hypothesis, along with a literature control to validate the method.

RESULTS AND DISCUSSION

To demonstrate our ACV procedure, we used 1-allyl nicotinamide bromide (**1-Br**) as a model substrate for its ease of synthesis and good solubility. Figure 2.1A illustrates the input potential (blue) and the output current (orange) over time during a representative ACV scan of **1-Br**, with an experimental CV superimposed on the ACV for comparison. In ACV, a sinusoidal potential is added to the linear sweep potential of CV experiments, generating a sinusoidal current added to the traditional “duck”-shaped current of CV experiments. Three datasets can be extracted from an ACV experiment: 1) the direct current, I_{DC} , is the average of the measured current over each period of the sine wave; 2) the alternating current magnitude, ΔI , is half the peak-to-valley current difference in one cycle; 3) the phase angle, φ , is the difference in time between the current and potential sine waves (mentioned above; $360^\circ =$ one cycle). Figure 2.1B illustrates how ΔI and φ are found in a given cycle.

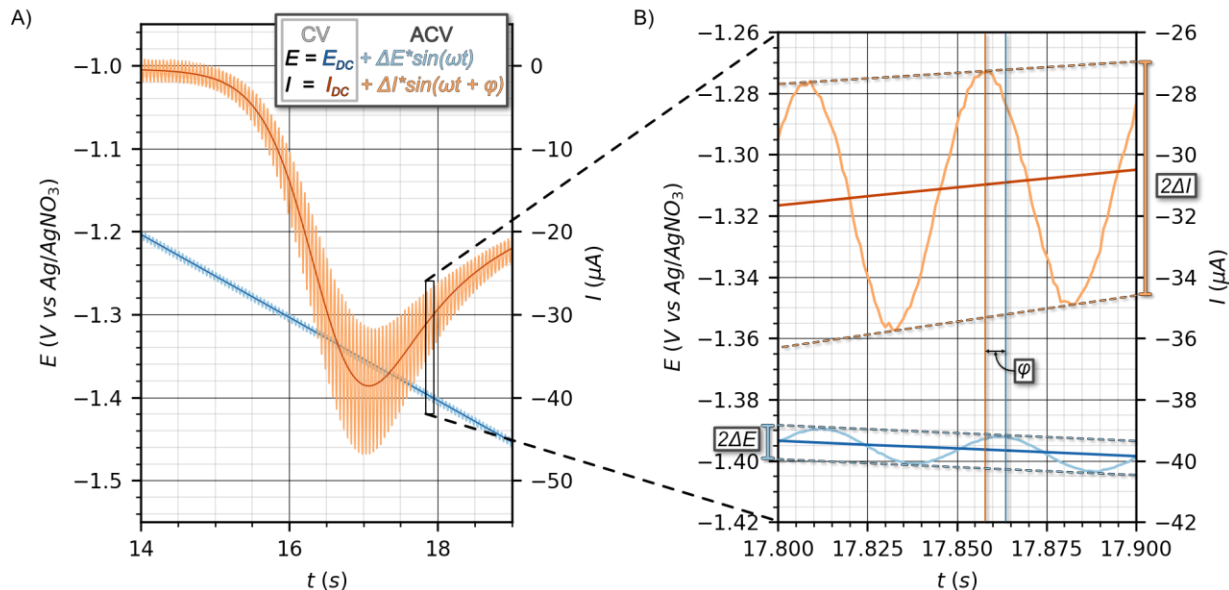


Figure 2.1. A) Representative cyclic voltammogram (dark orange = current, dark blue = potential) and alternating current voltammogram (light orange = current, light blue = potential). B) The alternating current magnitude ΔI , the alternating potential magnitude ΔE , and the phase angle ϕ are visible in the inset on the right. The difference in time between the alternating potential and the alternating current is given by the phase angle ϕ ($360^\circ =$ one cycle). Experimental conditions: 2 mM **1-Br** and 200 mM Bu_4NPF_6 in acetonitrile, with a 3 mm glassy carbon working electrode, Pt wire counter electrode, and Ag/AgNO_3 reference electrode at 22 °C. The solution was purged with nitrogen before each scan. For CV, $\nu = 50 \text{ mV s}^{-1}$; for ACV, $\nu = 50 \text{ mV s}^{-1}$, $\Delta E = 5 \text{ mV}$, and $\omega = 2\pi \cdot 20 \text{ Hz}$.

One advantage of adding the sinusoidal potential to a linear sweep potential, rather than to a constant potential, is that the experiment remains short enough for the approximation of 1-D semiinfinite diffusion to be valid ($< 30 \text{ s}$).⁴¹ With this approximation, the direct current I_{DC} can be separated from the alternating current and used to predict the theoretical alternating current (described below). Figure 2.2 illustrates this process for **1-Br**, showing how a raw dataset is transformed into a polar plot that allows comparison between theory and experiment. After the experimental dataset is measured, a Fourier transform shows peaks of the current at integer multiples of the applied frequency. The direct current is isolated as the peak near 0 Hz, and it is used to predict the alternating current. Meanwhile, the fundamental harmonic current is isolated as the peak near the applied frequency. The polar plot is generated from the alternating current by fitting the current to the form $I(\omega t) = \Delta I \cdot \sin(\omega t + \phi)$, over each cycle of the alternating potential, with ΔI as the radius of the plot and ϕ as the angle. The faradaic current is isolated by subtracting the effects of cell resistance and background current. Finally, the unknown parameters are iterated

until the predicted alternating current agrees with the experimental alternating current.

It should be noted that the process of isolating different harmonics is used in Fourier transform ACV (FTACV), where several harmonics are generated at once from a high-amplitude sinusoidal potential ($\Delta E \sim 50$ mV), and ΔI is analyzed for each harmonic.^{42–44} In contrast to FTACV, here we use a small-amplitude sinusoidal potential ($\Delta E = 5$ mV) to generate only the fundamental harmonic, and we analyze both ΔI and ϕ . Harmonics arise from a Taylor series expansion of the exponential terms in the Butler-Volmer equation (see Eqs. S19 and S20 in the appendix).

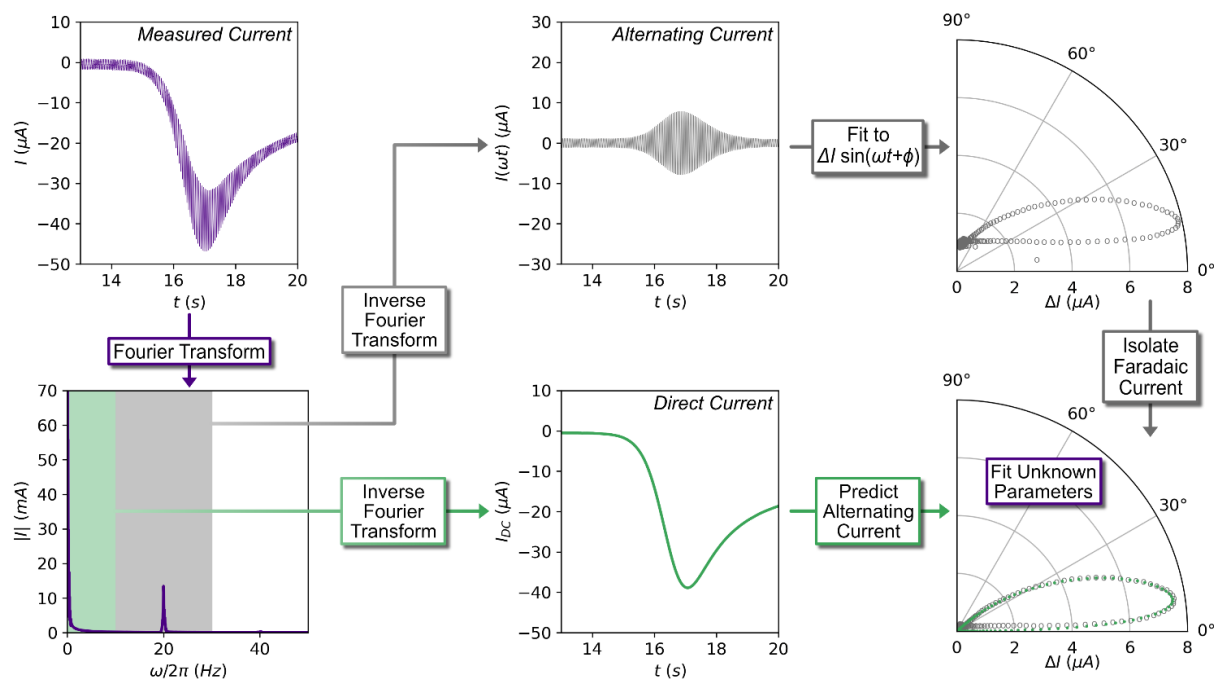


Figure 2.2. Schematic of the data extraction/fitting process using representative data from **1-Br**. The direct current is separated from the alternating current, and it is used to predict the theoretical alternating current. Best-fit parameters are found when the prediction agrees with the isolated faradaic alternating current. Experimental conditions: 2 mM **1-Br** and 0.2 M Bu₄NPF₆ in acetonitrile, with a 3 mm glassy carbon working electrode, Pt wire counter electrode, and Ag/AgNO₃ reference electrode at 22 °C. The solution was purged with nitrogen before each scan. For the applied potential, $\nu = 50$ mV s⁻¹, $\Delta E = 5$ mV, and $\omega = 2\pi \cdot 20$ Hz.

Isolating the Faradaic current in the polar plot involves corrections for both cell resistance and background current, illustrated in Figure 2.3 for **1-Br**. The polar plot has the advantageous feature of retaining the size and shape of the current throughout these corrections. Subtraction of the cell resistance (along a vector parallel to the measured current but in the opposite direction) essentially rotates the current counterclockwise, increasing the phase angle from ϕ_m to ϕ' while

lowering the alternating potential magnitude from ΔE_m to ΔE (Figure 2.3A).⁴⁵ After correction for cell resistance, the background current can be subtracted.

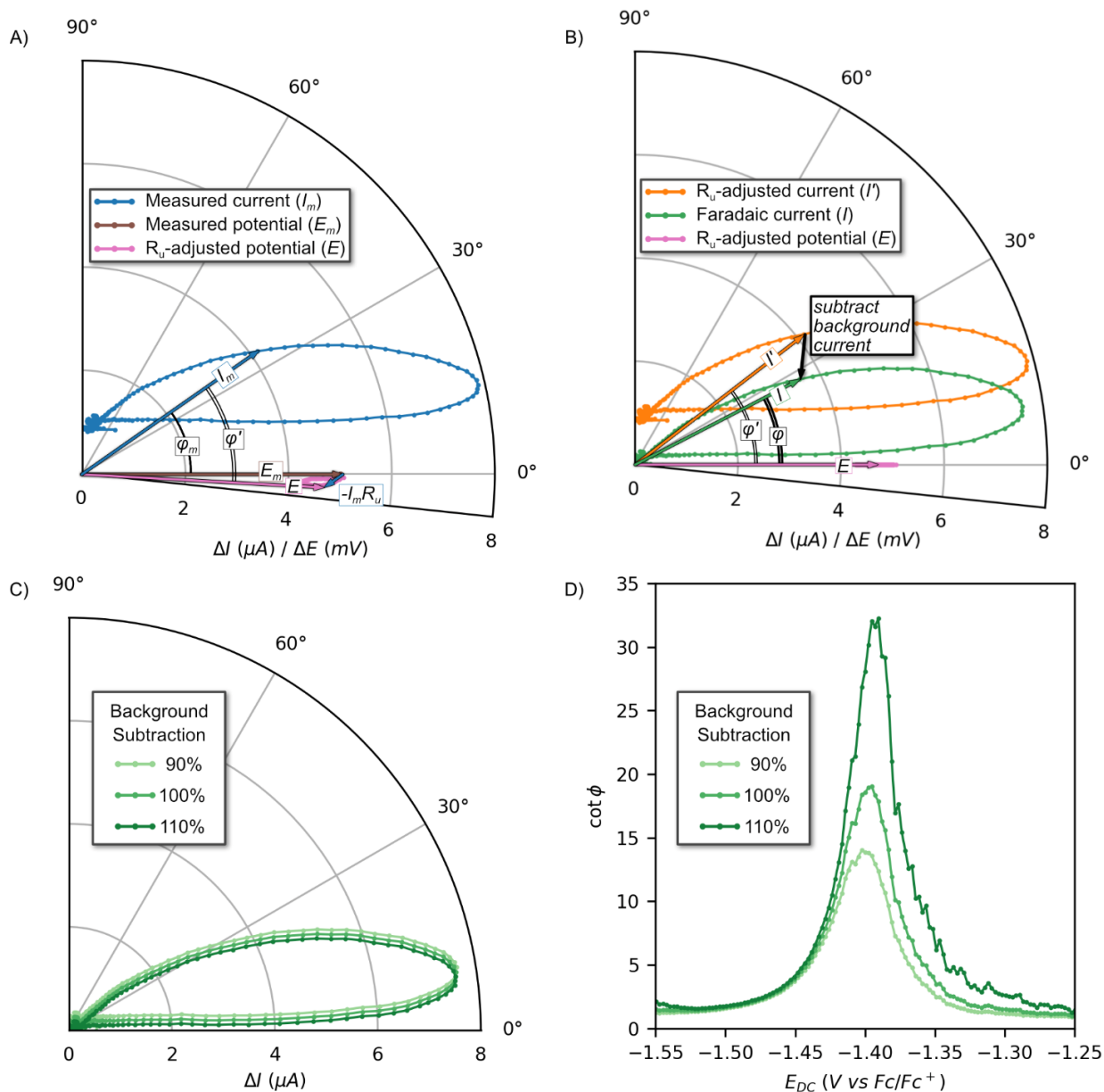


Figure 2.3. Experimental corrections for cell resistance and background current, illustrated for **1-Br**. A) Correction for cell resistance. B) Correction for background current. C) Sensitivity of a polar plot to variations in background subtractions. D) Sensitivity of a $\cot(\phi)$ plot to the same variations in background subtractions. Experimental conditions: 2 mM **1-Br** and 0.2 M Bu₄NPF₆ in acetonitrile, with a 3 mm glassy carbon working electrode, Pt wire counter electrode, and Ag/AgNO₃ reference electrode at 22 °C. The solution was purged with nitrogen before each scan. For the applied potential, $\nu = 50 \text{ mV s}^{-1}$, $\Delta E = 5 \text{ mV}$, and $\omega = 2\pi \cdot 20 \text{ Hz}$.

The polar plots here offer another benefit, immediately revealing the necessary background

subtraction, which only requires displacing the current to start/end at the origin (Figure 2.3B). The retention of the shape and size of a polar plot of the current allows qualitative interpretation of data, even with small variations in these corrections (Figure 2.3C). By contrast, the historically favored plots of $\cot(\varphi)$ give no indication of how much background current to subtract, and small changes in the subtraction can cause large variations in the plot for systems with rapid dimerization kinetics (Figure 2.3D).

Once the faradaic current has been isolated, it can be fit to the theory for electron transfer with subsequent dimerization. Here, we present a refined theoretical description of the concentration of the neutral radical c_r , accounting for its dependence on position, in contrast to previous descriptions.^{31,40,45} A full derivation of the fundamental harmonic solution is provided in the Supporting Information.

The concentration of radical intermediate is governed by the nonlinear equation:

$$\frac{\partial}{\partial t} c_r = D \frac{\partial^2}{\partial x^2} c_r - k_D c_r^2$$

where D is the diffusion coefficient. The concentration c_r can be written as the sum of direct (c_{r0}) and alternating (c_{r1}) components, analogous to the current. Expanding in this way affords the governing equations for c_{r0} and c_{r1} :

$$\begin{aligned} \frac{\partial}{\partial t} c_{r0} &= D \frac{\partial^2}{\partial x^2} c_{r0} - k_D c_{r0}^2 \\ \frac{\partial}{\partial t} c_{r1} &= D \frac{\partial^2}{\partial x^2} c_{r1} - 2k_D c_{r0} c_{r1} \end{aligned}$$

assuming that c_{r1}^2 is negligibly small. The first of these equations can be solved analytically for sufficiently fast k_D with a steady-state assumption, $\partial/\partial t \approx 0$, which gives the following form for c_{r0} :

$$c_{r0} = \frac{6D/k_D}{(x - \Lambda)^2}$$

where Λ is an arbitrary constant. Incorporating the flux boundary condition (Eq. S6 in the Supplementary Information) gives an expression for c_{r0} at the electrode surface throughout the experiment:

$$c_{r0}|_{x=0} = \left(\frac{I_{DC}}{nFA} \right)^{2/3} \left(\frac{3}{2Dk_D} \right)^{1/3}$$

In this way, $c_{r0}|_{x=0}$ is calculated from the experimental I_{DC} , instead of from external simulations.

The governing equation for c_{r1} is linear, so a Laplace transform may be taken. Doing so gives the following equation:

$$\frac{\partial^2}{\partial x^2} \overline{c_{r1}} = \left(\frac{s}{D} + \frac{2k_D c_{r0}}{D} \right) \overline{c_{r1}}$$

where s is the Laplace variable and an overbar denotes a Laplace transformed function. If c_{r0} is assumed to be constant with respect to position, this equation has a solution of the form

$$\overline{c_{r1}} = e^{-x \sqrt{\frac{s}{D} + \frac{2k_D c_{r0}}{D}}}$$

whose inverse transform gives the result previously published.⁴⁰ By contrast, incorporating the position-dependent expression for c_{r0} above gives the equation

$$\frac{\partial^2}{\partial x^2} \overline{c_{r1}} = \left(\frac{s}{D} + \frac{12}{(x - \Lambda)^2} \right) \overline{c_{r1}}$$

which has a Whittaker function for a solution (see Supporting Information). The full equation used to predict the fundamental harmonic alternating current is provided in Eq. S117 in the Supplementary Information.

We used this refined theory to simulate the data shown below in Figure 2.4, which illustrates the dependence of faradaic AC voltammograms on eight parameters (the diffusion coefficient D , the alternating potential magnitude ΔE , the bulk concentration of substrate c^0 , the linear potential scan rate ν , the dimerization rate constant k_D , the alternating frequency ω , the electron transfer rate constant k^0 , and the symmetry coefficient α). The effects of the different parameters are tied to the rates of dimerization and charge transfer on the timescale of the ACV experiment. If less dimerization takes place on the ACV timescale (for example, from a slower k_D or a faster ω), the system approaches a flat line at 45° (fully reversible behavior). On the other hand, if the dimerization rate constant k_D is very fast, the loop becomes fat and nearly horizontal, sitting on the x -axis. A slow electron transfer rate constant k^0 adds resistance to the experiment, lowering both the magnitude of the current and its phase angle. As k^0 is raised, the loop approaches an upper size limit (this effect is also seen in CV, where the peak current approaches an upper limit for a "fully reversible" redox system with fast electron transfer kinetics). There are also parameters which affect the magnitude of the current but have little effect on its phase angle, for example the diffusion coefficient D , the alternating potential magnitude ΔE , the bulk concentration c^0 , and the linear potential scan rate ν . These parameters all affect the amount of charge passed more than they affect the relative rates of dimerization and charge transfer on the experimental timescale. Finally,

the symmetry coefficient α has no significant effect either on the amount of charge passed or on the relative rates of dimerization and charge transfer.

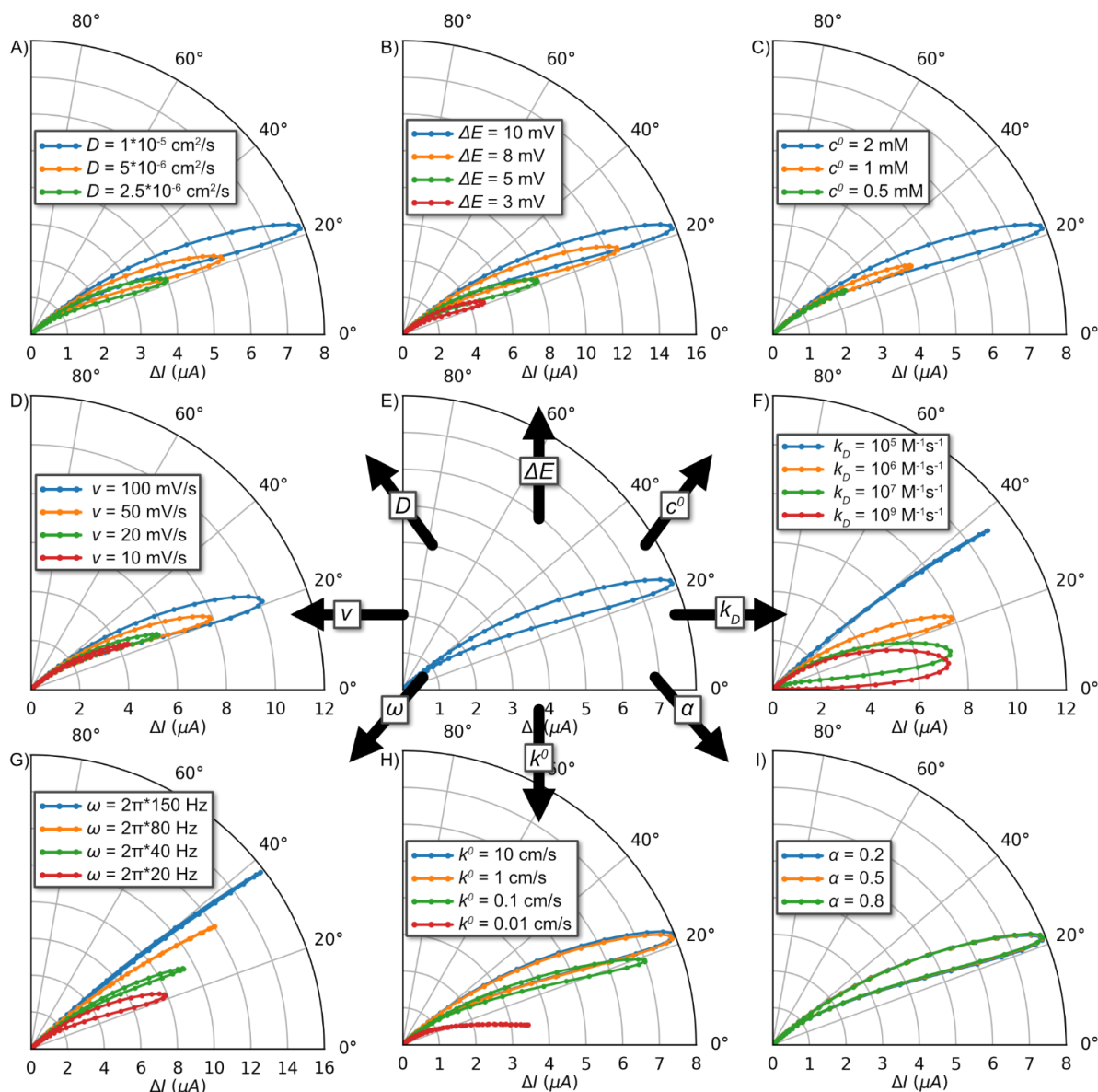


Figure 2.4. Simulated ACV polar plots, showing the influence of different parameters on the fundamental harmonic current. The plots were predicted from Equation 117 in the Supporting Information, with simulated CV data from DigiElch for I_{DC} , c_{o0} , and c_{r0} . The plot in the center was produced with the following parameters: $c^0 = 2 \text{ mM}$, $\Delta E = 5 \text{ mV}$, $D = 10^{-5} \text{ cm}^2 \text{ s}^{-1}$, $k^0 = 1 \text{ cm s}^{-1}$, $\omega = 2\pi \cdot 20 \text{ Hz}$, $\alpha = \beta = 0.5$, $v = 50 \text{ mV s}^{-1}$, $k_D = 10^6 \text{ M}^{-1} \text{ s}^{-1}$, $T = 295 \text{ K}$, $n = 1$, $A = 0.0707 \text{ cm}^2$. The parameters used for the remaining plots are illustrated on the plots.

With this ACV fitting procedure in hand, we synthesized and tested a family of 12 mNAD^+X^- ($\text{X} = \text{Br}, \text{Cl}$), including two from the literature with enzymatic activity (**2** and **6**).⁴ We also synthesized and tested a literature control, 1-methyl-4-*tert*-butyl pyridinium perchlorate

(MP), to validate the fitting method. In order to have a diverse representation of structures, the mimetics included both X = Br and X = Cl as counterions, as well as a mixture of sp^2 and sp^3 C-H functional groups in the 1-position. Representative fits of the experimental data are shown in Figure 2.5 (gray circles = experiment, green dots = theory).

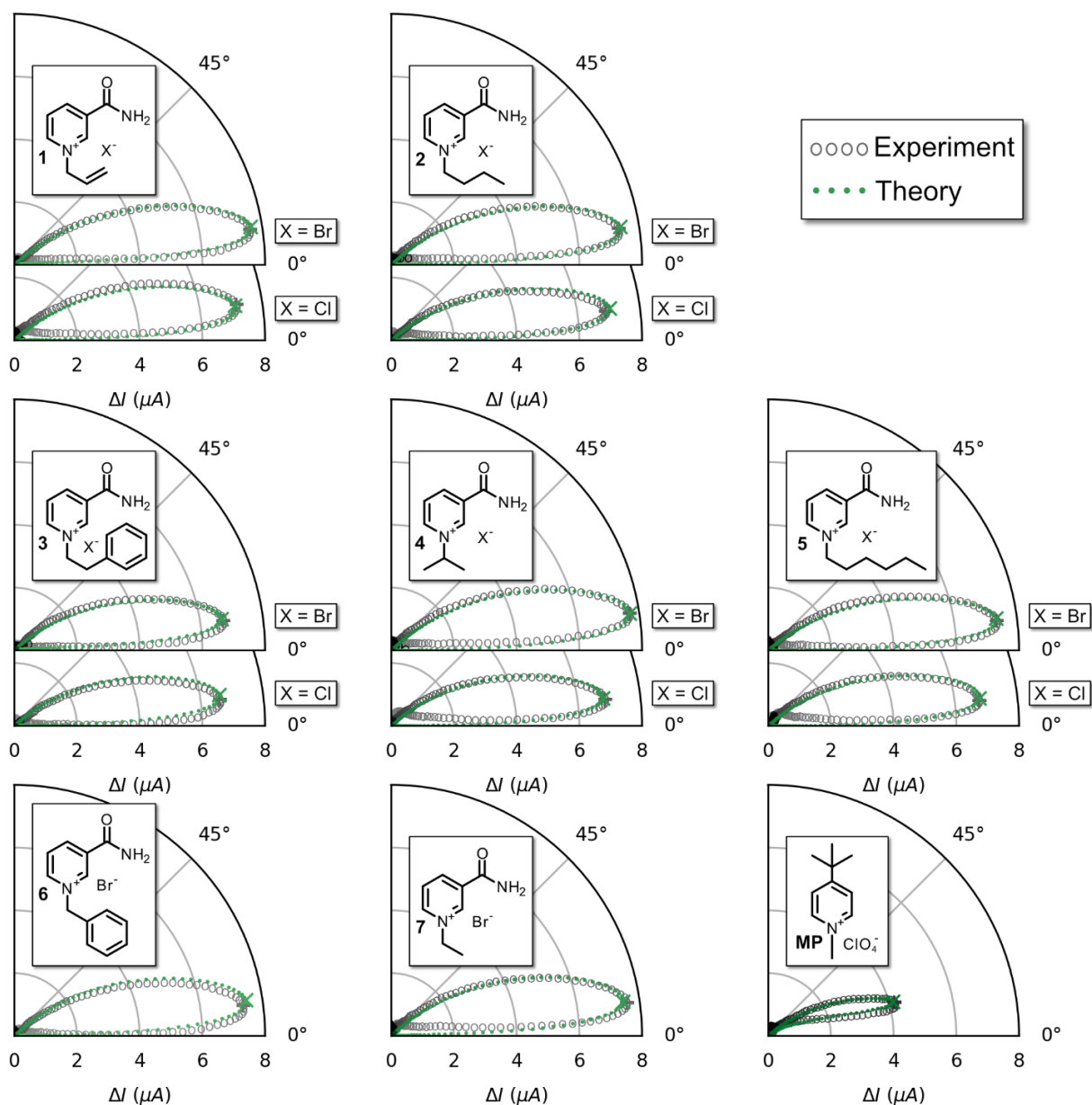


Figure 2.5. Experimental ACV data (gray circles) and representative fits (green dots) for each of the twelve $mNAD^+X^-$, and for the control **MP**. Experimental conditions: 3 mm glassy carbon working electrode, Pt wire counter electrode, and Ag/AgNO₃ reference electrode at 22 °C. The solution was purged with nitrogen before each scan. Potential input was a 50 mV s⁻¹ linear sweep potential plus a sinusoidal potential with a magnitude of 5 mV and a frequency of 20 Hz. For $mNAD^+X^-$, the solution was 2 mM substrate and 0.2 M Bu₄NPF₆ in acetonitrile. For **MP**, the solution was 1 mM substrate and 0.25 M LiClO₄ in acetonitrile.

To make the linear scan potential E_{DC} visible in the plot, the potential at peak ΔI_m (peak signal/noise) was marked with a small indicator (gray “+” for experiment, green “x” for theory). Thus, not only were the parameters E^0 , k^0 , k_D , and α iterated until the loops were the same shape and size, but they were also iterated until the predicted potential at peak signal was the same between experiment and theory. In this fitting process, we assumed that the diffusion coefficients of the oxidized and reduced mNAD were the same. The diffusion coefficient D was found from convolution voltammetry, by manually iterating D until the change in the convolution integral equaled the change in the bulk concentration (the method, also called semiintegration, is described by Oldham and Spainer⁴⁶). We also used the corrected potential ΔE in place of the nominal potential ΔE_m when predicting the fundamental harmonic current. For the 12 mNAD⁺X⁻, the experiments were run with 2 mM substrate and 200 mM Bu₄NPF₆ supporting electrolyte in acetonitrile. For **MP**, the experiments were run with 1 mM substrate and 250 mM LiClO₄ supporting electrolyte in acetonitrile, according to the procedure of Hermolin and coworkers.²⁹

The experimental plots of the current in Figure 2.5 can be interpreted qualitatively by reference to Figure 2.4. The broad, horizontal ovals resting on the x -axis for mNAD⁺X⁻ are consistent with dimerization rate constants near $10^9 \text{ M}^{-1} \text{ s}^{-1}$ for these compounds. The slight decrease in ΔI when X = Br is replaced with X = Cl is characteristic of a smaller diffusion coefficient and/or a smaller electron transfer rate constant. The polar plot for **MP**, in contrast to those of mNAD⁺X⁻, rises off the x -axis at a small angle, indicating a dimerization rate constant near $10^6 - 10^7 \text{ M}^{-1} \text{ s}^{-1}$. The smaller concentration of **MP** is also visible as a smaller ΔI .

To quantify the error in the fits as a function of the parameters k_D , k^0 , E^0 , and α , we took the mean absolute error of those data points where the faradaic ΔI was at least 10% of the maximum value, and we weighted each data point by the relative intensity of ΔI at that point (see Figure 2.S24 in the Supplementary Information). Sweeping the parameter space afforded contour plots like those in Figure 2.6, which show the error of the fit as a function of the parameters. For the literature control, **MP**, the fit converged on a small range of best-fit values around $k_D = 6 \times 10^6 \text{ M}^{-1} \text{ s}^{-1}$, identical with the previously reported dimerization rate constant in acetonitrile.²⁹ In other cases, for example **1-Br**, the fits provided a lower limit for k_D and an upper limit for E^0 . For those cases when ACV provided only a lower bound for k_D and an upper bound for E^0 , we utilized density functional theory (DFT) to compute relative values of the reduction potentials E^0 .^{47,48} The relative reduction potential was computed as the difference in energy between the oxidized and

reduced forms of a given mNAD⁺, and the absolute reduction potentials were found by uniform subtraction of a correction factor until all the reduction potentials were less than or equal to the experimental upper bound determined by ACV measurements (see Table 2.S8). Because the upper bound for E^0 depended on the counterion (compare, for example, Figures 2.S27 and 2.S34), a different correction factor was applied for X = Cl and X = Br. Once E^0 was found for each compound, the dimerization rate constant k_D was taken as the range of k_D values at the computed E^0 for which the weighted error was less than 0.15 μA . The results for these and other parameters are listed in Table 2.1.

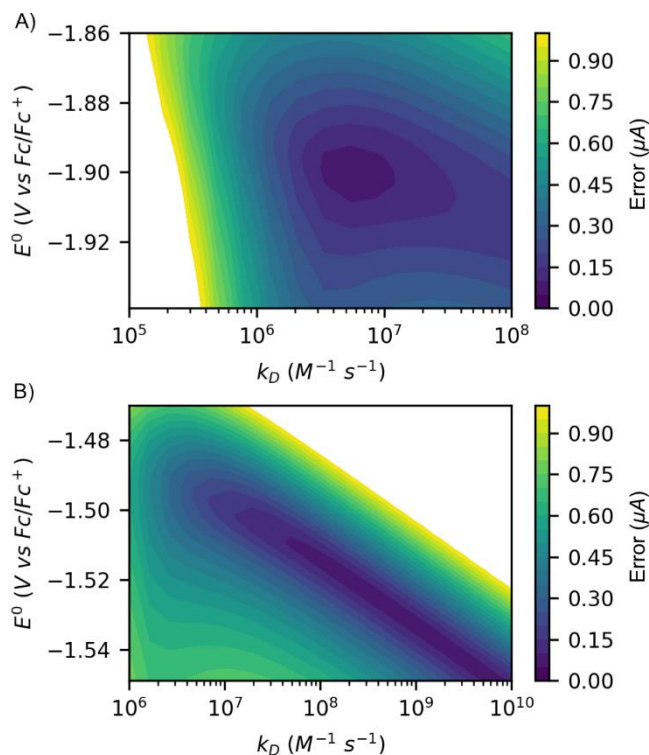


Figure 2.6. Weighted error as a function of the unknown parameters E^0 and k_D , for the substrates A) **MP** and B) **1-Br**. Experimental conditions: 3 mm glassy carbon working electrode, Pt wire counter electrode, and Ag/AgNO₃ reference electrode at 22 °C. The solution was purged with nitrogen before each scan. The applied potential had $\nu = 50 \text{ mV s}^{-1}$, $\Delta E = 5 \text{ mV}$, and $\omega = 2\pi \cdot 20 \text{ Hz}$. For **MP**, the solution was 1 mM substrate and 0.25 M LiClO₄ in acetonitrile. For **1-Br**, the solution was 2 mM substrate and 0.2 M Bu₄NPF₆ in acetonitrile.

$m\text{NAD}^+$	${}^{[a]}R =$	$X =$	E^0 (V vs Fc/Fc ⁺)	k^0 (cm/s)	α	D (10^{-5} cm ² s ⁻¹)	Expt. $\log_{10}(k_D)$ (M ⁻¹ s ⁻¹)	Pred. $\log_{10}(k_D)$ (M ⁻¹ s ⁻¹)	Diffusion Limit $\log_{10}(k_D)$ (M ⁻¹ s ⁻¹)
1	allyl	Br	-1.515	≥ 2	≤ 0.4	1.50	8.0 ± 0.3	8.1 ± 0.3	9.5
2	butyl	Br	-1.564	≥ 2	≤ 0.5	1.38	8.6 ± 0.3	9.0 ± 0.3	9.4
3	phenethyl	Br	-1.534	≥ 2	^[b]	1.16	7.9 ± 0.3	8.0 ± 0.3	9.4
4	isopropyl	Br	-1.591	≥ 2	^[b]	1.49	9.2 ± 0.2	9.1 ± 0.2	9.5
5	hexyl	Br	-1.591	≥ 1	≤ 0.3	1.42	9.6 ± 0.3	9.7 ± 0.3	9.5
6	benzyl	Br	-1.505	≥ 2	≤ 0.4	1.41	8.6 ± 0.3	8.5 ± 0.3	9.5
7	ethyl	Br	-1.567	≥ 2	^[b]	1.43	8.4 ± 0.3	8.7 ± 0.3	9.5
1	allyl	Cl	-1.538	≥ 1	≤ 0.6	1.35	8.9 ± 0.3	8.5 ± 0.3	9.4
2	butyl	Cl	-1.587	2 ± 1	≤ 0.3	1.27	9.2 ± 0.2	9.3 ± 0.2	9.4
3	phenethyl	Cl	-1.557	1 ± 0.5	≤ 0.4	1.11	8.5 ± 0.3	8.3 ± 0.3	9.4
4	isopropyl	Cl	-1.614	2 ± 1	≤ 0.4	1.22	9.6 ± 0.3	9.4 ± 0.3	9.4
5	hexyl	Cl	-1.614	2 ± 1	≤ 0.3	1.20	10.4 ± 0.3	10.1 ± 0.3	9.4

Table 2.1. Best-fit parameters for the family of $m\text{NAD}^+\text{X}^-$ under study. Experimental conditions: 3 mm glassy carbon working electrode, Pt wire counter electrode, and Ag/AgNO₃ reference electrode at 22 °C. Solutions were purged with nitrogen before each scan. Potential input was a 50 mV/s linear sweep potential plus a sinusoidal potential with a magnitude of 5 mV and a frequency of 20 Hz. Compounds **1-7** were run at 2 mM in acetonitrile with 0.2 M Bu₄NPF₆, while **MP** was run at 1 mM in acetonitrile with 0.25 M LiClO₄. [a] Compounds listed are 1-substituted salts of nicotinamide. [b] In these cases, α did not significantly affect the quality of the fit.

Inspection of the data in Table 2.1 shows that the reduction potential E^0 becomes more negative when the counterion $X = \text{Br}$ is replaced with $X = \text{Cl}$, and that E^0 becomes more positive when sp^2 carbons rather than sp^3 carbons are closer to the redox active nicotinamide site. The ability of the counterion to influence the reduction potential suggests that $m\text{NAD}^+\text{X}^-$ may be reduced as ion pairs, rather than as lone $m\text{NAD}^+$ ions.

The best-fit values for k^0 are rapid in all cases ($k^0 \geq 1$ cm s⁻¹), consistent with the frequently made assumption of Nernstian electron transfer kinetics in systems with rapid dimerization.⁴⁹ The counterion does appear to have a small effect on electron transfer kinetics, however, as evidenced by best-fit k^0 values less than about 3 cm s⁻¹ for $X = \text{Cl}$, while no upper limit of k^0 was observed for $X = \text{Br}$.

The symmetry coefficient α is in most cases less than 0.5, which may indicate a “product-like” transition state for the one-electron reduction of $m\text{NAD}^+\text{X}^-$.¹⁶ However, the effect of α on the quality of the fit was very small, and in several cases negligible.

The values of the diffusion coefficient D for $m\text{NAD}^+\text{X}^-$ range between 1.1 – 1.5 x 10⁻⁵ cm² s⁻¹, with a slight drop when $X = \text{Br}$ is replaced with $X = \text{Cl}$. In the CVs used to determine the diffusion coefficients, we observed a non-faradaic prewave just before the reduction event for $m\text{NAD}^+\text{Cl}^-$, which was virtually absent for $m\text{NAD}^+\text{Br}^-$. By ACV, this prewave had a phase angle larger than 45°, indicating capacitance-like behavior, perhaps due to adsorption. Differential subtraction of this prewave from the convolution voltammograms may be a reason for the

differences in D . An alternative explanation is that a higher extent of ionic aggregation with $X = \text{Cl}$ may cause these mimetics to diffuse more slowly compared to $X = \text{Br}$.

For the dimerization rate constant k_D , best-fit values are at or near the respective diffusion limits in acetonitrile, with **5-Cl** notably dimerizing faster than the diffusion limit. The diffusion-limited k_D values were found from $4\pi rDN_A$, where r is the radius of the compound and N_A is Avogadro's number.⁵⁰ We assumed that reactivity was localized to the nicotinamide site, independent of the mimetic 1-substituent, and therefore that r was the same for all compounds. We determined a value of $r = 2.7 \text{ \AA}$ from the crystal structure for **1-Br**, measured as half the distance between nearest-neighbor pyridinium N atoms; this value agreed with the collision radii of the similarly-sized benzene ($r = 2.7 \text{ \AA}$) and pyridine ($r = 2.9 \text{ \AA}$).^{51,52}

To investigate which molecular features influence the dimerization rate constant, we turned to quantitative structure-activity relationship (QSAR) modeling,⁵³ and we found that the logarithm of k_D correlated with the steric size of the pyridinium 1-substituent, and inversely with the reduction potential E^0 (Figure 2.7; a brief explanation of QSAR is provided with Table 2.S9). The Sterimol $B5$ parameter, which measures the largest radius of a group perpendicular to the axis of attachment, was used as a descriptor of steric size.^{54,55}

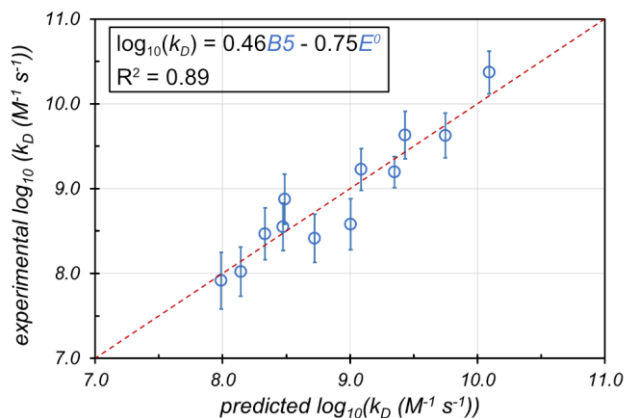


Figure 2.7. Predicted and experimental $\log_{10}(k_D)$ values from linear regression analysis. The Sterimol $B5$ parameter was used as a measure of the steric size of the pyridinium 1-substituent.

The positive correlation between sterics at the pyridinium 1-position and dimerization rate may indicate preferential dimerization at the 4-position. Dimerization of 1-substituted pyridine radicals is known to be possible at either the 4-position or the 6-position.²⁴ When the 4-position is blocked, dimerization at the 6-position is favored, and increasing sterics at the 1-position can slow down decomposition rates.^{29,56} In our case, the 4-position is available, and bulky 1-substituents

could force mNAD^+X^- aggregates in solution to adopt head-to-head orientations, placing the 4-positions near each other. Such an explanation would account, for example, for the faster dimerization of **6-Br** over **3-Br**: although the phenethyl group of **3-Br** is longer than the benzyl group of **6-Br**, the phenethyl group can extend nearly parallel to the axis of attachment, while the benzyl group must extend away from the axis of attachment at a large angle, giving a faster dimerization rate.

The data for reduction potential, electron transfer rate constant, diffusion coefficient, and dimerization rate constant, are all consistent with an electrochemical reduction of mNAD^+X^- ion pairs rather than lone mNAD^+ ions. Switching the mimetic counterion from $\text{X} = \text{Br}$ to the more strongly coordinating $\text{X} = \text{Cl}$ causes an increase in the dimerization rate constant k_D , and it causes a decrease in the reduction potential E^0 , in the diffusion coefficient D , and in the electron transfer rate constant k^0 . These correlations suggest that the electrochemistry of mNAD^+ is heavily influenced by ionic interactions in solution; indeed, interactions between mNAD^+ and X^- are visible in concentration-dependent NMR experiments, shown in Figure 2.8 for compound **2**. The ionic interactions are located at the pyridinium 2- and 4-positions, with the strongest interaction at an amide proton adjacent to the 2-position. This ionic interaction dominates over complementary H-bonding interactions between amide groups, which are not observed at these concentrations in acetonitrile. Crystal structures show that the amide group is sometimes inverted, placing proton H_E near the 4-position (see, for example, Figures 2.S17 and 2.S20 in the Supplementary Information). The possibility for one mNAD^+ to interact with X^- in at least two different locations suggests that higher order aggregation of mNAD^+X^- may indeed be happening in solution, accounting for the observed trend in dimerization rates.

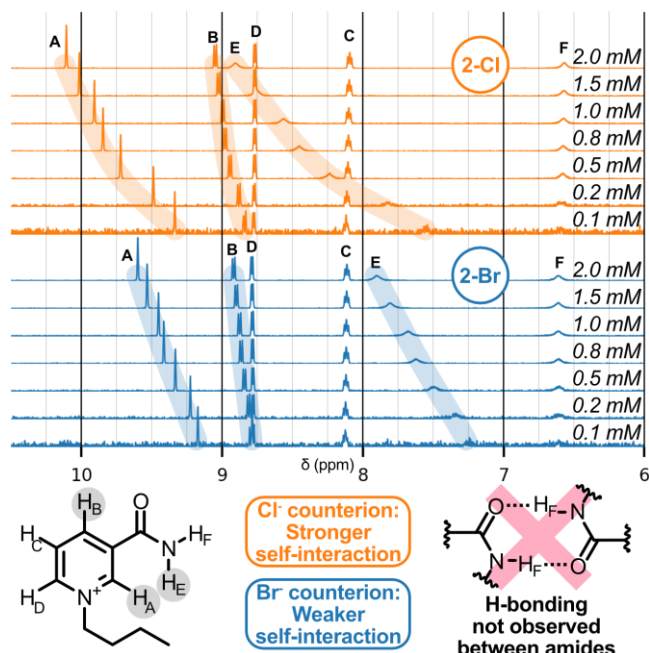


Figure 2.8. Concentration-dependent NMR data for **2-Cl** and **2-Br**, showing downfield chemical shifts of protons in the 2- and 4- positions (H_A and H_B), as well as of the amide proton *cis* to the aromatic ring (H_E), at higher concentrations. Downfield shifts are also observed upon replacing Cl with Br at a given concentration. The mimetic was diluted with CD_3CN to the concentration listed, and spectra were gathered on an Agilent 500 MHz NMR spectrometer.

CONCLUSION

ACV is a powerful electrochemical tool, able to probe the challenging kinetic systems relevant to bioelectrocatalysis. By applying ACV to a family of $mNAD^+$, analogues of one of the most common biological redox cofactors, we found the rate constants for electrochemical dimerization were close to the theoretical diffusion limit in acetonitrile ($k_D = 10^8 - 10^{10} M^{-1}s^{-1}$). Estimates for these dimerization rate constants could be obtained by visual inspection of polar plots of ACV data, after familiarization with a few plots of simulated data. This ability to interpret ACV data intuitively recommends the technique for broad application to electrochemical systems. The positive correlation between k_D and sterics at the pyridinium 1-position, together with the counterion-dependence of E^0 , k^0 , and D , all suggest that the reduction of this family of $mNAD^+X^-$ involves the reduction of aggregates of ion pairs rather than the reduction of lone $mNAD^+$ ions, with preferential dimerization at the pyridinium 4-position. The reliability of ACV results was validated by replicating literature results for a model pyridinium compound, **MP**. The combination of ACV with computational chemistry offers a high degree of insight on the structure-reactivity relationships of $mNAD^+$, enabling design of regenerable $mNADH$ systems for bioelectrocatalysis.

CHAPTER 3: IMPACT OF SODIUM PYRUVATE ON THE ELECTROCHEMICAL REDUCTION OF NAD⁺ BIOMIMETICS^k

ABSTRACT

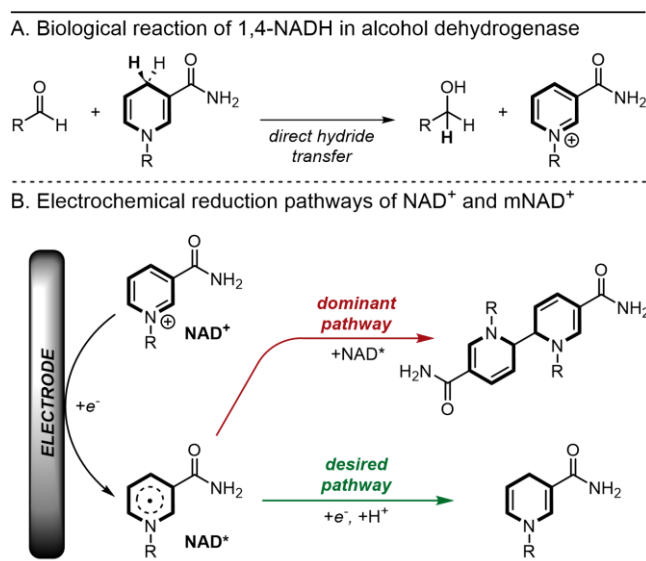
Biomimetics of nicotinamide adenine dinucleotide (mNADH) are promising cost-effective alternatives to their natural counterpart for biosynthetic applications; however, attempts to recycle mNADH often rely on coenzymes or precious metal catalysts. Direct electrolysis is an attractive approach for recycling mNADH, but electrochemical reduction of the oxidized mimetic (mNAD⁺) primarily results in the formation of an enzymatically inactive dimer. Herein, we find that aqueous electrochemical reduction of an NAD⁺ mimetic, 1-*n*-butyl-3-carbamoylpyridinium bromide (**1**⁺), to its enzymatically active form, 1,4-dihydro-1-*n*-butyl nicotinamide (**1H**), is favored in the presence of sodium pyruvate as a supporting electrolyte. Maximum formation of **1H** is achieved in the presence of a large excess of pyruvate in combination with a large excess of a co-supporting electrolyte. Formation of **1H** is found to be favored at pH 7, with an optimized product ratio of ~50/50 dimer/**1H** observed by cyclic voltammetry. Furthermore, sodium pyruvate is shown to promote electroreductive generation of the 1,4-dihydro form of several additional mNADH as well as NADH itself. This method provides a general strategy for regenerating 1,4-dihydro-nicotinamide mimetics of NADH from their oxidized forms.

INTRODUCTION

Recently there has been a significant expansion in the use of bioelectrocatalysis for environmentally friendly organic synthesis.⁶² In bioelectrocatalysis, redox enzymes drive highly selective redox reactions under mild aqueous conditions, and the corresponding enzyme cofactor is regenerated with an electrode as the terminal oxidant/reductant. One cofactor, nicotinamide adenine dinucleotide (phosphate) (NAD(P)⁺/NAD(P)H), holds special appeal for bioelectrocatalysis, because it is used by half of documented oxidoreductases³⁶; however, its commercial utilization is limited by its high cost. A promising step towards low-cost redox cofactors was demonstrated with simple NADH mimetics (mNADH), such as 1-*n*-butyl-1,4-dihydronicotinamide (**1H**), that were shown to exhibit activity with enoate reductase, hydroxybiphenyl monooxygenase, and BM3 cytochrome p450.^{4,9,63-65} Both the natural cofactor, NADH, and its mimetics commonly function as hydride donors, undergoing a concerted two-

^k This chapter previously appeared in *Faraday Discussions*, 2023, 247, 87-100. Reprinted with permission.

electron/one-proton transfer to yield the oxidized form, NAD^+ ; however, direct electrochemical reduction of NAD^+ and its mimetics proceeds via sequential single electron/proton transfers. These reductions can be intercepted after the first electron transfer, with rapid formation of enzymatically inactive dimers (rate constant for dimerization exceeds $10^7 \text{ M}^{-1}\text{s}^{-1}$).²⁸ The first one-electron reduction of NAD^+ occurs between -0.9 V and -1.2 V , and the resulting neutral pyridine radical can be further reduced near -1.6 V to form the enzymatically active 1,4-dihydropyridine (all potentials reported vs SCE).^{66,67}



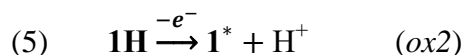
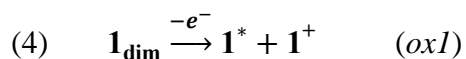
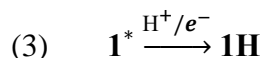
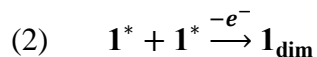
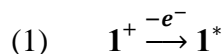
Scheme 3.1. (A) Example biological reaction involving NADH , where alcohol dehydrogenase catalyzes the reduction of an aldehyde to an alcohol. The reaction proceeds via hydride transfer. (B) Mechanism for direct electrochemical reduction of NAD^+ . The reaction proceeds via sequential electron-proton transfer and is intercepted after the first electron to form dimer rather than the desired biologically active NADH .

In practice, however, the electrochemical yields of enzymatically-active NADH from constant potential electrolysis are near 65-76%, and no NADH is observed at moderate reduction potentials (*ca.* -1.2 V).²⁴ While methods do exist to optimize the yield of electrochemically generated NADH above even 90%, for example Rh hydride-transfer catalysts^{3,64} and Pt -patterned glassy carbon electrodes⁶⁸, these methods are limited by slow turnover rates and a sensitivity to the precise voltage/metal surface coverage. While the operational simplicity of direct electrochemistry and its high theoretical (m) NADH regeneration rate (limited only by mass transport) hold promise for bioelectrocatalysis, its use is still limited by the undesired dimerization reaction.

While it is known that the supporting electrolyte can play a critical role in governing the product distribution of electrochemically-coupled chemical reactions,⁶⁹⁻⁷⁴ little attention has been given to the role of supporting electrolyte in the electrochemical reduction of NAD⁺ or its mimetics.⁷⁵ In light of this, we considered the possibility that dimerization could be minimized in electrochemical (m)NAD⁺ reduction through judicious choice of supporting electrolyte. We chose **1H** as a model cofactor, hypothesizing that supporting electrolyte could lower the relative rate of dimerization and increase the relative rate of **1H** formation during electrochemical reduction of the mimetic's oxidized form, 1-*n*-butyl nicotinamide bromide (**1**⁺). To test this hypothesis, we screened the electrochemistry of the bromide salt of **1**⁺ in 28 different supporting electrolytes at a boron-doped-diamond electrode, and we compared this against the electrochemistry of **1H** formed by dithionite reduction. We used cyclic voltammetry for its operational simplicity, and for the ease with which information about concentration profiles and product distributions could be extracted.

RESULTS AND DISCUSSION

The cyclic voltammogram (CV) for 2 mM **1**⁺ in aqueous 200 mM sodium bicarbonate reveals an irreversible reduction peak at -1.3 V and an irreversible oxidation peak at -0.05 V (*ox1*) (all potentials reported vs SCE). The potential of *ox1* is consistent with that of a dimer formed by electrochemically generated neutral radical species of **1**⁺ (i.e., **1**^{*}).²⁷ By contrast, CVs of the chemically prepared, pure form of **1H** result in no peak at 0 V during the initial scan, but instead a large irreversible oxidation peak is observed near 0.44 V (*ox2*) followed by a reduction peak at -1.3 V matching that of **1**⁺. After the first cycle, an oxidation peak consistent with *ox1* becomes visible (Figure 1). A summary of this general reaction mechanism is given by:



where **1**_{dim} is the electrochemically dimerized mimetic. The presence of two distinct peaks corresponding to electrochemical oxidation of the dimer (*ox1*) and oxidation of the 1,4-dihydropyridine **1H** (*ox2*) provides a convenient means to measure the relative amounts of dimer and **1H** generated upon electrochemical reduction under variable conditions.

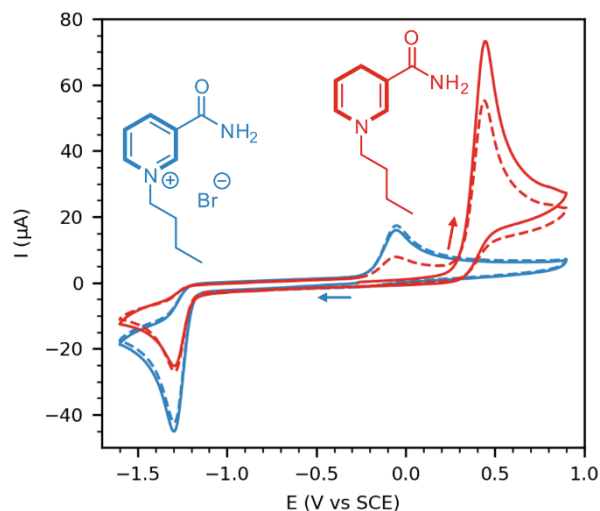


Figure 3.1. Representative cyclic voltammograms of 2 mM 1-*n*-butyl nicotinamide bromide, **1**⁺, (blue) and 2 mM 1,4-dihydro-1-*n*-butyl nicotinamide, **1H**, (red). Solid curves represent the first CV scans, while dashed lines represent the second CV scans. Experiments were performed using a 2 mm boron doped diamond working electrode, saturated calomel reference electrode, and platinum wire counter electrode, with 200 mM aqueous NaHCO₃ purged with N₂ and at 25 °C and 800 mV s⁻¹.

To determine the impact of supporting electrolyte on the distribution of peaks corresponding to dimer and dihydro species (*ox1* and *ox2*, respectively), CVs of 2 mM **1**⁺ were performed in 28 different supporting electrolytes, including Na⁺, K⁺, Li⁺, Ca²⁺, Mg²⁺, NH₄⁺, or organic ammonium cations with halide, sulfate, phosphate, nitrate, carbonate, azide, or borate anions. Additionally, sodium and potassium salts of several organic anions were tested, including acetate, citrate, oxalate, gluconate, propionate, and pyruvate. The resulting voltammograms are summarized in Table 3.1. For most of the electrolytes studied, **1_{dim}** was the only observable reduction product. The CVs were qualitatively nearly identical with only small variations in the reduction event ($E_{pc} = -1.3$ V, $i_{pc} = 35\text{--}45$ mA) and moderate variations in *ox1* ($E_{pa1} = -0.07\text{--}0$ V, $i_{pa1} = 11\text{--}19$ mA). A small additional oxidation event ($E_{pa2} = 0.35$ V, $i_{pa2} < 0.1$ mA) was observed in the most acidic solutions (NaH₂PO₄ and NH₄H₂PO₄, where pH < 5), indicating a general pH dependence for the product distribution of electrochemically reduced **1**⁺.

Electrolyte	peak current / μA			peak potential / V vs SCE ^[a]			pH
	1^+ reduction	dimer oxidation (ox1)	1H oxidation (ox2)	1^+ reduction	dimer oxidation (ox1)	1H oxidation (ox2)	
Na ₂ CO ₃	42.5 ± 0.2	17.4 ± 0.1	-	-1.295 ± 0.001	-0.049	-	11.2
NaN ₃	43.76 ± 0.07	18.22 ± 0.01	-	-1.296	-0.056	-	10.1
Na ₂ B ₄ O ₇ ^[b]	41.35 ± 0.03	15.62 ± 0.06	-	-1.307	-0.049	-	9.6
K ₂ HPO ₄	41.45 ± 0.01	16.7 ± 0.1	-	-1.299	-0.036 ± 0.001	-	9.2
Na ₂ HPO ₄	39.7 ± 0.1	14.81 ± 0.05	-	-1.305 ± 0.001	-0.001 ± 0.001	-	9.1
NaHCO ₃	42.56 ± 0.09	17.41 ± 0.05	-	-1.295 ± 0.001	-0.052 ± 0.002	-	8.9
CaCl ₂	35.7 ± 0.2	13.35 ± 0.08	-	-1.31	0.017 ± 0.002	-	8.8
(NH ₄) ₂ HPO ₄	40.46 ± 0.04	15.14 ± 0.02	-	-1.302	-0.019	-	8.3
Na ₂ SO ₄	41.2 ± 0.1	16.89 ± 0.09	-	-1.304 ± 0.001	-0.012 ± 0.003	-	7.7
KNO ₃	43.6 ± 0.2	17.2 ± 0.04	-	-1.301 ± 0.001	-0.029	-	7.3
LiBr	43.2 ± 0.1	16.73 ± 0.09	-	-1.296	-0.051 ± 0.001	-	7.3
KCl	44.3 ± 0.2	16.95 ± 0.07	-	-1.303	-0.02 ± 0.002	-	7.2
MgSO ₄	41.1 ± 0.1	16.4 ± 0.02	-	-1.299	-0.041	-	7.2
KBr	43.3 ± 0.1	16.59 ± 0.01	-	-1.302 ± 0.001	-0.032 ± 0.001	-	7.1
NaCl	42.9 ± 0.1	18.06 ± 0.09	-	-1.293 ± 0.001	-0.056 ± 0.001	-	6.9
NaBr	43.78 ± 0.05	17.78 ± 0.01	-	-1.301 ± 0.001	-0.039 ± 0.002	-	6.6
NaNO ₃	42.1 ± 0.2	17.0 ± 0.2	-	-1.3 ± 0.001	-0.038	-	6.5
NH ₄ Cl	44.57 ± 0.02	16.31 ± 0.02	-	-1.307 ± 0.001	0.000 ± 0.001	-	6.2
NH ₄ H ₂ PO ₄	40.9 ± 0.1	11.92 ± 0.02	0.04	-1.312	0.012 ± 0.003	0.35 ± 0.002	4.7
NaH ₂ PO ₄	38.3 ± 0.2	10.88 ± 0.03	0.07	-1.303	-0.025 ± 0.001	0.35 ± 0.001	4.6
Na ₃ C ₆ H ₅ O ₇ (citrate)	42 ± 0.2	16.4 ± 0.2	-	-1.304 ± 0.001	-0.036 ± 0.001	-	8.9
K ₂ C ₂ O ₄ (oxalate)	44.49 ± 0.03	18.1 ± 0.1	-	-1.301	-0.033 ± 0.001	-	7.8
Bu ₄ NBr	38.1 ± 0.2	14.42 ± 0.04	-	-1.283	-0.001 ± 0.001	-	7.2
Pr ₄ NBr	39.3 ± 0.2	15.21 ± 0.03	-	-1.289	-0.025 ± 0.001	-	7.2
NaC ₃ H ₃ O ₃ (pyruvate)	44.29 ± 0.07	12.66 ± 0.01	4.4 ± 0.1	-1.314	-0.008 ± 0.001	0.489 ± 0.002	7.0
NaC ₂ H ₃ O ₂ (acetate)	41.2 ± 0.1	15.39 ± 0.09	-	-1.309 ± 0.001	-0.039	-	6.9
NaC ₃ H ₅ O ₂ (propionate)	38.88 ± 0.05	14.85 ± 0.02	-	-1.309	-0.025 ± 0.002	-	6.7
KC ₆ H ₁₁ O ₇ (D- gluconate)	40.7 ± 0.2	15.38 ± 0.05	-	-1.303	-0.037 ± 0.003	-	6.7

Table 3.1. CV output data from inorganic (top) and organic (bottom) electrolytes tested with 1^+ , including the peak currents and peak potentials for 1^+ reduction, 1_{dim} oxidation (ox1), and **1H** oxidation (ox2). Values are reported as the average and one standard deviation with $n = 3$. Experiments were performed using 2 mM 1^+ with 200 mM supporting electrolyte purged with N₂ and at 25 °C and 800 mV s⁻¹. [a] Unless otherwise noted, the standard deviation for a given peak potential was less than 1 mV. [b] 100 mM Sodium tetraborate decahydrate was used.

Among the electrolytes tested, sodium pyruvate stood out for its ability to promote **1H** formation, even at neutral pH ($E_{pa2} = 0.49$ V, $i_{pa2} = 4$ mA at pH 7.0). To better understand the unique effect of sodium pyruvate on the electrochemistry of **1**⁺, we used convolution voltammetry to compare the product distributions in the presence and absence of pyruvate (see Supporting Information for a brief description of convolution voltammetry).^{25,46,76} Convolution voltammetry shows the effective concentration change of a redox-active substrate at the electrode surface, assuming that the substrate participates only in diffusion and electron transfer. The height of the convolution integral is proportional to the number of electrons transferred per molecule. Figure 3.2 shows CVs (top, solid curves) and convolution integrals (bottom, dashed curves) of **1**⁺ at pH 7, in 100 mM sodium phosphate (blue) and in 100 mM sodium phosphate plus 100 mM sodium pyruvate (red). Both graphs show the appearance of *ox2* when sodium pyruvate is added. The convolution integral, when normalized for a one-electron reduction (Figure 3.2B), shows that the concentration of **1**⁺ drops by 2 mM (i.e., the bulk concentration) when reduced without sodium pyruvate, and that it returns to the bulk concentration after *ox1*. By contrast, the effective concentration change with sodium pyruvate is over 4 mM after the reduction event. Part of this change is attributable to the change in mechanism, from a one-electron reduction (**1**⁺ to **1_{dim}**) to a two-electron reduction (**1**⁺ to **1H**). However, part of the change is due to the irreversible reduction of a species other than **1**⁺ in the presence of sodium pyruvate, evidenced by an offset in the convolution integral of ~0.5 mM from the baseline after both oxidation events. With sodium pyruvate, the concentration changes after *ox1* and *ox2* are roughly equal, showing that the concentrations of **1_{dim}** and **1H** are approximately the same after the reduction event (corresponding to ~30% selectivity for **1H** formation).

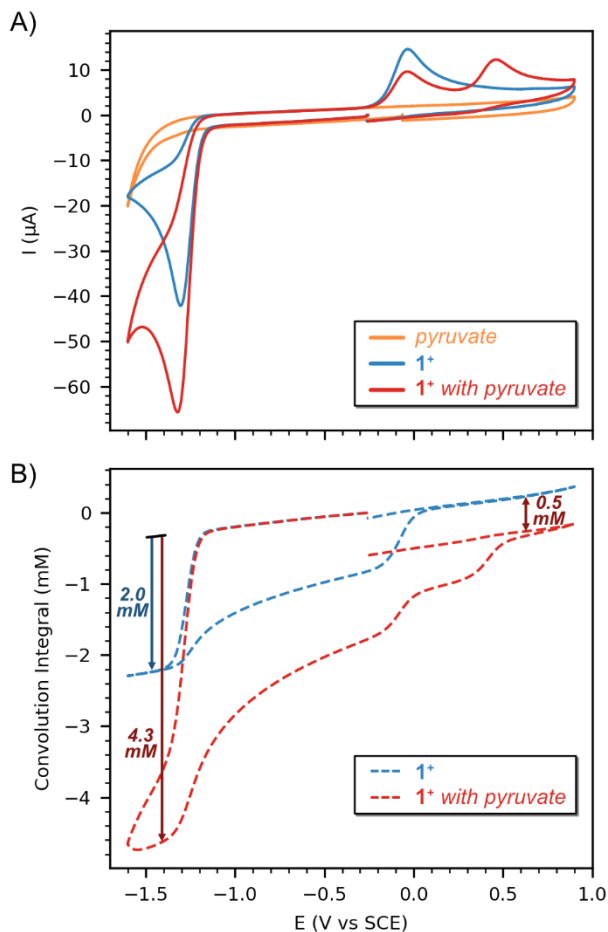


Figure 3.2. (A) Representative cyclic voltammograms and (B) the corresponding convolution integrals of 2 mM 1^+ in the absence (blue) or presence (red) of 100 mM sodium pyruvate, or 100 mM sodium pyruvate alone (orange). Experiments were performed using a 2 mm boron doped diamond working electrode with 100 mM sodium phosphate supporting electrolyte purged with N_2 and at pH 7.0, 25 °C and 800 mV s^{-1} .

To better understand the mechanism of action of sodium pyruvate, we studied the dependence of 1^+ reduction on the concentration of pyruvate, the reduction potential, and the pH of the solution. Voltammetry of 1^+ with variable pyruvate concentration (using sodium bicarbonate as a co-supporting electrolyte to maintain a total supporting electrolyte concentration of 200 mM) revealed that trace amounts of 1H are formed with as little as 2 mM sodium pyruvate (1 eq. with respect to 1^+) (Figure 3.3). Although raising the concentration of sodium pyruvate increased the yield of 1H at low pyruvate concentrations, too much sodium pyruvate was detrimental to the yield of 1H . For example, a 50:50 mixture of sodium bicarbonate/sodium pyruvate yielded more 1H than sodium pyruvate alone, which might suggest a synergistic interaction between pyruvate and the co-supporting electrolyte. A similar result was also observed with a 50/50 mixture of sodium

phosphate/sodium pyruvate, which yielded more **1H** than sodium pyruvate alone.

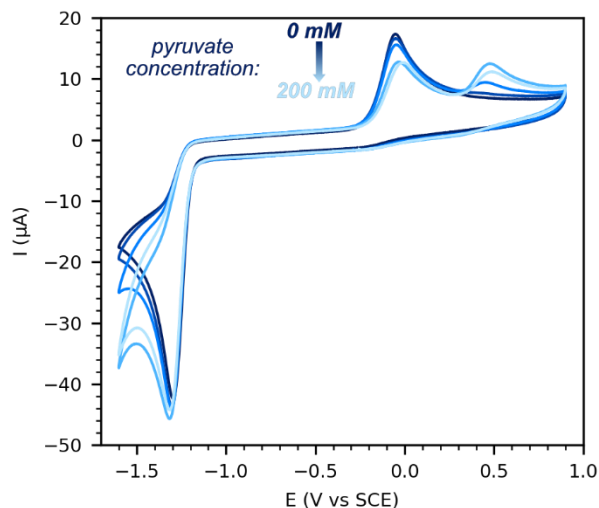


Figure 3.3. Representative cyclic voltammograms of 2 mM **1**⁺ with varying ratios of sodium bicarbonate/sodium pyruvate: 100/0 (darkest), 99/1, 90/10, 50/50, and 0/100 (lightest). Experiments were performed using a 2 mm boron doped diamond working electrode at 25 °C and 800 mV s⁻¹. Solutions were purged with nitrogen before scanning.

We next sought to determine the impact of switching potential on the peak currents corresponding to *ox1* and *ox2* (i_{pa1} and i_{pa2} , respectively) exhibited in CVs of **1**⁺. In sodium pyruvate (200 mM, pH 7.0), both **1**_{dim} and **1H** are formed in the same reduction event, with **1H** favored at lower potentials and **1**_{dim} favored at higher potentials (Figure 3.4A). At a turnaround potential of -1.25 V (green curve), only a trace amount of **1**⁺ is generated during *ox2*, but this amount grows significantly as the potential is lowered to -1.6 V (blue curve). By contrast, the amount of **1**⁺ generated during *ox1* grows more slowly at lower turnaround potentials. Without sodium pyruvate (200 mM sodium phosphate, pH 9.1), no observable **1H** is formed by -1.6 V. Additionally, there is minimal change in product distribution between -1.6 V and -2.1 V (Figure 3.4B). Below -2.1 V, the product distribution shifts away from dimer, yet **1H** is not formed exclusively: at least three new oxidation peaks are observed, and dimer is still the major product. The comparison of these two electrolytes shows a general pH dependence for the electrochemical reduction of **1**⁺ to **1H**, a reaction that happens both more selectively and more quickly with sodium pyruvate than without it.

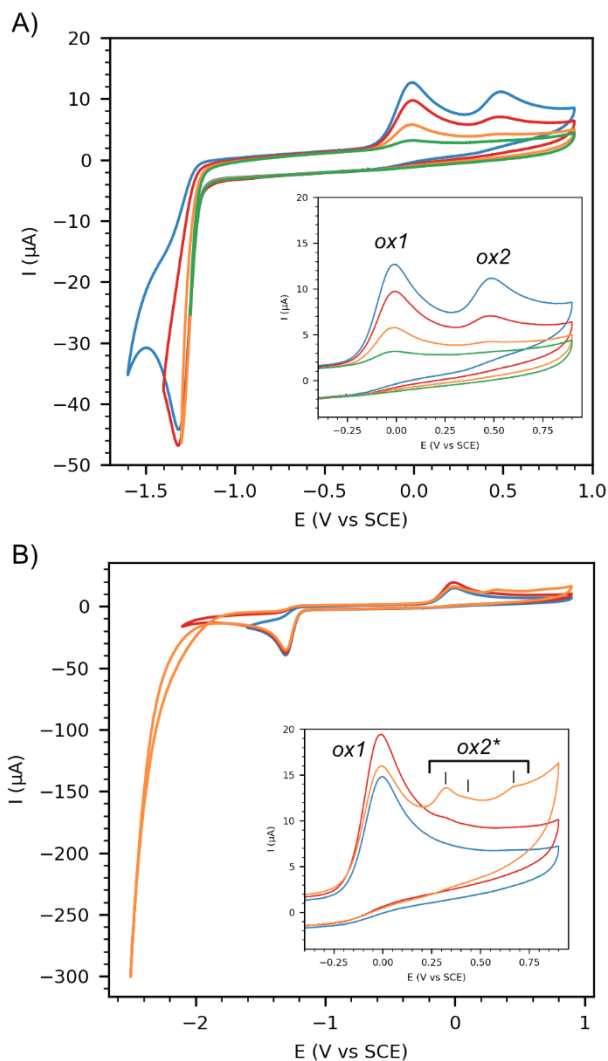


Figure 3.4. (A) Representative cyclic voltammograms of 2 mM $\mathbf{1}^+$ with 200 mM sodium pyruvate with variable turnaround potentials: -1.6 V (blue), -1.4 V (red), -1.3 V (orange), and -1.25 V (green). (B) Representative cyclic voltammograms of 2 mM $\mathbf{1}^+$ with 200 mM Na_2HPO_4 with different turnaround potentials: -1.6 V (blue), -2.1 V (red), and -2.5 V (orange). Experiments were performed using a 2 mm boron doped diamond working electrode at 25 °C and 800 mV s⁻¹. Solutions were purged with nitrogen before scanning.

We also explored the pH dependence of $\mathbf{1}^+$ reduction in 100 mM sodium phosphate, with and without 100 mM sodium pyruvate. In the absence of pyruvate, the peak current for *ox1* changed weakly with pH, and only trace evidence of *ox2* was observed at more acidic pH (see Table 3.1 above). Under neutral or slightly basic conditions, there was no impact on the reduction peak and only *ox1* was observed. In slightly acidic solutions, a small oxidation peak near 0.38 V could be seen; however, this peak represents a negligible fraction of the total products formed during the electrochemical reduction of $\mathbf{1}^+$. In the presence of 100 mM sodium pyruvate, by

contrast, the peak reduction current had a pronounced pH dependence (Figure 3.5A, i_{pc} grows from 43 μA at pH 9 to 112 μA at pH 5). The two-electron product **1H** was clearly visible at every pH, although the product ratio **1H**:**1_{dim}** exhibited a maximum value at pH 7 (Figure 3.5B). At more basic pH, the formation of **1H** increased with the peak reduction current, but at more acidic pH, even though the peak reduction current continued to grow, the amount of **1H** fell and dimer was again the major product. It should be noted that the sum of i_{pa1} and i_{pa2} at each pH was nearly unchanged; assuming the diffusivities of **1_{dim}** and **1H** are independent of pH, this suggests that **1*** is reacting via only two competitive reaction pathways, one pathway that forms **1_{dim}** and one that forms **1H**. The decrease in $ox1$ at pH 5 may be due to acid-promoted decomposition of the dimer; for example, the dimer of 1-methyl nicotinamide has a first-order decomposition rate constant of 6400 s^{-1} at pH 4.4.⁷⁷

While the total amount of **1H** and **1_{dim}** formed is approximately constant as the pH is lowered from 9 to 5, the peak reduction current continues to increase, showing that the reduction of the species other than **1⁺** (described as causing the offset of 0.5 M in the convolution integral in Figure 2B above) is acid-promoted. Additionally, the pH maximum for **1H** formation indicates that the competing reduction event has a higher-order dependence on proton concentration than the reduction of **1⁺** to **1H**, because its rate grows more rapidly with proton concentration than the rate of formation of **1H**. Further inspection of the CVs with and without sodium pyruvate indicates that this competing reaction may be pyruvate reduction. Control experiments indicate that sodium pyruvate is electrochemically active, with a peak reduction potential of -2.2 V at 400 mV/s in pH 7 phosphate buffer. Although this potential is well beyond the -1.6 V cutoff for the CVs of **1⁺** shown here, the onset of the pyruvate reduction wave is still visible in background scans (this can be seen in Figure 3.2 above). An alternative explanation is that a synergistic interaction between **1⁺** and pyruvate may enable electrocatalytic proton reduction. However, we could not observe an interaction between sodium pyruvate and **1⁺** in bulk solution by ¹H-NMR (see Supporting Information). Ongoing research is aimed at understanding this secondary reaction/interaction.

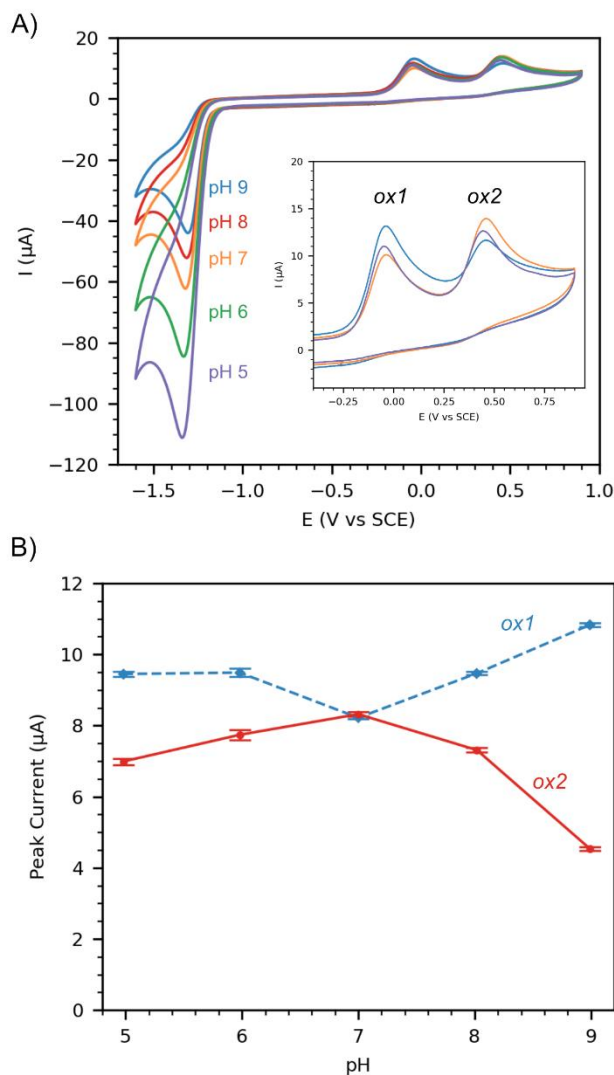


Figure 3.5. (A) Representative cyclic voltammograms of 2 mM **1**⁺ in 100 mM sodium phosphate with 100 mM sodium pyruvate, at pH 9 (blue), 8 (red), 7 (orange), 6 (green), and 5 (purple). (B) Normalized peak currents for *ox1* and *ox2* at the same pH values, showing a maximum of *ox2* (**1H**) and a minimum of *ox1* (**1dim**) at pH 7. Error bars represent one standard deviation from the mean where $n = 3$. Experiments were performed using a 2 mm boron doped diamond working electrode at 25 °C and 800 mV s⁻¹. Solutions were purged with nitrogen before scanning.

Finally, we explored the ability for other pyridinium electrolytes to be regenerated by sodium pyruvate. To that end, we varied the 1-substituent to include ethyl (**2**), isopropyl (**3**), and allyl (**4**) derivatives, as well as NAD⁺ itself (**5**). All of these pyridinium compounds showed both *ox1* and *ox2* in a mixture of 100 mM sodium phosphate and 100 mM sodium pyruvate (pH 7). The effect of sodium pyruvate was most pronounced for the substrate with the smallest 1-substituent, 1-ethyl nicotinamide bromide (**2**), and it was least pronounced for the substrate with the largest 1-substituent, NAD⁺ (**5**). Although the 1-substituent can have a significant effect on the extent of

interaction between pyruvate and the pyridinium electrolyte, the interaction appears to be general for nicotinamide-based electrolytes, suggesting that the ability of pyruvate to promote the electrochemical generation of **1H** from **1⁺** presents a general strategy for direct electrochemical regeneration of NADH analogues and NADH itself.

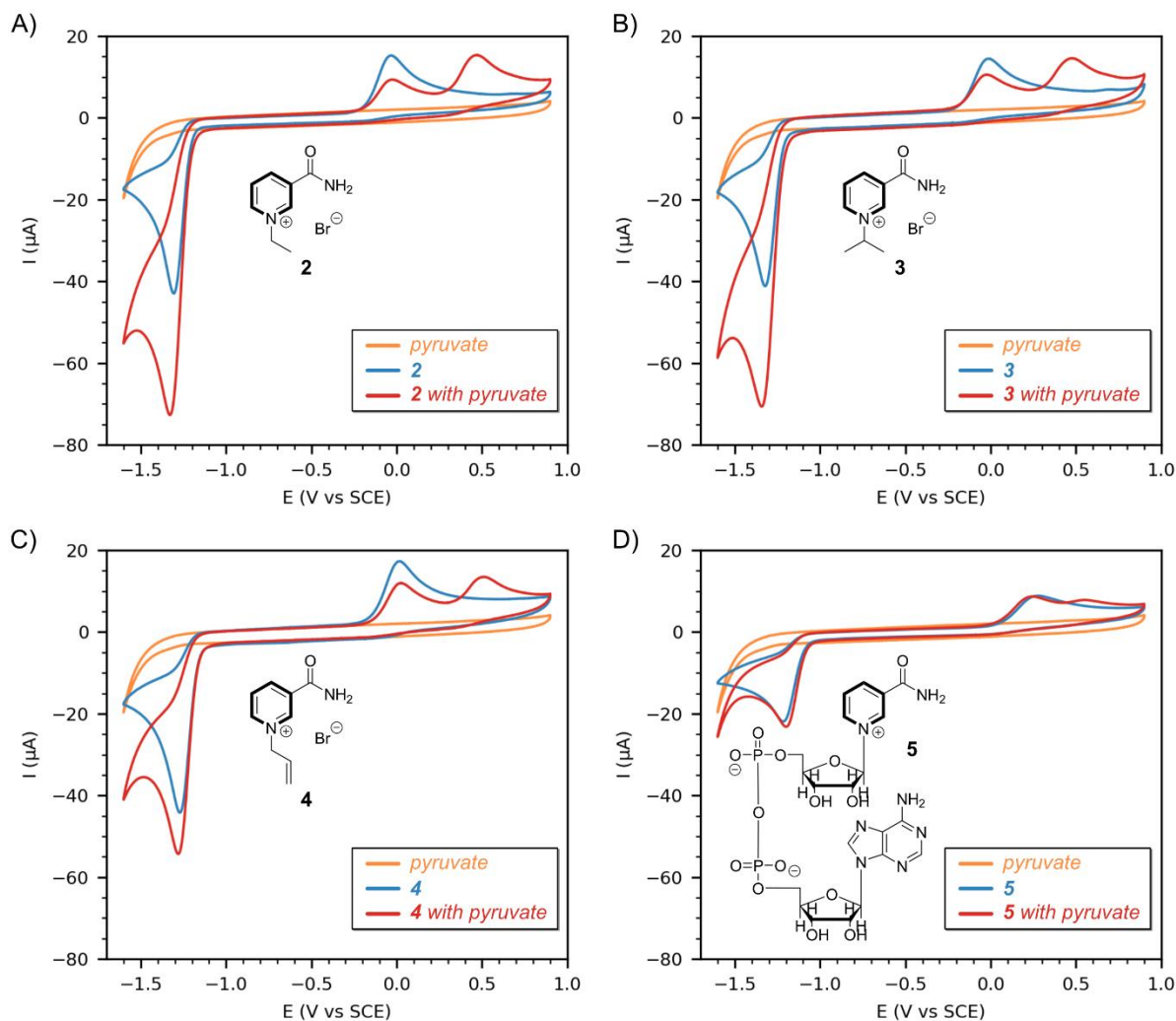


Figure 3.6. Representative cyclic voltammograms of 2 mM pyridinium electrolyte in 100 mM sodium phosphate in the presence (red) or absence (blue) of 100 mM sodium pyruvate, or 100 mM sodium pyruvate alone (orange): (A) 1-ethyl nicotinamide bromide, **2**; (B) 1-isopropyl nicotinamide bromide, **3**; (C) 1-allyl nicotinamide bromide, **4**; (D) nicotinamide adenine dinucleotide, **5**. Experiments were performed using a 2 mm boron doped diamond working electrode at 25 °C and 800 mV s⁻¹. Solutions were purged with nitrogen before scanning.

CONCLUSION

We screened the electrochemical reduction of 1-*n*-butyl nicotinamide bromide (**1⁺**) in 28 different supporting electrolytes and compared against the electrochemical oxidation of 1,4-dihydro-1-*n*-butyl nicotinamide (**1H**). While **1⁺** reduction yielded only dimer in most of the

electrolytes tested, sodium pyruvate gave rise to a significant amount of **1H** alongside the dimer. The interaction with sodium pyruvate is optimized when a large excess of sodium pyruvate is combined with a large excess of a co-supporting electrolyte, such as bicarbonate or phosphate. The interaction with pyruvate is also favored at low potentials and at neutral pH; however, it could not be observed in bulk solution by ¹H-NMR. Several different pyridinium electrolytes, including NAD⁺, are susceptible to the interaction with sodium pyruvate, suggesting that addition of sodium pyruvate can be a general strategy for regenerating NADH analogues and NADH itself from their oxidized forms.

Experimental:

1-n-butyl-3-carbamoylpyridinium bromide (**1⁺**): Nicotinamide (1.235 g, 10.1 mmol), acetonitrile (10 mL), 1-bromobutane (2.15 mL, 20 mmol), and a stir bar were added to a 20 mL scintillation vial with a pressure release cap. The mixture was stirred at 50 °C for 2 h and then at 80-100 °C for 10 h. The contents were quantitatively transferred with ethanol to a 100 mL round bottom flask, and the solvent was removed in vacuo. The soapy residue was crystallized from cyclohexane/ethanol to afford the product as white crystals (1.457 g, 56%).

1-n-butyl-1,4-dihydronicotinamide (**1H**): Adapted from a previous procedure⁴. Water (10 mL), dichloromethane (5 mL), sodium bicarbonate (390 mg, 4.6 mmol), and mNAD⁺ (200 mg, 0.77 mmol) were added to a 25 mL round bottom flask with a stir bar. Dry sodium dithionite (540 mg, 3.1 mmol) was added to an addition funnel, which was clipped to the top of the flask and sealed with a rubber stopper. The flask was lowered into an ice bath, and the contents were mixed while a Schlenk line was used to remove oxygen from the system. The addition funnel was opened and the dithionite added slowly over 10-15 min. After mixing for 2 h in the dark, the organic layer was washed three times with cold water, dried over MgSO₄, and concentrated in vacuo to yield the title product as a yellow-orange, semicrystalline residue (25 mg, 18%).

1-allyl-3-carbamoylpyridinium bromide: Nicotinamide (1.241 g, 10.2 mmol), acetonitrile (10 mL), allyl bromide (0.840 mL, 9.9 mmol), and a stir bar were added to a 20 mL scintillation vial with a pressure-release cap. The mixture was stirred at 50 °C for 12 h. The contents were quantitatively transferred with ethanol to a 100 mL round bottom flask, and the solvent was removed in vacuo. The solid was recrystallized from ethanol/hexanes to afford the product as a light brown crystalline solid (1.509 g, 61%).

1-isopropyl-3-carbamoylpyridinium bromide: Nicotinamide (122.5 mg, 1.00 mmol), 2-

bromopropane (0.1878 mL, 2.00 mmol), and acetonitrile (2 mL) were added to a Parr bomb reactor, and the contents were heated at 100 °C for 24 h. After cooling, the contents were quantitatively transferred with methanol to a round-bottom flask, the solvent was boiled away, and the residue was recrystallized from ethanol/hexanes to afford the product as a white powder (84.3 mg, 34%).

Electrochemistry

Unless otherwise noted, supporting electrolyte solutions were prepared by dissolving 2.00 mmol of electrolyte in a small amount of water and diluting to 10.0 mL. (Heat was needed to dissolve sodium tetraborate decahydrate). Solutions of sodium acetate and sodium propionate were prepared by combining equal amounts of the acid and sodium bicarbonate.

For electrochemical testing, 6 μmol (1.55 mg for **1**⁺, 1.08 mg for **1H**) of substrate was added to a 10 mL glass beaker and dissolved in 3 mL of supporting electrolyte solution (the volume was scaled accordingly if more or less substrate was added). The solution was purged with nitrogen for several minutes before scanning and for ~10 seconds between scans. The electrodes were boron-doped-diamond (working), saturated calomel (reference), and platinum wire (counter). Unless otherwise noted, scans were run at 800 mV/s between -1.6 V and 0.9 V, starting from the open circuit potential.

Acknowledgements

The authors wish to acknowledge the ACS Petroleum Research Fund (PRF #65477-DNI4) for their support of this research.

CHAPTER 4: MECHANISTIC INSIGHTS ON THE CO-REDUCTION OF NAD⁺ MIMETICS AND PYRUVATE DERIVATIVES

ABSTRACT

In this chapter, the interaction of pyruvate with NAD⁺ mimetics is explored in more detail. The ability to generate *ox2* is common to several pyruvate derivatives, all of which have vicinal dicarbonyls; pyruvanilide (**P**) and N,N-dimethylpyruvamide (**DMP**) are here given particular attention. The generation of *ox2* is shown to be first order in both mNAD⁺ concentration and in dicarbonyl concentration, and its appearance seems to require mNAD radicals and dicarbonyl radicals to be present together. Electron transfer to the dicarbonyl becomes faster when a small amount of mNAD⁺ is present, suggesting mediated electron transfer from an mNAD radical to the dicarbonyl. Computations show a stable adduct between an mNAD radical and **DMP** places the spin density almost entirely on the **DMP** unit, consistent with mediation, although the energy of this structure is too high to support its existence in these experiments. Kinetic isotope experiments show no significant effect when H₂O is replaced with D₂O, or when the CH₃ group of sodium pyruvate is replaced with CD₃, although the amount of *ox2* does fall when the CH₃ group of **P** is replaced with CD₃. Bulk electrolysis shows that the primary product of mNAD⁺ reduction is the 4,4'-dimer, and other nicotinamide-based compounds appear as minor products. Electrolysis of **DMP** shows that the major products are the dimer and the lactamide, formed in roughly equal amounts. Electrolysis of a mixture of mNAD⁺ and **DMP** shows formation of a heterodimer, but no detectable amounts of a 1,4-dihydropyridine corresponding to mNADH. Electrochemical measurements in this thesis are interpreted in light of heterodimer formation rather than mNADH formation.

INTRODUCTION

The findings of Chapter 3 raised more questions than they answered. The two overarching questions were: 1) How are sodium pyruvate and mNAD⁺ interacting?, and 2) Is *ox2* really attributable to mNADH formation? We sought to answer these questions with a mixture of electroanalytical experiments and bulk electrolysis experiments. The electroanalytical experiments were to test for reaction order, kinetic isotope effects, interaction mechanism (radical-radical or radical-substrate), and catalysis during co-reduction. The bulk electrolysis experiments were to create enough product to be spectroscopically characterized. Before either of these experiments were run, however, curiosity invited us to explore the generality of the interaction with pyruvate.

Sodium pyruvate generated *ox2* with several mimetics, but would any other pyruvate derivatives generate *ox2* with a given mimetic? Based upon the compounds tested in Chapter 3, it appeared that the additive should be redox active in the window where mNAD⁺ is redox active. We considered that electrolytes with a similar structure to sodium pyruvate – specifically, retaining the *alpha*-dicarbonyl group – might have the same effect as pyruvate itself. We use a few different mimetics in the present chapter– methyl pyruvate, pyruvanilide, and N,N-dimethylpyruvamide (Figure 4.1) – to test the validity of this idea.

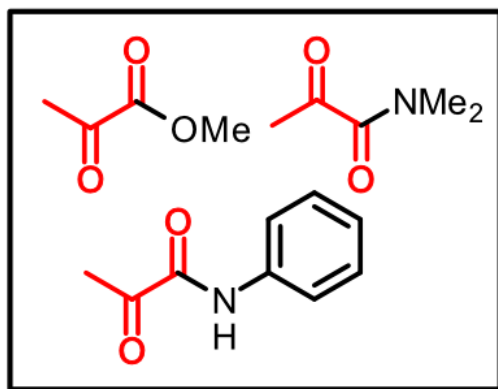


Figure 4.1. Pyruvate derivatives used in the present study: methyl pyruvate (**MeP**, top left), N,N-dimethylpyruvamide (**DMP**, top right), and pyruvanilide (**P**, bottom).

RESULTS AND DISCUSSION

The first new compound we tried was the methyl ester of sodium pyruvate, which indeed generated *ox2* like the parent acid (Figure 4.2). The appearance of *ox2* is first order in methyl pyruvate (**MeP**) when mNAD⁺ is in excess, and it is first order in mNAD⁺ when **MeP** is in excess. The ratio of the peak current of *ox2* to the sum of the peak currents for *ox1* and *ox2* is fairly constant (near 0.2). Finally, we looked for the involvement of any protons in the rate limiting step of *ox2* formation by replacing H₂O with D₂O; however, any solvent kinetic isotope effect (KIE) was too small to be detected.

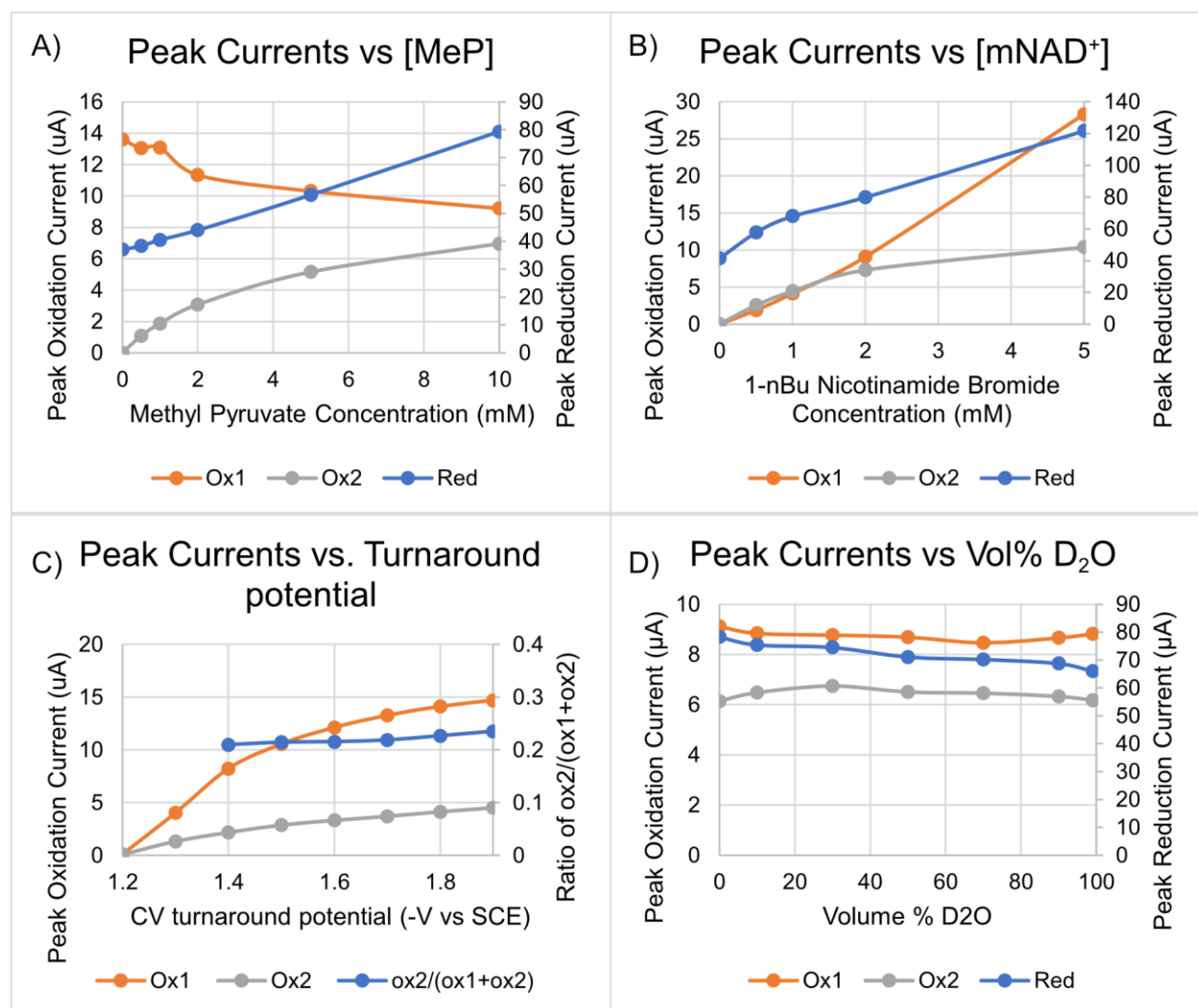


Figure 4.2. Cyclic voltammetry data for concentration study of methyl pyruvate (MeP) with 1-butyl nicotinamide bromide (mNAD⁺). The blue traces correspond to the right-hand y-axis, and the orange and gray traces correspond to the left-hand y-axes. A) Peak currents as a function of MeP concentration. B) Peak currents as a function of mNAD⁺ concentration. C) Peak currents as a function of the turnaround potential during the CV. D) Peak currents as a function of the volume % D₂O. Experimental conditions: 100 mM pH 7.03 sodium phosphate buffer, boron doped diamond working electrode, SCE reference electrode, Pt wire counter electrode. Potential sweep rate was 800 mV/s with a turnaround potential of -1.6 V, unless otherwise noted. Solutions were purged with nitrogen before scanning.

Although **MeP** is ~10x more effective than sodium pyruvate for *ox2* formation (only 5 eq are needed to reach ~50% *ox2* formation, compared to 50 eq of sodium pyruvate, cf. Figure 3.3), it has the downside of hydrolyzing very quickly in water (CVs decay noticeably within 30 minutes of solution preparation). As a result, we sought out a synthetic route to new pyruvate derivatives that were more resistant to hydrolysis. We reasoned that amides are more stable than esters, so we

found a three-step route to pyruvamides from tartaric acid, initially choosing to make pyruvanilide (**P**) for its ease of purification and resistance to hydrolysis (decomposes over 1-3 days in water). Pyruvanilide also had the benefit of being more active than either sodium pyruvate or **MeP**, with only 1 eq. of **P** affording *ox2* in ~50% yield.

With compound **P** in hand, we explored its effect on the reduction of 1-ethyl nicotinamide bromide (**m**⁺), which had better solubility compared to 1-butyl nicotinamide bromide. We investigated both the potential dependence and the concentration dependence of *ox2* formation (hereafter called **mH**). In one set of experiments, we kept the concentration of **m**⁺ constant at 1 mM, and we varied the concentration of **P** from 0 mM to 1 mM. In another set of experiments, we kept the concentration of **P** constant at 1 mM and varied the **m**⁺ concentration from 0 mM to 1 mM. The products were assigned as shown in Figure 4.3 below, based on the change in the convolution integral during each redox event. The reduction products of **P** are denoted **P**₂, although the identity of the reduction product was not confirmed for these experiments (reduction of pyruvic acid may afford either pinacol dimer or lactate, depending on the reduction conditions⁸¹); the label **P**₂ is meant to include all non-oxidizable reduction products of **P**.

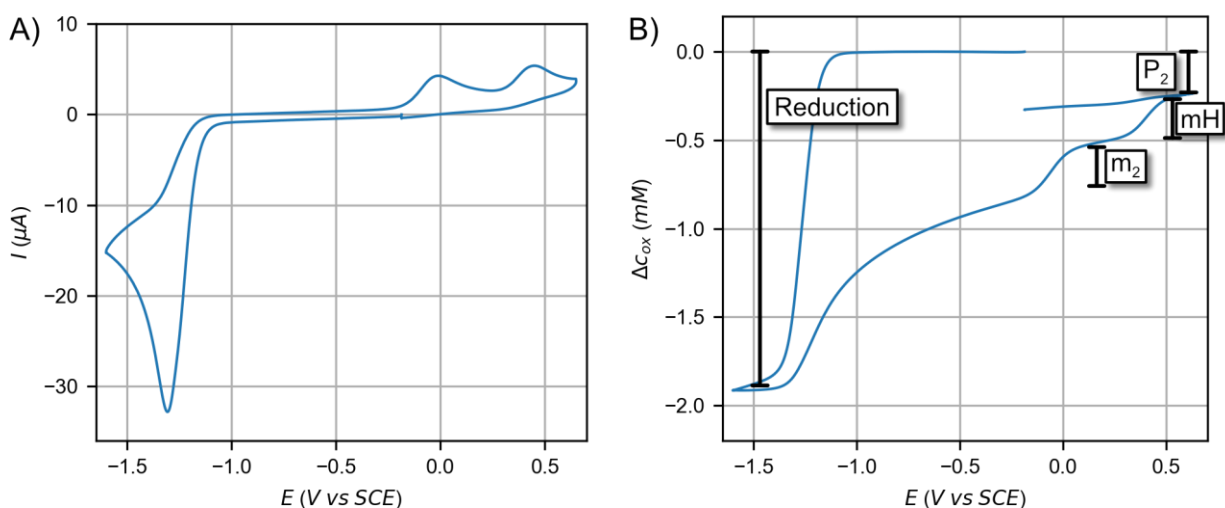


Figure 4.3. Assignment of redox events for concentration study. A) Representative CV of a mixture of 1 mM **m**⁺ and 1 mM **P**. B) Convolution of the same CV, showing how the relative concentrations of different species were assigned. Scan was taken at 800 mV s⁻¹ in 0.1 M pH 7.10 sodium phosphate buffer at a boron doped diamond electrode, with Pt counter electrode and SCE reference electrode. Sample was purged with nitrogen before scanning.

We hypothesized that **mH** formation involved a reaction between a mimetic radical (**m**[•]) and a pyruvate radical (**P**[•] and/or **PH**[•]). This hypothesis was based on observations in Chapter 2,

where we showed that ox_2 formation is favored at lower potentials, where sodium pyruvate was reduced more quickly, and on observations with **MeP**, which is reduced at more positive potentials and which gives **mH** in higher yields. To test this hypothesis, we explored the potential dependence of **m⁺** reduction with **P**, which has a reduction event onset at more positive potentials than **m⁺** reduction. If the interaction between **m⁺** and **P** required both radicals to be present, we would expect **mH** formation to be favored over **m₂** formation at more positive potentials. As shown in Figure 4.4, this is indeed the case. At the start of the reduction event ($E \geq -1.25$ V), the amount of **P₂** formed is the same in a mixture of **m⁺** and **P** compared to a solution of only **P**, but at lower potentials – where **m⁺** is reduced under normal circumstances – the rate of **P₂** appearance starts to fall, and **mH** starts to appear. The small amount of **m₂** dimer that forms near -1.25 V is suppressed in the mixture of **m⁺** and **P**, first appearing at -1.30 V. As the potential sweeps lower, the amount of **mH**, **m₂**, and **P₂** all grow together, eventually approaching a 1:1:1 ratio.

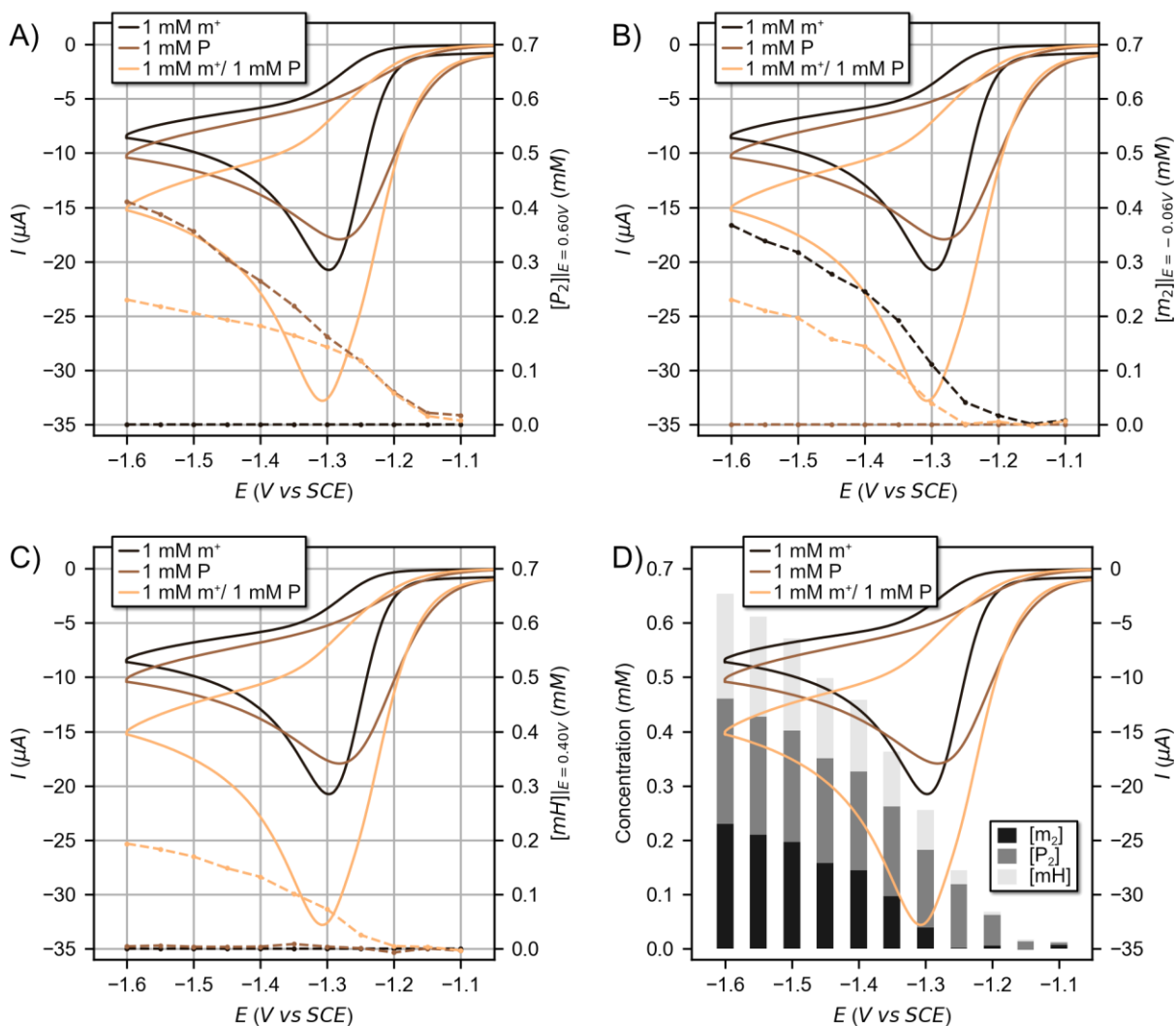
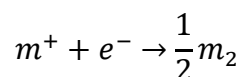
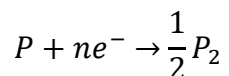


Figure 4.4. Cyclic voltammograms (solid curves) superimposed on the potential-dependent yields (dashed curves) for A) pyruvanilide dimer (\mathbf{P}_2), B) mimetic dimer (\mathbf{m}_2), and C) 1,4-dihydro mimetic (\mathbf{mH}). The three scans in each plot correspond to 1 mM \mathbf{m}^+ (black), 1 mM \mathbf{P} (brown), and combined 1 mM \mathbf{m}^+ / 1 mM \mathbf{P} (orange). Plot D) shows the potential-dependent yields of \mathbf{m}_2 , \mathbf{P}_2 , and \mathbf{mH} for the combined 1 mM \mathbf{m}^+ / 1 mM \mathbf{P} sample, with the CVs of the pure compounds shown for comparison. All scans were taken at 800 mV s^{-1} in 0.1 M pH 7.10 sodium phosphate buffer at boron-doped-diamond electrode, with Pt counter electrode and SCE reference electrode. Samples were purged with nitrogen before scanning.

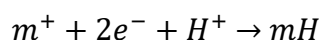
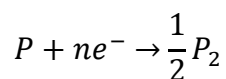
The reaction order of the $\mathbf{m}^+/\mathbf{P}^-$ interaction appears to be first order in both compounds, (Figure 4.5), similar to the results for \mathbf{MeP} above. At a large excess of pyruvanilide, the appearance of \mathbf{mH} is first order in the concentration of \mathbf{m}^+ . As the concentration of \mathbf{m}^+ increases, the rate of \mathbf{m}_2 formation grows faster than the rate of \mathbf{mH} formation, consistent with a second order dimerization outpacing a first order \mathbf{mH} formation. A similar trend holds for \mathbf{P} when \mathbf{m}^+ is in

excess, the appearance of **mH** is first order in pyruvanilide, although the appearance of **P₂** may also be first order in **P**, based on the smaller curvature of the graph.

We also sought evidence for catalytic behavior of **P**, whereby **P** might regenerate itself after the reduction of **m⁺** to **mH**. We reasoned that, if catalysis were happening, the total number of electrons passed should be greater when **m⁺** and **P** are reduced together compared to when they are reduced separately, as the overall reactions



(for which $n + 1$ electrons are passed per molecule) would instead become



(for which $n + 2$ electrons are passed per molecule). Assuming a 50% yield of **mH**, this means the convolution integral of the mixture should be about 1.3x or 1.2x the sum of the independent convolution integrals (according as $n = 1$ or $n = 2$, respectively). However, convolution integral for the reduction event grows only to 0.8x the sum of the independent convolution integrals (from ~1.1 to 1.8), as shown in Figure 4.5B. The same trend is seen on the oxidation end in Figure 4.5A, where the total amount of products ($m_2 + P_2 + mH$) grows to 0.9x the sum of the independent convolution integrals. As such, we could not conclude that **P^{•-}** or **PH[•]** were acting as a catalyst to a significant extent during CVs.

Evidence does suggest mediated electron transfer in the opposite direction, however, from **m[•]** to the pyruvate derivative. Alternating current voltammetry (ACV) revealed that **m⁺** increases the effective rate of electron transfer to **P**, with the addition of only 5 mol % **m⁺** to a solution of **P** increasing the alternating current magnitude by ~35% (Figure 4.6), characteristic of an increase in k^0 (see Figure 2.4 above). The same phenomenon was also visible in studies from Chapter 2, where a small amount of **m⁺** increased the rate of electron transfer to sodium pyruvate. Here we reproduce a modified form of Figure 3.2 (Figure 4.7) to illustrate this point, including the convolution integral of the sodium pyruvate baseline. The convolution integral offset – a measure of the amount of reduced sodium pyruvate – increases 3.5x (0.14 to 0.5) in the presence of 2 mol % mNAD⁺ (Figure 4.7). In summary, when a pyruvate derivative is reduced at more positive potentials than **m⁺**, the

mediated reduction by \mathbf{m}^- appears as a faster effective k^0 , and when the pyruvate derivative is reduced at more negative potentials than \mathbf{m}^+ , the mediated reduction by \mathbf{m}^- appears as a larger amount of the pyruvate derivative reduced.

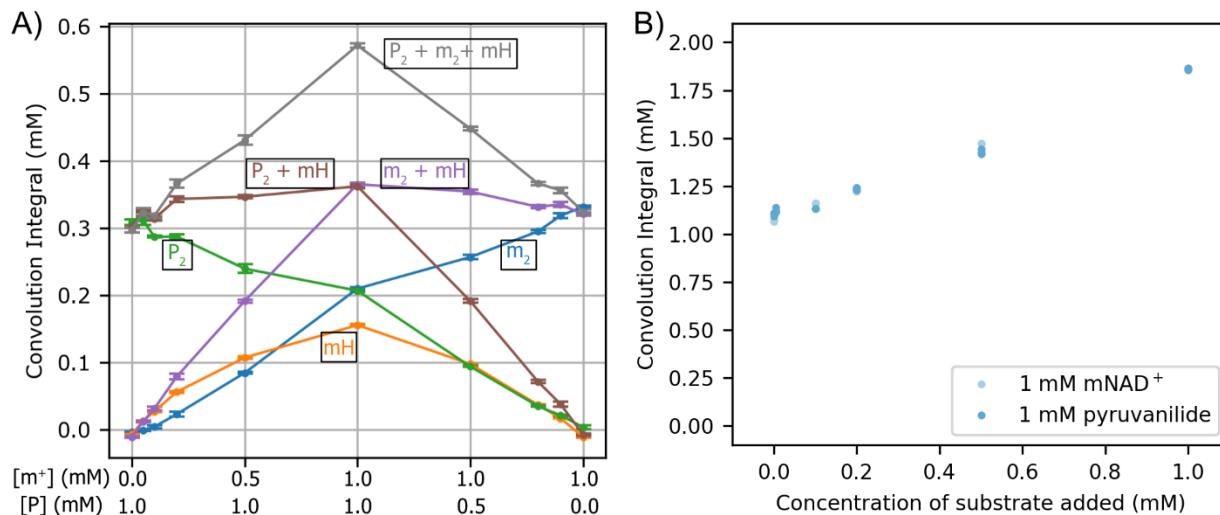


Figure 4.5. A) Concentration-dependent yields for mH (orange), m_2 (blue), and P_2 (green), along with their combined yields ($P_2 + mH$ in brown, $m_2 + mH$ in purple, $P_2 + m_2 + mH$ in gray). B) Concentration-dependent yield for the total amount of material reduced. All scans were taken at 800 mV s^{-1} in 0.1 M pH 7.10 sodium phosphate buffer at boron doped diamond electrode, with Pt counter electrode and SCE reference electrode. Samples were purged with nitrogen before scanning.

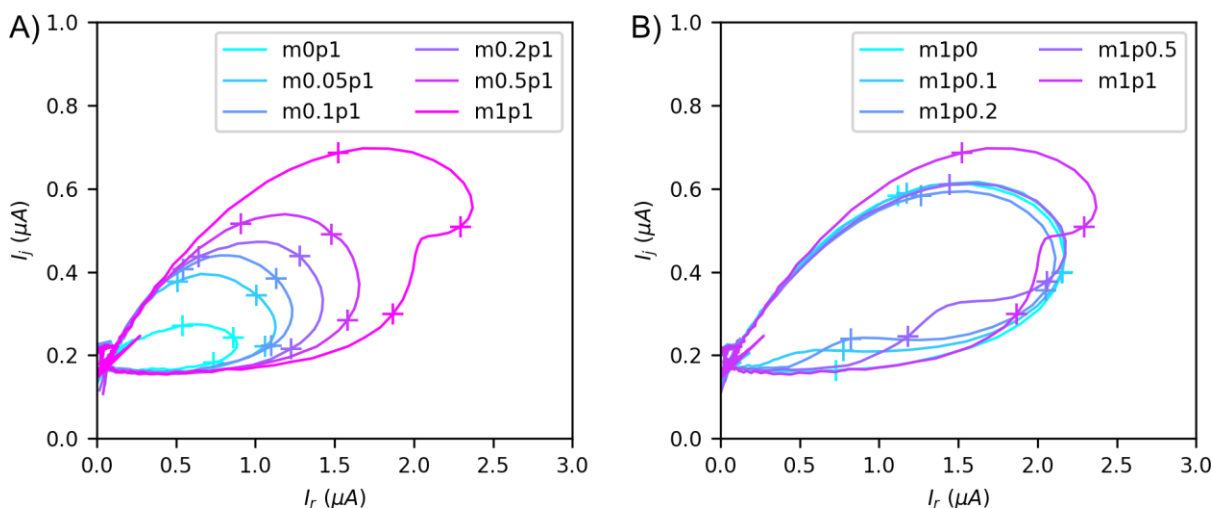


Figure 4.6. ACV data for the concentration study with pyruvanilide (p) and 1-ethyl nicotinamide bromide (m). The numbers in the legends are the concentrations of substrate (mM) in each scan. The “+” tick marks indicate -1.3 V , -1.25 V , and -1.2 V vs SCE, going clockwise from the top of the graph. A) The addition of m to p shows a large increase in electron transfer rate. B) The addition of p to m introduces a shoulder in the graph, showing a change in reduction mechanism. All scans were taken at 800 mV s^{-1} in 0.1 M pH 7.10 sodium phosphate buffer. Electrodes: boron doped diamond working, Pt counter, SCE reference. Samples were purged with nitrogen before scanning.

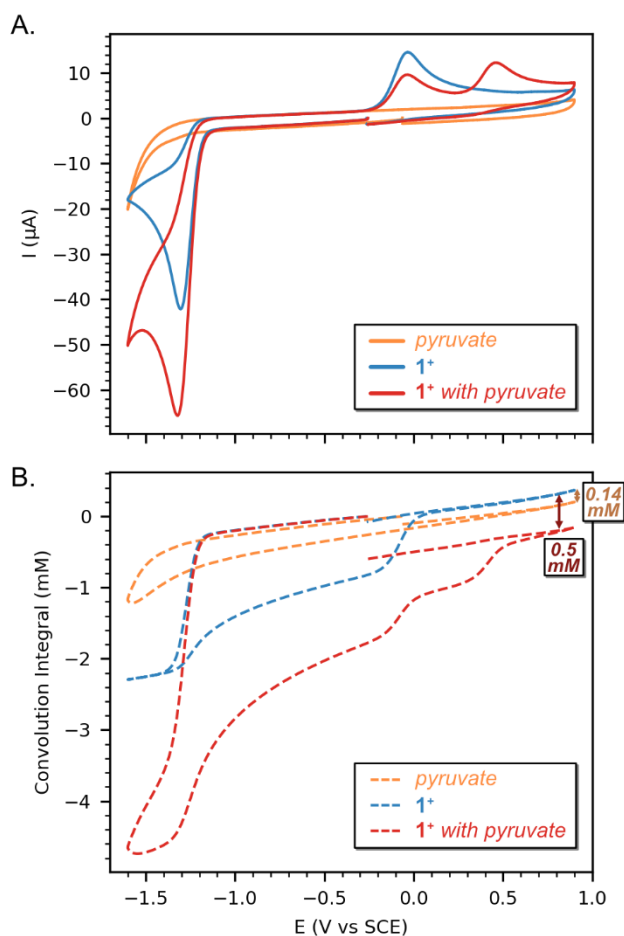
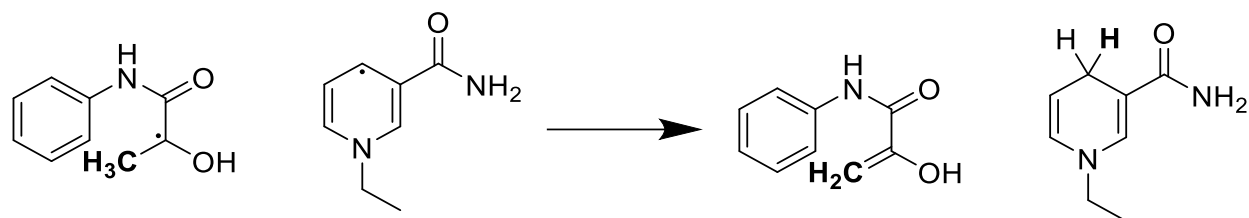


Figure 4.7. Representative cyclic voltammograms and (B) the corresponding convolution integrals of 2 mM 1^+ in the absence (blue) or presence (red) of 100 mM sodium pyruvate, or 100 mM sodium pyruvate alone (orange). Experiments were performed using a 2 mm boron doped diamond working electrode with 100mM sodium phosphate supporting electrolyte at 800 mV s^{-1} , purged with N_2 and at pH 7.0, and $25 \text{ }^\circ\text{C}$. Adapted from Reference ⁸² with permission.

Another mechanistic question is the source of the H atom transferred to \mathbf{m}^\bullet during reduction. Based upon the lack of solvent KIE observed with \mathbf{MeP} above, we hypothesized that the reduction of \mathbf{m}^\bullet to \mathbf{mH} could take place by H atom transfer from the methyl group of the pyruvate derivative, according to the following reaction (shown for the pyruvanilide radical \mathbf{PH}^\bullet):



Scheme 4.1. Hypothesized H-atom transfer pathway to generate a 1,4-dihydropyridine.

To test this hypothesis, we deuterated the methyl groups of two compounds, pyruvanilide and sodium pyruvate, by heating in D₂O until the methyl groups were silenced on ¹H-NMR. We compared against controls in D₂O that were not heated, and against two additional controls in H₂O with and without heat, to isolate the effect of heat from the effect of H/D exchange. The results are shown below in Figure 4.8. The data for pyruvanilide are consistent with H atom transfer from the methyl group. The relative amounts of **m₂**, **mH**, and **PH** are roughly the same in H₂O as in D₂O, and heating the sample increases the **mH/m₂** ratio in H₂O (due to more dissolved pyruvanilide) but decreases the **mH/m₂** ratio in D₂O (consistent with the hypothesized mechanism). In contrast to the data for pyruvanilide, the data for sodium pyruvate do not support the H atom transfer hypothesis: heating the sample has a very small effect in both H₂O and D₂O, and the **mH/m₂** ratio is uniformly lower in D₂O compared to H₂O. The different conclusions suggest that the mechanism of interaction between **P^{•+}** and **m[•]** may depend on the identity of **P^{•+}**.

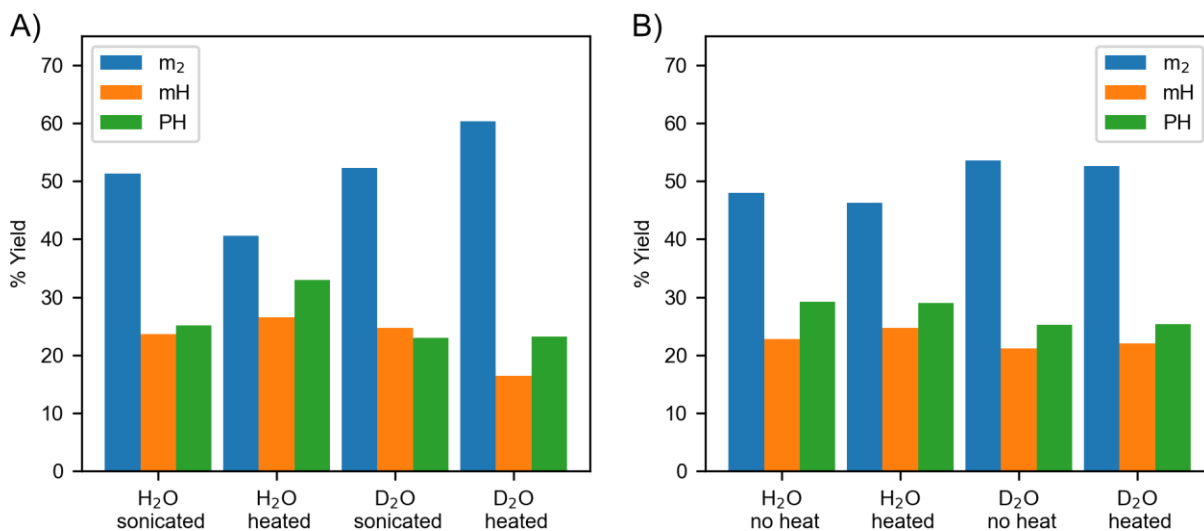


Figure 4.8. Relative product yields for the KIE studies for 1 mM **m^{•+}** with A) 1 mM pyruvanilide, and B) 50 mM sodium pyruvate. Experimental conditions: 100 mM NaHCO₃, boron doped diamond working electrode, SCE reference electrode, Pt wire counter electrode. Potential sweep rate was 800 mV/s with a turnaround potential of -1.6 V. Solutions were purged with nitrogen before scanning. Note that **P** was poorly soluble without heat, so the concentration of **P** in the sonicated samples in A) is less than 1 mM.

Because the poor solubility of pyruvanilide complicated electrochemical modeling, we turned to other more soluble pyruvate derivatives. We synthesized pyruvanilide-4-carboxylic acid, which was indeed more soluble, but which had the downsides of hydrolyzing in minutes in water and adsorbing onto the electrode surface during each CV cycle. We also tried diacetyl (2,3-butanedione), which was more soluble and resistant to hydrolysis. However, diacetyl did not afford a significant amount of **mH**, and determination of product yield was complicated by a small oxidation peak near 0.4 V after the reduction of diacetyl alone (Figure 4.9).

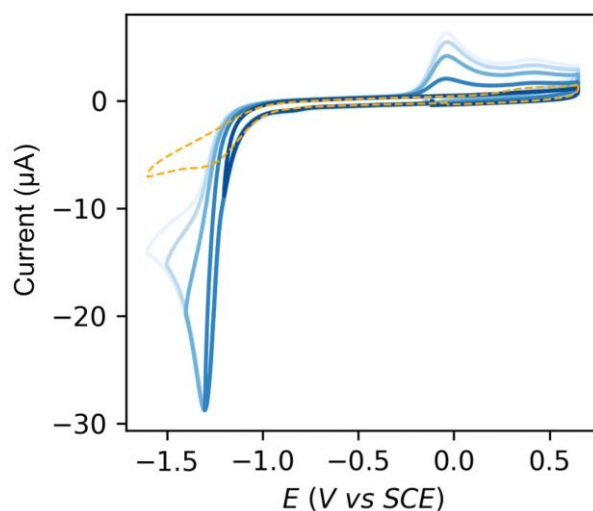


Figure 4.9. Potential dependence of cyclic voltammetry of \mathbf{m}^+ with diacetyl (solid blue traces) compared with a cyclic voltammogram of diacetyl alone (orange dashed trace). Experimental conditions: 1 mM \mathbf{m}^+ , 1 mM diacetyl, 0.1 M pH 7.10 sodium phosphate buffer, boron doped diamond electrode, Pt counter electrode, and SCE reference electrode. Scan rate 800 mV s⁻¹. Samples were purged with nitrogen before scanning.

We finally settled on N,N-dimethylpyruvamide (**DMP**), which is effective at **mH** formation (Figure 4.10), very soluble in water, resistant to hydrolysis, non-adsorbing, and non-hydrating (many of the other pyruvate derivatives, including pyruvic acid, hydrate to give a geminal diol, which is not redox active and which also complicates electrochemical modeling).

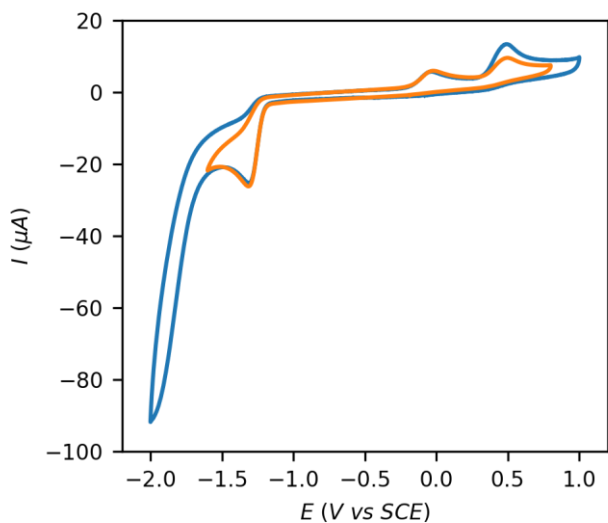


Figure 4.10. Cyclic voltammograms of \mathbf{m}^+ with **DMP**. Experimental conditions: 1 mM \mathbf{m}^+ , 5 mM **DMP**, 0.25 M aqueous NaHCO_3 , boron doped diamond electrode, Pt counter electrode, and SCE reference electrode. Scan rate 800 mV s^{-1} . Samples were purged with nitrogen before scanning.

The observation that \mathbf{m}^\cdot could speed up electron transfer to a pyruvate derivative sparked interest in the possibility of a covalent adduct between the two species. We turned to computational chemistry to model an adduct between a neutral \mathbf{m}^\cdot radical and a neutral **DMP** molecule at the pyridine 4-position (the same site where sulfinate attaches during the reduction with dithionite^{7,83}). Computations showed that, for an interaction between \mathbf{m}^\cdot radical and neutral **DMP**, two stable structures were possible, bound through the O atoms of **DMP**, with the radical density residing almost entirely on the **DMP** fragment (Figure 4.11). While the energy of these structures was too high to support their existence in solution ($\sim 30 \text{ kcal/mol}$ higher than the energies of \mathbf{m}^\cdot and **DMP** alone), they do offer an interesting perspective on the possibility of homogeneous electron transfer from \mathbf{m}^\cdot to **P**. Computations did not converge for a 1-electron adduct bound through the acetyl $\text{C}=\text{O}$ carbon of **DMP**. In contrast to computations for a 1-electron adduct, computations for an adduct between \mathbf{m}^\cdot and \mathbf{P}^\cdot showed that a bond through the acetyl $\text{C}=\text{O}$ carbon was more favorable than a bond through either oxygen atom, by about 18 kcal/mol . Structures and relative energies are provided in the Supporting Information. Transition state computations were not included as part of this study, although they would be needed for more decisive claims about mechanistic pathways.

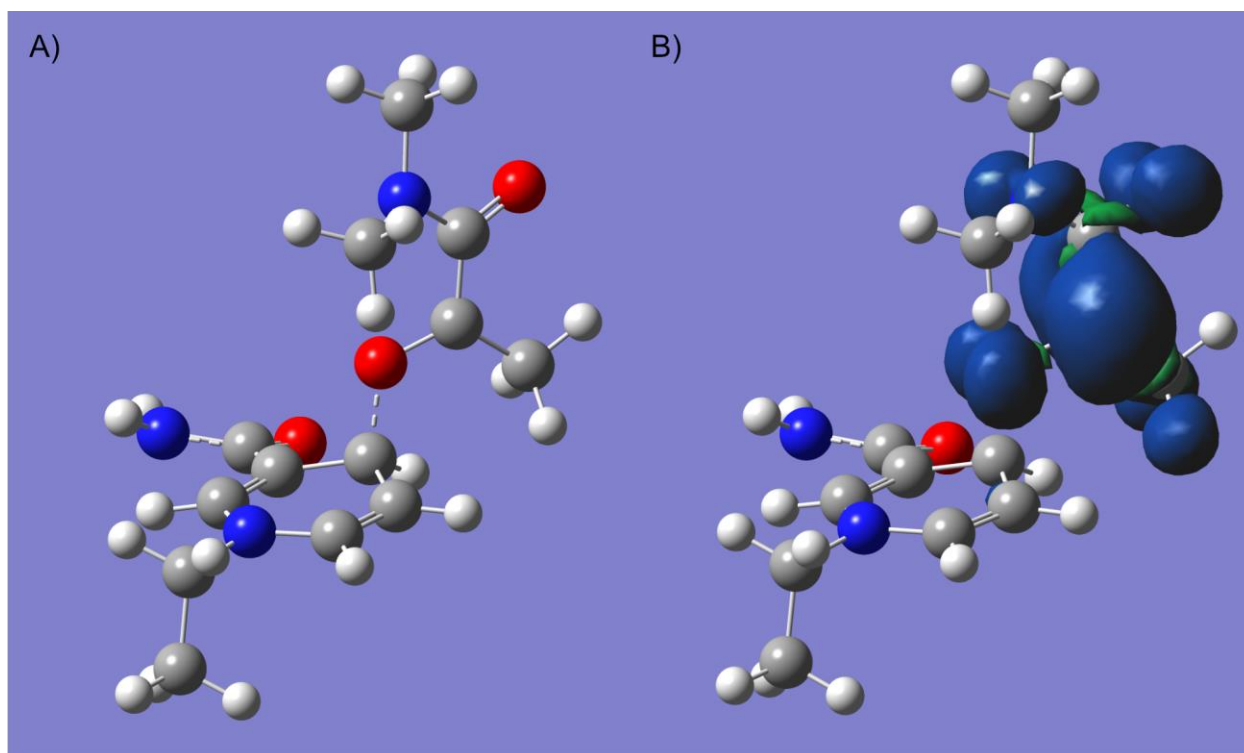


Figure 4.11. A) Optimized geometry for one of the adducts between dimethylpyruvamide (DMP) and the neutral radical of 1-ethyl nicotinamide. B) The electron spin density of the adduct resides almost entirely on the DMP unit. Computations were carried out with Gaussian 16, Revision C.01, with the following input: *opt freq=noraman b3lyp/6-31+g(d,p) scrf=(cpcm,solvent=water) pop=nbo geom=connectivity*.

Finally, we turned to bulk electrolysis as a way to characterize the effect of **DMP** on the reduction of **m⁺**. We here echo the insightful words of Petrovich and Baizer:

Any mechanistic study requires an unequivocal identification of the reaction products. A controlled potential electrolysis on a scale sufficiently large to allow identification of reaction products is imperative. Without this tool mechanistic studies are largely speculative; with it interpretations must be cautious.⁸⁴

To this end, we undertook five different electrolysis experiments: three in H₂O (one of **m⁺**, one of **DMP**, and one of a mixture of **m⁺** and **DMP**) were extracted with CDCl₃ and subjected to 1D and 2D NMR experiments, and two kinetic studies of a mixture of **m⁺** and **DMP** (one in H₂O and one in D₂O) were monitored in real-time with a flow 1D NMR setup. In all of the electrolyses, a complex mixture of products formed, and characterization was necessarily limited to major products.¹

¹ UV-Vis could not characterize **mH** formation as both the dimer **m₂** and the 1,4-dihydro mNADH have UV absorption peaks at 361 nm (a region characteristic of 1,4-dihydropyridines).

Before describing the results, a brief explanation of 2D NMR may be helpful for those unfamiliar with the technique. The classic 1D experiment, $^1\text{H-NMR}$, provides information about the chemical environment of protons on a molecule. The 2D NMR experiments can tell which protons are connected to which carbons (HSQC), which protons are adjacent to which other protons (COSY), and which carbons are close to a given proton (HMBC). The process of interpreting the spectra starts with identifying a proton-carbon fragment on HSQC. Once a proton-carbon fragment is identified, COSY is used to find nearby protons (usually on neighboring carbon atoms). Next, HMBC is used to find which carbons are close enough to “see” the proton of interest (usually 2-3 bonds away). Then, the ^1H spectrum is consulted for splitting type and coupling constants for the proton peak of interest. Once the fragment and its neighbors are identified, a new HSQC peak that matches one of the peaks on COSY and/or HMBC is identified, and the process repeats. The process continues to repeat until no new fragments are found to connect with the ones already identified. If protons do not appear on HSQC – for example, OH and NH protons, which are not bound to carbon – HMBC can provide connectivity information by revealing which carbons are close to these protons. Once all of the connected fragments are known, the fragments are assigned to molecular groups (for example a tertiary alcohol, or an amide C=O) based upon literature assignments of similar compounds. Finally, the groups are connected to each other based upon the NMR data (here HMBC is particularly helpful) and a healthy dose of intuition.

In the electrolysis of \mathbf{m}^+ , the major product is the 4,4'-dimer \mathbf{m}_2 (Table 4.1). This is consistent with the findings of Chapter 3, where a positive correlation between steric bulk at the 1-position and dimerization rate suggested that dimerization preferentially occurs at the 4-position. This reactivity is also consistent with the observed reactivity of related mNAD^+ at the 4-position during dithionite reduction, and with the observed dimerization of electrochemically-reduced 1-propyl nicotinamide at the 4-position. Another product appears to be the 4,4'-dimer after expulsion of two equivalents of ethane, to form 4,4'-bipyridine- 3,3'-dicarboxamide (Table 4.2). A third product was inferred to be 2,5-dicarboxamidopyrazine, from fusion of two nicotinamide rings (Table 4.3)

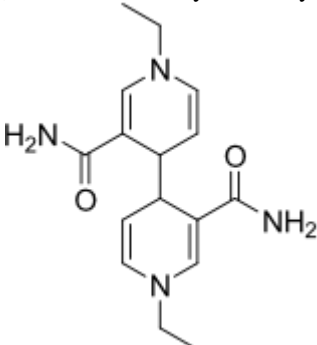
1H	bound to ^{13}C	next to 1H	network to ^{13}C	Assignment
1.18 (t, J = 7.2 Hz)	15.4 (3°/1°)	3.22 (q, J = 7.2 Hz)	48.9	Ethyl CH3
3.22 (q, J = 7.2 Hz)	48.9 (2°)	1.18 (t, J = 7.2 Hz)	15.4, 129.2, 138.2	Ethyl CH2
5.96 (dd, J = 7.8 Hz, 1.6 Hz)	129.1 (3°/1°)	4.68 (dd, J = 7.9 Hz, 4.7 Hz); 7.01 (d, J = 1.5 Hz)	39.6, 48.9, 104.1, 138.2	Pyridine C6-H
7.01 (d, J = 1.5 Hz)	138.3 (3°/1°)	5.96 (dd, J = 7.8 Hz, 1.6 Hz)	39.6, 49.0, 101.2, 129.2, 170.9	Pyridine C2-H
4.68 (dd, J = 7.9 Hz, 4.7 Hz)	104.1 (3°/1°)	3.48 (d, J = 4.7 Hz); 5.97 (dd, J = 7.8 Hz, 1.6 Hz)	39.6, 101.2, 129.2, 170.9	Pyridine C5-H
3.48 (d, J = 4.7 Hz)	39.6 (3°/1°)	4.68 (dd, J = 7.9 Hz, 4.7 Hz)	39.6, 101.2, 104.1, 129.2, 138.2, 170.9	Pyridine C4-H
5.82 (br s)	-	-	-	Amide NH2
-	101.2 (4°)	-	-	Pyridine C3
-	170.9 (4°)	-	-	Amide C=O
Proposed structure: 4,4'-dimer of 1-ethyl-1,4-dihydro nicotinamide (A1)				
				

Table 4.1. NMR data for the assignment of structure A1 from the electrolysis of m^+ . See Supporting Information for experimental conditions.

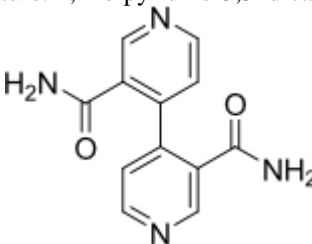
1H	bound to ^{13}C	next to 1H	network to ^{13}C	Assignment
8.40 (dd, J = 1.7 Hz, 0.5 Hz)	130.1 (3°/1°)	-	132.0, 136.7, 166.0	Pyridine C2-H
8.21 (dd, J = 8.0 Hz, 1.7 Hz)	132.0 (3°/1°)	7.76 (dd, J = 8.0 Hz, 0.5 Hz)	130.1, 136.7, 166.0	Pyridine C6-H
-	136.7 (4°)	-	-	Pyridine C3
7.76 (dd, J = 8.0 Hz, 0.5 Hz)	128.8 (3°/1°)	8.21 (dd, J = 8.0 Hz, 1.7 Hz)	132.0, 167.3	Pyridine C5-H
-	166.0 (4°)	-	-	Amide C=O
-	167.3 (4°)	-	-	Pyridine C4
Proposed structure: 4,4'-bipyridine-3,3'-dicarboxamide (A2)				
				

Table 4.2. NMR data for the assignment of structure A2 from the electrolysis of m^+ . See Supporting Information for experimental conditions.

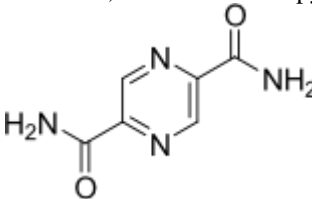
1H	bound to ^{13}C	next to 1H	network to ^{13}C	Assignment
8.09 (s)	129.5 (3°/1°)	-	129.5, 134.3, 166.0	Pyrazine C3-H
-	134.3 (4°)	-	-	Pyrazine C2
-	166.0 (4°)	-	-	Amide C=O
Proposed structure: 2,5-dicarboxamidopyrazine (A3)				
				

Table 4.3. NMR data for the assignment of structure A3 from the electrolysis of m^+ . See Supporting Information for experimental conditions.

In the electrolysis of **DMP**, the major products are the pinacol dimers of **DMP** (the *meso* dimer (*R,S*) and the chiral dimers (*R,R*) and (*S,S*)) and the two electron product N,N-dimethyl lactamide. The dimer with the more downfield hydroxyl 1H chemical shift was assigned to be the chiral dimer, and the dimer with the more upfield hydroxyl 1H was assigned as the *meso* dimer. These structures were assigned based upon the cooperativity between sterics and internal hydrogen bonding in the chiral dimer, where the repulsion between dimethylcarboxamide groups places the hydroxyl groups near each other, deshielding the hydroxyl protons. In the *meso* dimer, by contrast, steric repulsion places the hydroxyl groups apart from each other, making internal

hydrogen bonding less probable. The formation of a mixture of dimer and lactamide is consistent with the observed reactivity of sodium pyruvate during electrochemical reduction, which can yield a mixture of lactate and pinacol dimer.⁸¹

1H	bound to ^{13}C	next to 1H	network to ^{13}C	Assignment
3.42 (s, 3H)	38.4 (3°/1°)	-	37.5, 178.5	Amide N-CH3
2.94 (s, 3H)	37.5 (3°/1°)	-	38.4, 178.5	Amide N-CH3
-	178.5 (4°)	-	-	Amide C=O
1.47 (d, J = 1 Hz, 3H)	18.4 (3°/1°)	6.17 (q, 1.1 Hz)	80.0, 178.5	C(4°)-CH3
6.17 (q, J = 1.1 Hz, 1H)	-	1.47 (d, J = 1 Hz)	18.4, 80.0, 178.5	C(4°)-OH
-	80.0 (4°)	-	-	C(4°)

Proposed structure: *meso* dimer of N,N-dimethylpyruvamide (B1)

Table 4.4. NMR data for the assignment of structure B1 from the electrolysis of **DMP**. See Supporting Information for experimental conditions.

1H	bound to ^{13}C	next to 1H	network to ^{13}C	Assignment
3.43 (s, 3H)	39.2 (3°/1°)	-	37.8, 176.0	Amide N-CH3
2.98 (s, 3H)	37.8 (3°/1°)	-	39.2, 176.0	Amide N-CH3
-	176.0 (4°)	-	-	Amide C=O
1.61 (s, 3H)	22.4 (3°/1°)	-	80.0, 176.0	C(4°)-CH3
6.82 (s, 1H)	-	-	80.0, 176.0	C(4°)-OH
-	80.0 (4°)	-	-	C(4°)

Proposed structure: chiral dimer of N,N-dimethylpyruvamide (B2)

Table 4.5. NMR data for the assignment of structure B2 from the electrolysis of **DMP**. See Supporting Information for experimental conditions.

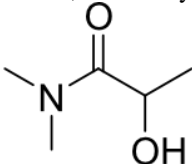
1H	bound to ^{13}C	next to 1H	network to ^{13}C	Assignment
3.03 (s, 3H)	35.9 (3°/1°)	-	36.4, 175.1	Amide N-CH3
3.01 (s, 3H)	36.4 (3°/1°)	-	35.9, 175.1	Amide N-CH3
-	175.1 (4°)	-	-	Amide C=O
1.35 (d, J = 6.6 Hz, 3H)	21.0 (3°/1°)	4.48 (p, J = 6.7 Hz)	64.2, 175.1	C(3°)-CH3
3.84 (d, J = 7.3 Hz, 1H)	-	4.48 (p, J = 6.7 Hz)	64.2, 175.1	C(3°)-OH
4.48 (p, J = 6.7 Hz, 1H)	64.2 (4°)	1.35 (d, J = 6.6 Hz); 3.84 (d, J = 7.3 Hz)	21.0, 175.1	C(3°)-H
Proposed structure: N,N-dimethylactamide (B3)				
				

Table 4.6. NMR data for the assignment of structure B3 from the electrolysis of **DMP**. See Supporting Information for experimental conditions.

The electrolysis of **m**⁺ with **DMP** afforded a new set of peaks on the HMBC spectrum (Figure 4.S21), corresponding to the C4 proton of a 1,4-dihydropyridine (a proton near 4.00 ppm resonating with carbons near 99, 102, 130, and 140 ppm, corresponding to a proton at the C4 position able to “see” the pyridine C5, C3, C6, and C2 carbons, respectively; compare with Table 4.1 above). In addition to resonating with dihydropyridine carbons, this proton at 4.00 ppm also resonated with carbons near 22 and 81 ppm, in the same range as the C(4°)-methyl and the C(4°) carbons from the **DMP** dimers (compare with Tables 4.4 and 4.5 above). The visibility of all of these carbons from a single proton suggested the formation of an **m-DMP** heterodimer. The NMR assignments for this compound are given in Table 4.7 (the two amide methyl groups were unable to be assigned, however). Although NMR suggested formation of a heterodimer, there was no evidence for **mH** formation by HMBC. That is, no protons resonated with pyridine C2, C3, C5, and C6 carbons, other than those protons attributable to the **m**₂ homodimer and the **m-DMP** heterodimer.

1H	bound to ^{13}C	next to 1H	network to ^{13}C	Assignment
4.00 (d, J = 5.8 Hz)	40.9 (3°/1°)	4.73 (dd, J = 5.7 Hz, 7.6 Hz)	22.1, 81.2, 99.3, 102.5, 129.8, 139.9, 172.1	Pyridine C4
4.73 (dd, J = 5.7 Hz, 7.6 Hz)	102.4 (3°/1°)	4.00 (d, J = 5.8 Hz), 6.09 (dd, J = 7.6 Hz, 1.3 Hz)	40.9, 99.3, 129.8	Pyridine C5
6.09 (dd, J = 7.6 Hz, 1.3 Hz)	129.8 (3°/1°)	4.73 (dd, J = 5.7 Hz, 7.6 Hz)	40.9, 49.1, 102.5, 139.9	Pyridine C6
7.20 (t, J = 1.1 Hz)	139.9 (3°/1°)	-	40.9, 49.1, 99.3, 129.8, 172.1	Pyridine C2
3.31 (q, J = 7.2 Hz)	49.1 (2°)	1.23 (t, J = 7.1 Hz)	15.4, 129.8, 139.9	Ethyl CH2
1.23 (t, J = 7.1 Hz)	1.54 (3°/1°)	3.31 (q, J = 7.2 Hz)	49.1	Ethyl CH3
-	99.3 (4°)	-	-	Pyridine C3
-	172.1 (4°)	-	-	Amide C=O (pyridine)
5.11 (s)	-	-	22.0, 40.9, 81.2, 174.4	C(4°)-OH
-	81.2 (4°)	-	-	C(4°)
1.39 (s)	22.0 [a]	-	40.9, 81.2, 174.4	C(4°)-CH3
-	174.4 (4°)	-	-	Amide C=O
not assigned	not assigned	not assigned	not assigned	Amide N-CH3
not assigned	not assigned	not assigned	not assigned	Amide N-CH3

Proposed structure: **m-DMP** heterodimer

Table 4.7. NMR data for the assignment of structure C1 from the electrolysis of a mixture of **m**⁺ and **DMP**. See Supporting Information for experimental conditions. [a] This peak could not be assigned directly from HSQC due to low signal/noise in the region of interest.

We sought further spectroscopic evidence for **mH** formation by comparing electrolyses in H₂O and D₂O. We hypothesized that, if **mH** were formed in the reduction of **m**⁺ with **DMP**, electrolysis in D₂O should afford the deuterated **mD**, which would have a characteristic peak near 3 ppm in a ²H-NMR spectrum. We tested this hypothesis by monitoring bulk electrolyses with a flow NMR setup, taking ¹H-NMR spectra before, during, and after the electrolyses, and ²H-NMR spectra before and after the electrolysis in D₂O. The only peaks that were visible on ²H-NMR, however, were from the deuterated acetyl methyl groups of **DMP** and its reduction products

(Figure 4.S25). Neither was **mD** able to be distinguished from **m₂** in the ¹H-NMR spectra of the electrolysis in D₂O. We considered that comparison of electrolyses in H₂O and D₂O could reveal the **mH** peak by inspecting which peak was present in the H₂O sample that was absent (or weaker) in the D₂O sample. In fact there are two small peaks, at 2.697 ppm and at 2.734 ppm, which are present in the H₂O electrolysis but which are nearly absent in the D₂O electrolysis (Figure 4.S23). These peaks are in the same region as the hydride peaks for NADH in D₂O (~2.70 ppm).⁸⁵ However, the peaks were unable to be assigned without accompanying 2D spectra.

Taken together, the bulk electrolysis experiments suggest that the oxidation event called **mH** is more probably due to an **m-DMP** heterodimer than to **mH**. No detectable amount of **mH** was found by 1D or 2D NMR experiments, either during real-time monitoring or in extracts after the electrolysis was complete. By contrast, NMR evidence does support the existence of an **m-DMP** heterodimer, albeit in low yields under the given conditions. The formation of a heterodimer rather than the protonated 1,4-dihydropyridine would explain much of the electrochemistry data in this thesis. For example, no significant solvent KIE would be expected for heterodimer formation, and none is observed. The lack of KIE for the sodium pyruvate CH₃/CD₃ exchange also makes sense in light of this explanation – no H atom would be transferred. The convolution data for reduction (Figure 4.5B) are also explained. From bulk electrolysis experiments, the reduction of **DMP** affords dimer and lactamide in roughly equal amounts, corresponding to $n \sim 1.5$ in the equations on p.121 above. If the presence of **m⁺** causes heterodimer formation, some of the **DMP** would be intercepted after one-electron reduction to form the heterodimer, causing n to fall closer to 1.0. If n did fall from 1.5 to 1.0 for **P**, the total number of electrons transferred to **m⁺** and **DMP** would drop from 2.5 (1 for **m⁺** reduction + 1.5 for **P** reduction) when reduced separately to 2.0 when reduced together, affording an 80% growth in the convolution integral, close to the measured value. Heterodimer formation also helps explain electrochemistry data from Chapter 2, for example the difference in peak currents between the oxidation of chemically prepared **1H** (near 75 μA at 2 mM, Figure 3.1 above) and *ox2* (no greater than 15 μA near 1 mM, see figures in Chapter 2). Finally, the conclusion of heterodimer formation makes sense from the perspective of the inherent reactivities of the two species: pyridine radicals are reactive at the 4-position, and pyruvate radicals are reactive at the acetyl C=O carbon, so when they are together it would make sense for them to react at these positions. In light of these observations, we suggest that, for mNADH formation to be favored by direct electrochemical reduction, an ideal co-reductant should

place radical density on a hydrogen atom, so that an H[•] radical would be transferred to the pyridine C4 position, rather than the acetyl C[•] radical as is currently done with pyruvate.

CONCLUSION

In this chapter, we investigated the mechanism of pyruvate-promoted mNADH formation with cyclic voltammetry, alternating current voltammetry, quantum mechanical computations, and bulk electrolysis. The reduction mechanism appears to involve an interaction between mNAD and pyruvate radicals, and the interaction is common to many pyruvate derivatives, including pyruvate itself, methyl pyruvate, and several pyruvamides. The mNAD radical increases the rate of electron transfer to the pyruvate derivative, suggesting mediated electron transfer, although a covalent adduct between an mNAD radical and a neutral pyruvate compound was too high in energy to support its existence in these experiments. Bulk electrolysis experiments showed that the major product of mNAD⁺ reduction is the 4,4' dimer, and that the major products of pyruvamide reduction are a mixture of dimer and lactamide. Electrolysis of a mixture of mNAD⁺ and a pyruvamide afforded what was characterized as a heterodimer between the two species, bound between the pyridine C4 carbon and the pyruvamide acetyl C=O carbon. By contrast, no evidence was found for a 1,4-dihydropyridine corresponding to the protonated mNADH. In light of these observations, we suggest that the new oxidation peak from the co-reduction of mNAD⁺ with pyruvate derivatives is in fact due to the heterodimer, and not due to mNADH. Such a conclusion explains other electrochemistry data in this thesis, including the apparent drop in the number of electrons transferred when **m**⁺ and **DMP** are reduced together, the lack of observation of a significant solvent KIE, and oxidation peak currents that are significantly lower than the two-electron oxidation event observed for chemically prepared mNADH. Finally, the formation of a heterodimer makes sense in light of the inherent reactivity of pyruvate and mNAD radicals. We suggest that, for direct electrochemical reduction of mNAD⁺ to mNADH, an ideal co-reductant would transfer radical density onto a hydrogen atom, instead of (as is the case with pyruvates) onto an acetyl carbon.

CHAPTER 5: SUGGESTIONS FOR FUTURE WORK

The experimental work in this thesis might be summarized with the following sentence: Electrochemical reduction of NAD^+ mimetics generates radicals that react rapidly, and indiscriminately, with other radicals, preferentially at the pyridine 4-position. While some progress was made in this thesis toward understanding the structural features that correlate with dimerization rates (Chapter 2), namely that out-of-plane pyridine 1-substituents afford faster dimerization rates, a method to regenerate mNADH from mNAD⁺ has not yet been found. The overlap of the potential of *ox2* with the potential of mNADH oxidation (Chapter 3) appears to have been a coincidence, with bulk electrolysis experiments showing formation of a pyridine-pyruvate heterodimer but no detectable amounts of mNADH (Chapter 4). The study of NAD^+ mimetics may be continued in several directions, a few of which will be suggested here. It goes without saying that the suggestions below are only prompts to spark thought in a given direction. A creative mind can certainly conceive of many other approaches besides the ones proposed here. A conversation between creative minds would beget still more research ideas.

One method invited by the summary sentence at the start of this chapter would be to explore H atom transfer reagents as co-reductants alongside mNAD⁺. If the co-reductant could localize radical density on a hydrogen atom, perhaps this hydrogen atom would react with the mNAD radical to form the desired mNADH. One example of an H atom transfer reagent is 4-cobaltocenyl-N,N-dimethylaniline, which upon reduction can donate an H atom to a nickel catalyst for hydrogenation of alkenes and alkynes.⁸⁸ Certainly many other H atom transfer reagents could be found with a good literature search. Once a suitable H atom transfer reagent is found, it may be desirable to attach this to the mimetic, creating a self-recycling NADH analogue. As an alternative to homogeneous co-reductants, the electrode surface itself could be modified to place labile, adsorbed H atoms near to the mNAD radical.¹⁸

Instead of H atom transfer to an mNAD[•] radical, research could explore mediated hydride transfer to mNAD⁺, reducing a homogeneous mediator (a rhodium catalyst, for example³) that reduces mNAD⁺ directly, or a mediator that reduces mNAD⁺ with the help of an enzyme catalyst (for example, pyruvate \rightarrow lactate, then lactate + mNAD⁺ \rightarrow pyruvate + mNADH, with help of lactate dehydrogenase). Other schemes can also be envisioned. Perhaps the mediators could be co-localized with the mNAD⁺ in a polymer hydrogel, bound to an electrode surface.⁸⁹

A third avenue for future work would be to more fully characterize the heterodimer from

bulk electrolysis of mNAD^+ with pyruvate. While the NMR data in Chapter 4 support the formation of a pyruvate- mNAD heterodimer more than they support the formation of a protonated mNADH , the most certain test to correlate $\text{ox}2$ with the heterodimer would be to purify the heterodimer, characterize it by NMR, and run electrochemistry on it. However, the fruitfulness of such an endeavor is questionable. The experiment would undoubtedly require extended troubleshooting of reaction and, especially, separation conditions, and even if the assignment were made with certainty it would not address the question of how to regenerate mNADH from mNAD^+ . In spite of these reservations, characterizing the heterodimer may still be a useful endeavor, if only for developing in the scientist an ability to isolate and characterize bulk electrolysis products. This skill would be most useful for convincing a skeptical reviewer of mNADH formation, in the event that electrolysis conditions that favor its formation are found.^m

A fourth avenue for future work could be to explore synthetic applications of the $(\text{mNAD})_2$ dimer. For example, it may be capable of acting as a reducing agent, akin to mNADH . However, it is difficult to see what advantage an $(\text{mNAD})_2$ dimer could offer as a reducing agent over more conventional choices such as hydrogen gas and sodium borohydride, especially considering that the dimer is enzymatically inactive. A different application of the 4,4' dimer could be as an electrode film during bulk electrolysis; for example, the 4,4' dimer of 1-(p-tolyl)pyridine mitigated proton reduction during the reduction of CO_2 .⁹⁰ Certainly other possible applications of the dimer could be envisioned.

Yet another avenue for future work could be in a different direction, extending the theory of alternating current voltammetry to account for more interesting electrochemical systems. Analytic solutions of the ACV equation are frequently only available for first-order reactions, with second-order reactions requiring either quasi-first-order experimental conditions (where one of the two reagents is present in large excess) or numerical modeling to obtain a solution. A simulation software such as COMSOL could be used to model electrochemical systems with an arbitrary number of components that interact with each other in arbitrary ways. If such a model could be obtained, it would allow kinetic and thermodynamic values to be extracted from ACV data of

^m A quick-and-dirty test for mNADH formation could be HSQC NMR of the electrolysis mixture (or an extract thereof). HSQC reveals carbon-hydrogen connectivity, and CH_2 groups appear as downward-facing peaks while CH and CH_3 groups appear as upward facing peaks (carbon atoms not bound to a proton are silent on HSQC). If the mNAD^+ has no CH_2 groups – for example, 1-methyl nicotinamide, or 1-isopropyl nicotinamide – it would make the dihydropyridine CH_2 group a little easier to identify in a crude sample.

mixtures of redox-active compounds; alternatively, it could allow reaction schemes to be identified for an unknown experimental system based upon the progression of the alternating current. While such an endeavor would not directly answer the question of how to regenerate mNADH from mNAD⁺, it would become another electrochemical tool for interpreting rapid chemical reactions like those involved in radical dimerization (and presumably also in mNADH formation). The greater electrochemistry community may also appreciate a computational model to predict the alternating current for an arbitrary electrochemical reaction scheme.

It is hoped that the findings in this thesis, and the suggestions offered in this last chapter, point future research in a direction that intersects an answer to the fascinating and challenging question of how to regenerate mNADH from mNAD⁺.

REFERENCES

- (1) Sellés Vidal, L.; Kelly, C. L.; Mordaka, P. M.; Heap, J. T. Review of NAD(P)H-Dependent Oxidoreductases: Properties, Engineering and Application. *Biochimica et Biophysica Acta - Proteins and Proteomics*. Elsevier B.V. February 1, 2018, pp 327–347. <https://doi.org/10.1016/j.bbapap.2017.11.005>.
- (2) Rodkey, F. L. The Effect of Temperature on the Oxidation-Reduction Potential of the Diphosphopyridine Nucleotide System. *J Biol Chem* **1959**, *234* (1), 188–190. [https://doi.org/10.1016/s0021-9258\(18\)70361-x](https://doi.org/10.1016/s0021-9258(18)70361-x).
- (3) Hollmann, F.; Schmid, A.; Steckhan, E. The First Synthetic Application of a Monooxygenase Employing Indirect Electrochemical NADH Regeneration. *Angew. Chem. Int. Ed* **2001**, *40* (1).
- (4) Paul, C. E.; Gargiulo, S.; Opperman, D. J.; Lavandera, I.; Gotor-Fernández, V.; Gotor, V.; Taglieber, A.; Arends, I. W. C. E.; Hollmann, F. Mimicking Nature: Synthetic Nicotinamide Cofactors for C=C Bioreduction Using Enoate Reductases. *Org Lett* **2013**, *15* (1), 180–183. <https://doi.org/10.1021/ol303240a>.
- (5) Shanks, B. H.; Broadbelt, L. J. A Robust Strategy for Sustainable Organic Chemicals Utilizing Bioprivileged Molecules. *ChemSusChem* **2019**, *12* (13), 2970–2975. <https://doi.org/10.1002/cssc.201900323>.
- (6) Takeda, J.; Ohta, S.; Hirobe, M. Steric and Electronic Effects of Methyl Substituents at the 2- and 6-Positions on N-Benzyl-1, 4-Dihydronicotinamide. *Chem Pharm Bull (Tokyo)* **1987**, *35* (7), 2661–2667. <https://doi.org/10.1248/CPB.35.2661>.
- (7) Carelli, V.; Liberatore, F.; Scipione, L.; Di Rienzo, B.; Tortorella, S. Dithionite Adducts of Pyridinium Salts: Regioselectivity of Formation and Mechanisms of Decomposition. *Tetrahedron* **2005**, *61* (43), 10331–10337. <https://doi.org/10.1016/J.TET.2005.07.096>.
- (8) Ryan, J. D.; Fish, R. H.; Clark, D. S. Engineering Cytochrome P450 Enzymes for Improved Activity towards Biomimetic 1,4-NADH Cofactors. *ChemBioChem* **2008**, *9* (16), 2579–2582. <https://doi.org/10.1002/CBIC.200800246>.
- (9) Löw, S. A.; Löw, I. M.; Weissenborn, M. J.; Hauer, B. Enhanced Ene-Reductase Activity through Alteration of Artificial Nicotinamide Cofactor Substituents. *ChemCatChem* **2016**, *8* (5), 911–915. <https://doi.org/10.1002/cctc.201501230>.
- (10) *The Pyridine Nucleotide Coenzymes*; Everse, J., Anderson, B., You, K.-S., Eds.; Academic Press: New York, 1982.
- (11) Lutz, J.; Hollmann, F.; Ho, T. V.; Schnyder, A.; Fish, R. H.; Schmid, A. Bioorganometallic Chemistry: Biocatalytic Oxidation Reactions with Biomimetic NAD⁺/NADH Co-Factors and [Cp*Rh(Bpy)H]⁺ for Selective Organic Synthesis. *J Organomet Chem* **2004**, *689* (25 SPEC. ISS.), 4783–4790. <https://doi.org/10.1016/j.jorganchem.2004.09.044>.

- (12) Warburg, O.; Christian, W.; Griese, A. Wasserstoffübertragendes Co-Ferment, Seine Zusammensetzung Und Wirkungsweise. *Biochem Z* **1935**, 282, 157–205.
- (13) Paiss, Y.; Stein, G. The Mechanism of the Reduction of Some Nicotinamide Derivatives. *J Chem Soc* **1958**, 2905–2909.
- (14) Taylor, K. E.; Jones, J. B. Nicotinamide Coenzyme Regeneration by Dihydropyridine and Pyridinium Compounds. *J Am Chem Soc* **1976**, 98 (18), 5689–5694.
<https://doi.org/10.1021/ja00434a047>.
- (15) Bryan Jones, B. J.; Sneddon, D. W.; Higgins, W.; Lewis, A. J. *Preparative-Scale Reductions of Cyclic Ketone and Aldehyde Substrates of Horse Liver Alcohol Dehydrogenase with in Situ Sodium Dithionite Recycling of Catalytic Amounts of NAD*; 1972.
- (16) Kalyanasundaram, K.; Colassis, T.; Humphry-Baker, R.; Grätzel, M.; Savarino, P.; Barni, E.; Pelizzetti, E. Luminescence, Charge-Transfer Complexes, and Photoredox Processes Involving N-Alkylnicotinamide/Dihydronicotinamide Surfactants. *J Am Chem Soc* **1989**, 111 (9), 3300–3311. <https://doi.org/10.1021/ja00191a029>.
- (17) Wienkamp, R.; Steckhan, E. Selective Generation of NADH by Visible Light**. *Angew. Chem. Int. Ed. Engl.* **1983**, 22 (6), 497.
- (18) Ali, I.; Gill, A.; Omanovic, S. Direct Electrochemical Regeneration of the Enzymatic Cofactor 1,4-NADH Employing Nano-Patterned Glassy Carbon/Pt and Glassy Carbon/Ni Electrodes. *Chemical Engineering Journal* **2012**, 188, 173–180.
<https://doi.org/10.1016/j.cej.2012.02.005>.
- (19) Ali, I.; Khan, T.; Omanovic, S. Direct Electrochemical Regeneration of the Cofactor NADH on Bare Ti, Ni, Co and Cd Electrodes: The Influence of Electrode Potential and Electrode Material. *J Mol Catal A Chem* **2014**, 387, 86–91.
<https://doi.org/10.1016/j.molcata.2014.02.029>.
- (20) Barin, R.; Rashid-Nadimi, S.; Biria, D.; Asadollahi, M. A. Direct Electrochemical Regeneration of 1,4-NADH at the Copper Foam and Bimetallic Copper Foam. *Electrochim Acta* **2017**, 247, 1095–1102. <https://doi.org/10.1016/j.electacta.2017.07.096>.
- (21) Wang, X.; Saba, T.; Yiu, H. H. P.; Howe, R. F.; Anderson, J. A.; Shi, J. Cofactor NAD(P)H Regeneration Inspired by Heterogeneous Pathways. *Chem.* Elsevier Inc 2017, pp 621–654. <https://doi.org/10.1016/j.chempr.2017.04.009>.
- (22) Lancaster, L.; Bulutoglu, B.; Banta, S.; Wheeldon, I. Enzyme Colocalization in Protein-Based Hydrogels. *Methods Enzymol* **2019**, 617, 265–285.
<https://doi.org/10.1016/bs.mie.2018.12.006>.
- (23) Geraskina, M. R.; Dutton, A. S.; Juetten, M. J.; Wood, S. A.; Winter, A. H. The Viologen Cation Radical Pimer: A Case of Dispersion-Driven Bonding. *Angew. Chem. Int. Ed.* **2017**, 56, 9435–9439. <https://doi.org/10.1002/ange.201704959>.

- (24) Burnett, J. N.; Underwood, A. L. Electrochemical Reduction of 1-Methyl-3-Carbamidopyridinium Chloride. *Journal of Organic Chemistry* **1965**, *30*, 1154–1158.
- (25) Blaedel, W. J.; Haas, R. G. Electrochemical Oxidation of NADH Analogs. *Anal. Chem.* **1970**, *42* (8), 918–927.
- (26) Hapiot, P.; Savéant, J. M.; Moiroux, J. Electrochemistry of NADH/NAD⁺ Analogues. A Detailed Mechanistic Kinetic and Thermodynamic Analysis of the 10-Methylacridan/10-Methylacridinium Couple in Acetonitrile. *J Am Chem Soc* **1990**, *112* (4), 1337–1343. https://doi.org/10.1021/JA00160A007/ASSET/JA00160A007.FP.PNG_V03.
- (27) Schmakel, C. O.; Santhanam, K. S. V.; Elving, P. J. Nicotinamide and N'-Methylnicotinamide: Electrochemical Redox Pattern: Behavior of Free Radical, Dimeric, and Dihydropyridine Species. *J Electrochem Soc* **1974**, *121* (3), 345. <https://doi.org/10.1149/1.2401814>.
- (28) Jensen, M. A.; Elving, P. J. Nicotinamide Adenine Dinucleotide (NAD⁺): Formal Potential of the NAD⁺/NAD[•] Couple and NAD[•] Dimerization Rate. *Biochim Biophys Acta Bioenerg* **1984**, *764*, 310–315.
- (29) Hermolin, J.; Talmor, D.; Kirowa-Eisner, E. Reverse Pulse Voltammetry in EC2 Reactions: Electrochemistry of 1-Alkyl-4-t-Butylpyridinium Ions. *Journal of Electroanalytical Chemistry* **1982**, *139*, 81–95.
- (30) Rueda, M.; Compton, R. G.; Alden, J. A.; Prieto ~', F. Impedance Voltammetry of Electro-Dimerization Mechanisms: Application to the Reduction of the Methyl Viologen Di-Cation at Mercury Electrodes and Aqueous Solutions. *Journal of Electroanalytical Chemistry* **1998**, *443*, 227–235.
- (31) Pospíšil, L.; Hromadová, M.; Sokolová, R.; Lanza, C. Kinetics of Radical Dimerization. Simple Evaluation of Rate Constant from Convolution Voltammetry and Faradaic Phase Angle Data. *Electrochim Acta* **2019**, *300*, 284–289. <https://doi.org/10.1016/j.electacta.2019.01.119>.
- (32) Andrieux, C. P.; Savéant, J. M. Electrodimerization: II. Reduction Mechanism of Immonium Cations. *J Electroanal Chem Interfacial Electrochem* **1970**, *26* (2–3), 223–235. [https://doi.org/10.1016/S0022-0728\(70\)80307-2](https://doi.org/10.1016/S0022-0728(70)80307-2).
- (33) Yang, H.; Wipf, D. O.; Bard, A. J. Application of Rapid Scan Cyclic Voltammetry to a Study of the Oxidation and Dimerization of N,N-Dimethylaniline in Acetonitrile. *Journal of Electroanalytical Chemistry* **1992**, *331* (1–2), 913–924. [https://doi.org/10.1016/0022-0728\(92\)85014-T](https://doi.org/10.1016/0022-0728(92)85014-T).
- (34) Matsubara, Y. A Small yet Complete Framework for a Potentiostat, Galvanostat, and Electrochemical Impedance Spectrometer. *J Chem Educ* **2021**, *98* (10), 3362–3370. <https://doi.org/10.1021/acs.jchemed.1c00228>.
- (35) Andrieux, C. P.; Hapiot, P.; Saveant, J.-M. Fast Potential Step Techniques at

- Ultramicroelectrodes. Application to the Kinetic Characterization of Electrochemically Generated Short-Lived Species. *Journal of Physical Chemistry* **1988**, *92*, 5992–5995.
- (36) Sellés Vidal, L.; Kelly, C. L.; Mordaka, P. M.; Heap, J. T. Review of NAD(P)H-Dependent Oxidoreductases: Properties, Engineering and Application. *Biochimica et Biophysica Acta - Proteins and Proteomics*. Elsevier B.V. February 1, 2018, pp 327–347. <https://doi.org/10.1016/j.bbapap.2017.11.005>.
- (37) de Miranda, A. S.; Milagre, C. D. F.; Hollmann, F. Alcohol Dehydrogenases as Catalysts in Organic Synthesis. *Frontiers in Catalysis* **2022**, *2*, 900554. <https://doi.org/10.3389/FCTLS.2022.900554>.
- (38) Sheldon, R. A.; Woodley, J. M. Role of Biocatalysis in Sustainable Chemistry. *Chem Rev* **2018**, *118* (2), 801–838. https://doi.org/10.1021/ACS.CHEMREV.7B00203/ASSET/IMAGES/LARGE/CR-2017-002034_0025.JPEG.
- (39) Bergquist, P. L.; Siddiqui, S.; Sunna, A. Cell-Free Biocatalysis for the Production of Platform Chemicals. *Front Energy Res* **2020**, *8*, 572701. <https://doi.org/10.3389/FENRG.2020.00193/BIBTEX>.
- (40) Hayes, J. W.; Ruić, I.; Smith, D. E.; Booman, G. L.; Delmastro, J. R. Fundamental Harmonic a.c. Polarography with Irreversible Dimerization Following the Charge Transfer Step. Theory and Experimental Results with the Benzaldehyde System. *Journal of Electroanalytical Chemistry* **1974**, *51* (2), 269–285. [https://doi.org/10.1016/S0022-0728\(74\)80244-5](https://doi.org/10.1016/S0022-0728(74)80244-5).
- (41) Bard, A. J.; Faulkner, L. R. *Electrochemical Methods: Fundamentals and Applications*, 2nd ed.; John Wiley: New York, 2000.
- (42) Fleming, B. D.; Zhang, J.; Bond, A. M.; Bell, S. G.; Wong, L. L. Separation of Electron-Transfer and Coupled Chemical Reaction Components of Biocatalytic Processes Using Fourier Transform Ac Voltammetry. *Anal Chem* **2005**, *77* (11), 3502–3510. <https://doi.org/10.1021/AC048151Y/ASSET/IMAGES/MEDIUM/AC048151YE00012.GIF>.
- (43) Dale-Evans, A. R.; Robinson, M. J.; Lloyd-Laney, H. O.; Gavaghan, D. J.; Bond, A. M.; Parkin, A. A Voltammetric Perspective of Multi-Electron and Proton Transfer in Protein Redox Chemistry: Insights From Computational Analysis of Escherichia Coli HypD Fourier Transformed Alternating Current Voltammetry. *Front Chem* **2021**, *9*, 424. <https://doi.org/10.3389/FCHEM.2021.672831>.
- (44) Lloyd-Laney, H. O.; Robinson, M. J.; Bond, A. M.; Parkin, A.; Gavaghan, D. J. A Spotter's Guide to Dispersion in Non-Catalytic Surface-Confined Voltammetry Experiments. *Journal of Electroanalytical Chemistry* **2021**, 894. <https://doi.org/10.1016/J.JELECTHEM.2021.115204>.
- (45) Smith, D. E. AC Polarography and Related Techniques: Theory and Practice. In

Electroanalytical Chemistry: A Series of Advances; Bard, A. J., Ed.; Marcel Dekker: New York, 1966; Vol. 1, pp 1–155.

- (46) Oldham, K. B.; Spanier, J. The Replacement of Fick's Laws by a Formulation Involving Semidifferentiation. *J Electroanal Chem Interfacial Electrochem* **1970**, *26* (2–3), 331–341. [https://doi.org/10.1016/S0022-0728\(70\)80316-3](https://doi.org/10.1016/S0022-0728(70)80316-3).
- (47) Baik, M. H.; Friesner, R. A. Computing Redox Potentials in Solution: Density Functional Theory as a Tool for Rational Design of Redox Agents. *Journal of Physical Chemistry A* **2002**, *106* (32), 7407–7412. https://doi.org/10.1021/JP025853N/SUPPL_FILE/JP025853N_S.PDF.
- (48) Samaroo, S.; Hengesbach, C.; Bruggeman, C.; Carducci, N. G. G.; Mtemeri, L.; Staples, R. J.; Guarr, T.; Hickey, D. P. C–H··· π Interactions Disrupt Electrostatic Interactions between Non-Aqueous Electrolytes to Increase Solubility. *Nat Chem* **2023**, *15* (10), 1365–1373. <https://doi.org/10.1038/s41557-023-01291-1>.
- (49) Andrieux, C. P.; Nadjo, L.; Savéant, J. M. Electrodimerization: I. One-Electron Irreversible Dimerization. Diagnostic Criteria and Rate Determination Procedures for Voltammetric Studies. *J Electroanal Chem Interfacial Electrochem* **1970**, *26* (1), 147–186. [https://doi.org/10.1016/S0022-0728\(70\)80072-9](https://doi.org/10.1016/S0022-0728(70)80072-9).
- (50) Pilling, M. J.; Seakins, P. W. *Reaction Kinetics*; Oxford University Press: Oxford, 1995.
- (51) Tee, L. S.; Gotoh, S.; Stewart, W. E. Molecular Parameters for Normal Fluids: Lennard-Jones 12-6 Potential. *Industrial and Engineering Chemistry Fundamentals* **1966**, *5* (3), 356–363. https://doi.org/10.1021/I160019A011/ASSET/I160019A011.FP.PNG_V03.
- (52) Hudson, G. H.; McCoubrey, J. C.; Ubbelohde, A. R. Vapour Diffusion Coefficients and Collision Parameters for Cyclic Molecules. *Transactions of the Faraday Society* **1960**, *56* (0), 1144–1151. <https://doi.org/10.1039/TF9605601144>.
- (53) Harper, K. C.; Bess, E. N.; Sigman, M. S. Multidimensional Steric Parameters in the Analysis of Asymmetric Catalytic Reactions. *Nature Chemistry* **2012**, *4* (5), 366–374. <https://doi.org/10.1038/nchem.1297>.
- (54) Verloop, A.; Hoogenstraaten, W.; Tipker, J. Development and Application of New Steric Substituent Parameters in Drug Design. *Drug Design* **1976**, 165–207. <https://doi.org/10.1016/B978-0-12-060307-7.50010-9>.
- (55) Brethomé, Brethomé, A. V.; Fletcher, S. P.; Paton, R. S. Conformational Effects on Physical-Organic Descriptors: The Case of Sterimol Steric Parameters. *ACS Catal* **2019**, *9*, 2313–2323. <https://doi.org/10.1021/acscatal.8b04043>.
- (56) Sevov, C. S.; Hickey, D. P.; Cook, M. E.; Robinson, S. G.; Barnett, S.; Minteer, S. D.; Sigman, M. S.; Sanford, M. S. Physical Organic Approach to Persistent, Cyclable, Low-Potential Electrolytes for Flow Battery Applications. *J Am Chem Soc* **2017**, *139* (8), 2924–2927. <https://doi.org/10.1021/jacs.7b00147>.

- (57) Lettré, H.; Haede, W.; Ruhbaum, E. Zur Darstellung von Derivaten Des Nicotinsäureamids. *Justus Liebigs Ann Chem* **1953**, 579 (2), 123–132. <https://doi.org/10.1002/JLAC.19535790207>.
- (58) Kosower, E. M.; Teuerstein, A.; Burrows, H. D.; Swallow, A. J. Bimolecular Reactions of Pyridinyl Radicals in Water and the Mechanism of NAD⁺-NADH Dehydrogenase Reactions. *J Am Chem Soc* **1978**, 100 (16), 5185–5190. <https://doi.org/10.1021/JA00484A047>.
- (59) Churchill, R. *Operational Mathematics*, 2nd ed.; McGraw-Hill, Inc.: New York, 1958.
- (60) Whittaker, E. T. An Expression of Certain Known Functions as Generalized Hypergeometric Functions. *Bull. Amer. Math. Soc.* **1903**, 10, 125–134.
- (61) Whittaker, E. T.; Watson, G. N. *A Course of Modern Analysis*, 4th ed.; Cambridge University Press: Cambridge, 1927.
- (62) Chen, H.; Dong, F.; Minter, S. D. The Progress and Outlook of Bioelectrocatalysis for the Production of Chemicals, Fuels and Materials. *Nature Catalysis*. Nature Research March 1, 2020, pp 225–244. <https://doi.org/10.1038/s41929-019-0408-2>.
- (63) Paul, C. E.; Arends, I. W. C. E.; Hollmann, F. Is Simpler Better? Synthetic Nicotinamide Cofactor Analogues for Redox Chemistry. *ACS Catalysis*. March 7, 2014, pp 788–797. <https://doi.org/10.1021/cs4011056>.
- (64) Lutz, J.; Hollmann, F.; Ho, T. V.; Schnyder, A.; Fish, R. H.; Schmid, A. Bioorganometallic Chemistry: Biocatalytic Oxidation Reactions with Biomimetic NAD⁺/NADH Co-Factors and [Cp*Rh(Bpy)H]⁺ for Selective Organic Synthesis. In *Journal of Organometallic Chemistry*; Elsevier B.V., 2004; Vol. 689, pp 4783–4790. <https://doi.org/10.1016/j.jorganchem.2004.09.044>.
- (65) Ryan, J. D.; Fish, R. H.; Clark, D. S. Engineering Cytochrome P450 Enzymes for Improved Activity towards Biomimetic 1,4-NADH Cofactors. *ChemBiochem* **2008**, 9 (16), 2579–2582. <https://doi.org/10.1002/cbic.200800246>.
- (66) Elving, P. J.; Bresnahan, W. T.; Moiroux, J.; Samec, Z. 524—NAD/NADH as a Model Redox System: Mechanism, Mediation, Modification by the Environment. *J Electroanal Chem Interfacial Electrochem* **1982**, 141 (3), 365–378. [https://doi.org/10.1016/0022-0728\(82\)85223-6](https://doi.org/10.1016/0022-0728(82)85223-6).
- (67) Jensen, M. A.; Elving, P. J. Nicotinamide Adenine Dinucleotide (NAD⁺). Formal Potential of the NAD⁺/NAD[•] Couple and NAD[•] Dimerization Rate. *Biochimica et Biophysica Acta (BBA) - Bioenergetics* **1984**, 764 (3), 310–315. [https://doi.org/10.1016/0005-2728\(84\)90101-4](https://doi.org/10.1016/0005-2728(84)90101-4).
- (68) Ali, I.; Gill, A.; Omanovic, S. Direct Electrochemical Regeneration of the Enzymatic Cofactor 1,4-NADH Employing Nano-Patterned Glassy Carbon/Pt and Glassy Carbon/Ni Electrodes. *Chemical Engineering Journal* **2012**, 188, 173–180.

<https://doi.org/10.1016/j.cej.2012.02.005>.

- (69) Murray, R. W.; Hiller, L. K. Supporting Electrolyte Effects in Nonaqueous Electrochemistry: Coordinative Relaxation Reactions of Reduced Metal Acetylacetonates in Acetonitrile. *J. Anal. Chem.* **1967**, *39* (11), 1221–1229.
- (70) Kaneco, S.; Iiba, K.; Yabuuchi, M.; Nishio, N.; Ohnishi, H.; Katsumata, H.; Suzuki, T.; Ohta, K. High Efficiency Electrochemical CO₂-to-Methane Conversion Method Using Methanol with Lithium Supporting Electrolytes. *Ind Eng Chem Res* **2002**, *41* (21), 5165–5170. <https://doi.org/10.1021/ie0200454>.
- (71) Stone, N. J.; Swelgart, D. A.; Bond, A. M. Effects of Temperature and Supporting Electrolyte on the Electrochemical Oxidation of (Benzene)Tricarbonylchromium and Other π Hydrocarbon Complexes. *Organometallics* **1986**, *5*, 2553–2555. <https://doi.org/10.1021/om00143a027>.
- (72) L J. Duić; Z. Mandić; F. Kovačiček. The Effect of Supporting Electrolyte on the Electrochemical Synthesis, Morphology, and Conductivity of Polyaniline. *J Polym Sci A Polym Chem* **1994**, *32*, 105–111. <https://doi.org/10.1002/pola.1994.080320112>.
- (73) Katsounaros, I.; Kyriacou, G. Influence of the Concentration and the Nature of the Supporting Electrolyte on the Electrochemical Reduction of Nitrate on Tin Cathode. *Electrochim Acta* **2007**, *52* (23), 6412–6420. <https://doi.org/10.1016/j.electacta.2007.04.050>.
- (74) Peters, B. K.; Rodriguez, K. X.; Reisberg, S. H.; Beil, S. B.; Hickey, D. P.; Kawamata, Y.; Collins, M.; Starr, J.; Chen, L.; Udyavara, S.; Klunder, K.; Gorey, T. J.; Anderson, S. L.; Neurock, M.; Minter, S. D.; Baran, P. S. Scalable and Safe Synthetic Organic Electroreduction Inspired by Li-Ion Battery Chemistry. *Science (1979)* **2019**, *363* (6429), 838–845. <https://doi.org/10.1126/science.aav5606>.
- (75) Elving, P. J.; Milazzo, ; G; Dryhurst, ; G; Moiroux, ; J; Jensen, ; A J; Ohnishi, ; Y; Kikuchi, Y.; Kitami, M. The Role of Adsorption in the Initial One-Electron Electrochemical Reduction of Nicotinamide Adenine Dinucleotide (NAD⁺). *J Am Chem Soc* **1981**, *103* (9), 2379–2386.
- (76) Oldham, K. B. A Signal-Independent Electroanalytical Method. *Anal Chem* **1972**, *44* (1), 196–198. <https://doi.org/10.1021/ac60309a028>.
- (77) Miller, M.; Czochralska, B.; Shugar, D. Red-Ox Transformations of NAD⁺ Model Compounds. *J Electroanal Chem Interfacial Electrochem* **1982**, *141* (3), 287–298. [https://doi.org/10.1016/0022-0728\(82\)85215-7](https://doi.org/10.1016/0022-0728(82)85215-7).
- (78) Matsuda, H.; Ayabe, Y. Zur Theorie Der Randles-Sevčik'schen Kathodenstrahl-Polarographie. *Zeitschrift für Elektrochemie, Berichte der Bunsengesellschaft für physikalische Chemie* **1955**, *59* (6), 494–503. <https://doi.org/10.1002/BBPC.19550590605>.

- (79) Imbeaux, J. C.; Savéant, J. M. Convolutive Potential Sweep Voltammetry: I. Introduction. *J Electroanal Chem Interfacial Electrochem* **1973**, *44* (2), 169–187. [https://doi.org/10.1016/S0022-0728\(73\)80244-X](https://doi.org/10.1016/S0022-0728(73)80244-X).
- (80) Oldham, K. B. A Signal-Independent Electroanalytical Method. *Anal Chem* **1972**, *44* (1), 196–198. <https://doi.org/10.1021/ac60309a028>.
- (81) Martin, C.; Huser, H.; Servat, K.; Kokoh, K. B. Electrosynthesis of Lactic Acid and 2,3-Dimethyltartaric Acid from Pyruvic Acid on Lead Cathode in Aqueous Medium. *Tetrahedron Lett* **2006**, *47* (20), 3459–3462. <https://doi.org/10.1016/j.tetlet.2006.03.035>.
- (82) Bruggeman, C.; Gregurash, K.; Hickey, D. P. Impact of Sodium Pyruvate on the Electrochemical Reduction of NAD⁺ Biomimetics. *Faraday Discuss* **2023**, *247*, 87–100. <https://doi.org/10.1039/D3FD00047H>.
- (83) Yarmolinsky, M. B.; Colowick, S. P. On the Mechanism of Pyridine Nucleotide Reduction by Dithionite. *Biochim Biophys Acta* **1956**, *20* (C), 177–189. [https://doi.org/10.1016/0006-3002\(56\)90276-1](https://doi.org/10.1016/0006-3002(56)90276-1).
- (84) Baizer, M. M.; Petrovich, J. P. Electrolytic Reductive Coupling: Synthetic and Mechanistic Aspects. In *Progress in Physical Organic Chemistry*; John Wiley & Sons, Inc., 1970; Vol. 7, pp 189–227.
- (85) Hoch, J. C.; Baskaran, K.; Burr, H.; Chin, J.; Eghbalian, H. R.; Fujiwara, T.; Gryk, M. R.; Iwata, T.; Kojima, C.; Kurisu, G.; Maziuk, D.; Miyanoiri, Y.; Wedell, J. R.; Wilburn, C.; Yao, H.; Yokochi, M. Biological Magnetic Resonance Data Bank. *Nucleic Acids Res* **2023**, *51* (D1), D368–D376. <https://doi.org/10.1093/NAR/GKAC1050>.
- (86) Wohl, A.; Oesterlin, C. Ueberführung Der Weinsäure in Oxalessigsäure Durch Wasserabspaltung Bei Niedriger Temperatur. *Berichte der deutschen chemischen Gesellschaft* **1901**, *34* (1), 1139–1148. <https://doi.org/10.1002/CBER.190103401191>.
- (87) Owen, T. C.; Austin, D. J. The Pyridine Salts of Hydroxymaleic Anhydride. *Journal of Organic Chemistry* **1993**, *58* (3), 756–758. https://doi.org/10.1021/JO00055A036/ASSET/JO00055A036.FP.PNG_V03.
- (88) Derosa, J.; Garrido-Barros, P.; Li, M.; Peters, J. C. Use of a PCET Mediator Enables a Ni-HER Electrocatalyst to Act as a Hydride Delivery Agent. *J Am Chem Soc* **2022**, *144* (43), 20118–20125. https://doi.org/10.1021/JACS.2C09786/ASSET/IMAGES/LARGE/JA2C09786_0008.JPEG.
- (89) Abdellaoui, S.; Milton, R. D.; Quah, T.; Minter, S. D. NAD-Dependent Dehydrogenase Bioelectrocatalysis: The Ability of a Naphthoquinone Redox Polymer to Regenerate NAD. *Chemical Communications* **2016**, *52* (6), 1147–1150. <https://doi.org/10.1039/C5CC09161F>.
- (90) Nie, W.; Heim, G. P.; Watkins, N. B.; Agapie, T.; Peters, J. C. Organic Additive-Derived

Films on Cu Electrodes Promote Electrochemical CO₂ Reduction to C₂+ Products Under Strongly Acidic Conditions. *Angewandte Chemie International Edition* **2023**, 62 (12), e202216102. <https://doi.org/10.1002/ANIE.202216102>.

- (91) Bruice, T. C. Some Pertinent Aspects of Mechanism as Determined with Small Molecules. *Annu Rev Biochem* **1976**, 45, 331–374. <https://doi.org/10.1146/ANNUREV.BI.45.070176.001555>.
- (92) Chan, S. S.; Nordlund, T. M.; Frauenfelder, H.; Harrison, J. E.; Gunsalus, I. C. Enzymatic Reduction of Nicotinamide Adenine Dinucleotide Phosphate Induced by Radiolysis. *Journal of Biological Chemistry* **1975**, 250 (2), 716–719. [https://doi.org/10.1016/s0021-9258\(19\)41954-6](https://doi.org/10.1016/s0021-9258(19)41954-6).
- (93) Shrestha, N.; Tripathi, A. K.; Govil, T.; Sani, R. K.; Urgan-Demirtas, M.; Kasthuri, V.; Gadhamshetty, V. Electricity from Lignocellulosic Substrates by Thermophilic *Geobacillus* Species. *Scientific Reports 2020 10:1* **2020**, 10 (1), 1–9. <https://doi.org/10.1038/s41598-020-72866-y>.
- (94) Elving, P. J.; Bresnahan, W. T.; Moiroux, J.; Samec, Z. NAD/NADH as a Model Redox System: Mechanism, Mediation, Modification by the Environment. *J. Electroanal Chem.* **1982**, 141 (9), 365–378.

APPENDIX FOR CHAPTER 2

Experimental:

Unless otherwise noted, all electrochemistry experiments were performed in acetonitrile with 2 mM mNAD⁺X⁻ and 0.2 M tetrabutylammonium hexafluorophosphate. All samples were run in an airtight Dr. Bob cell (Gamry), and data were gathered on a BioLogic VSP potentiostat. A glassy carbon working electrode (3 mm diameter), a platinum wire counter electrode, and a silver/silver nitrate reference electrode (0.01 M AgNO₃ with 0.2 M tetrabutylammonium hexafluorophosphate in acetonitrile) were used. Solutions were purged with nitrogen before scanning, and if necessary the glassy carbon electrode was polished between scans (usually needed for X = Cl; a "throwaway" scan is needed after polishing, to clean the electrode). Cyclic voltammograms were run at 800, 400, 200, 100, and 50 mV/s. Electrochemical impedance spectroscopy (1 Hz to 1 MHz at the open circuit potential) was used to find the cell resistance R_u , as the high-frequency limit of the real part of the impedance. Alternating current voltammetry was run from the open circuit potential to -1.8 V vs reference, with a potential sweep rate of 50 mV/s, an alternating potential magnitude of 5 mV, and a frequency of 20 Hz. At the conclusion of the alternating current voltammetry scan, the potential was immediately held at +0.1 V vs reference for 10 seconds, to minimize buildup of dimer in solution. Finally, a small amount of ferrocene (<1 mg) was added after all the scans were finished, and the oxidation potential of ferrocene was found with square wave voltammetry. For 1-methyl-4-*tert*-butyl pyridinium perchlorate, 1 mM substrate was used in acetonitrile with 0.25 M lithium perchlorate, according to the procedure of Hermolin and coworkers.²⁹

Crystals were grown either by slow evaporation of an acetonitrile solution of the mimetic, or by vapor diffusion of diethyl ether into a solution of the mimetic in acetonitrile. For this latter method, a 4 mL vial was filled halfway with a solution of mimetic in acetonitrile, and this vial was placed upright, uncapped, into a 40 mL vial containing ~5 mL of diethyl ether. The large vial was capped and left undisturbed at room temperature for several days, during which crystal growth could be observed in the small vial. Crystal structures were obtained on a Rigaku Synergy S Diffractometer.

NMR spectra were gathered on an Agilent 500 MHz NMR spectrometer in DMSO-*d*₆.

Synthesis:

1-(2,4-dinitrophenyl) nicotinamide chloride (9-Cl): Adapted from a previous procedure.⁵⁷ 1-Chloro-2,4-dinitrobenzene (2.026 g, 10 mmol), nicotinamide (1.221 g, 10 mmol), and ethanol (0.5 mL) were sealed in a glass vial with a pressure-release cap at 90 °C for 21 h, to give a dark red solid. After this time, a small amount of boiling ethanol was added to the vial, saturated with the crude product, and transferred to a 250 mL round bottom flask with a stir bar on a hot sand bath. This process was repeated until all of the product had been dissolved and transferred to the round bottom flask (83 mL ethanol needed in total). The clear orange solution was brought to a boil with stirring, and cyclohexane was added dropwise until the solution remained imperceptibly cloudy (25 mL cyclohexane needed). Then, the stir bar was removed, the heat was turned off, and the flask was covered with aluminum foil and left on the sand bath to cool overnight. The flask was then cooled in an ice bath to precipitate more product. The liquid was decanted, and the solids were rinsed with a 1:1 v/v mixture of ethanol/cyclohexane (3 x 3 mL). The solids were transferred to a 20 mL collection vial with a minimum amount of methanol, and dried overnight on a rotary evaporator (95 mbar, 40 °C). The final product was collected as a dark red-orange foamy solid (1.658 g = 51%).

¹H NMR (500 MHz, dmsO) δ 9.84 (t, *J* = 1.6 Hz, 1H), 9.49 (dt, *J* = 6.2, 1.3 Hz, 1H), 9.29 (dt, *J* = 8.3, 1.4 Hz, 1H), 9.11 (d, *J* = 2.5 Hz, 1H), 8.98 (dd, *J* = 8.7, 2.5 Hz, 1H), 8.78 (s, 1H), 8.53 (dd, *J* = 8.2, 6.1 Hz, 1H), 8.42 (d, *J* = 8.7 Hz, 1H), 8.29 (s, 1H).

Notes:

- The shelf-life of **9-Cl** is less than one year. However, old product can be re-purified by dissolving as much as possible in boiling ethanol, decanting the liquid away from any insoluble residue, and recrystallizing the product with cyclohexane as before.

1-(2,4-dinitrophenyl) nicotinamide bromide (9-Br): 1-Bromo-2,4-dinitrobenzene (2.51 g, 10.2 mmol) and nicotinamide (1.24 g, 10.2 mmol) were dissolved in ethanol (20 mL) in a 250 mL round bottom flask. The contents were mixed overnight at 100 °C without a reflux condenser. The following morning, the deep orange-red solution was brought to a boil, and it solidified to a dark red, bubbly resin over 2 h. Then, 120 mL ethanol was added to the flask and brought to a boil with mixing. Once the resin was dissolved, cyclohexane was added dropwise until the solution remained imperceptibly cloudy (21 mL cyclohexane was needed). Then the stir bar was removed, the heat was turned off, and the flask was covered with aluminum foil and left on the sand bath to cool to

room temperature. Once cooled, the flask was stoppered and placed in the freezer overnight. Then, the liquid was decanted, and the solids were rinsed with a 1:1 v/v mixture of ethanol/cyclohexane (3 x 7 mL). The crystalline yellow solid was dried on high vacuum while still in the flask, then transferred to a 20 mL collection vial and dried further under high vacuum. The final product was collected as a fluffy yellow solid (3.052 g, 83%).

^1H NMR (500 MHz, dmsO) δ 9.78 (t, J = 1.6 Hz, 1H), 9.49 (dt, J = 6.2, 1.3 Hz, 1H), 9.25 (dt, J = 8.2, 1.5 Hz, 1H), 9.11 (d, J = 2.5 Hz, 1H), 8.98 (dd, J = 8.7, 2.5 Hz, 1H), 8.66 (s, 1H), 8.54 (dd, J = 8.2, 6.1 Hz, 1H), 8.41 (d, J = 8.7 Hz, 1H), 8.29 (s, 1H).

Notes:

- The reaction does not need to proceed overnight; essentially identical yields are achieved, so long as the ethanol is boiled away to leave a hard resin (take care not to burn the product).
- **9-Br** is hygroscopic and has a shelf-life of less than 6 months (somewhat longer if stored in a desiccator). The purity of the product corresponds with its solubility in methanol. Making a fresh batch is recommended instead of purifying old product.

1-allyl nicotinamide bromide (1-Br): Allyl bromide (840 μL , 9.9 mmol), nicotinamide (1.241 g, 10.2 mmol), and acetonitrile (10 mL) were added to a 20 mL vial with a pressure release cap, and mixed at 50 °C for 12 h. The contents were transferred to a 100 mL round bottom flask, using ethanol as needed to dissolve solids. The product was crystallized from ethanol/hexanes, and was collected as a light brown crystalline solid (1.509 g, 61%).

^1H NMR (500 MHz, dmsO) δ 9.45 (t, J = 1.6 Hz, 1H), 9.15 (dt, J = 6.1, 1.3 Hz, 1H), 8.97 (dt, J = 8.1, 1.5 Hz, 1H), 8.60 (s, 1H), 8.29 (dd, J = 8.1, 6.1 Hz, 1H), 8.19 (s, 1H), 6.18 (ddt, J = 16.7, 10.4, 6.3 Hz, 1H), 5.50 – 5.42 (m, 2H), 5.33 (dt, J = 6.2, 1.4 Hz, 2H).

1-allyl nicotinamide chloride (1-Cl): Nicotinamide (0.122 g, 1 mmol) was dissolved in acetonitrile (2 mL) at 70-80 °C in a 20 mL vial. Then, allyl chloride (89.6 μL , 1.1 mmol) was added, and the mixture was capped and heated at 55 °C for 15 h. The product was crashed out with a 1:1 v/v mixture of diethyl ether/tetrahydrofuran (15 mL). The liquid was decanted, and the solids were rinsed with a 1:1 v/v mixture of diethyl ether/tetrahydrofuran (3 x 5 mL), using a centrifuge to help separate the solids. The title product was collected as a fluffy, cream-colored powder (9 mg, 4.5%).

^1H NMR (500 MHz, dmsO) δ 9.48 (s, 1H), 9.14 (d, J = 6.1 Hz, 1H), 8.98 (d, J = 8.1 Hz, 1H), 8.66 (s, 1H), 8.28 (ddd, J = 7.9, 6.1, 1.3 Hz, 1H), 8.18 (s, 1H), 6.17 (ddt, J = 16.8, 10.5, 6.3 Hz, 1H), 5.48 – 5.42 (m, 2H), 5.31 (dd, J = 6.2, 1.4 Hz, 2H).

Notes:

- Heat in excess of 55 °C tends to burn the allyl chloride.
- **1-Cl** has an extremely high affinity for polar solvents. If dissolved in methanol, the methanol will not come off, even under vacuum.
- During crystallization, if the polarity of the antisolvent is too different from the polarity of the solvent (e.g. hexanes and ethanol, or diethyl ether and acetonitrile), the crystallization will fail, and instead of one phase there will be two liquid phases.

1-benzyl nicotinamide bromide (**6-Br**): Adapted from a literature procedure.⁴ Benzyl bromide (280 μL , 2.35 mmol), nicotinamide (0.287 g, 2.35 mmol), and acetonitrile (10 mL) were added to a 50 mL Erlenmeyer flask. The liquid was brought to a boil with gentle swirling for 5 min, during which time a white crystalline solid precipitated. The mixture was cooled to room temperature, and the solids were vacuum filtered over filter paper, rinsed with diethyl ether (~5 mL), and dried under vacuum. The title product was collected as a fluffy white, static-y, crystalline powder (0.239 g, 35%).

¹H NMR (500 MHz, dmsO) δ 9.60 (t, $J = 1.6$ Hz, 1H), 9.27 (dd, $J = 6.2, 1.4$ Hz, 1H), 8.94 (dt, $J = 8.2, 1.6$ Hz, 1H), 8.58 (s, 1H), 8.27 (dd, $J = 8.1, 6.1$ Hz, 1H), (s, 1H), 7.60 – 7.51 (m, 2H), 7.49 – 7.38 (m, 3H), 5.90 (s, 2H).

Notes:

- The yield can be increased substantially with a longer reaction time.

1-phenethyl nicotinamide bromide (**3-Br**): Phenethylamine (63.0 μL , 0.5 mmol) was added to a solution of **9-Br** (73.7 mg, 0.200 mmol) in methanol (3 mL). The contents were mixed at room temperature for 8 minutes, after which diethyl ether (25 mL) was added to crash out the product. When the solid had settled, the contents of the flask were filtered through a plug of sand, and the plug was rinsed with diethyl ether until the eluent was colorless. The plug was flushed with methanol into a collection vial, and the solvent was removed in vacuo to yield the title product as a yellow crystalline solid (54.6 mg, 89%).

¹H NMR (500 MHz, dmsO) δ 9.49 (s, 1H), 9.11 (d, $J = 6.1$ Hz, 1H), 8.91 (dt, $J = 8.2, 1.5$ Hz, 1H), 8.56 (s, 1H), 8.23 (dd, $J = 8.1, 6.1$ Hz, 1H), 8.17 (s, 1H), 7.28 (m, $J = 28.6, 8.0, 6.0$ Hz, 5H), 4.91 (t, $J = 7.6$ Hz, 2H), 3.29 (t, $J = 7.6$ Hz, 2H).

1-phenethyl nicotinamide chloride (**3-Cl**): Phenethylamine (63.0 μL , 0.5 mmol) was added to a solution of **9-Cl** (64.5 mg, 0.199 mmol) in methanol (3 mL). The contents were mixed at room

temperature for 11 minutes, after which diethyl ether (25 mL) was added to crash out the product. When the solid had settled, the contents of the flask were filtered through a plug of Celite, and the plug was rinsed with diethyl ether until the eluent was colorless. The plug was flushed with methanol into a collection vial, and the solvent was removed in vacuo. The product was redissolved in methanol and passed through a short silica plug to remove traces of Celite, and the solvent was again removed in vacuo. The title product was collected as an orange crystalline solid (43.0 mg, 82%).

^1H NMR (500 MHz, dmso) δ 9.58 (s, 1H), 9.14 – 9.09 (d, J = 6.1 Hz, 1H), 8.95 (dt, J = 8.1, 1.5 Hz, 1H), 8.70 (s, 1H), 8.22 (dd, J = 8.1, 6.1 Hz, 1H), 8.17 (s, 1H), 7.34 – 7.21 (m, 5H), 4.90 (t, J = 7.6 Hz, 2H), 3.30 (t, J = 7.6 Hz, 2H).

Notes:

- The need for a second filtration may be omitted by replacing Celite with silica gel in the first filtration.

1-butyl nicotinamide bromide (2-Br): Adapted from a literature procedure.⁴ 1-Bromobutane (2.15 mL, 19.9 mmol), nicotinamide (1.235 g, 10.1 mmol), and acetonitrile (10 mL) were added to a 20 mL vial with a pressure-release cap. The contents were mixed at 50 °C for 2 h, then at 80-100 °C for 10 h. The contents were transferred to a 100 mL round bottom flask, using ethanol as needed to dissolve solids, and the solvent was removed under vacuum to yield a white soapy residue. The residue was crystallized from cyclohexane/ethanol. The title product was collected as off-white crystals (1.457 g, 56%).

^1H NMR (500 MHz, dmso) δ 9.48 (t, J = 1.5 Hz, 1H), 9.20 (dt, J = 6.1, 1.3 Hz, 1H), 8.91 (dt, J = 8.2, 1.5 Hz, 1H), 8.55 (s, 1H), 8.25 (dd, J = 8.1, 6.0 Hz, 1H), 8.16 (s, 1H), 4.64 (t, J = 7.5 Hz, 2H), 1.91 (dq, J = 9.3, 7.6 Hz, 2H), 1.29 (h, J = 7.4 Hz, 2H), 0.90 (t, J = 7.4 Hz, 3H).

1-butyl nicotinamide chloride (2-Cl): Butylamine (49.4 μL , 0.5 mmol) was added to a solution of **9-Cl** (64.9 mg, 0.200 mmol) in methanol (3 mL). The contents were mixed at room temperature for 10-14 minutes, after which diethyl ether (25 mL) was added to crash out the product. When the solid had settled, the contents of the flask were filtered through a plug of Celite, and the plug was rinsed with diethyl ether until the eluent was colorless. The plug was flushed with methanol into a collection vial, and the solvent was removed in vacuo. The product was redissolved in methanol and passed through a short silica plug to remove traces of Celite, and the solvent was again removed in vacuo. The title product was collected as a flaky orange soapy solid (35.9 mg,

84%).

^1H NMR (500 MHz, dmsO) δ 9.56 (s, 1H), 9.21 (d, $J = 6.1$ Hz, 1H), 8.96 (d, $J = 8.5$ Hz, 1H), 8.69 (s, 1H), 8.32 – 8.22 (dd, $J = 8.0, 6.3$ Hz, 1H), 8.17 (s, 1H), 4.65 (t, $J = 7.5$ Hz, 2H), 1.92 (p, $J = 7.6$ Hz, 2H), 1.30 (h, $J = 7.4$ Hz, 2H), 0.91 (t, $J = 7.5$ Hz, 3H).

Notes:

- The need for a second filtration may be omitted by replacing Celite with silica gel in the first filtration.

1-isopropyl nicotinamide bromide (4-Br): 2-Bromopropane (540 μL , 5.75 mmol), nicotinamide (0.140 g, 1.15 mmol), and acetonitrile (1 mL) were heated in a Parr bomb reactor at 100-110 $^\circ\text{C}$ for 24 h. After cooling to room temperature, the contents were transferred to a 50 mL round bottom flask, using methanol as necessary to dissolve solids (~10 mL needed). The contents were concentrated to a powder *in vacuo*, and recrystallized from ethanol/hexanes. The title product was collected as a flaky, fluffy white crystalline solid (152 mg, 54%).

^1H NMR (500 MHz, dmsO) δ 9.49 (s, 1H), 9.32 (d, $J = 6.1$ Hz, 1H), 8.92 (d, $J = 8.0$ Hz, 1H), 8.59 (s, 1H), 8.31 – 8.24 (dd, $J = 7.7, 6.6$ Hz, 1H), 8.18 (s, 1H), 5.10 (hept, $J = 6.8$ Hz, 1H), 1.63 (d, $J = 6.6$ Hz, 6H).

1-isopropyl nicotinamide chloride (4-Cl): 2-Aminopropane (42.8 μL , 0.5 mmol) was added to a solution of **9-Cl** (65.0 mg, 0.200 mmol) in methanol (3 mL). The contents were mixed at room temperature for 55 minutes, after which diethyl ether (25 mL) was added to crash out the product. When the solid had settled, the contents of the flask were filtered through a plug of sand, and the plug was rinsed with diethyl ether until the eluent was colorless. The plug was flushed with methanol into a 25 mL round bottom flask, and the solution was passed twice through a short silica plug before being concentrated *in vacuo*. The title product was collected as an orange crystalline solid (34.9 mg, 87%).

^1H NMR (500 MHz, dmsO) δ 9.61 (s, 1H), 9.32 (d, $J = 6.2$ Hz, 1H), 8.95 (d, $J = 8.7$ Hz, 1H), 8.78 (s, 1H), 8.27 (dd, $J = 8.0, 6.1$ Hz, 1H), 8.18 (s, 1H), 5.10 (p, $J = 6.9$ Hz, 1H), 1.64 (d, $J = 6.6$ Hz, 6H).

Notes:

- The need for a second filtration may be omitted by replacing Celite with silica gel in the first filtration.

1-ethyl nicotinamide bromide (7-Br): Bromoethane (1.50 mL, 20.1 mmol), nicotinamide (1.239 g,

10.1 mmol), and acetonitrile (10 mL) were heated in a Parr bomb reactor at 90 °C for 41 h. After cooling to room temperature, the contents were transferred to a 100 mL round bottom flask, using methanol as needed to dissolve solids. The solvent was removed under vacuum, and the residue (0.426g) was crystallized from ethanol (42 mL) and hexanes (9.6 mL). The title product was collected as large white crystals (1.91 g, 82%).

¹H NMR (500 MHz, dmsO) δ 9.48 (t, *J* = 1.8 Hz, 1H), 9.21 (dt, *J* = 6.1, 1.3 Hz, 1H), 8.91 (dt, *J* = 8.1, 1.5 Hz, 1H), 8.55 (s, 1H), 8.26 (dd, *J* = 8.1, 6.1 Hz, 1H), 8.17 (s, 1H), 4.68 (q, *J* = 7.3 Hz, 2H), 1.56 (t, *J* = 7.3 Hz, 3H).

1-hexyl nicotinamide bromide (5-Br): Hexylamine (66.6 μL, 0.5 mmol) was added to a solution of **9-Br** (73.7 mg, 0.200 mmol) in methanol (3 mL). The contents were mixed at room temperature for 8 minutes, after which diethyl ether (25 mL) was added to crash out the product. When the solid had settled, the contents of the flask were filtered through a short plug of silica, and the plug was rinsed with diethyl ether until the eluent was colorless. The plug was flushed with methanol into a collection vial, and the solvent was removed under vacuum. The product was soaked in diethyl ether to remove any residual 2,4-dinitroaniline. The title product was collected as a brownish-white, soapy, semicrystalline residue (48.1 mg, 84%).

¹H NMR (500 MHz, dmsO) δ 9.50 (s, 1H), 9.21 (d, *J* = 6.1 Hz, 1H), 8.92 (dd, *J* = 8.1, 1.6 Hz, 1H), 8.57 (s, 1H), 8.26 (dd, *J* = 8.1, 6.1 Hz, 1H), 8.18 (s, 1H), 4.64 (t, *J* = 7.6 Hz, 2H), 1.92 (m, 2H), 1.28 (m, 6H), 0.85 (m, 3H).

Notes:

- The diethyl ether soak did not appear to be necessary.

1-hexyl nicotinamide chloride (5-Cl): Hexylamine (66.6 μL, 0.5 mmol) was added to a solution of **9-Cl** (64.7 mg, 0.199 mmol) in methanol (3 mL). The contents were mixed at room temperature for 13 minutes, after which diethyl ether (25 mL) was added to crash out the product. When the solid had settled, the contents of the flask were filtered through a plug of Celite, and the plug was rinsed with diethyl ether until the eluent was colorless. The plug was flushed with methanol into a collection vial, and the solvent was removed in vacuo. The product was redissolved in methanol and passed through a short silica plug to remove traces of Celite, and the solvent was again removed in vacuo. The title product was collected as a soapy, orange, semicrystalline solid (37.0 mg, 77%).

¹H NMR (500 MHz, dmsO) δ 9.59 (s, 1H), 9.22 (d, *J* = 6.0 Hz, 1H), 8.96 (d, *J* = 8.4 Hz, 1H), 8.71

(s, 1H), 8.26 (dd, $J = 8.1, 6.1$ Hz, 1H), 8.17 (s, 1H), 4.64 (t, $J = 7.6$ Hz, 2H), 1.94 (m, 2H), 1.28 (m, 6H), 0.88 – 0.81 (m, 3H).

Notes:

- The need for a second filtration may be omitted by replacing Celite with silica gel in the first filtration.

1-methyl-4-*tert*-butyl pyridinium perchlorate (MP): Adapted from a literature procedure.⁵⁸ 4-*tert*-Butyl pyridine (0.135 g, 1 mmol) and methyl iodide (0.71 g, 5 mmol) were heated together at 60 °C for 2 minutes in a closed vial, then left uncovered overnight at room temperature. The orange-yellow resinous fluid was dissolved in a trace amount of acetonitrile (< 1 mL), and the pyridinium salt was crashed out with a mixture of ethyl acetate and diethyl ether. This process was repeated once to yield an orange resinous fluid (0.223 mg, 79% yield), which was dissolved in methanol (5 mL). In a separate container, silver perchlorate hydrate (0.23 g, 1 mmol silver perchlorate) was dissolved in methanol (10 mL). The silver solution was added dropwise to the pyridinium solution, until no additional silver iodide formed (ethyl acetate and acetonitrile were also added to help with solubility). The fluid was decanted from the silver iodide, passed through a small plug of silica, and concentrated in vacuo. The crude product was dissolved in dichloromethane (10 mL) and washed once with water (10 mL) to remove excess silver salts. The dichloromethane layer was dried over magnesium sulfate, and the product was crashed out by the addition of hexanes (10 mL). The liquid was decanted away from the product, which was briefly concentrated under vacuum and finally collected as a hygroscopic, yellow-orange fluid (73 mg, 26%).

¹H NMR (500 MHz, dmsO) δ 8.85 (d, $J = 6.6$ Hz, 2H), 8.13 (d, $J = 6.8$ Hz, 2H), 4.26 (s, 3H), 1.34 (s, 9H).

Notes:

- The ethyl acetate and acetonitrile did not significantly affect the solubility.

NMR SPECTRA

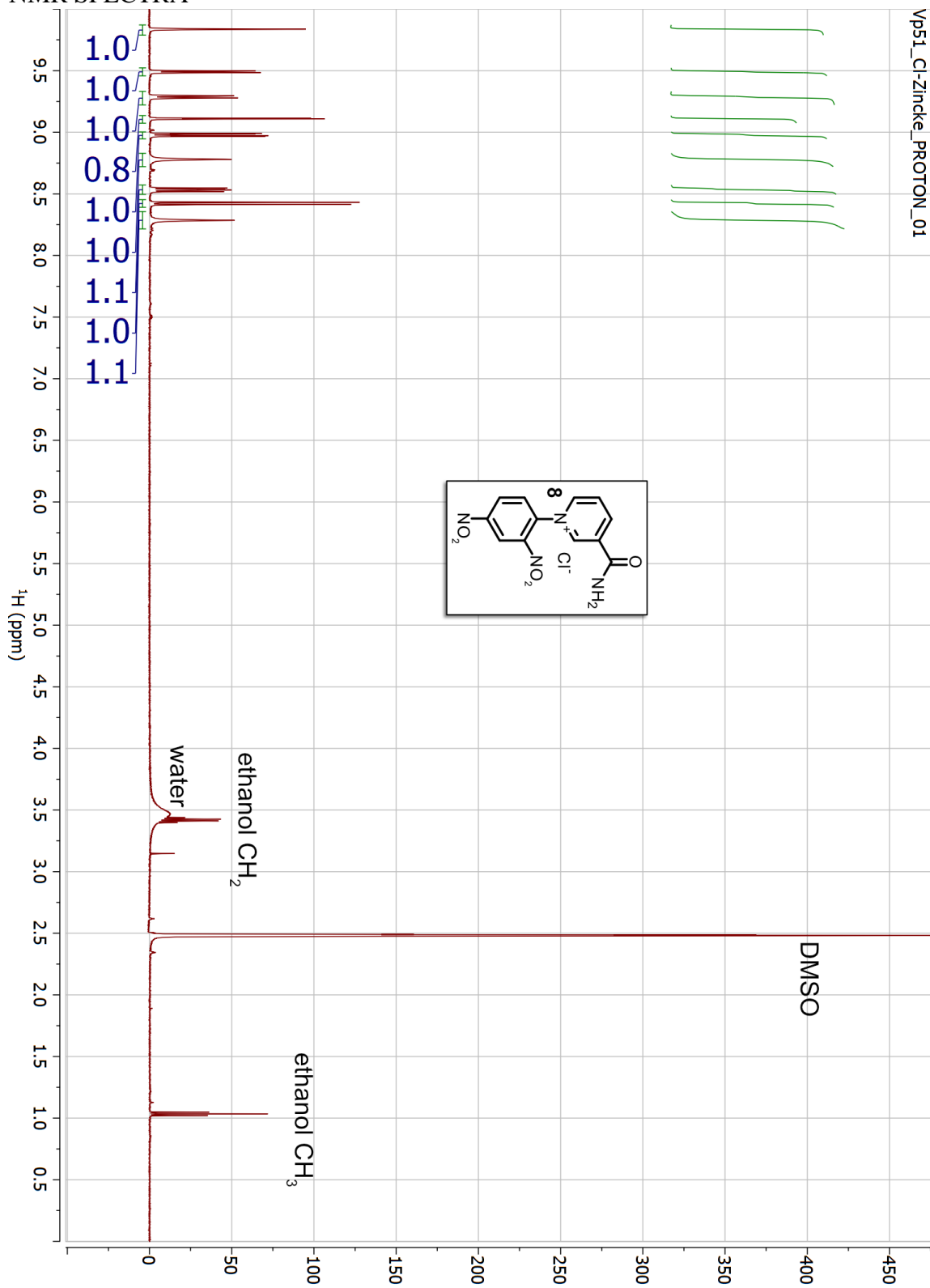


Figure 2.S1. ¹H NMR spectrum of 1-(2,4-dinitrophenyl) nicotinamide chloride (9-Cl).

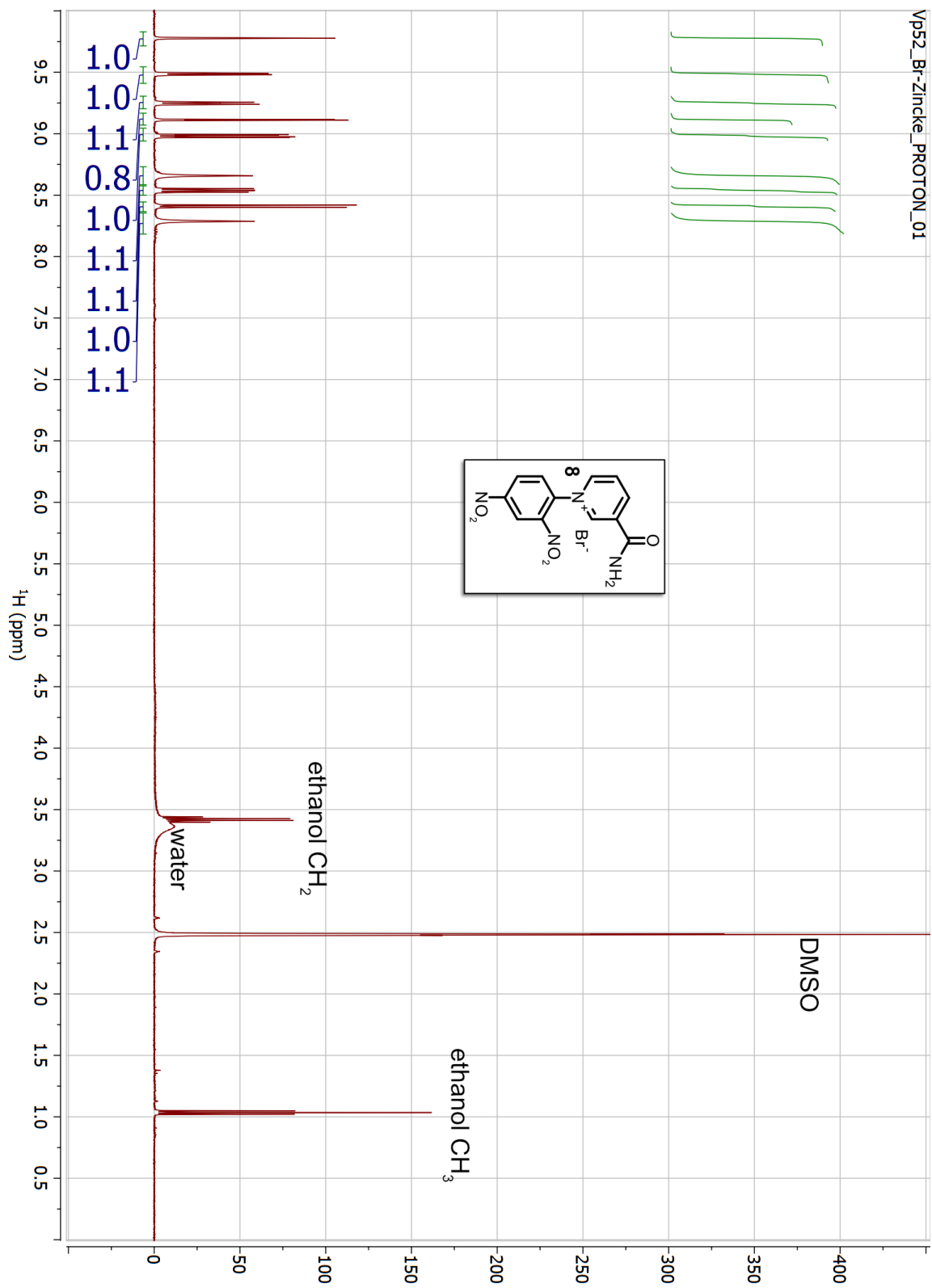


Figure 2.S2. ^1H NMR spectrum of 1-(2,4-dinitrophenyl) nicotinamide bromide (**9-Br**).

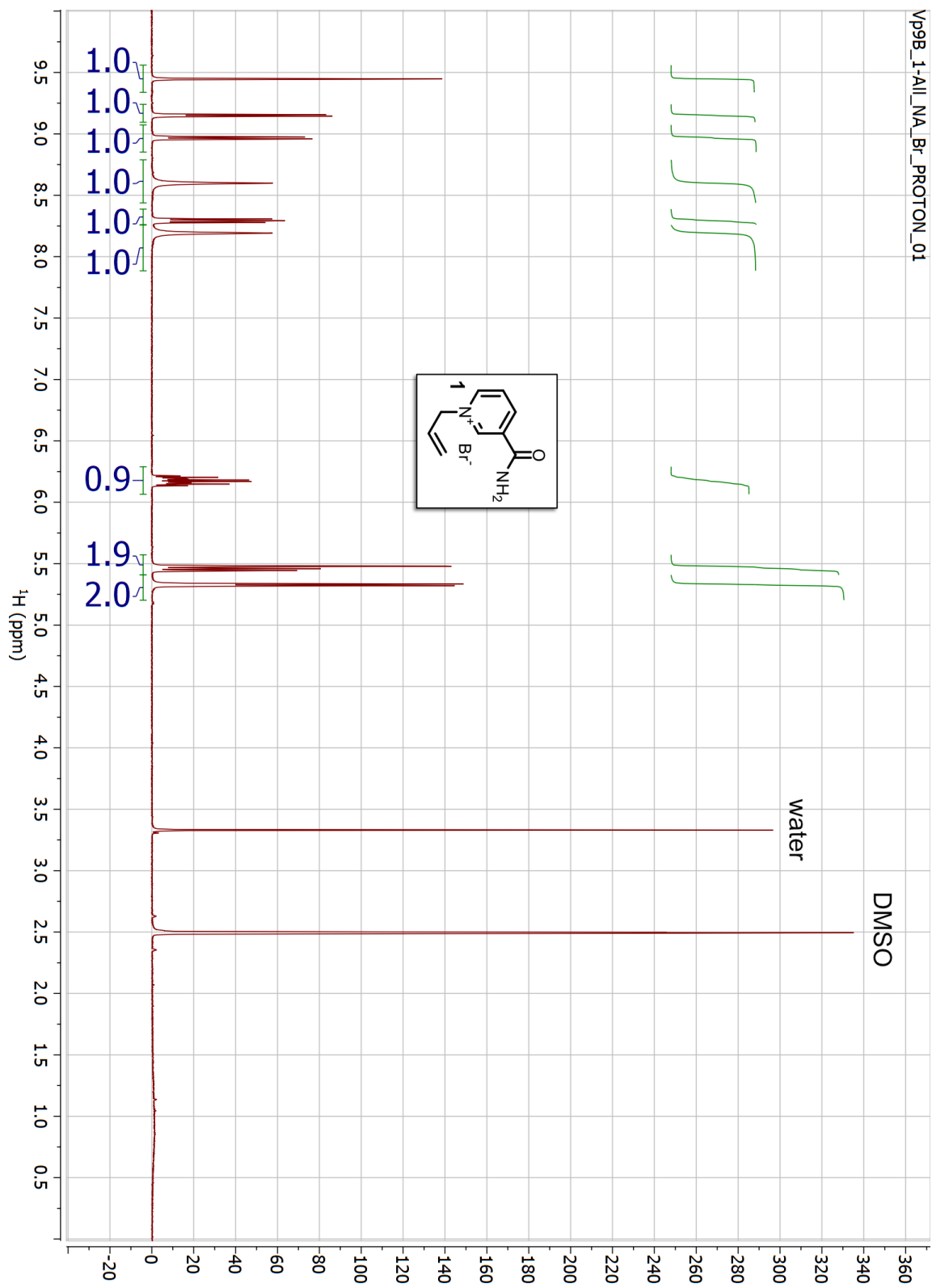


Figure 2.S3. ^1H NMR spectrum of 1-allyl nicotinamide bromide (**1-Br**).

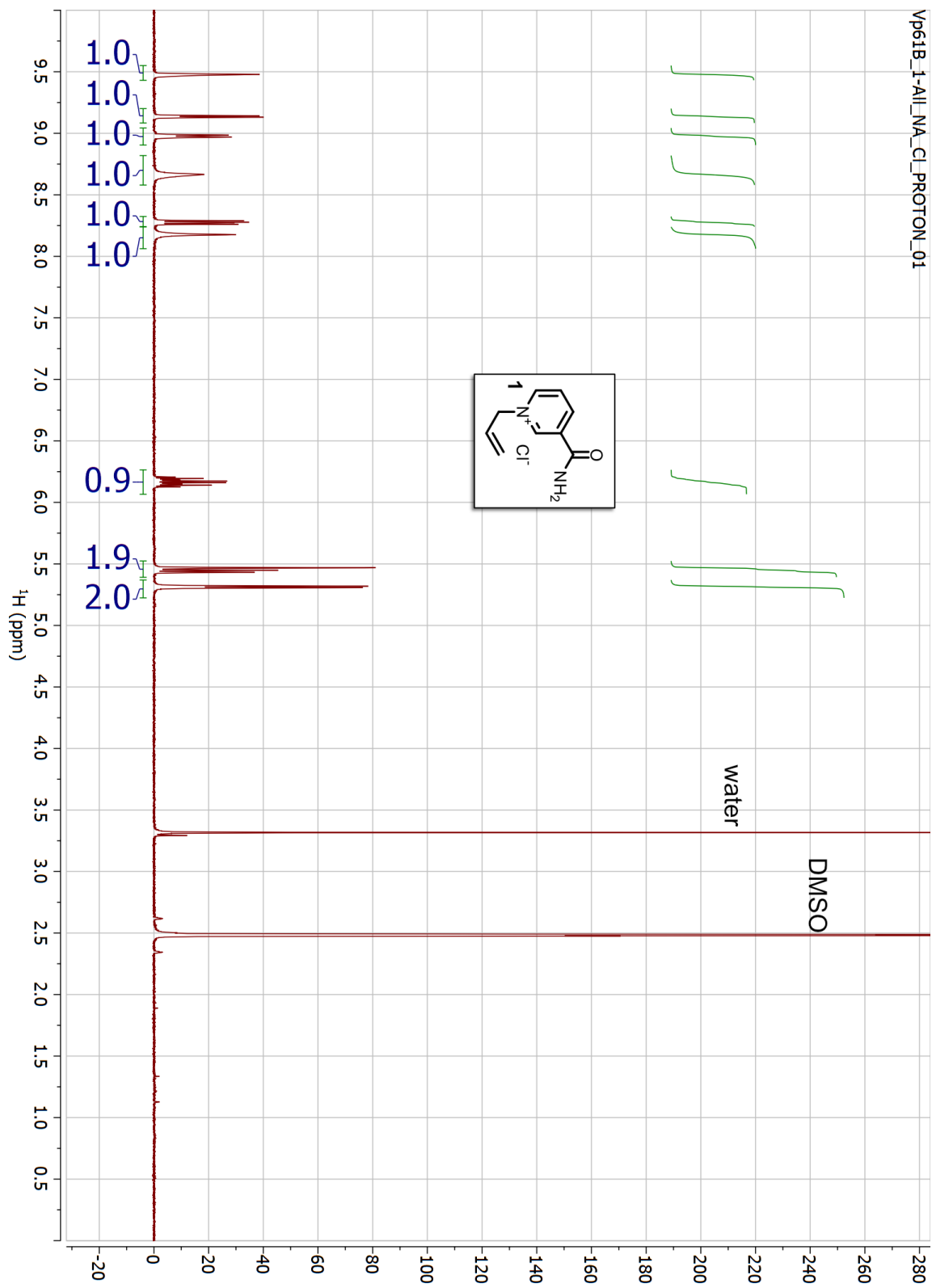


Figure 2.S4. ^1H NMR spectrum of 1-allyl nicotinamide chloride (**1-Cl**).

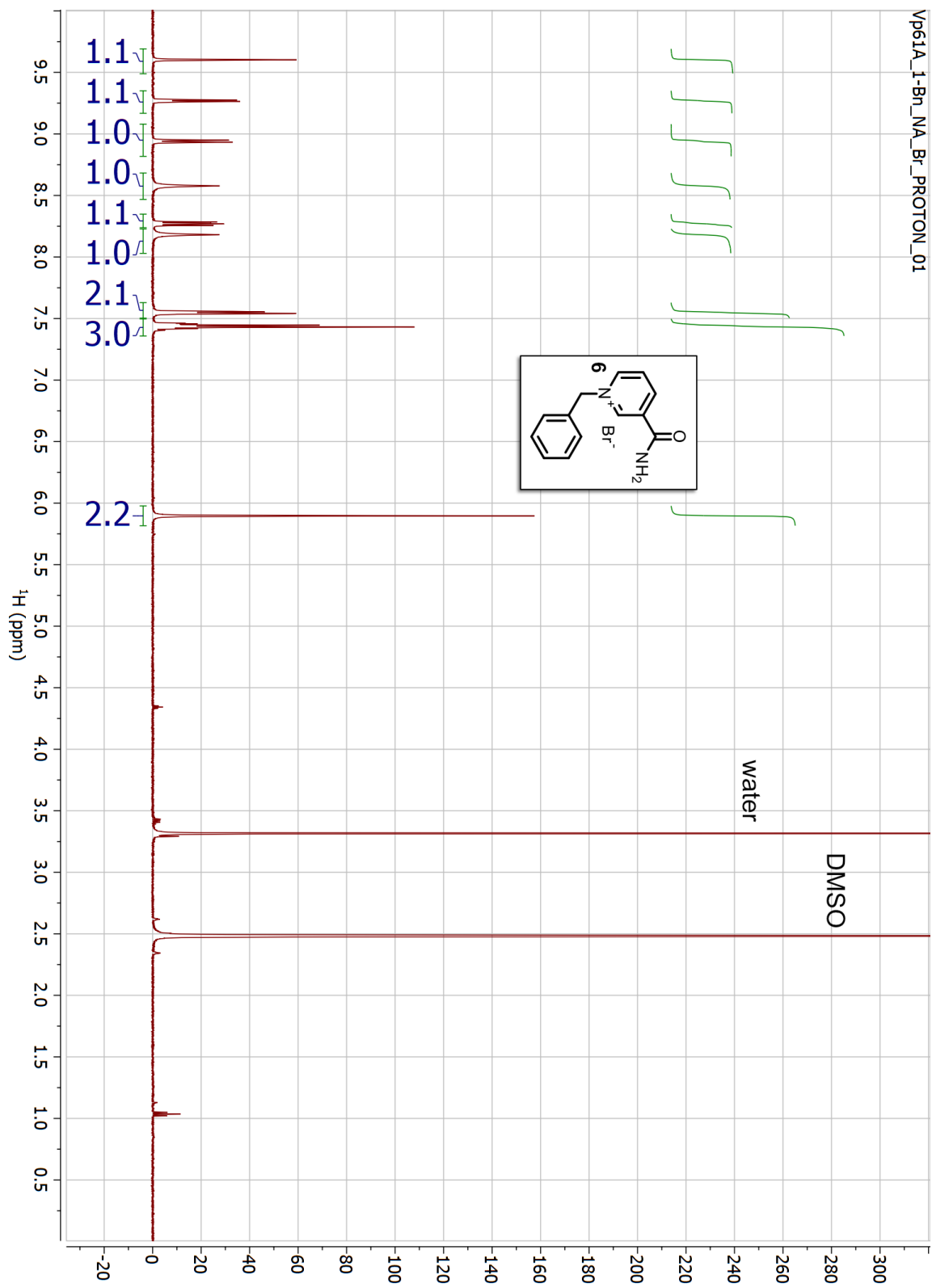


Figure 2.S5. ^1H NMR spectrum of 1-benzyl nicotinamide bromide (**6-Br**).

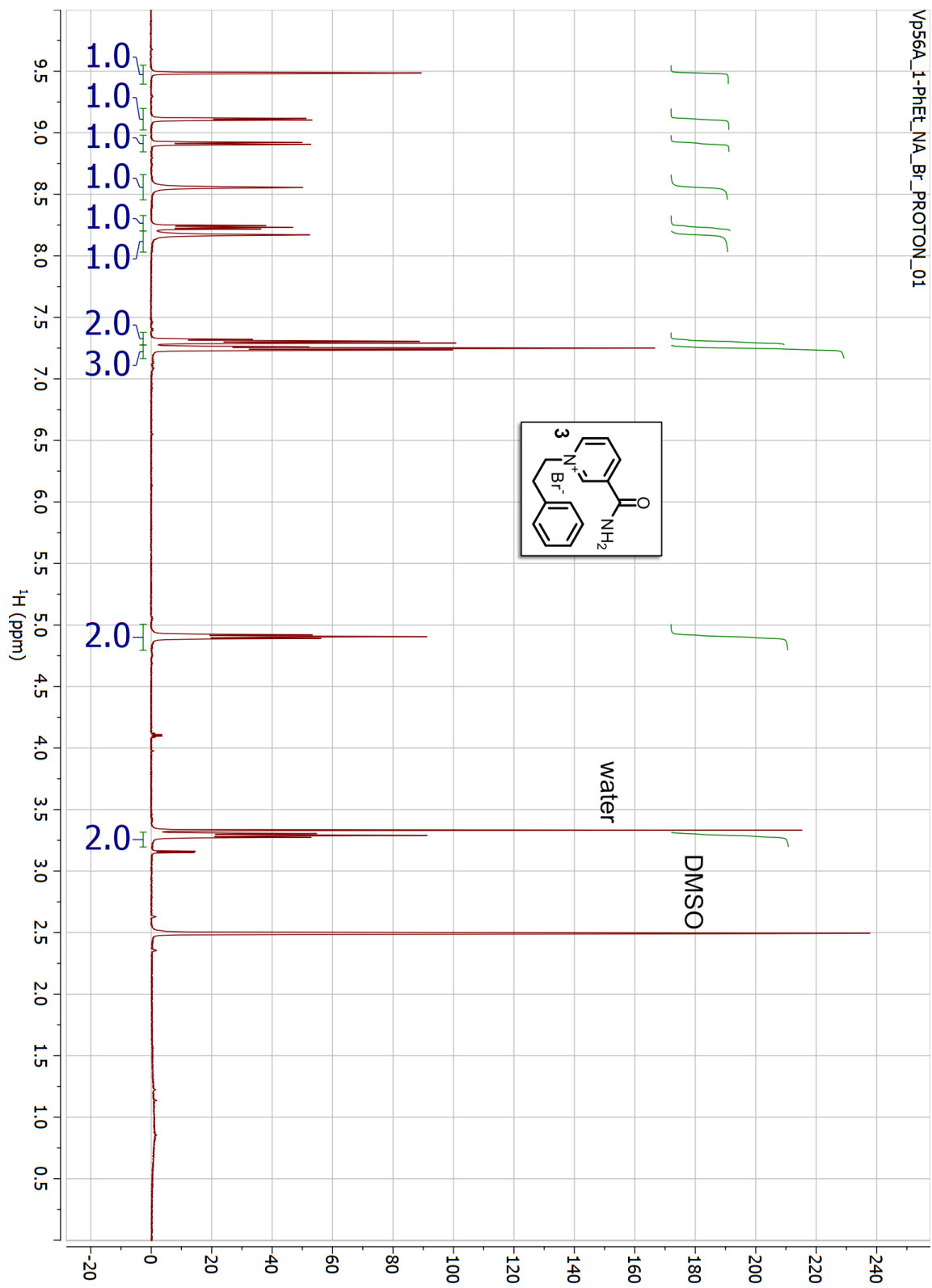


Figure 2.S6. ^1H NMR spectrum of 1-phenethyl nicotinamide bromide (**3-Br**).

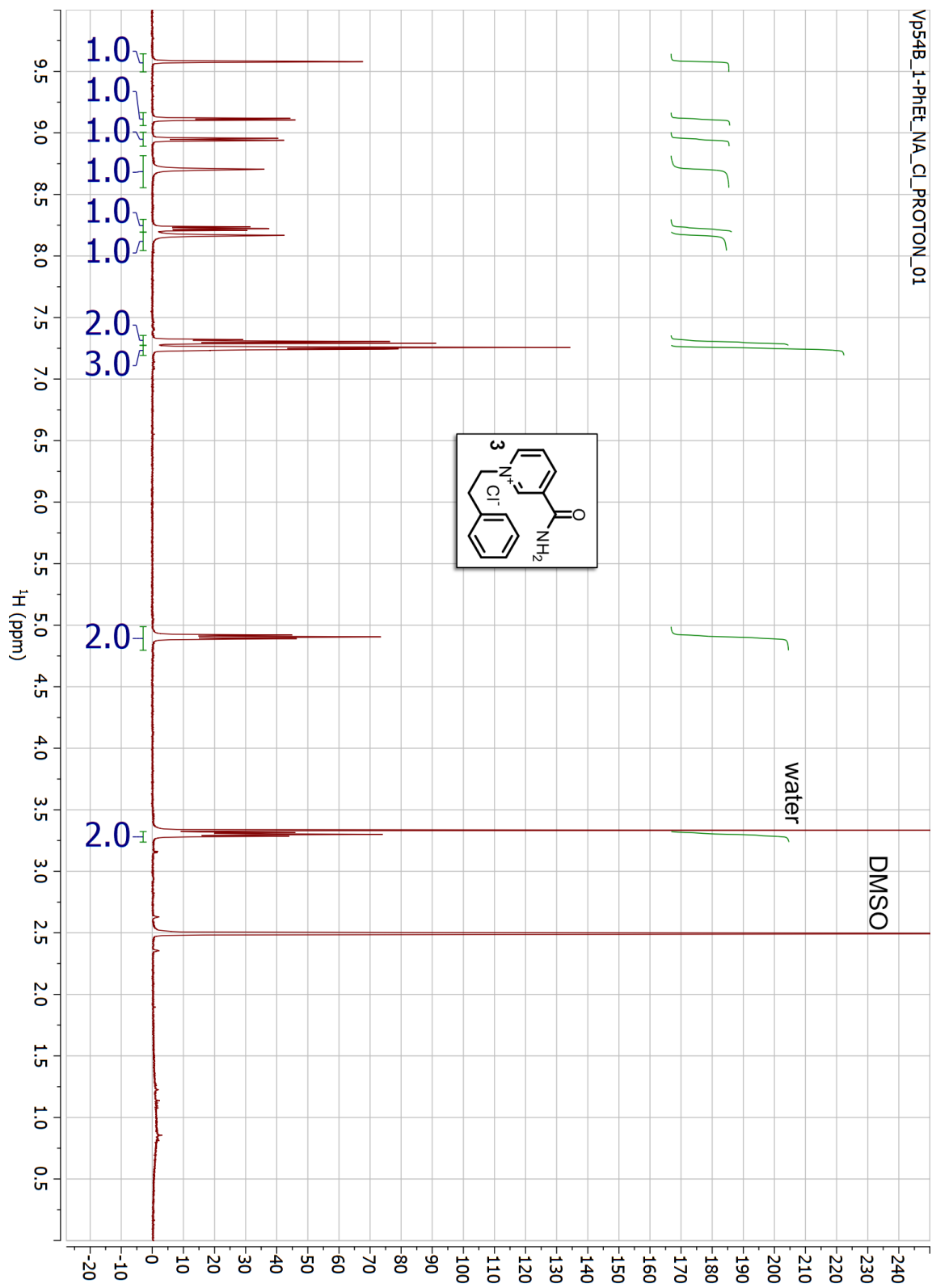


Figure 2.S7. ^1H NMR spectrum of 1-phenethyl nicotinamide chloride (**3-Cl**).

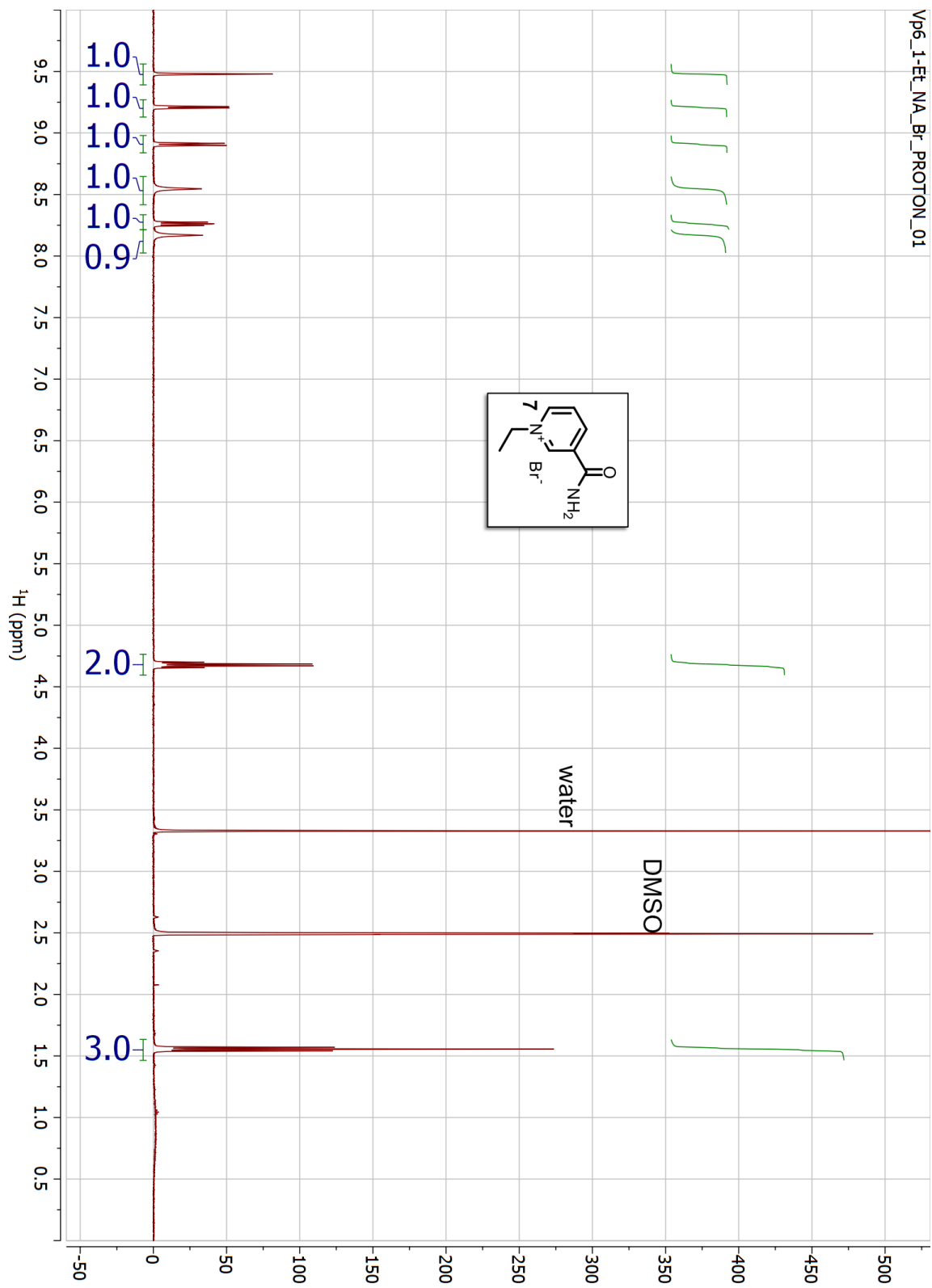


Figure 2.S8. ^1H NMR spectrum of 1-ethyl nicotinamide bromide (**7-Br**).

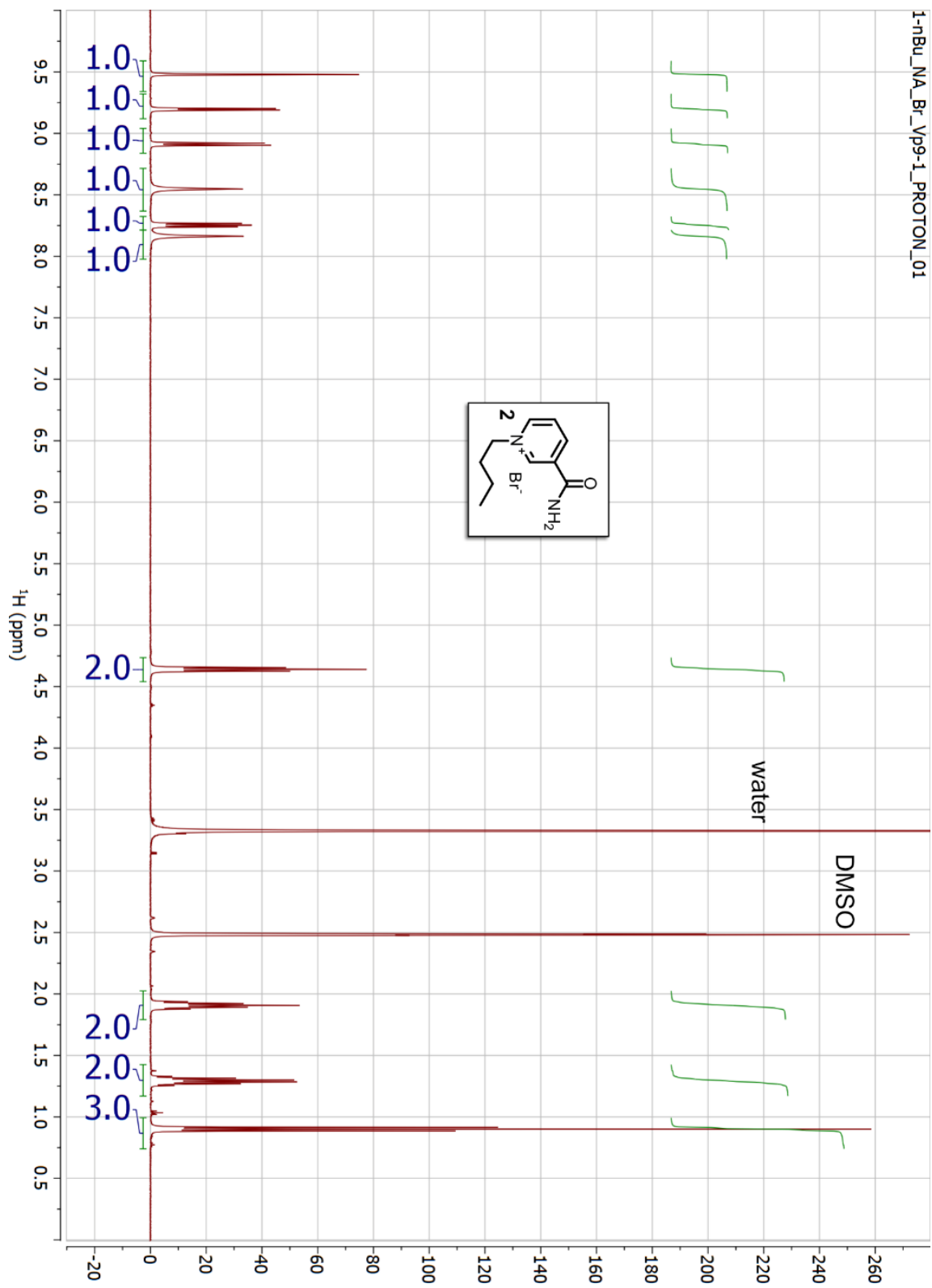


Figure 2.S9. ^1H NMR spectrum of 1-butyl nicotinamide bromide (2-Br).

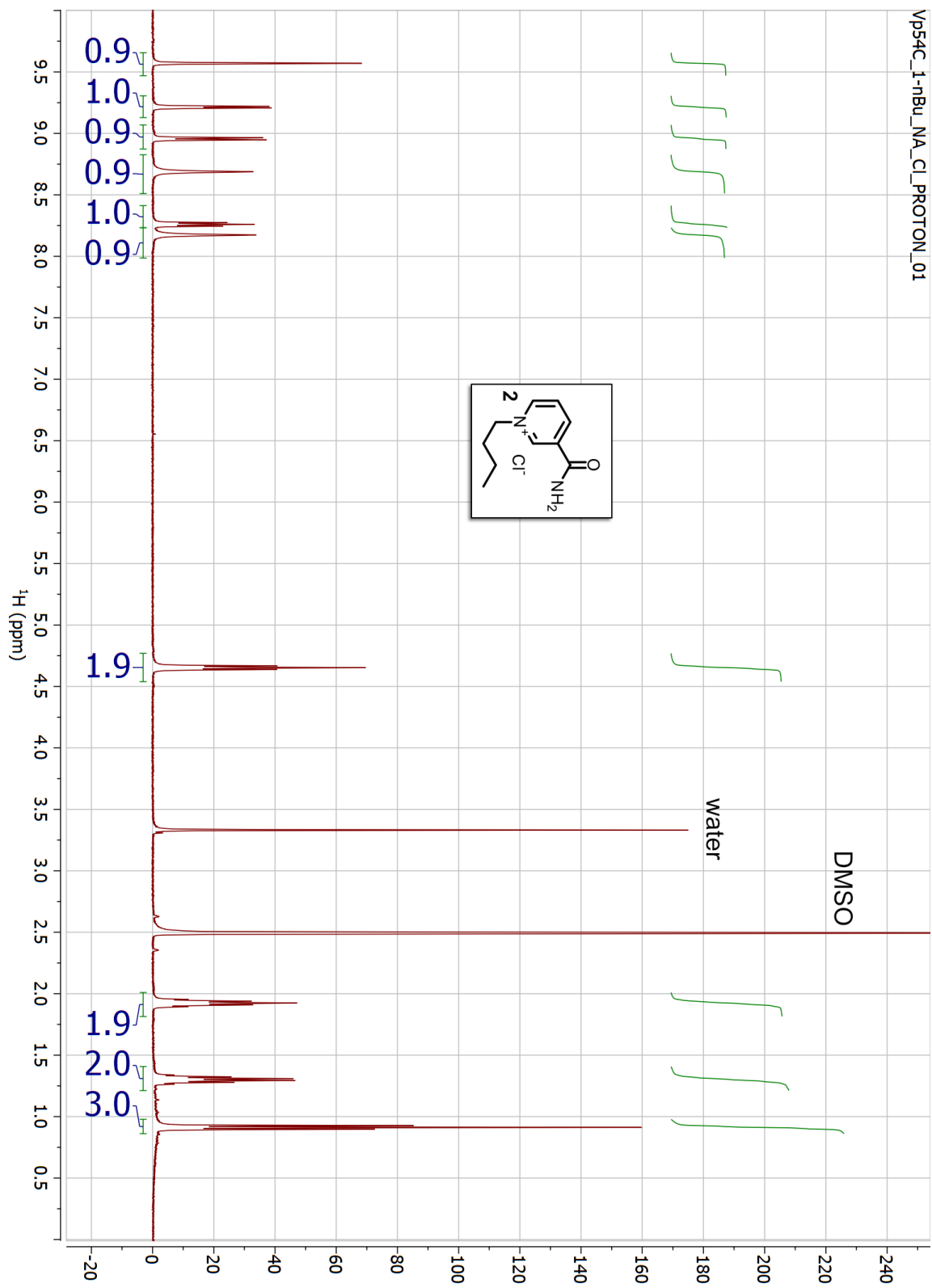


Figure 2.S10. ^1H NMR spectrum of 1-butyl nicotinamide chloride (2-Cl).

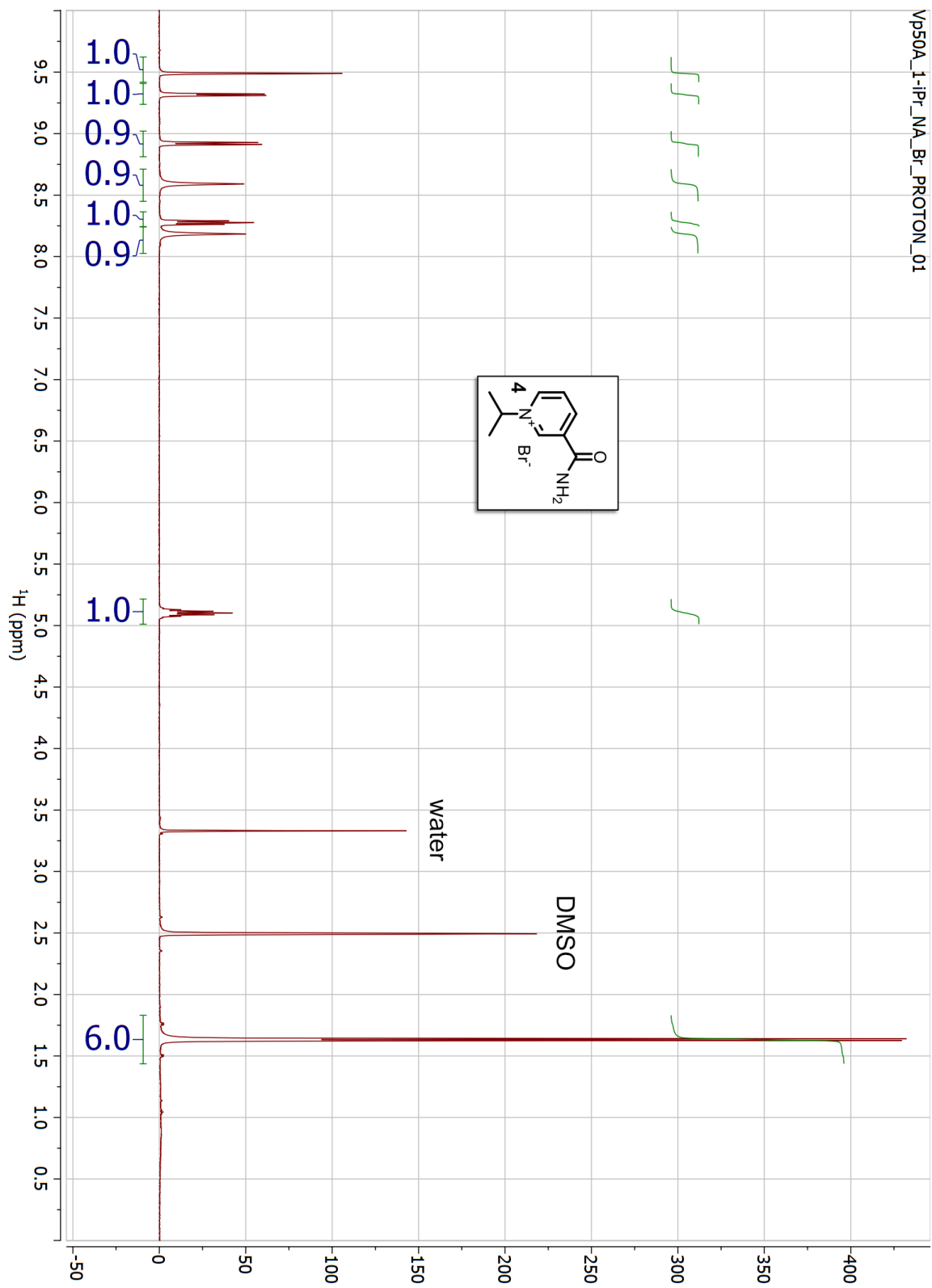


Figure 2.S11. ^1H NMR spectrum of 1-isopropyl nicotinamide bromide (**4-Br**).

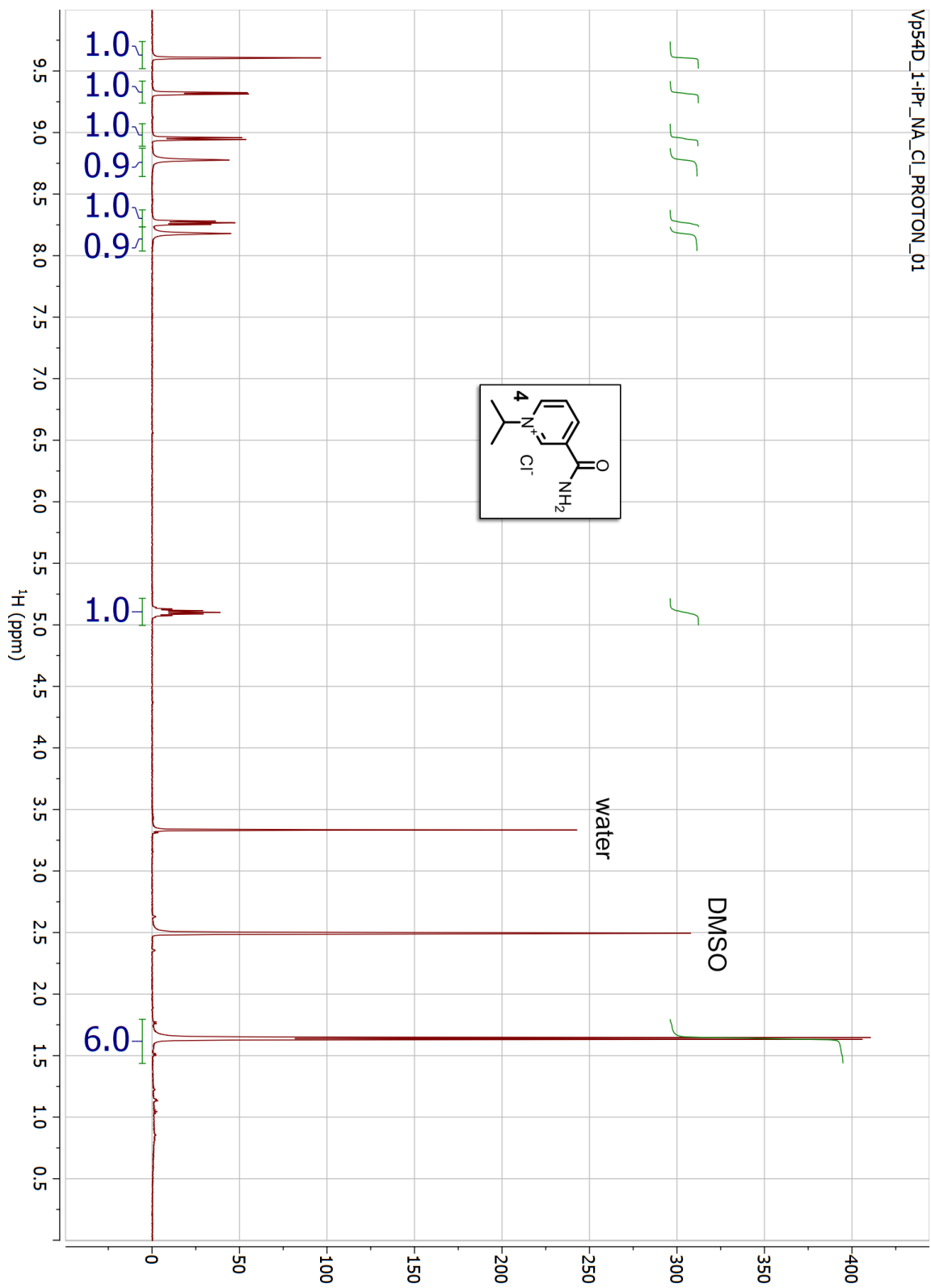


Figure 2.S12. ^1H NMR spectrum of 1-isopropyl nicotinamide chloride (**4-Cl**).

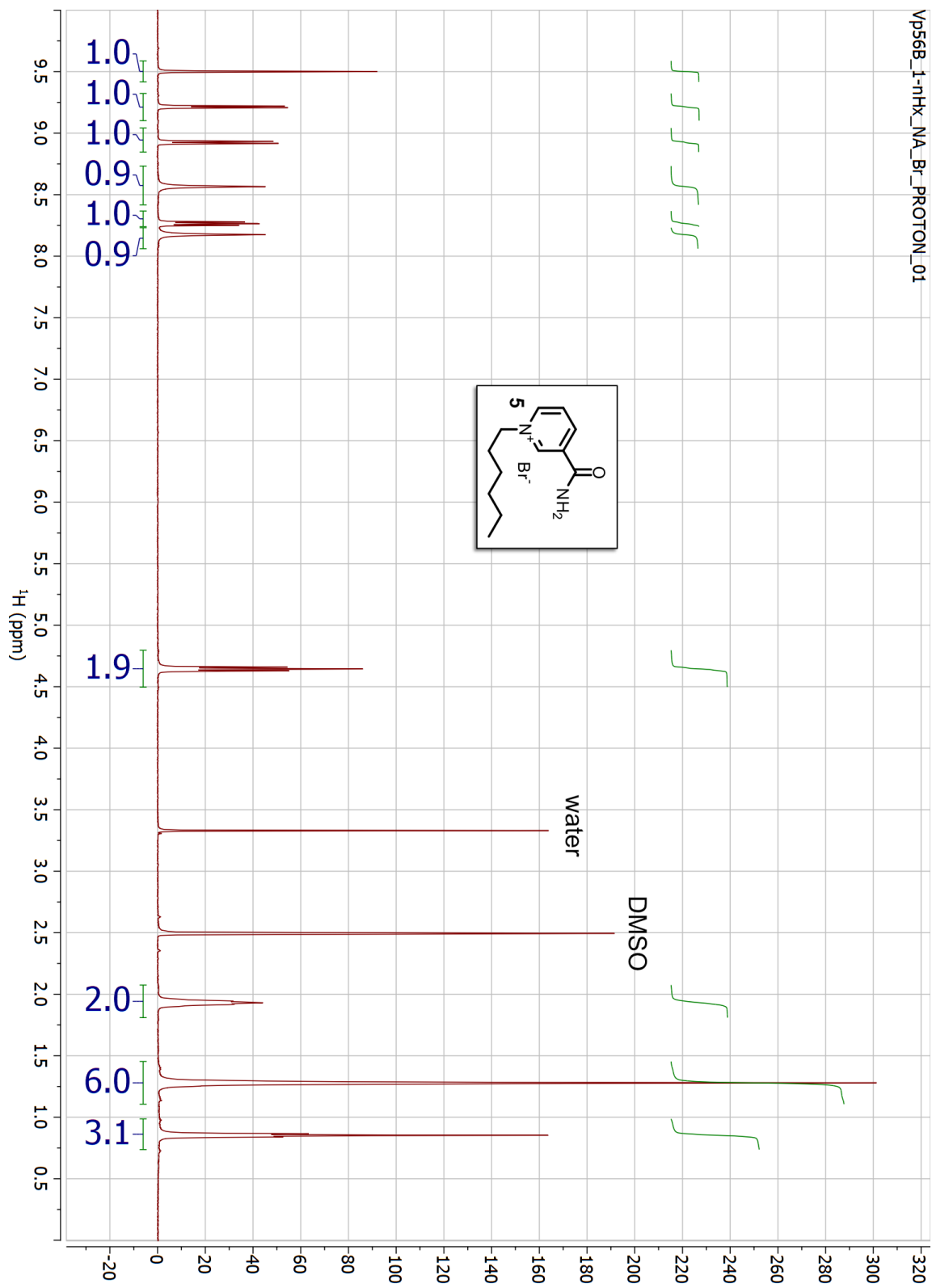


Figure 2.S13. ^1H NMR spectrum of 1-hexyl nicotinamide bromide (**5-Br**).

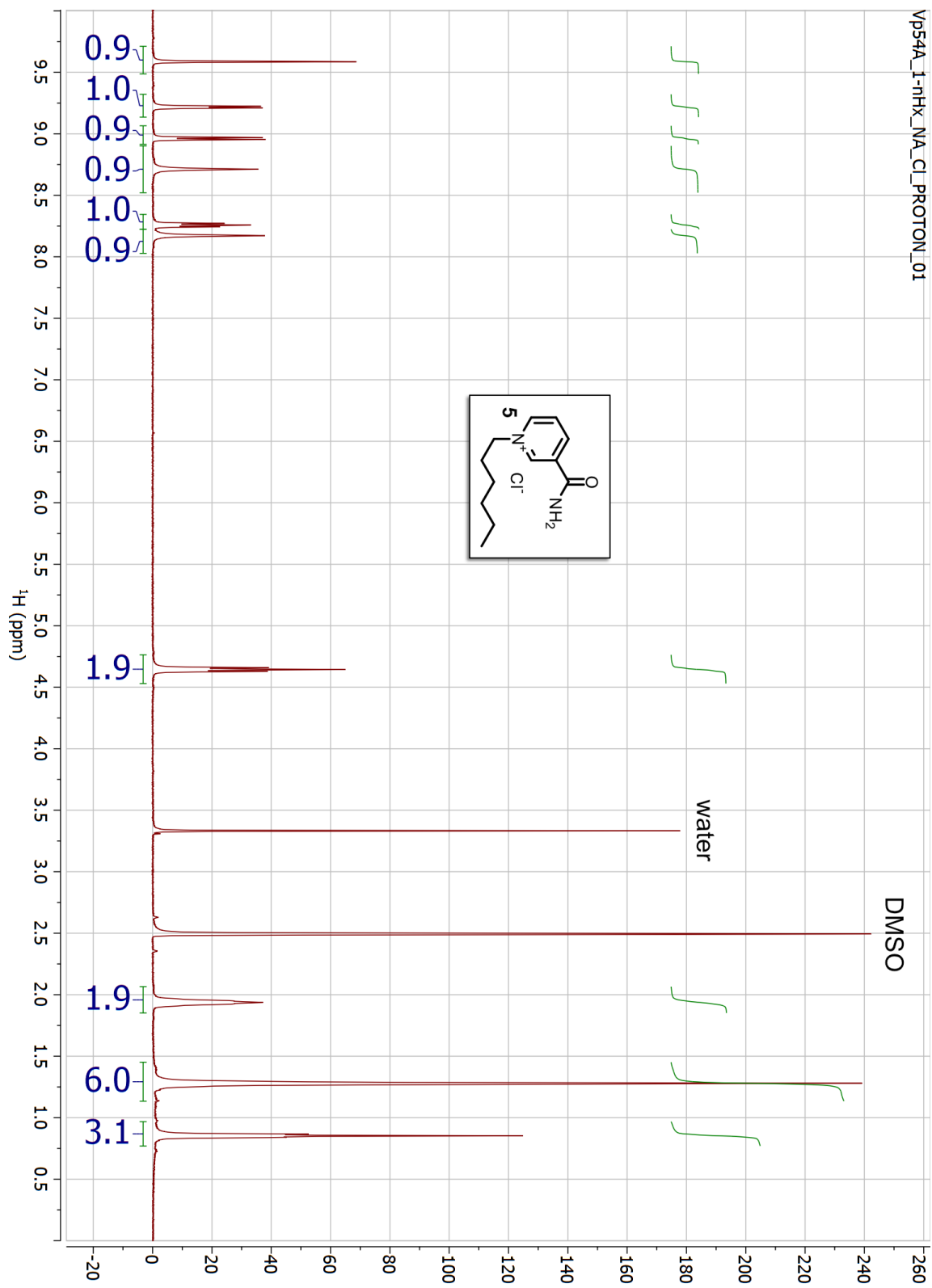


Figure 2.S14. ^1H NMR spectrum of 1-hexyl nicotinamide chloride (5-Cl).

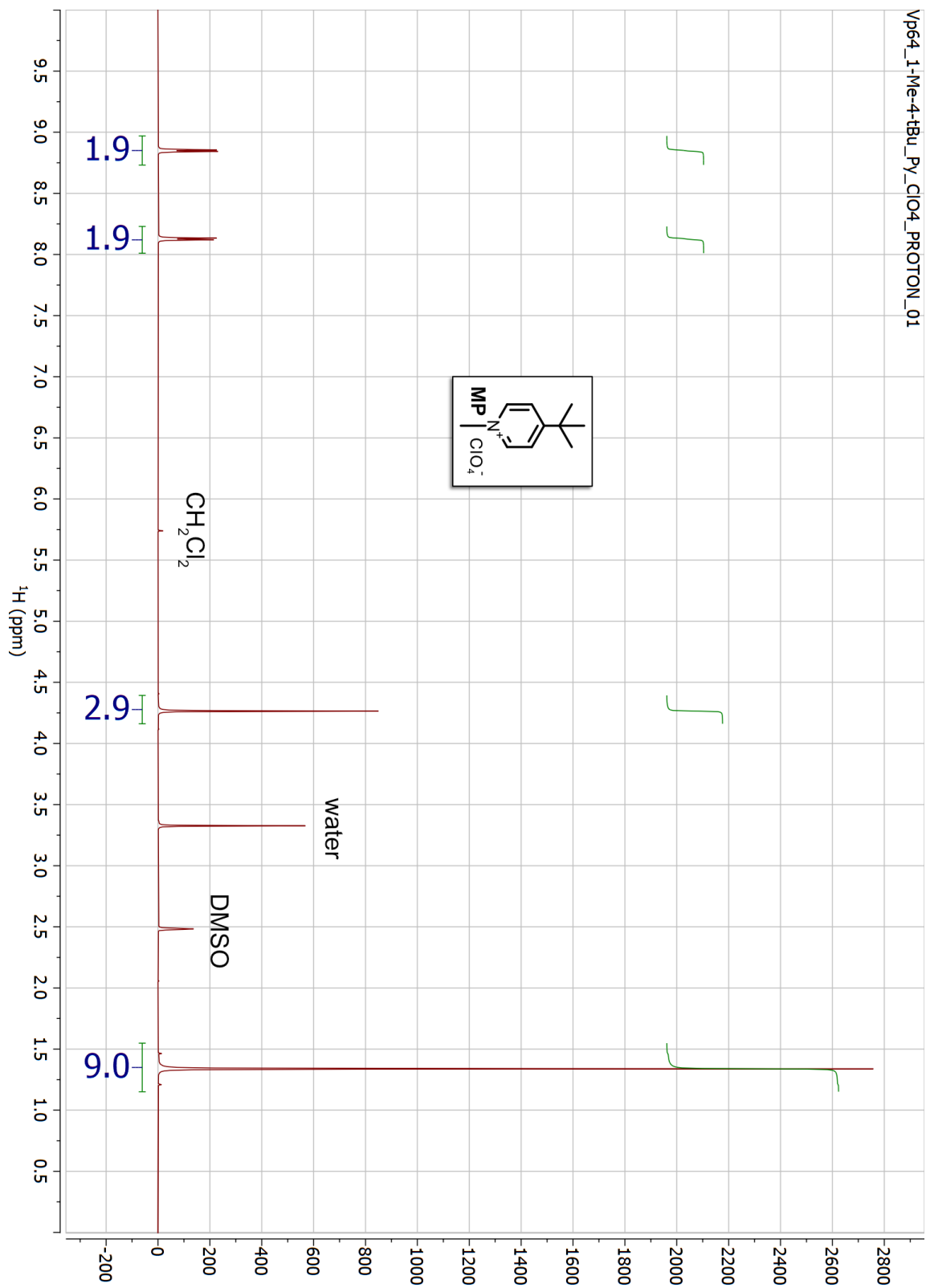


Figure 2.S15. ¹H NMR spectrum of 1-methyl-4-*tert*-butyl pyridinium perchlorate (MP).

CRYSTAL STRUCTURES

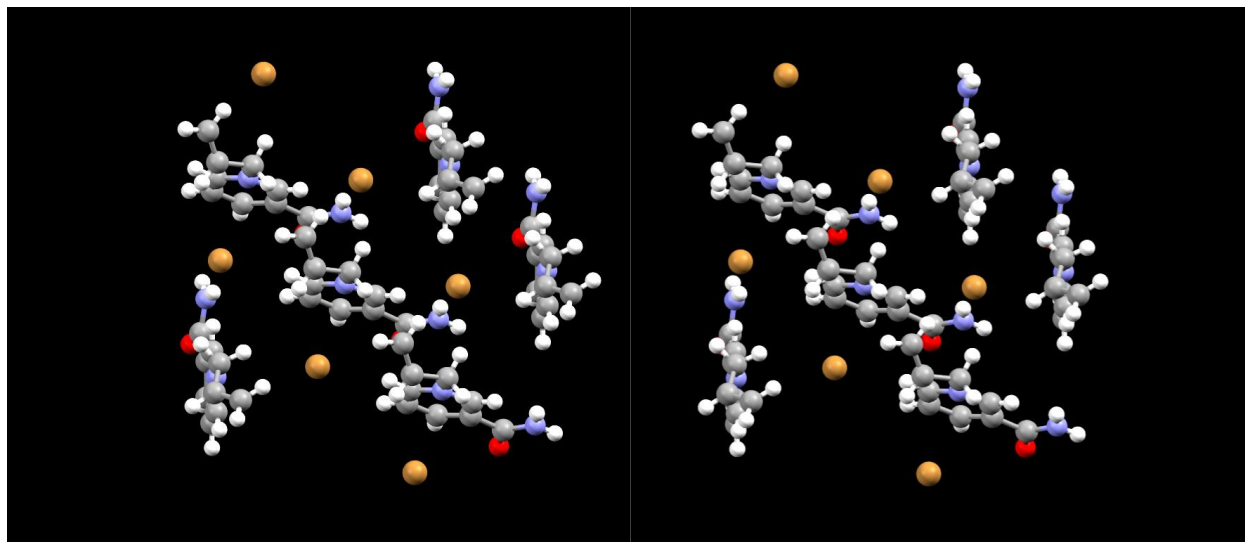


Figure 2.S16. Stereo image of the crystal structure of **1-Br**.

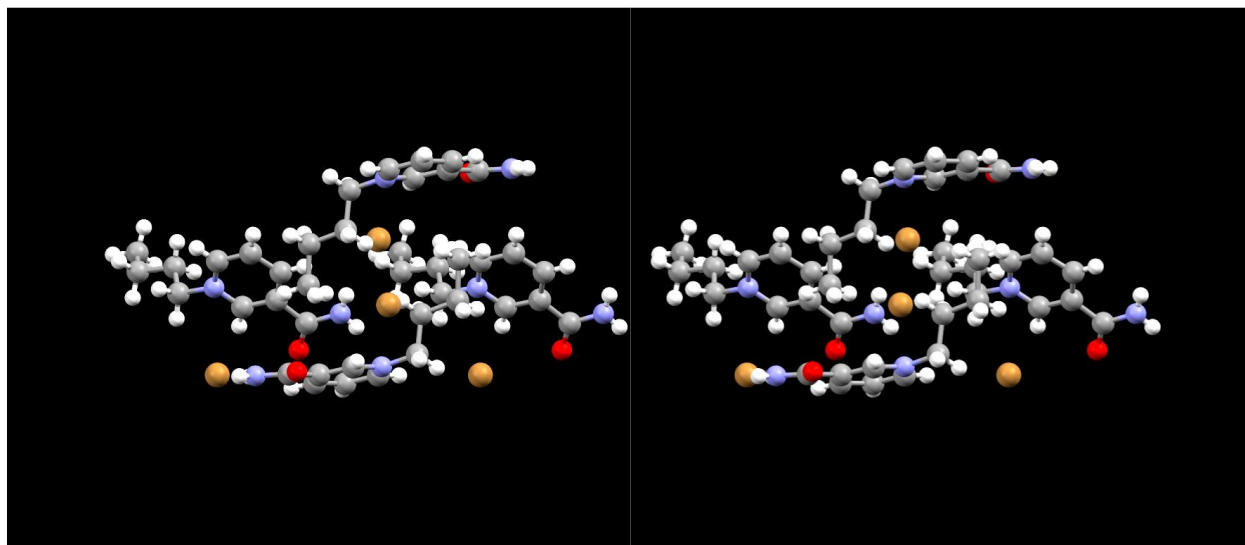


Figure 2.S17. Stereo image of the crystal structure of **2-Br**.

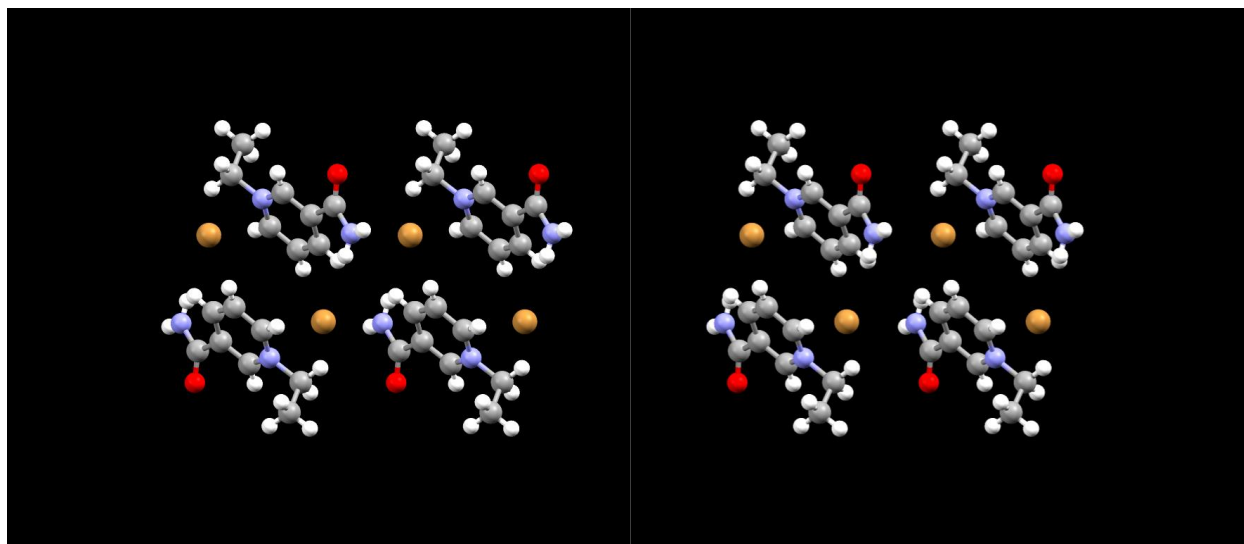


Figure 2.S20. Stereo image of the crystal structure of **7-Br**.

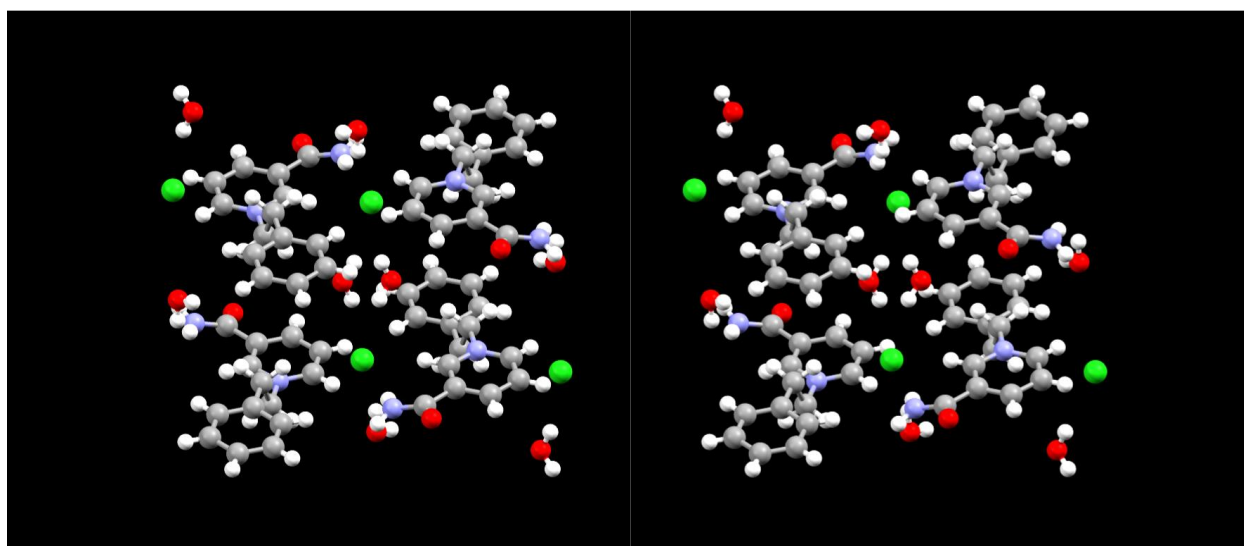


Figure 2.S21. Stereo image of the crystal structure of **3-Cl**.

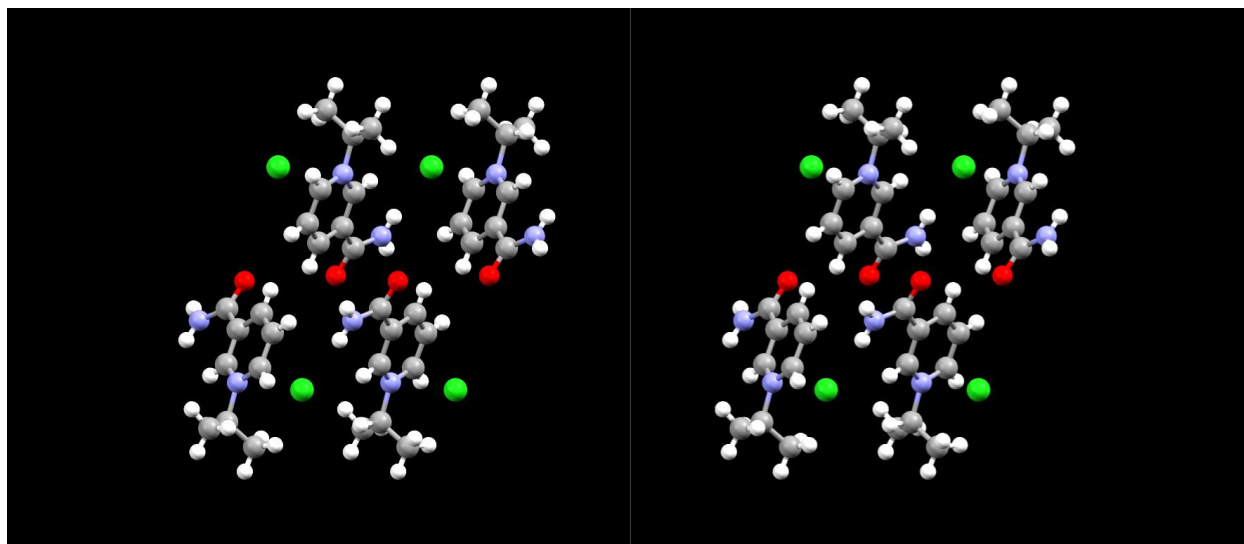


Figure 2.S22. Stereo image of the crystal structure of 4-Cl.

FUNDAMENTAL HARMONIC EQUATION DERIVATION

The following derivation is based on the derivations outlined by D.E. Smith.⁴⁵ The general ideas are the same, but here we account for the fact that c_{r0} is a function of position, whereas the treatment of Smith and coworkers assumed that the concentration of the radical c_{r0} was constant with respect to position.⁴⁰ Familiarity with the theory of residues and with Laplace transforms will be helpful in following the mathematical development. The convolution theorem, which is frequently invoked in the derivation, will be stated here to assist the reader (a formal derivation is provided by Churchill⁵⁹).

The convolution theorem:

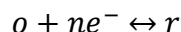
If $f(t)$ and $g(t)$ are two functions of time, with Laplace transforms $\mathcal{L}\{f(t)\} = \bar{f}(s)$ and $\mathcal{L}\{g(t)\} = \bar{g}(s)$, then the inverse Laplace transform of the product of the two Laplace-domain functions equals the convolution integral of the two time-domain functions. That is:

$$\mathcal{L}^{-1}\{\bar{f}(s)\bar{g}(s)\} = \int_0^t f(t-\tau)g(\tau)d\tau$$

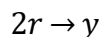
S1

Derivation of Fundamental Harmonic Current:

The system under consideration has irreversible dimerization following the charge transfer step:



S2



S3

where o is the pyridinium ion, r is the pyridine radical, and y is the dimer. The governing equations are:

$$\frac{\partial}{\partial t} c_o = D_o \frac{\partial^2}{\partial x^2} c_o$$

S4

$$\frac{\partial}{\partial t} c_r = D_r \frac{\partial^2}{\partial x^2} c_r - k_D c_r^2$$

S5

where t is time, x is position, k_D is the dimerization rate constant of the radical r , c_o and c_r are the concentrations of o and r , and D_o and D_r are the diffusion coefficients of o and r . The boundary conditions are, for one-dimensional semiinfinite diffusion:

$$t = 0, \text{ all } x \text{ and } t > 0, x = \infty:$$

$$c_o = c^0, c_r = 0$$

$$t > 0, x = 0:$$

$$\frac{I}{nFA} = -D_o \frac{\partial}{\partial x} c_o = D_r \frac{\partial}{\partial x} c_r$$

S6

where F is Faraday's constant and A is the electrode surface area. The Butler-Volmer equation is assumed to apply at the electrode surface ($x = 0$):

$$I = nFAk^0 \left\{ -f_o c_o e^{\left(\frac{-n\alpha F(E-E^0)}{RT}\right)} + f_r c_r e^{\left(\frac{n\beta F(E-E^0)}{RT}\right)} \right\}$$

S7

where k^0 is the heterogeneous electron transfer rate constant, f_o and f_r are the activity coefficients for o and r , E is the applied potential, E^0 is the thermodynamic potential, R is the ideal gas constant, T is the temperature, and α and β are symmetry coefficients such that $\alpha + \beta = 1$ and $0 \leq \alpha \leq 1$, $0 \leq \beta \leq 1$.

The potential E can be written as the sum of a linear sweep (E_{DC}) and an alternating ($\Delta E \sin(\omega t)$) component, that is:

$$E = E_{DC} + \Delta E \sin(\omega t)$$

S8

where it is assumed that E_{DC} is constant on the AC timescale. Plugging this expression into the Butler-Volmer equation yields:

$$I = nFAk^0 \left\{ -f_o c_o e^{\left(\frac{-n\alpha F}{RT}(E_{DC} + \Delta E \sin(\omega t) - E^0)\right)} + f_r c_r e^{\left(\frac{n\beta F}{RT}(E_{DC} + \Delta E \sin(\omega t) - E^0)\right)} \right\}$$

S9

We make an additional substitution for the reversible half-wave potential $E'_{1/2}$:

$$E^0 = E_{1/2}^r + \frac{RT}{nF} \ln \left(\frac{f_r}{f_o} \sqrt{\frac{D_o}{D_r}} \right)$$

S10

which yields:

$$I = nFAk^0 \left\{ - \left(f_r^\alpha f_o^\beta \sqrt{\frac{D_o^\alpha}{D_r^\alpha}} \right) c_o e^{\left(\frac{-n\alpha F}{RT} (E_{DC} + \Delta E \sin(\omega t) - E_{1/2}^r) \right)} \right. \\ \left. + \left(f_r^\alpha f_o^\beta \sqrt{\frac{D_r^\beta}{D_o^\beta}} \right) c_r e^{\left(\frac{n\beta F}{RT} (E_{DC} + \Delta E \sin(\omega t) - E_{1/2}^r) \right)} \right\}$$

S11

We also make a substitution for the dimensionless direct potential j :

$$j = \frac{nF}{RT} (E_{DC} - E_{1/2}^r)$$

S12

which, after some rearrangement, yields:

$$\frac{I}{nFAc^0 \sqrt{D_o}} = k^0 \frac{f_r^\alpha f_o^\beta}{\sqrt{D_r^\alpha D_o^\beta}} \left\{ - \frac{c_o}{c^0} e^{-\alpha j} e^{\left(\frac{-n\alpha F \Delta E}{RT} \sin(\omega t) \right)} + \left(\sqrt{\frac{D_r}{D_o}} \right) \frac{c_r}{c^0} e^{\beta j} e^{\left(\frac{n\beta F \Delta E}{RT} \sin(\omega t) \right)} \right\}$$

S13

Finally, we introduce the abbreviations:

$$f = f_r^\alpha f_o^\beta$$

S14

$$D = D_r^\alpha D_o^\beta$$

S15

$$\psi = \frac{I}{nFAc^0 \sqrt{D_o}}$$

S16

$$\delta = \frac{nF \Delta E}{RT}$$

S17

which affords the following form of the Butler-Volmer equation:

$$\psi = \frac{k^0 f}{\sqrt{D}} \left\{ -\frac{c_o}{c^0} e^{-\alpha j} e^{-\alpha \delta \sin(\omega t)} + \left(\sqrt{\frac{D_r}{D_o}} \right) \frac{c_r}{c^0} e^{\beta j} e^{\beta \delta \sin(\omega t)} \right\}$$

S18

In essence, these transformations were carried out so that the alternating potential ($\delta \sin(\omega t)$) and direct potential (j) terms would be separated in the exponential terms.

The theory behind alternating current voltammetry rests on a Taylor series expansion of the alternating potential terms $e^{-\alpha \delta \sin(\omega t)}$ and $e^{\beta \delta \sin(\omega t)}$. In general, $e^x = 1 + x + \frac{1}{2!}x^2 + \frac{1}{3!}x^3 + \dots$, and so we can write:

$$e^{-\alpha \delta \sin(\omega t)} = 1 - \alpha \delta \sin(\omega t) + \frac{1}{2!}[\alpha \delta \sin(\omega t)]^2 - \frac{1}{3!}[\alpha \delta \sin(\omega t)]^3 + \dots$$

S19

$$e^{\beta \delta \sin(\omega t)} = 1 + \beta \delta \sin(\omega t) + \frac{1}{2!}[\beta \delta \sin(\omega t)]^2 + \frac{1}{3!}[\beta \delta \sin(\omega t)]^3 + \dots$$

S20

Each additional term of the Taylor series introduces a higher harmonic into the experiment. For example, if $\delta = 0$, only the first term is significant, and the Butler-Volmer equation simplifies to the DC solution only. If the first two terms are significant ($\delta > 0$, but $\delta^2 \approx 0$), then the solution has both DC and fundamental harmonic components. If the first three terms of the Taylor series are significant, the solution has DC, fundamental harmonic, and second harmonic components, etc. The alternating potential magnitude ΔE controls the value of δ , and by extension the number of harmonics one will observe in an experiment.

For the fundamental harmonic experiment, we choose ΔE such that only the first two terms are significant. We also observe that the current and both concentration profiles can be written as the sums of direct (subscript 0) and fundamental harmonic (subscript 1) components, that is:

$$\psi = \psi_0 + \psi_1$$

S21

$$c_o = c_{o0} + c_{o1}$$

S22

$$c_r = c_{r0} + c_{r1}$$

S23

We plug these into the Butler-Volmer equation to give:

$$\psi_0 + \psi_1 = \frac{k^0 f}{\sqrt{D}} \left\{ -\frac{c_{o0} + c_{o1}}{c^0} e^{-\alpha j} (1 - \alpha \delta \sin(\omega t)) + \left(\sqrt{\frac{D_r}{D_o}} \right) \frac{c_{r0} + c_{r1}}{c^0} e^{\beta j} (1 + \beta \delta \sin(\omega t)) \right\}$$

S24

The DC terms can be gathered into one equation and the fundamental harmonic terms into another equation. The products of two fundamental harmonic terms (that is, $c_{o1}\alpha\delta\sin(\omega t)$ and $c_{r1}\beta\delta\sin(\omega t)$) are assumed to be vanishingly small (otherwise they would produce a second-harmonic term). The result is:

$$\psi_0 = \frac{k^0 f}{\sqrt{D}} \left\{ -\frac{c_{o0}}{c^0} e^{-\alpha j} + \left(\sqrt{\frac{D_r}{D_o}} \right) \frac{c_{r0}}{c^0} e^{\beta j} \right\}$$

S25

$$\psi_1 = \frac{k^0 f}{\sqrt{D}} \left\{ e^{-\alpha j} \frac{c_{o0}\alpha\delta \sin(\omega t) - c_{o1}}{c^0} + \left(\sqrt{\frac{D_r}{D_o}} \right) e^{\beta j} \frac{c_{r0}\beta\delta \sin(\omega t) + c_{r1}}{c^0} \right\}$$

S26

The goal is to predict ψ_1 , the fundamental harmonic alternating current. A straightforward way to accomplish this is to set

$$\psi_1 = A_1 \sin(\omega t) + B_1 \cos(\omega t)$$

S27

then to express c_{o1} and c_{r1} in terms of sine and cosine functions, and finally to equate the sine terms and cosine terms to find A_1 and B_1 . We will also need to find c_{o0} and c_{r0} from ψ_0 .

To find c_{o0} , c_{o1} , c_{r0} , and c_{r1} , we turn to the governing equations above. For c_o , we write:

$$\frac{\partial}{\partial t}(c_{o0} + c_{o1}) = D_o \frac{\partial^2}{\partial x^2}(c_{o0} + c_{o1})$$

S28

We again collect DC and fundamental harmonic terms, which affords the two equations:

$$\frac{\partial}{\partial t} c_{o0} = D_o \frac{\partial^2}{\partial x^2} c_{o0}$$

S29

$$\frac{\partial}{\partial t} c_{o1} = D_o \frac{\partial^2}{\partial x^2} c_{o1}$$

S30

These equations can be solved with Laplace techniques. For the first, we define the deviation variable $C_{o0} = c_{o0} - c^0$, and then a Laplace transform yields:

$$s\overline{C_{o0}} = D_o \frac{\partial^2}{\partial x^2} \overline{C_{o0}}$$

S31

where an overbar denotes a function in the Laplace domain, and s is the Laplace variable. This equation has the solution:

$$\overline{C_{o0}} = a_1 e^{x\sqrt{s/D_o}} + a_2 e^{-x\sqrt{s/D_o}}$$

S32

where a_1 and a_2 are constants. The boundary condition $C_{o0} = 0$ at $x = \infty$ forces $a_1 = 0$, and so the solution becomes:

$$\overline{C_{o0}} = a_2 e^{-x\sqrt{s/D_o}}$$

S33

The concentration can be expressed in terms of the faradaic current through the flux boundary condition:

$$\frac{\overline{I_0}}{nFA} = -D_o \left. \frac{\partial}{\partial x} \overline{C_{o0}} \right|_{x=0} = (\sqrt{D_o s}) \overline{C_{o0}}|_{x=0}$$

S34

$$\frac{\overline{I_0}}{nFA\sqrt{D_o s}} = \overline{C_{o0}}|_{x=0}$$

S35

The convolution theorem allows us to take this function from the Laplace domain back into the time domain, affordingⁿ:

$$C_{o0}|_{x=0} = c_{o0}|_{x=0} - c^0 = \frac{1}{nFA\sqrt{D_o}} \int_0^t \frac{I_0(t-\tau)}{\sqrt{\pi\tau}} d\tau$$

S36

or

ⁿ The convolution integral here is a half-order integral, or a semiintegral. (A semiintegral is an operation that, when performed twice on a function, returns the integral of that function.) Application of the convolution integral to electrochemical systems has been called "convolution voltammetry"⁷⁹ or "semiintegral electroanalysis"⁴⁶ by different authors.

$$\frac{c_{o0}|_{x=0}}{c^0} = 1 + \int_0^t \frac{\psi_0(t-\tau)}{\sqrt{\pi\tau}} d\tau$$

S37

By a similar transformation, we find:

$$\frac{c_{o1}|_{x=0}}{c^0} = \int_0^t \frac{\psi_1(t-\tau)}{\sqrt{\pi\tau}} d\tau$$

S38

To express $\frac{c_{o1}|_{x=0}}{c^0}$ in terms of sine and cosine functions, we rewrite the integral:

$$\frac{c_{o1}|_{x=0}}{c^0} = \int_0^t \frac{A_1 \sin \omega(t-\tau) + B_1 \cos \omega(t-\tau)}{\sqrt{\pi\tau}} d\tau$$

S39

With a steady-state approximation, $\int_0^t d\tau \approx \int_0^\infty d\tau$, and the integral becomes:

$$\frac{c_{o1}|_{x=0}}{c^0} = \int_0^\infty \frac{A_1 \sin \omega(t-\tau) + B_1 \cos \omega(t-\tau)}{\sqrt{\pi\tau}} d\tau$$

S40

We can expand the sine and cosine functions with the difference-of-angles formulae:

$$\sin \omega(t-\tau) = \sin \omega t \cos \omega \tau - \cos \omega t \sin \omega \tau$$

S41

$$\cos \omega(t-\tau) = \cos \omega t \cos \omega \tau + \sin \omega t \sin \omega \tau$$

S42

which gives the integral:

$$\frac{c_{o1}|_{x=0}}{c^0} = \int_0^\infty \frac{A_1(\sin \omega t \cos \omega \tau - \cos \omega t \sin \omega \tau) + B_1(\cos \omega t \cos \omega \tau + \sin \omega t \sin \omega \tau)}{\sqrt{\pi\tau}} d\tau$$

S43

The integrals $\int_0^\infty \frac{\sin \omega \tau}{\sqrt{\pi\tau}} d\tau$ and $\int_0^\infty \frac{\cos \omega \tau}{\sqrt{\pi\tau}} d\tau$ can be found with Laplace methods, by writing the sine and cosine functions as their complex Euler identities. In general:

$$\int_0^\infty e^{-st} t^n dt = \int_0^\infty e^{-x} \left(\frac{x}{s}\right)^n \frac{dx}{s} = \frac{\Gamma(n+1)}{s^{n+1}}$$

S44

assuming the integral converges. By substituting $n = -1/2$ and $s = \pm i\omega$, the following solution can be obtained for the above integrals:

$$\int_0^{\infty} \frac{\sin \omega \tau}{\sqrt{\pi \tau}} d\tau = \int_0^{\infty} \frac{\cos \omega \tau}{\sqrt{\pi \tau}} d\tau = \frac{1}{\sqrt{2\omega}}$$

S45

This solution affords the following expression for c_{o1} :

$$\frac{c_{o1}|_{x=0}}{c^0} = \frac{A_1 \sin \omega t}{\sqrt{2\omega}} - \frac{A_1 \cos \omega t}{\sqrt{2\omega}} + \frac{B_1 \cos \omega t}{\sqrt{2\omega}} + \frac{B_1 \sin \omega t}{\sqrt{2\omega}}$$

S46

Now that c_{o1} has been expressed in terms of the current, with the coefficients A_1 and B_1 , we can turn our attention to c_r . To find c_{r0} and c_{r1} , we return to the governing equation, writing c_r as the sum of direct and fundamental harmonic components:

$$\frac{\partial}{\partial t}(c_{r0} + c_{r1}) = D_r \frac{\partial^2}{\partial x^2}(c_{r0} + c_{r1}) - k_D(c_{r0} + c_{r1})^2$$

S47

We assume $c_{r1}^2 \approx 0$, so that the equation can be broken into direct current and fundamental harmonic components only. Collecting the direct current terms affords:

$$\frac{\partial}{\partial t} c_{r0} = D_r \frac{\partial^2}{\partial x^2} c_{r0} - k_D c_{r0}^2$$

S48

which, for sufficiently fast k_D , can be solved by the steady-state approximation:

$$D_r \frac{\partial^2}{\partial x^2} c_{r0} = k_D c_{r0}^2$$

S49

which has the solution

$$c_{r0} = \frac{6D_r}{k_D(x - \Lambda)^2}$$

S50

where Λ is some constant. The value of Λ can be found from the flux boundary condition:

$$\frac{I_0}{nFA} = D_r \frac{\partial}{\partial x} c_{r0} \Big|_{x=0} = \frac{12D_r^2}{k_D \Lambda^3}$$

S51

which, upon rearrangement, affords:

$$\Lambda = \left(\frac{12nFAD_r^2}{I_0 k_D} \right)^{1/3}$$

S52

(note that $\Lambda < 0$ because $I_0 < 0$ for reduction). Plugging this expression for Λ back into the equation for c_{r0} affords:

$$c_{r0}|_{x=0} = \left(\frac{I_0}{nFA}\right)^{2/3} \left(\frac{3}{2D_r k_D}\right)^{1/3}$$

S53

so that c_{r0} can be expressed in terms of the direct current I_0 .

Meanwhile, the equation for the fundamental harmonic term c_{r1} is:

$$\frac{\partial}{\partial t} c_{r1} = D_r \frac{\partial^2}{\partial x^2} c_{r1} - 2k_D c_{r0} c_{r1}$$

S54

We plug in the known expression for c_{r0} to find:

$$\frac{\partial}{\partial t} c_{r1} = D_r \frac{\partial^2}{\partial x^2} c_{r1} - \frac{12D_r}{(x - \Lambda)^2} c_{r1}$$

S55

To solve this equation, we take a Laplace transform, which yields:

$$\frac{\partial^2}{\partial x^2} \bar{c}_{r1} = \bar{c}_{r1} \left(\frac{s}{D_r} + \frac{12}{(x - \Lambda)^2} \right)$$

S56

which has a Whittaker function as a solution.^{60,61} To find the Whittaker function, make the substitution

$$z = 2 \sqrt{\frac{s}{D_r}} (x - \Lambda)$$

S57

which affords the equation

$$\frac{\partial^2}{\partial z^2} \bar{c}_{r1} = \bar{c}_{r1} \left(\frac{1}{4} + \frac{12}{z^2} \right)$$

S58

which has $W_{0,-7/2}(z)$ as a solution:

$$\bar{c}_{r1} = W_{0,-7/2}(z) = e^{-z/2} \left(\frac{120}{z^3} + \frac{60}{z^2} + \frac{12}{z} + 1 \right)$$

S59°

To express this concentration in terms of the current, use the flux boundary condition:

$$\frac{\bar{I}_1}{nFAD_r} = \frac{\partial}{\partial x} \bar{c}_{r1} \Big|_{x=0} = \frac{\partial z}{\partial x} \frac{\partial}{\partial z} \left[e^{-\frac{z}{2} + \ln\left(\frac{120}{z^3} + \frac{60}{z^2} + \frac{12}{z} + 1\right)} \right] \Big|_{z=-2\Lambda\sqrt{\frac{s}{D_r}}}$$

S60

$$\frac{\bar{I}_1}{nFAD_r} = \left(2\sqrt{\frac{s}{D_r}} \right) \left[-\frac{1}{2} - \frac{\frac{360}{z^4} + \frac{120}{z^3} + \frac{12}{z^2}}{\frac{120}{z^3} + \frac{60}{z^2} + \frac{12}{z} + 1} \right] \bar{c}_{r1} \Big|_{z=-2\Lambda\sqrt{\frac{s}{D_r}}}$$

S61

Rearranging yields:

$$\bar{c}_{r1} \Big|_{z=-2\Lambda\sqrt{\frac{s}{D_r}}} = \frac{-\bar{I}_1}{nFA\sqrt{D_r}} \left[\frac{\Lambda^4 s^{3/2} - 6\Lambda^3 s D_r^{1/2} + 15\Lambda^2 s^{1/2} D_r - 15\Lambda D_r^{3/2}}{\Lambda^4 s^2 - 6\Lambda^3 s^{3/2} D_r^{1/2} + 21\Lambda^2 s D_r - 45\Lambda s^{1/2} D_r^{3/2} + 45D_r^2} \right]$$

S62

The term in brackets is a fraction of two polynomials in $s^{1/2}$. We will expand it by partial fractions so that the inverse Laplace transform can be taken more easily. Evidently the term in brackets can be expanded into the form (after dividing the numerator and denominator by Λ^4):

$$\begin{aligned} & \frac{s^{3/2} - 6\Lambda^{-1} s D_r^{1/2} + 15\Lambda^{-2} s^{1/2} D_r - 15\Lambda^{-3} D_r^{3/2}}{s^2 - 6\Lambda^{-1} s^{3/2} D_r^{1/2} + 21\Lambda^{-2} s D_r - 45\Lambda^{-3} s^{1/2} D_r^{3/2} + 45\Lambda^{-4} D_r^2} \\ &= \frac{a_1}{\sqrt{s} + b_1} + \frac{a_2}{\sqrt{s} + b_2} + \frac{a_3}{\sqrt{s} + b_3} + \frac{a_4}{\sqrt{s} + b_4} \end{aligned}$$

S63

The roots of the polynomial in the denominator $-b_k$ ($k = 1, 2, 3, 4$) can be found numerically with a coding script. Once the b_k are found, the coefficients a_k can be found from the following four equations, which are obtained after bringing all of the partial fraction terms over a common denominator and equating coefficients of like powers of s :

$$a_1 + a_2 + a_3 + a_4 = 1$$

S64

$$a_1(b_2 + b_3 + b_4) + a_2(b_1 + b_3 + b_4) + a_3(b_1 + b_2 + b_4) + a_4(b_1 + b_2 + b_3) = -6\frac{\sqrt{D_r}}{\Lambda}$$

° Strictly speaking, $\bar{c}_{r1} = a_1 W_{0,-7/2}(z)$, where a_1 is an arbitrary constant. Incorporation of the flux boundary condition amounts to finding a_1 , although the constant is not explicitly identified as such.

S65

$$a_1(b_2b_3 + b_2b_4 + b_3b_4) + a_2(b_1b_3 + b_1b_4 + b_3b_4) + a_3(b_1b_2 + b_1b_4 + b_2b_4) \\ + a_4(b_1b_2 + b_1b_3 + b_2b_3) = 15 \frac{D_r}{\Lambda^2}$$

S66

$$a_1b_2b_3b_4 + a_2b_1b_3b_4 + a_3b_1b_2b_4 + a_4b_1b_2b_3 = -15 \frac{D_r^{3/2}}{\Lambda^3}$$

S67

Expressing these equations in matrix form affords the following equation:

$$\begin{bmatrix} 1 & 1 & 1 & 1 \\ b_2 + b_3 + b_4 & b_1 + b_3 + b_4 & b_1 + b_2 + b_4 & b_1 + b_2 + b_3 \\ b_2b_3 + b_2b_4 + b_3b_4 & b_1b_3 + b_1b_4 + b_3b_4 & b_1b_2 + b_1b_4 + b_2b_4 & b_1b_2 + b_1b_3 + b_2b_3 \\ b_2b_3b_4 & b_1b_3b_4 & b_1b_2b_4 & b_1b_2b_3 \end{bmatrix} \begin{bmatrix} a_1 \\ a_2 \\ a_3 \\ a_4 \end{bmatrix} \\ = \begin{bmatrix} 1 \\ 6\rho \\ 15\rho^2 \\ 15\rho^3 \end{bmatrix}$$

S68

where

$$\rho = \left(\frac{k_D c_{r0}|_{x=0}}{6} \right)^{1/2} = -\frac{\sqrt{D_r}}{\Lambda}$$

S69

Finally, we need to take the inverse Laplace transform of the concentration:

$$\frac{c_{r1}|_{x=0}}{c^0} = \mathcal{L}^{-1} \left\{ \frac{\bar{c}_{r1}|_{x=0}}{c^0} \right\} = \mathcal{L}^{-1} \left\{ \frac{-\bar{I}_1}{nFAc^0\sqrt{D_r}} \sum_{k=1}^4 \frac{a_k}{\sqrt{s} + b_k} \right\} = \mathcal{L}^{-1} \left\{ -\bar{\psi}_1 \sqrt{\frac{D_o}{D_r}} \sum_{k=1}^4 \frac{a_k}{\sqrt{s} + b_k} \right\}$$

S70

which requires us to know the inverse Laplace transform of $\frac{1}{\sqrt{s} + b_k}$. To find this transform, observe

that

$$\frac{1}{\sqrt{s} + b_k} = \frac{1}{\sqrt{s}} - \frac{b_k}{\sqrt{s}(\sqrt{s} + b_k)} = \frac{1}{\sqrt{s}} - \frac{b_k}{s - b_k^2} + \frac{b_k^2}{\sqrt{s}(s - b_k^2)}$$

S71

With the help of the convolution theorem, we find the inverse Laplace transform to be:

$$\mathcal{L}^{-1}\left\{\frac{1}{\sqrt{s+b_k}}\right\} = \mathcal{L}^{-1}\left\{\frac{1}{\sqrt{s}} - \frac{b_k}{s-b_k^2} + \frac{b_k^2}{\sqrt{s}(s-b_k^2)}\right\} = \frac{1}{\sqrt{\pi t}} - b_k e^{b_k^2 t} + b_k^2 \int_0^t \frac{e^{b_k^2(t-\tau)}}{\sqrt{\pi\tau}} d\tau$$

S72

The right-hand side of the equation can be written more compactly:

$$\frac{1}{\sqrt{\pi t}} - b_k e^{b_k^2 t} \left(1 - b_k \int_0^t \frac{e^{-b_k^2 \tau}}{\sqrt{\pi\tau}} d\tau\right) = \frac{1}{\sqrt{\pi t}} - b_k^2 e^{b_k^2 t} \int_t^\infty \frac{e^{-b_k^2 \tau}}{\sqrt{\pi\tau}} d\tau$$

S73

observing that the term in parentheses is the complementary error function of $b_k \tau^{1/2}$. To express c_{r1} in terms of sine and cosine functions, we again write $\psi_1 = A_1 \sin(\omega t) + B_1 \cos(\omega t)$, and again making use of the convolution theorem and the steady-state assumption we find:

$$\begin{aligned} \frac{c_{r1}|_{x=0}}{c^0} = & -\sqrt{\frac{D_o}{D_r}} \int_0^\infty (A_1 \sin \omega(t-\tau) + B_1 \cos \omega(t \\ & -\tau)) \sum_{k=1}^4 a_k \left(\frac{1}{\sqrt{\pi\tau}} - b_k^2 e^{b_k^2 \tau} \int_\tau^\infty \frac{e^{-b_k^2 \sigma}}{\sqrt{\pi\sigma}} d\sigma \right) d\tau \end{aligned}$$

S74

The sum on the right can be broken into two parts, the reversible component $\frac{1}{\sqrt{\pi\tau}}$ and the irreversible component $-b_k^2 e^{b_k^2 \tau} \int_\tau^\infty \frac{e^{-b_k^2 \sigma}}{\sqrt{\pi\sigma}} d\sigma$. For the reversible component, the convolution integral is identical to the solution above for c_{o1} , affording:

$$\begin{aligned} & -\sqrt{\frac{D_o}{D_r}} \sum_{k=1}^4 a_k \int_0^\infty \frac{(A_1 \sin \omega(t-\tau) + B_1 \cos \omega(t-\tau))}{\sqrt{\pi\tau}} d\tau \\ & = -\sqrt{\frac{D_o}{D_r}} \sum_{k=1}^4 a_k \left(\frac{A_1 \sin \omega t}{\sqrt{2\omega}} - \frac{A_1 \cos \omega t}{\sqrt{2\omega}} + \frac{B_1 \cos \omega t}{\sqrt{2\omega}} + \frac{B_1 \sin \omega t}{\sqrt{2\omega}} \right) \end{aligned}$$

S75

To solve the convolution integral for the irreversible component, we use the difference-of-angles formulae to write:

$$\sqrt{\frac{D_o}{D_r}} \sum_{k=1}^4 a_k b_k^2 \int_0^\infty (A_1(\sin \omega t \cos \omega \tau - \cos \omega t \sin \omega \tau) + B_1(\cos \omega t \cos \omega \tau + \sin \omega t \sin \omega \tau)) \left(e^{b_k^2 \tau} \int_\tau^\infty \frac{e^{-b_k^2 \sigma}}{\sqrt{\pi \sigma}} d\sigma \right) d\tau$$

S76

The integral $\int_\tau^\infty \frac{e^{-b_k^2 \sigma}}{\sqrt{\pi \sigma}} d\sigma$ may be found by switching the bounds of integration, observing that $\int_{\tau=0}^{\tau=\infty} \int_{\sigma=\tau}^{\sigma=\infty} d\sigma d\tau = \int_{\sigma=0}^{\sigma=\infty} \int_{\tau=0}^{\tau=\sigma} d\tau d\sigma$ (the domain being integrated is the gray triangle shown in Figure 2.S23 below).

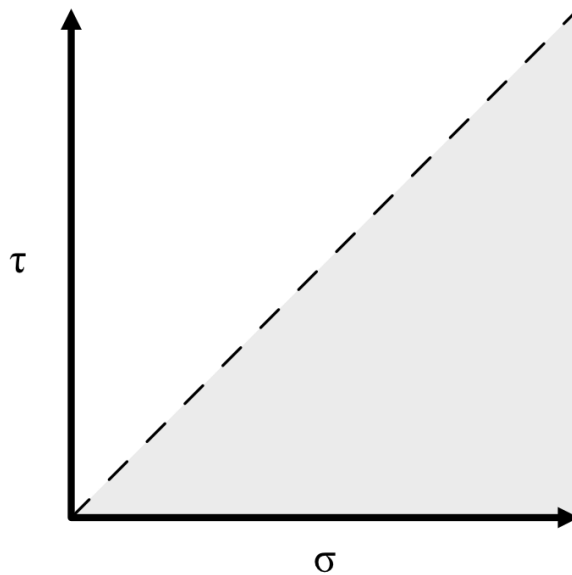


Figure 2.S23. The domain being integrated during the inverse Laplace transform of $c_{rI}|_{x=0}$.

With this transformation, and with the complex Euler identities for sine and cosine, this integral can be solved. Taking $e^{i\omega\tau}$ in place of, for example, $\sin\omega\tau$, we find:

$$\begin{aligned} \int_{\tau=0}^{\tau=\infty} e^{i\omega\tau} \left(e^{b_k^2 \tau} \int_{\sigma=\tau}^{\sigma=\infty} \frac{e^{-b_k^2 \sigma}}{\sqrt{\pi \sigma}} d\sigma \right) d\tau &= \int_{\sigma=0}^{\sigma=\infty} \frac{e^{-b_k^2 \sigma}}{\sqrt{\pi \sigma}} \int_{\tau=0}^{\tau=\sigma} e^{\tau(b_k^2 + i\omega)} d\tau d\sigma \\ &= \int_{\sigma=0}^{\sigma=\infty} \frac{e^{-b_k^2 \sigma}}{\sqrt{\pi \sigma}} \left[\frac{e^{\tau(b_k^2 + i\omega)}}{(b_k^2 + i\omega)} \right]_{\tau=0}^{\tau=\sigma} d\sigma \end{aligned}$$

S77

$$= \frac{1}{(b_k^2 + i\omega)} \int_{\sigma=0}^{\sigma=\infty} \frac{e^{i\omega\sigma}}{\sqrt{\pi\sigma}} - \frac{e^{-b_k^2\sigma}}{\sqrt{\pi\sigma}} d\sigma$$

S78

$$= \frac{1}{(b_k^2 + i\omega)} \left(\frac{1}{\sqrt{-i\omega}} - \frac{1}{b_k} \right)$$

S79

In a similar fashion, $e^{-i\omega t}$ affords:

$$\frac{1}{(b_k^2 - i\omega)} \left(\frac{1}{\sqrt{i\omega}} - \frac{1}{b_k} \right)$$

S80

Combining these as needed for $\sin\omega\tau$, we find:

$$\begin{aligned} \int_0^\infty \sin \omega\tau \left(e^{b_k^2\tau} \int_\tau^\infty \frac{e^{-b_k^2\sigma}}{\sqrt{\pi\sigma}} d\sigma \right) d\tau \\ = \frac{1}{2i} \left\{ \frac{1}{(b_k^2 + i\omega)} \left(\frac{1}{\sqrt{-i\omega}} - \frac{1}{b_k} \right) - \frac{1}{(b_k^2 - i\omega)} \left(\frac{1}{\sqrt{i\omega}} - \frac{1}{b_k} \right) \right\} \end{aligned}$$

S81

Rearranging affords:

$$\int_0^\infty \sin \omega\tau \left(e^{b_k^2\tau} \int_\tau^\infty \frac{e^{-b_k^2\sigma}}{\sqrt{\pi\sigma}} d\sigma \right) d\tau = \frac{1}{\sqrt{2\omega}(b_k^4 + \omega^2)} \left\{ b_k^2 - b_k\omega + \frac{\omega\sqrt{2\omega}}{b_k} \right\}$$

S82

Similarly, we find for $\cos\omega\tau$:

$$\int_0^\infty \cos \omega\tau \left(e^{b_k^2\tau} \int_\tau^\infty \frac{e^{-b_k^2\sigma}}{\sqrt{\pi\sigma}} d\sigma \right) d\tau = \frac{1}{\sqrt{2\omega}(b_k^4 + \omega^2)} \{ b_k^2 - b_k\sqrt{2\omega} + \omega \}$$

S83

Finally, we can plug these identities back into the equation above for $c_{r1}|_{x=0}$. Returning to the total expression, we can write:

$$\begin{aligned}
& \frac{c_{r1}|_{x=0}}{c^0} \\
&= -\sqrt{\frac{D_o}{D_r}} \sum_{k=1}^4 \left\{ a_k \int_0^\infty \frac{A_1(\sin \omega t \cos \omega \tau - \cos \omega t \sin \omega \tau) + B_1(\cos \omega t \cos \omega \tau + \sin \omega t \sin \omega \tau)}{\sqrt{\pi \tau}} d\tau \right. \\
&- \int_0^\infty [A_1(\sin \omega t \cos \omega \tau - \cos \omega t \sin \omega \tau) \\
&+ B_1(\cos \omega t \cos \omega \tau + \sin \omega t \sin \omega \tau)] b_k^2 e^{b_k^2 \tau} \int_\tau^\infty \frac{e^{-b_k^2 \sigma}}{\sqrt{\pi \sigma}} d\sigma d\tau \left. \right\}
\end{aligned}$$

S84

$$\begin{aligned}
\frac{c_{r1}|_{x=0}}{c^0} = & -\sqrt{\frac{D_o}{D_r}} \sum_{k=1}^4 \left\{ a_k \left(\frac{A_1 \sin \omega t}{\sqrt{2\omega}} - \frac{A_1 \cos \omega t}{\sqrt{2\omega}} + \frac{B_1 \cos \omega t}{\sqrt{2\omega}} + \frac{B_1 \sin \omega t}{\sqrt{2\omega}} \right) \right. \\
& - \left(\frac{A_1 \sin \omega t}{\sqrt{2\omega}(b_k^4 + \omega^2)} \{b_k^4 - b_k^3 \sqrt{2\omega} + b_k^2 \omega\} \right. \\
& - \frac{A_1 \cos \omega t}{\sqrt{2\omega}(b_k^4 + \omega^2)} \{b_k^4 - b_k^2 \omega + b_k \omega \sqrt{2\omega}\} \\
& + \frac{B_1 \cos \omega t}{\sqrt{2\omega}(b_k^4 + \omega^2)} \{b_k^4 - b_k^3 \sqrt{2\omega} + b_k^2 \omega\} \\
& \left. \left. + \frac{B_1 \sin \omega t}{\sqrt{2\omega}(b_k^4 + \omega^2)} \{b_k^4 - b_k^2 \omega + b_k \omega \sqrt{2\omega}\} \right) \right\}
\end{aligned}$$

S85

That is:

$$\begin{aligned}
\frac{c_{r1}|_{x=0}}{c^0} = & -\sqrt{\frac{D_o}{D_r}} \left\{ A_1 \sin \omega t \sum_{k=1}^4 \left(\frac{a_k}{\sqrt{2\omega}} \left[1 - \frac{1}{(b_k^4 + \omega^2)} \{b_k^4 - b_k^3 \sqrt{2\omega} + b_k^2 \omega\} \right] \right) \right. \\
& - A_1 \cos \omega t \sum_{k=1}^4 \left(\frac{a_k}{\sqrt{2\omega}} \left[1 - \frac{1}{(b_k^4 + \omega^2)} \{b_k^4 - b_k^2 \omega + b_k \omega \sqrt{2\omega}\} \right] \right) \\
& + B_1 \cos \omega t \sum_{k=1}^4 \left(\frac{a_k}{\sqrt{2\omega}} \left[1 - \frac{1}{(b_k^4 + \omega^2)} \{b_k^4 - b_k^3 \sqrt{2\omega} + b_k^2 \omega\} \right] \right) \\
& \left. + B_1 \sin \omega t \sum_{k=1}^4 \left(\frac{a_k}{\sqrt{2\omega}} \left[1 - \frac{1}{(b_k^4 + \omega^2)} \{b_k^4 - b_k^2 \omega + b_k \omega \sqrt{2\omega}\} \right] \right) \right\}
\end{aligned}$$

S86

Writing

$$L_S = \sum_{k=1}^4 \left(a_k \left[1 - \frac{1}{(b_k^4 + \omega^2)} \{b_k^4 - b_k^2 \omega + b_k \omega \sqrt{2\omega}\} \right] \right) \\ = \sum_{k=1}^4 \left(\frac{a_k}{(b_k^4 + \omega^2)} \{ \omega^2 + b_k \omega (b_k - \sqrt{2\omega}) \} \right)$$

S87

$$L_C = \sum_{k=1}^4 \left(a_k \left[1 - \frac{1}{(b_k^4 + \omega^2)} \{b_k^4 - b_k^3 \sqrt{2\omega} + b_k^2 \omega\} \right] \right) \\ = \sum_{k=1}^4 \left(\frac{a_k}{(b_k^4 + \omega^2)} \{ \omega^2 + b_k^2 (b_k \sqrt{2\omega} - \omega) \} \right)$$

S88

we have finally:

$$\frac{c_{r1}|_{x=0}}{c^0} = - \sqrt{\frac{D_o}{D_r}} \sqrt{\frac{1}{2\omega}} \{A_1 L_C \sin \omega t - A_1 L_S \cos \omega t + B_1 L_C \cos \omega t + B_1 L_S \sin \omega t\}$$

S89

We can plug the expressions for c_{o1} and c_{r1} into the Butler-Volmer equation above, which yields:

$$\psi_1 = A_1 \sin(\omega t) + B_1 \cos(\omega t) \\ = \frac{k^0 f}{\sqrt{D}} \left\{ e^{-\alpha j} \left(\frac{c_{o0} \alpha \delta \sin(\omega t)}{c^0} \right. \right. \\ \left. \left. - \left[\frac{A_1 \sin \omega t}{\sqrt{2\omega}} - \frac{A_1 \cos \omega t}{\sqrt{2\omega}} + \frac{B_1 \cos \omega t}{\sqrt{2\omega}} + \frac{B_1 \sin \omega t}{\sqrt{2\omega}} \right] \right) \right. \\ \left. + e^{\beta j} \sqrt{\frac{D_r}{D_o}} \left(\frac{c_{r0} \beta \delta \sin(\omega t)}{c^0} \right. \right. \\ \left. \left. - \sqrt{\frac{D_o}{D_r}} \left\{ \frac{A_1 L_C \sin \omega t}{\sqrt{2\omega}} - \frac{A_1 L_S \cos \omega t}{\sqrt{2\omega}} + \frac{B_1 L_C \cos \omega t}{\sqrt{2\omega}} + \frac{B_1 L_S \sin \omega t}{\sqrt{2\omega}} \right\} \right) \right\}$$

S90

Equating sine and cosine terms gives two equations for the two unknowns A_1 and B_1 :

$$A_1 = \frac{k^0 f}{\sqrt{D}} \left\{ e^{-\alpha j} \left(\frac{c_{o0} \alpha \delta}{c^0} - \frac{A_1}{\sqrt{2\omega}} - \frac{B_1}{\sqrt{2\omega}} \right) + e^{\beta j} \left(\sqrt{\frac{D_r}{D_o}} \frac{c_{r0} \beta \delta}{c^0} - \frac{A_1 L_C}{\sqrt{2\omega}} - \frac{B_1 L_S}{\sqrt{2\omega}} \right) \right\}$$

S91

$$B_1 = \frac{k^0 f}{\sqrt{D}} \left\{ e^{-\alpha j} \left(\frac{A_1}{\sqrt{2\omega}} - \frac{B_1}{\sqrt{2\omega}} \right) + e^{\beta j} \left(\frac{A_1 L_S}{\sqrt{2\omega}} - \frac{B_1 L_C}{\sqrt{2\omega}} \right) \right\}$$

S92

Solving for B_1 in terms of A_1 , we find:

$$B_1 \left(1 + \frac{k^0 f e^{-\alpha j}}{\sqrt{D} \sqrt{2\omega}} (1 + e^j L_C) \right) = \frac{k^0 f e^{-\alpha j}}{\sqrt{D} \sqrt{2\omega}} A_1 \{1 + e^j L_S\}$$

S93

$$B_1 = A_1 \frac{1 + e^j L_S}{\frac{\sqrt{D} \sqrt{2\omega}}{k^0 f e^{-\alpha j}} + 1 + e^j L_C} = A_1 \frac{\frac{1 + e^j L_S}{1 + e^j}}{\frac{\sqrt{D} \sqrt{2\omega}}{k^0 f (e^{-\alpha j} + e^{\beta j})} + \frac{1 + e^j L_C}{1 + e^j}}$$

S94

Solving for A_1 in terms of B_1 yields:

$$A_1 \left(1 + \frac{k^0 f e^{-\alpha j}}{\sqrt{D} \sqrt{2\omega}} (1 + e^j L_C) \right) = \frac{k^0 f e^{-\alpha j}}{\sqrt{D} \sqrt{2\omega}} \left\{ \left(\frac{c_{o0} \alpha \delta \sqrt{2\omega}}{c^0} - B_1 \right) + e^j \left(\sqrt{\frac{D_r}{D_o}} \frac{c_{r0} \beta \delta \sqrt{2\omega}}{c^0} - B_1 L_S \right) \right\}$$

S95

$$A_1 = \frac{\frac{1}{1 + e^j} \left(\frac{c_{o0} \alpha \delta \sqrt{2\omega}}{c^0} + \sqrt{\frac{D_r}{D_o}} \frac{c_{r0} \beta \delta \sqrt{2\omega}}{c^0} e^j \right) - B_1 \frac{1 + e^j L_S}{1 + e^j}}{\frac{\sqrt{D} \sqrt{2\omega}}{k^0 f (e^{-\alpha j} + e^{\beta j})} + \frac{1 + e^j L_C}{1 + e^j}}$$

S96

The absolute solutions for both coefficients will be easier to follow with a few shorthand notations:

$$v = \frac{\sqrt{D} \sqrt{2\omega}}{k^0 f (e^{-\alpha j} + e^{\beta j})} + \frac{1 + e^j L_C}{1 + e^j}$$

S97

$$u = \frac{1 + e^j L_S}{1 + e^j}$$

S98

$$H = \frac{1}{1 + e^j} \left(\frac{c_{o0} \alpha \delta \sqrt{2\omega}}{c^0} + \sqrt{\frac{D_r}{D_o}} \frac{c_{r0} \beta \delta \sqrt{2\omega}}{c^0} e^j \right)$$

S99

Then we have

$$B_1 = A_1 \frac{u}{v}$$

S100

$$A_1 = \frac{H - B_1 u}{v}$$

S101

Solving for B_1 affords:

$$B_1 = \left(\frac{H - B_1 u}{v} \right) \frac{u}{v} = \frac{Hu - B_1 u^2}{v^2}$$

S102

$$B_1 \left(1 + \frac{u^2}{v^2} \right) = \frac{Hu}{v^2}$$

S103

$$B_1 = \frac{Hu}{v^2 + u^2}$$

S104

And solving for A_1 affords:

$$A_1 = B_1 \frac{v}{u} = \frac{Hv}{v^2 + u^2}$$

S105

At this point, the equation for ψ_I has technically been solved – both the sine and the cosine coefficients are known. However, it remains to put ψ_I into the magnitude/phase angle form:

$$\psi_1 = A_1 \sin(\omega t) + B_1 \cos(\omega t) = \sqrt{A_1^2 + B_1^2} \sin(\omega t + \theta)$$

S106

$$\theta = \cot^{-1}\left(\frac{A_1}{B_1}\right)$$

S107

Plugging in the results for A_l and B_l , we find:

$$\psi_1 = \frac{H}{\sqrt{v^2 + u^2}} \sin(\omega t + \varphi)$$

S108

$$\varphi = \cot^{-1}\left(\frac{v}{u}\right)$$

S109

We are almost at the final solution. We write out H :

$$\psi_1 = \frac{\sqrt{2}}{\sqrt{v^2 + u^2}} \left\{ \frac{\sqrt{\omega}}{1 + e^j} \left(\frac{c_{o0}\alpha\delta}{c^0} + \sqrt{\frac{D_r}{D_o}} \frac{c_{r0}\beta\delta}{c^0} e^j \right) \right\} \sin(\omega t + \varphi)$$

S110

$$\psi_1 = \frac{\sqrt{2}}{\sqrt{v^2 + u^2}} \left\{ \frac{\delta\sqrt{\omega}(1 + e^{-j})}{4 \cosh^2(j/2)} \left(\frac{c_{o0}\alpha}{c^0} + \sqrt{\frac{D_r}{D_o}} \frac{c_{r0}\beta}{c^0} e^j \right) \right\} \sin(\omega t + \varphi)$$

S111

Denoting

$$F(t) = (1 + e^{-j}) \left(\frac{c_{o0}\alpha}{c^0} + \sqrt{\frac{D_r}{D_o}} \frac{c_{r0}\beta}{c^0} e^j \right)$$

S112

and

$$G(\omega) = \left[\frac{2}{v^2 + u^2} \right]^{1/2}$$

S113

we have

$$\psi_1 = \frac{nF\Delta E\sqrt{\omega}}{4RT \cosh^2(j/2)} F(t)G(\omega) \sin(\omega t + \varphi)$$

S114

$$I_1 = \frac{n^2 F^2 A c^0 (\omega D_o)^{1/2} \Delta E}{4RT \cosh^2(j/2)} F(t)G(\omega) \sin(\omega t + \varphi)$$

S115

Finally, by setting

$$I_{rev} = \frac{n^2 F^2 A c^0 (\omega D_o)^{1/2} \Delta E}{4RT \cosh^2(j/2)}$$

S116

we have the solution in the final form:

$$I_1 = I_{rev} F(t) G(\omega) \sin(\omega t + \varphi)$$

S117

The shorthand notation here was chosen to coincide with the literature notation.⁴⁰ It should be observed that the only changes we made were to the definitions of L_S and L_C (Eqs. S87-S88), which appear in u and v (S97-S98). Equation S117 may be expanded partially to illustrate more thoroughly what is being computed:

$$I_1 = \frac{n^2 F^2 A c^0 (\omega D_o)^{1/2} \Delta E}{4RT \cosh^2(j/2)} * (1 + e^{-j}) \left(\frac{c_{o0} \alpha}{c^0} + \sqrt{\frac{D_r}{D_o} \frac{c_{r0} \beta}{c^0}} e^j \right) * \left[\frac{2}{\left(\frac{\sqrt{D} \sqrt{2\omega}}{k^0 f(e^{-\alpha j} + e^{\beta j})} + \frac{1 + e^j L_C}{1 + e^j} \right)^2 + \left(\frac{1 + e^j L_S}{1 + e^j} \right)^2} \right]^{1/2} * \sin \left(\omega t + \cot^{-1} \left(\frac{\frac{\sqrt{D} \sqrt{2\omega}}{k^0 f(e^{-\alpha j} + e^{\beta j})} + \frac{1 + e^j L_C}{1 + e^j}}{\frac{1 + e^j L_S}{1 + e^j}} \right) \right)$$

S118

Sample python script for implementing this code, and for computing the error in the ACV fit (described on the following page), may be found on Github: <<https://github.com/Chase-Bruggeman/Electrochemistry>>. Representative ACV and CV data for **1-Br** are also provided in this repository.

ERROR CONTOUR PLOTS

The error ε (units of μA) for the ACV fits was found with the following equation:

$$\varepsilon = \frac{1}{N} \sum_{k=1}^N \frac{\Delta I_{exp,k}}{\Delta I_{exp,max}} \sqrt{\Delta I_{exp,k}^2 + \Delta I_{theor,k}^2 - 2\Delta I_{exp,k}\Delta I_{theor,k} \cos(\varphi_{exp,k} - \varphi_{theor,k})}$$

where N is the number of data points, ΔI_{exp} is the experimental faradaic alternating current magnitude, ΔI_{theor} is the theoretical faradaic alternating current magnitude according to Eq. 117 above, φ_{exp} is the experimental faradaic phase angle, and φ_{theor} is the theoretical faradaic phase angle according to Eq. 117. The square root term is the offset between theoretical and experimental data points on a polar plot of the current. The preceding term inside the sum weights the offset by the intensity of the measured signal. Only those data points where $\Delta I_{exp} > 0.1 * \Delta I_{exp,max}$ were considered in the sum.

An equivalent expression for the error is:

$$\varepsilon = \frac{1}{N} \sum_{k=1}^N \frac{\Delta I_{exp,k}}{\Delta I_{exp,max}} \sqrt{(I_{r,exp,k} - I_{r,theor,k})^2 + (I_{j,exp,k} - I_{j,theor,k})^2}$$

where I_r and I_j are the real and imaginary components of the current ($I_r = \Delta I * \cos(\varphi)$, $I_j = \Delta I * \sin(\varphi)$).

The error is illustrated schematically in Figure 2.S24.

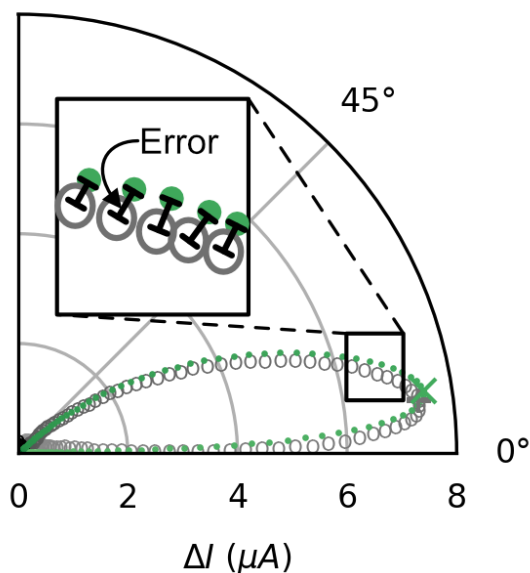


Figure 2.S24. Illustration of the error as the magnitude of the difference between the theoretical (green dots) and experimental (gray circles) alternating current.

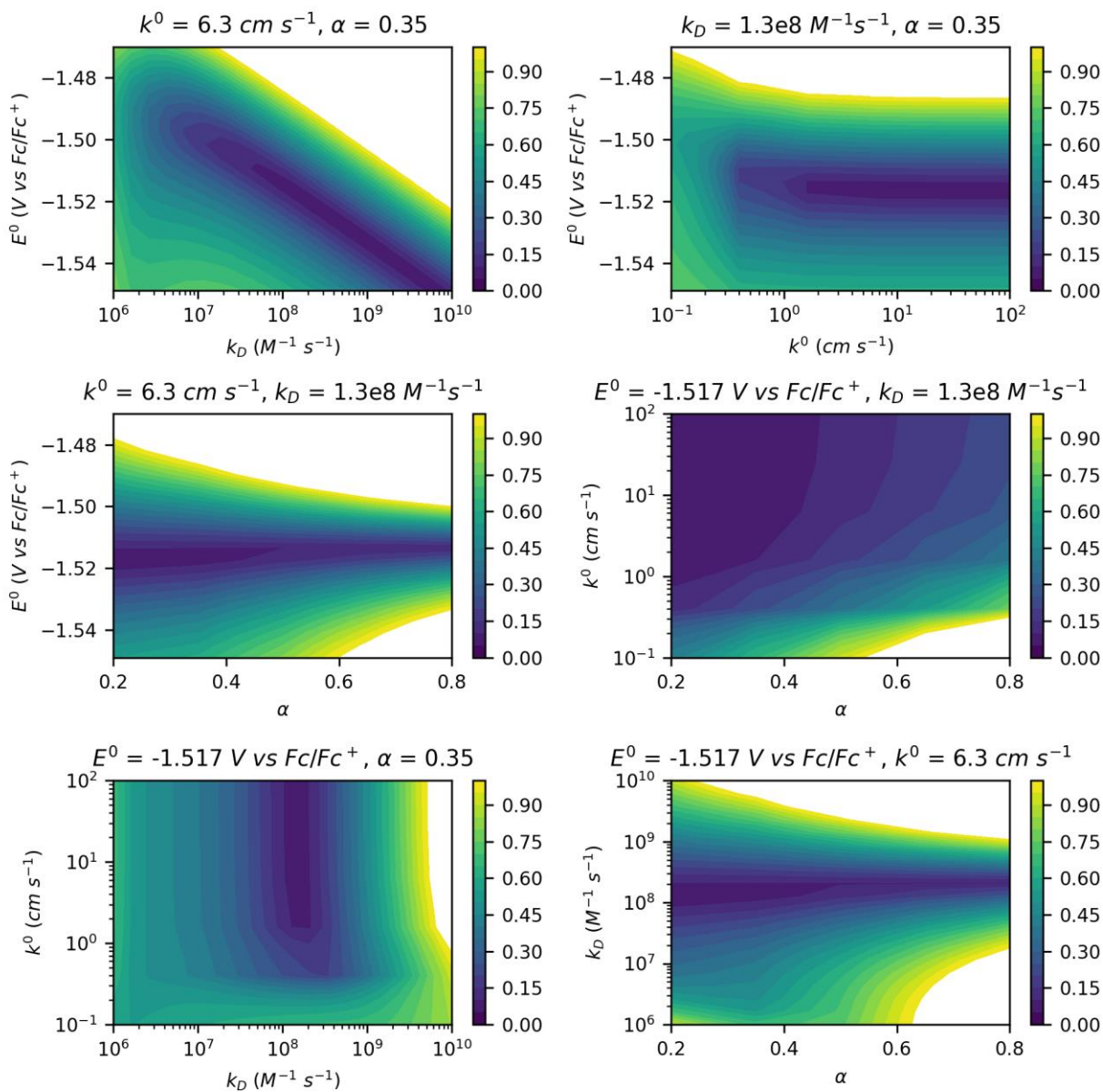


Figure 2.S25. Contour plot of error in ACV fit for 1-allyl nicotinamide bromide (**1-Br**).

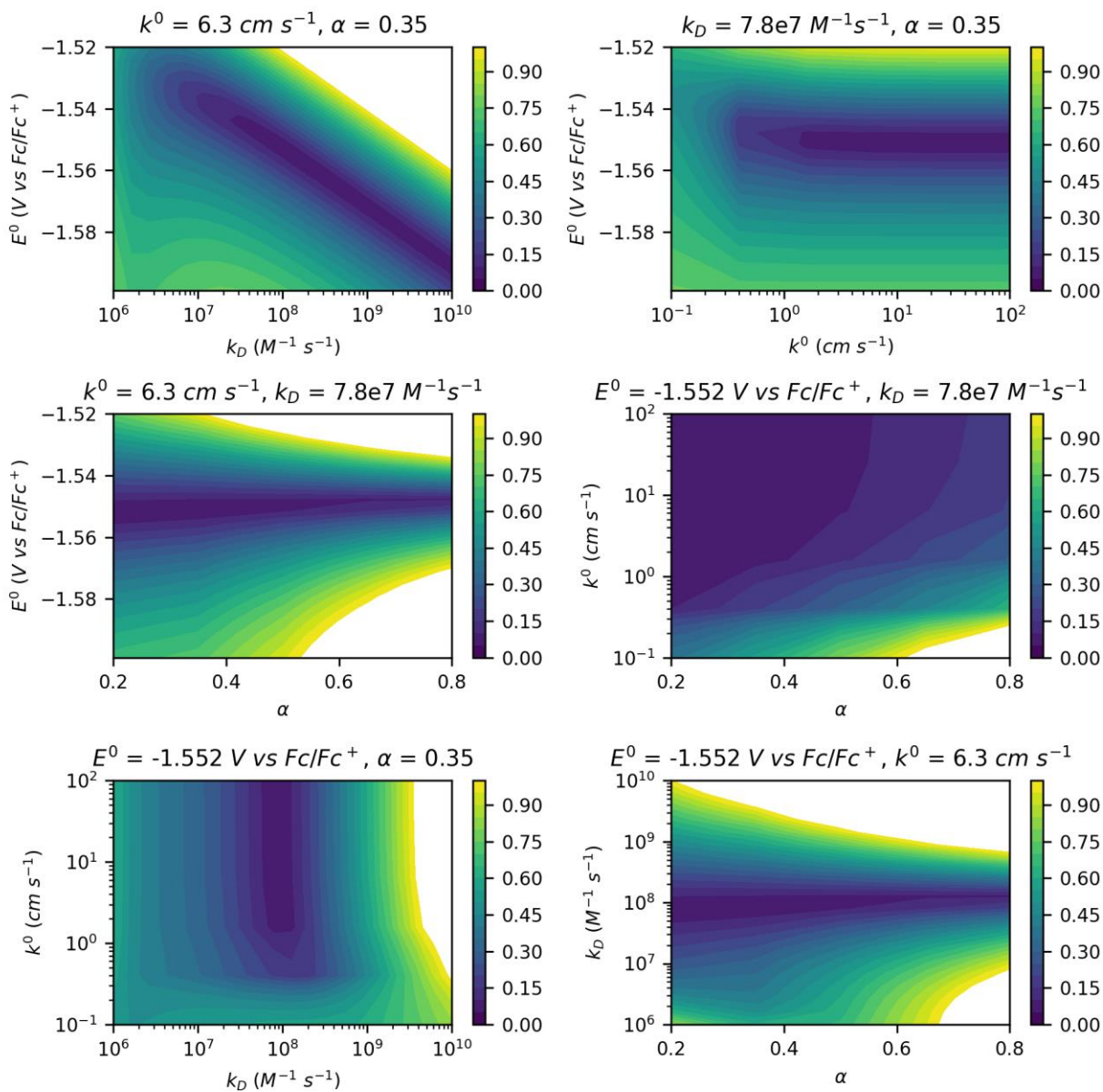


Figure 2.S26. Contour plot of error in ACV fit for 1-butyl nicotinamide bromide (2-Br).

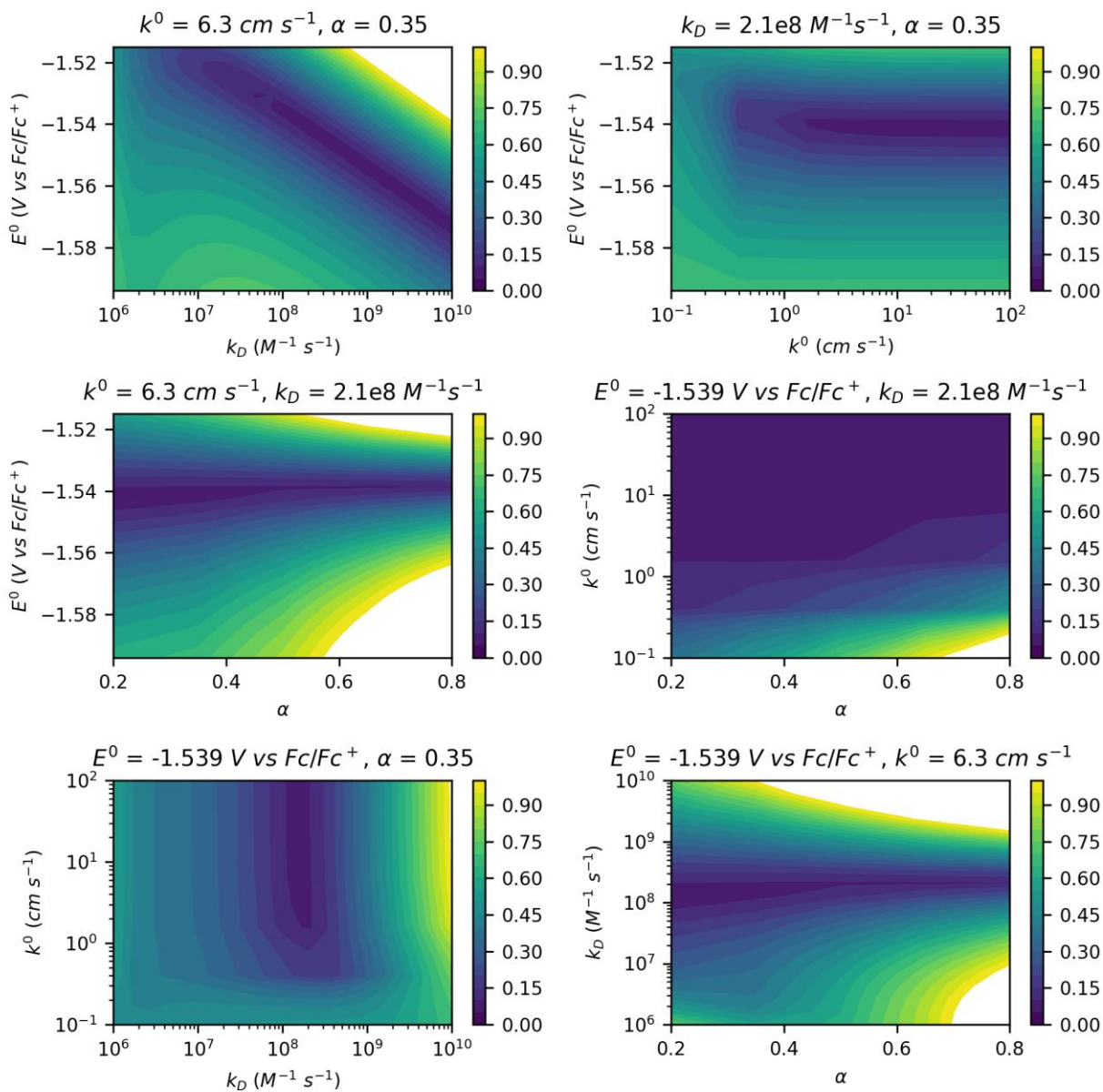


Figure 2.S27. Contour plot of error in ACV fit for 1-phenethyl nicotinamide bromide (**3-Br**).

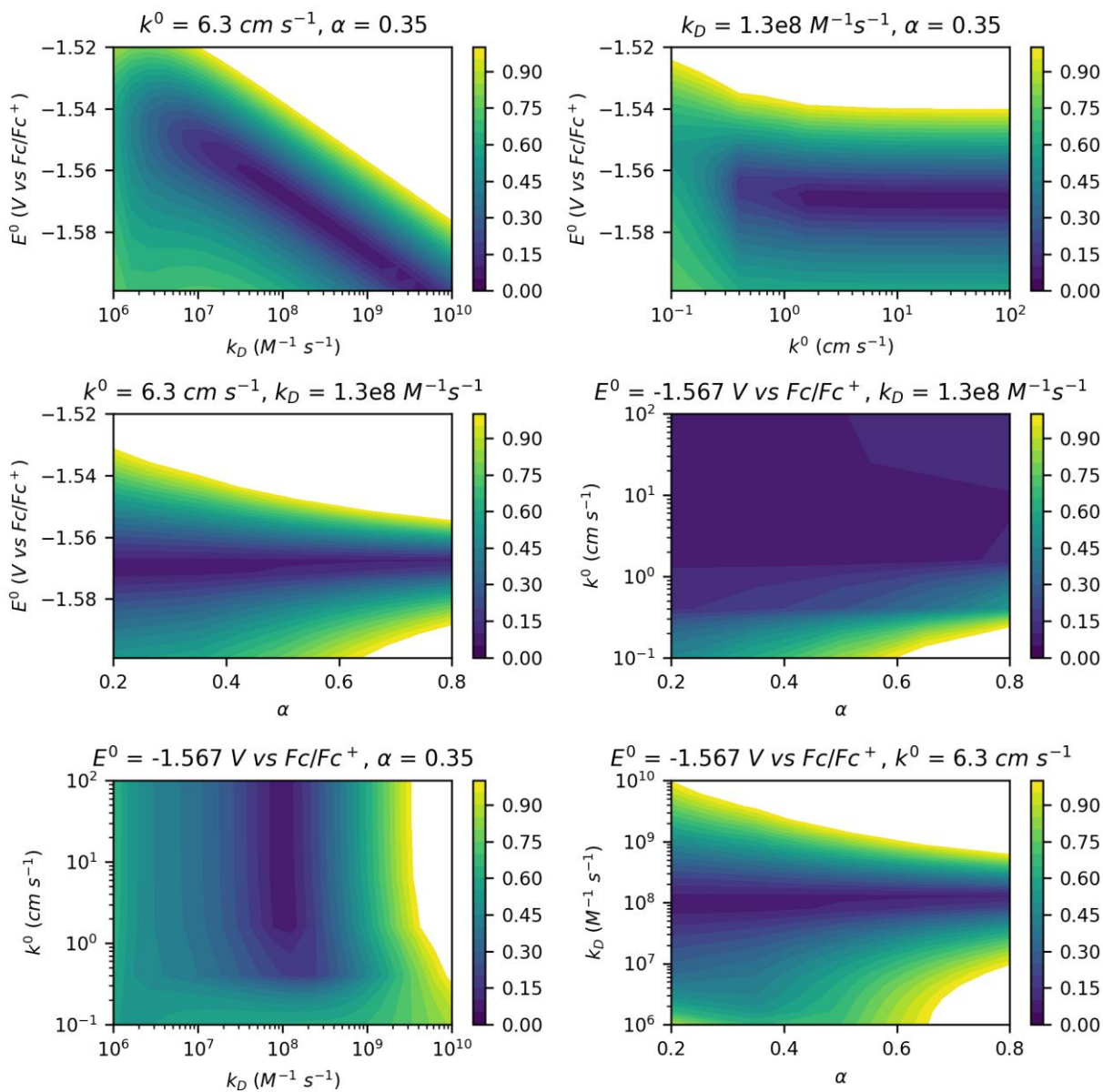


Figure 2.S28. Contour plot of error in ACV fit for 1-isopropyl nicotinamide bromide (**4-Br**).

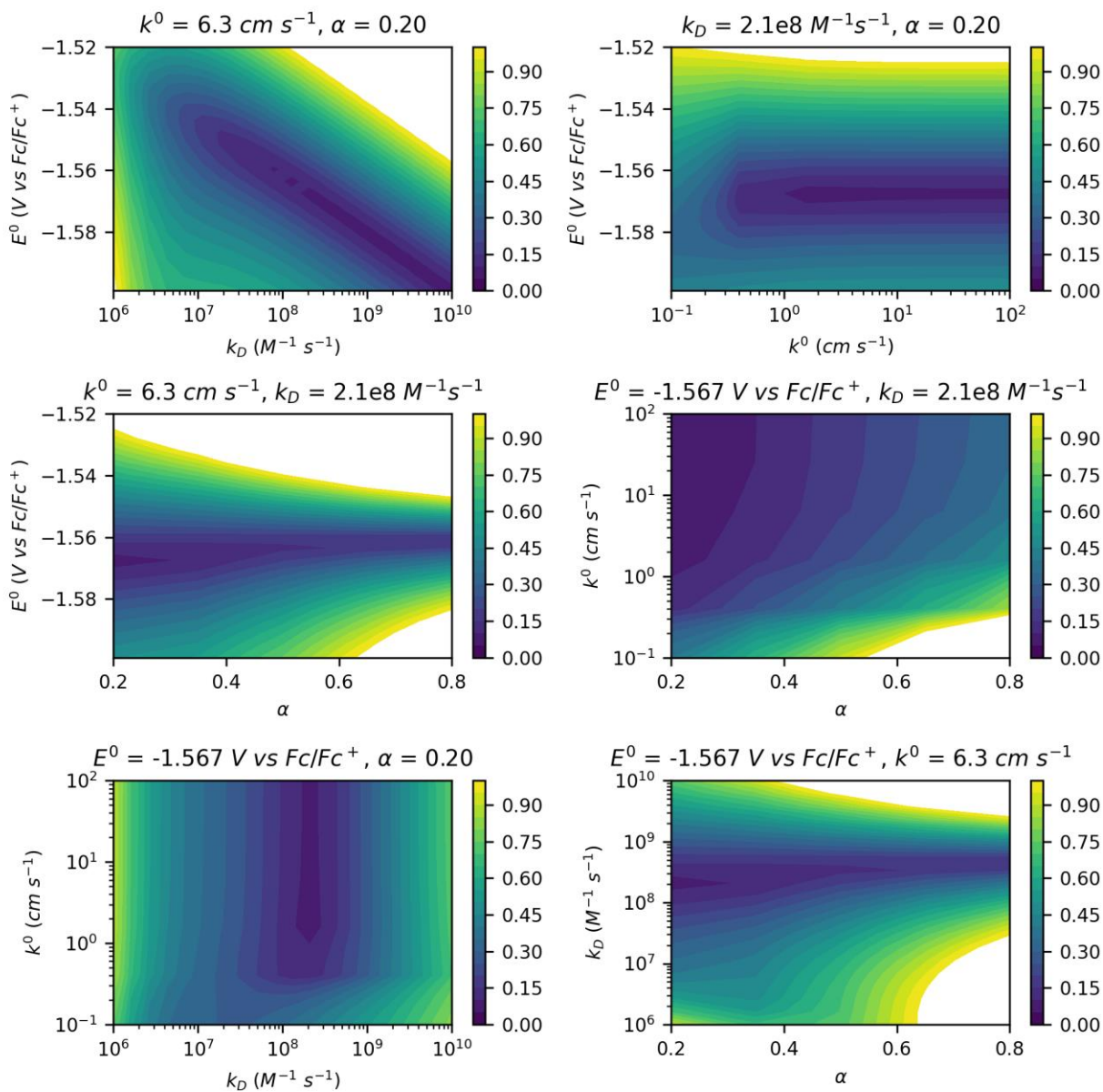


Figure 2.S29. Contour plot of error in ACV fit for 1-hexyl nicotinamide bromide (5-Br).

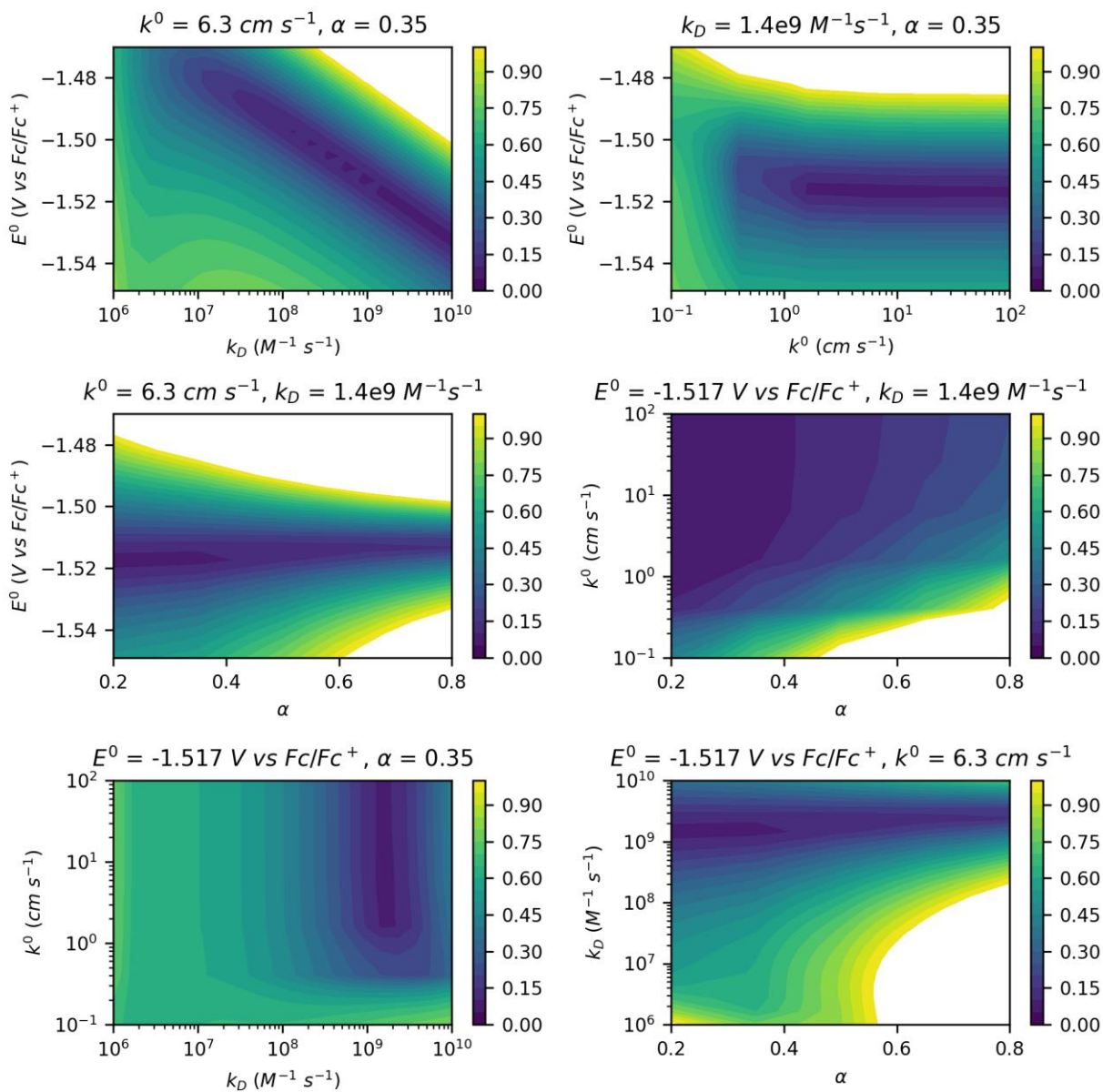


Figure 2.S30. Contour plot of error in ACV fit for 1-benzyl nicotinamide bromide (**6-Br**).

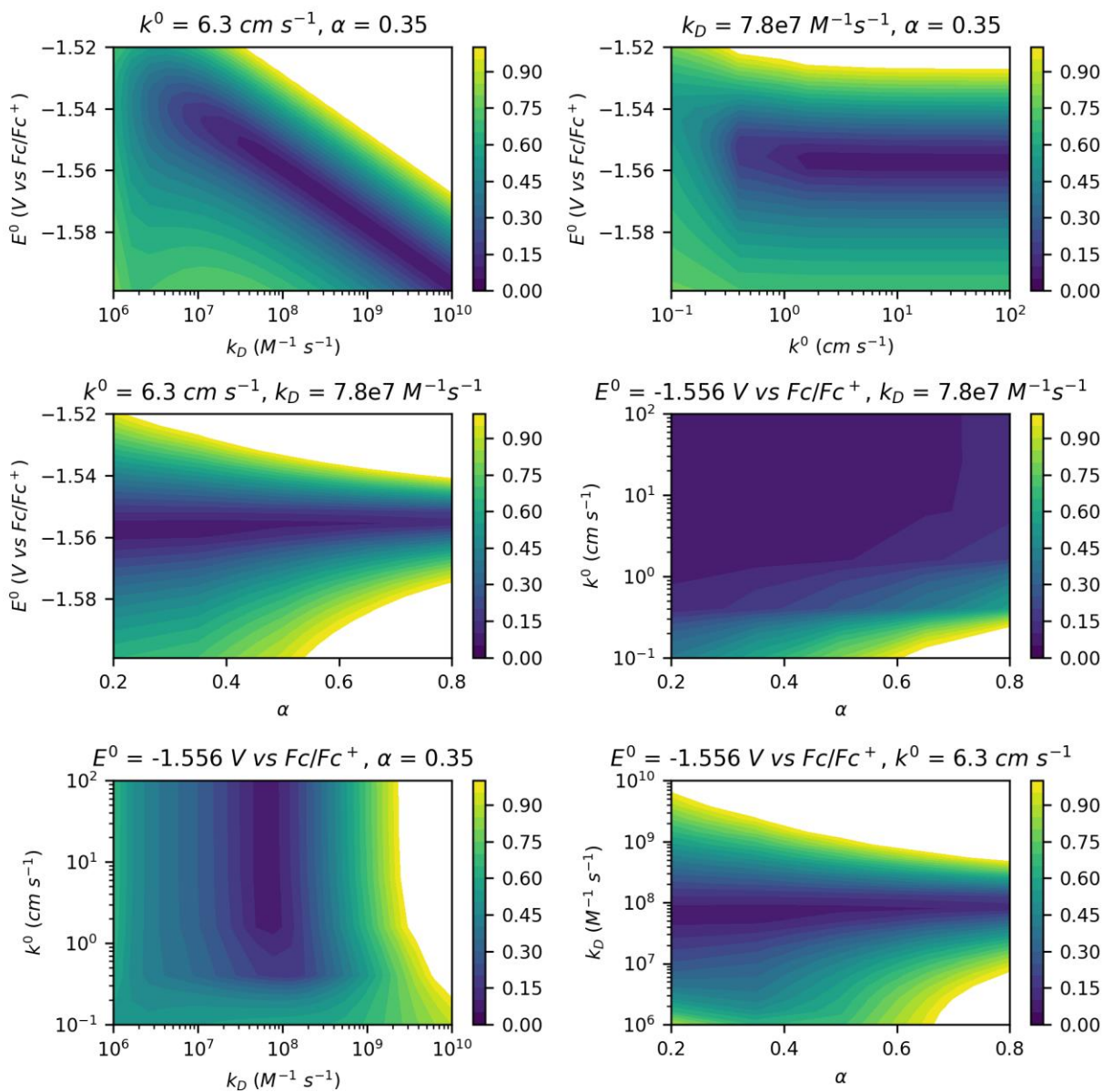


Figure 2.S31. Contour plot of error in ACV fit for 1-ethyl nicotinamide bromide (**7-Br**).

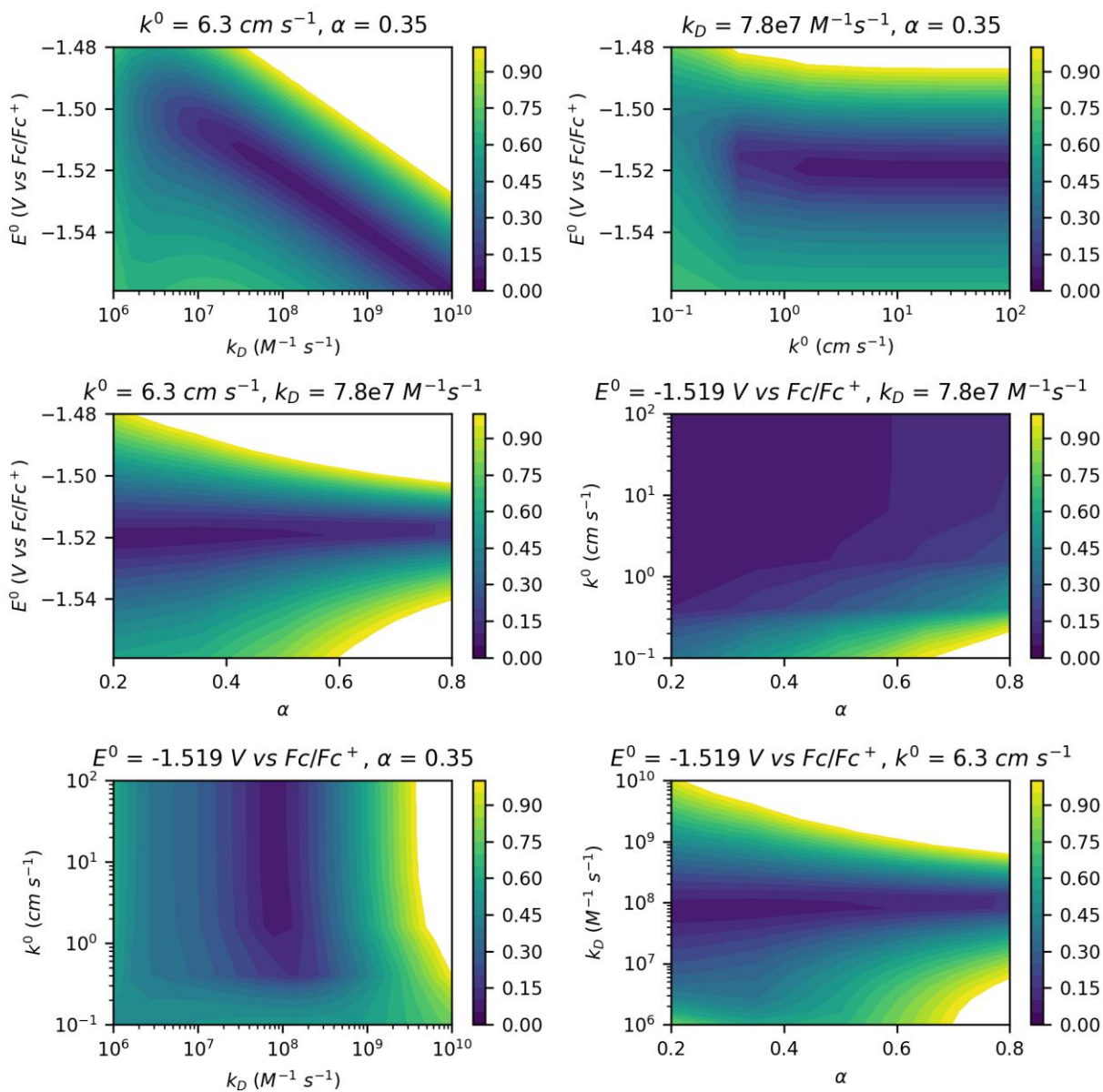


Figure 2.S32. Contour plot of error in ACV fit for 1-allyl nicotinamide chloride (1-Cl).

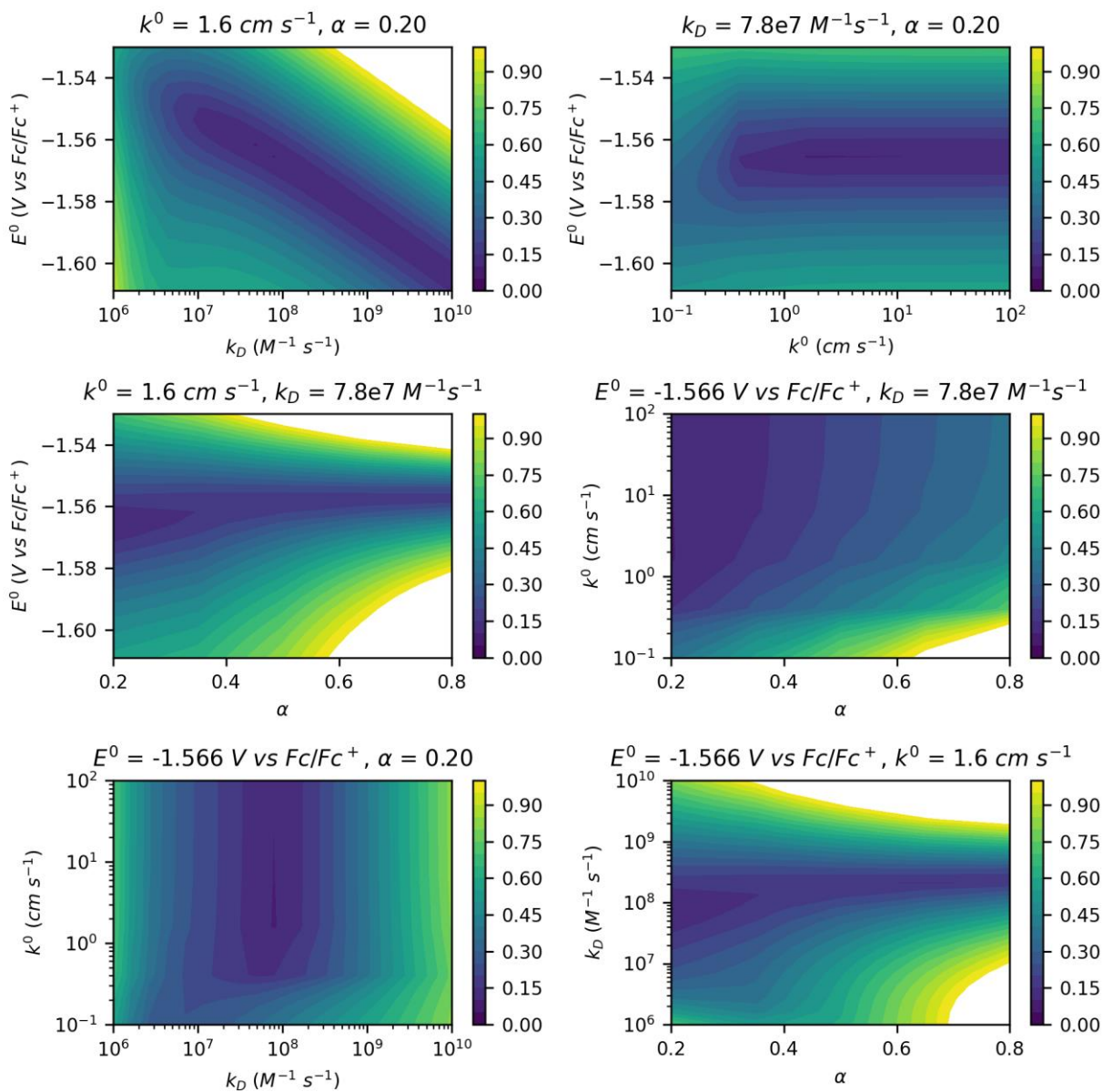


Figure 2.S33. Contour plot of error in ACV fit for 1-butyl nicotinamide chloride (**2-Cl**).

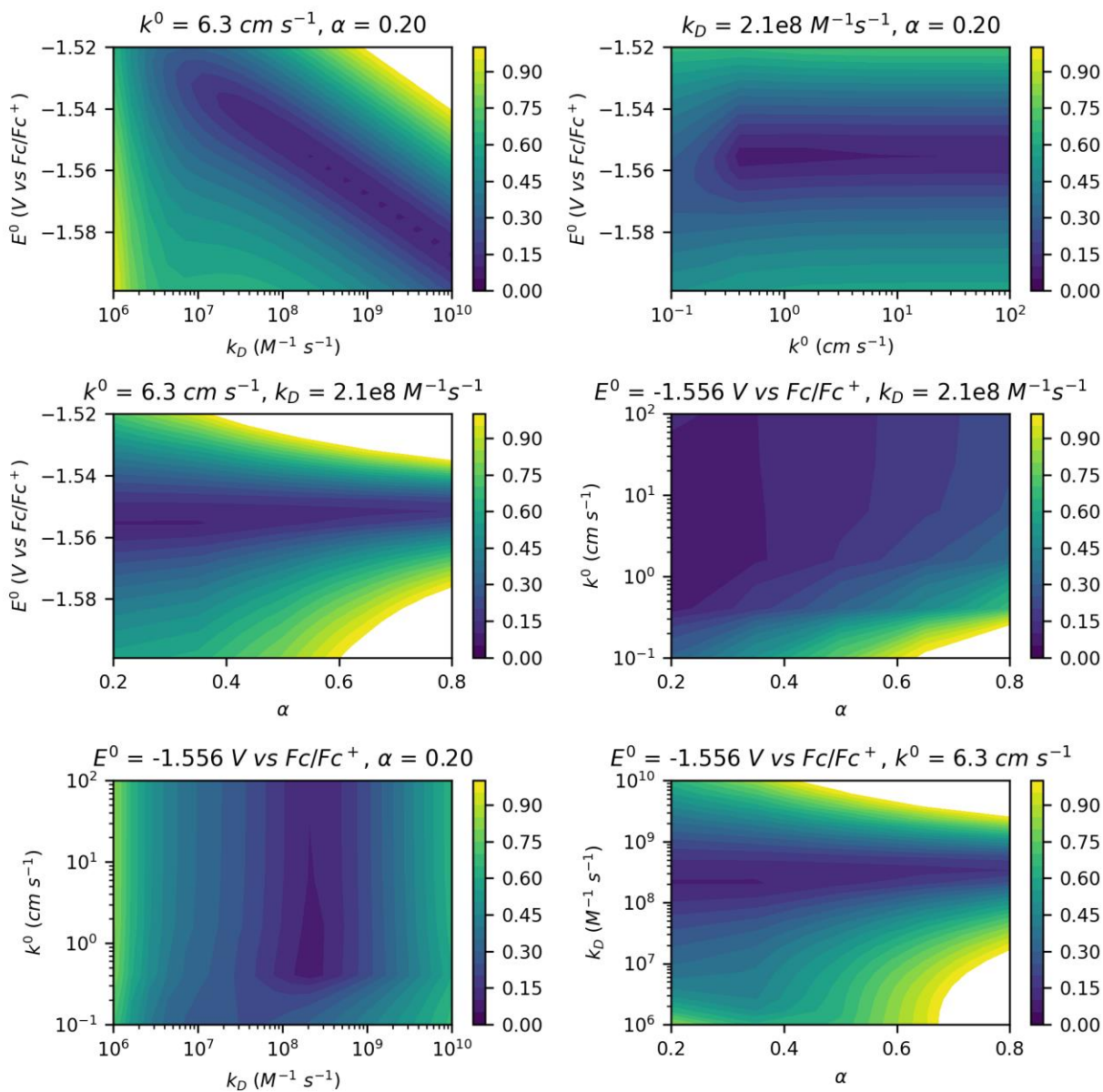


Figure 2.S34. Contour plot of error in ACV fit for 1-phenethyl nicotinamide chloride (3-Cl).

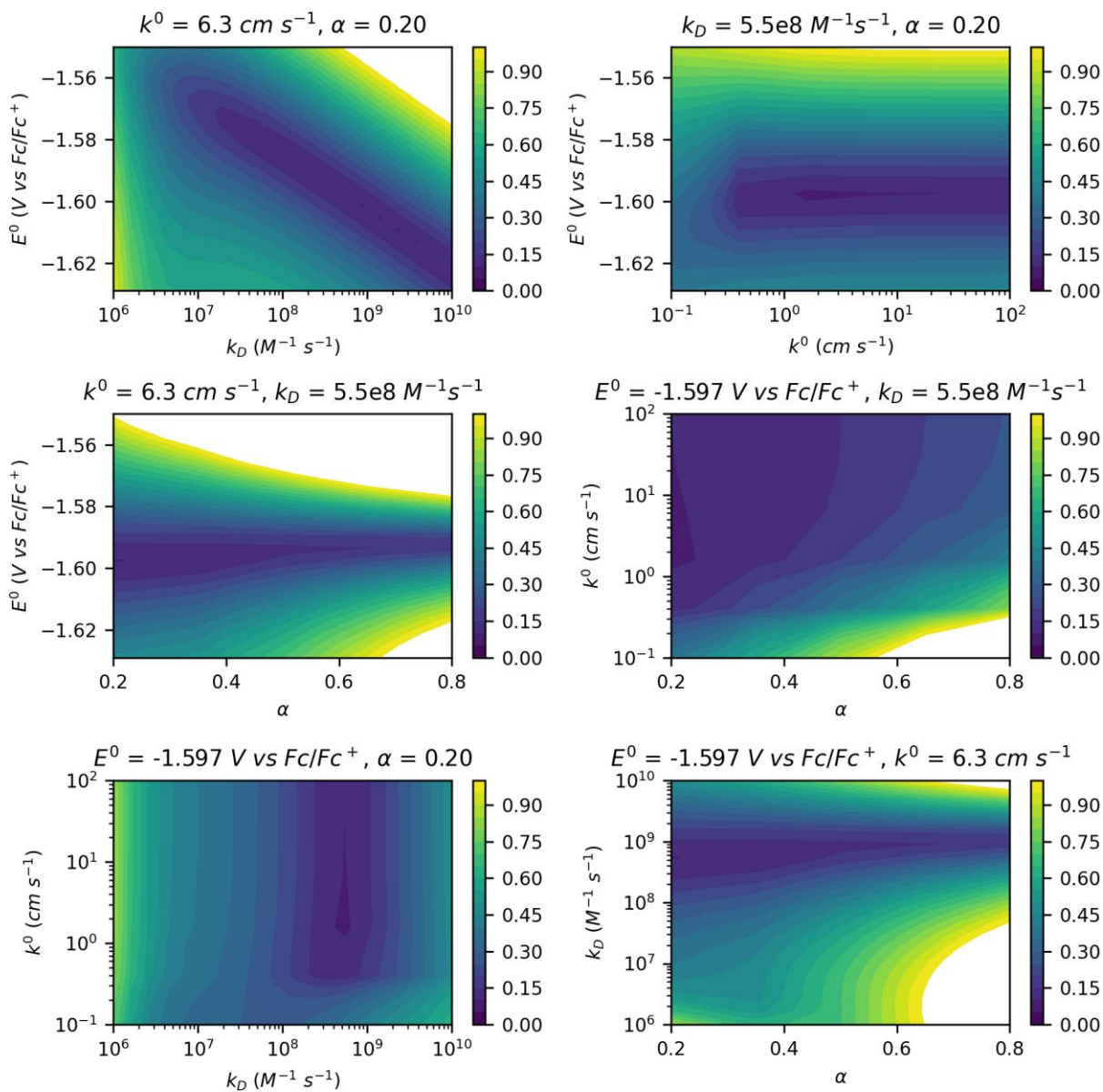


Figure 2.S35. Contour plot of error in ACV fit for 1-isopropyl nicotinamide chloride (4-Cl).

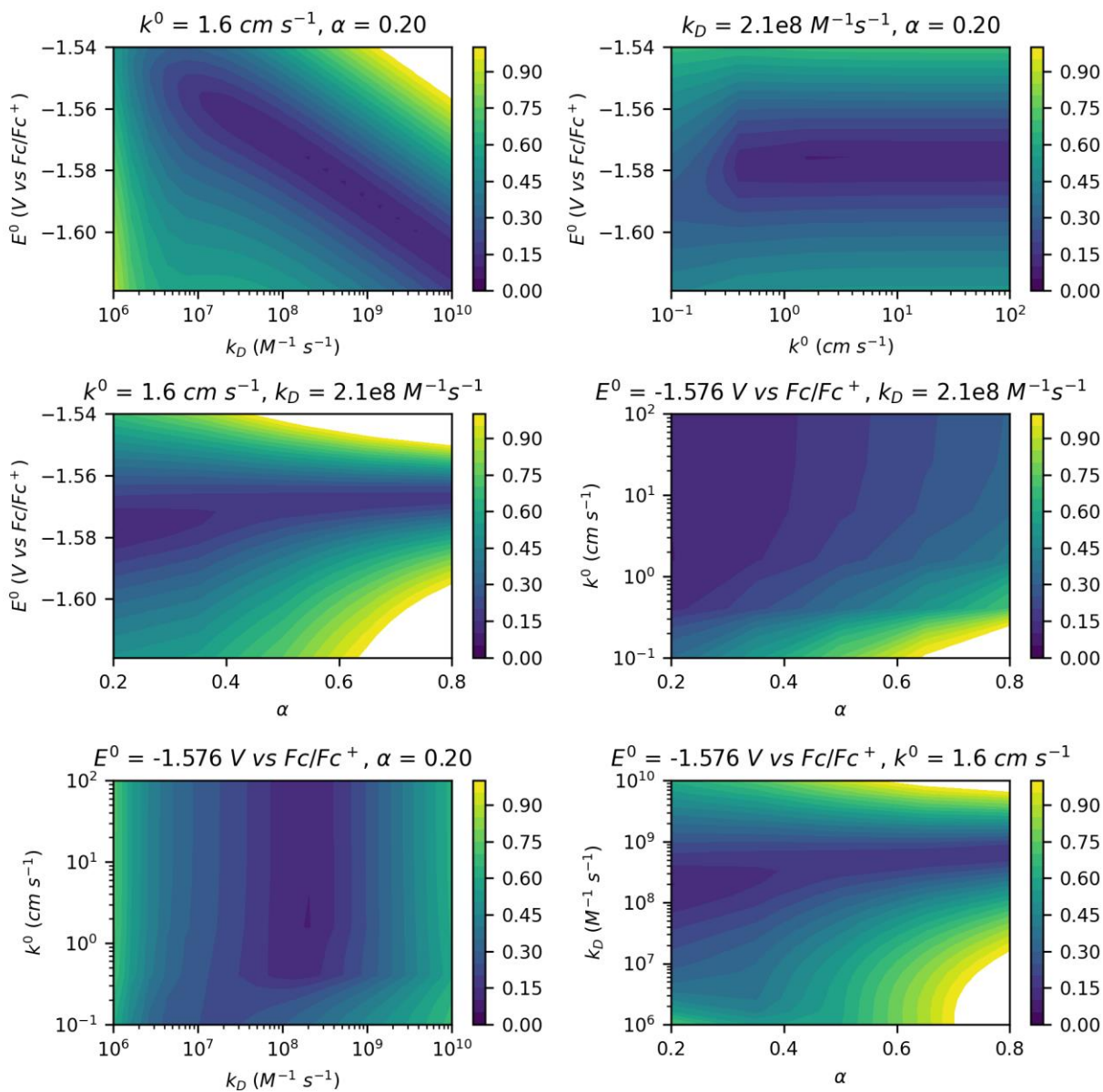


Figure 2.S36. Contour plot of error in ACV fit for 1-hexyl nicotinamide chloride (5-Cl).

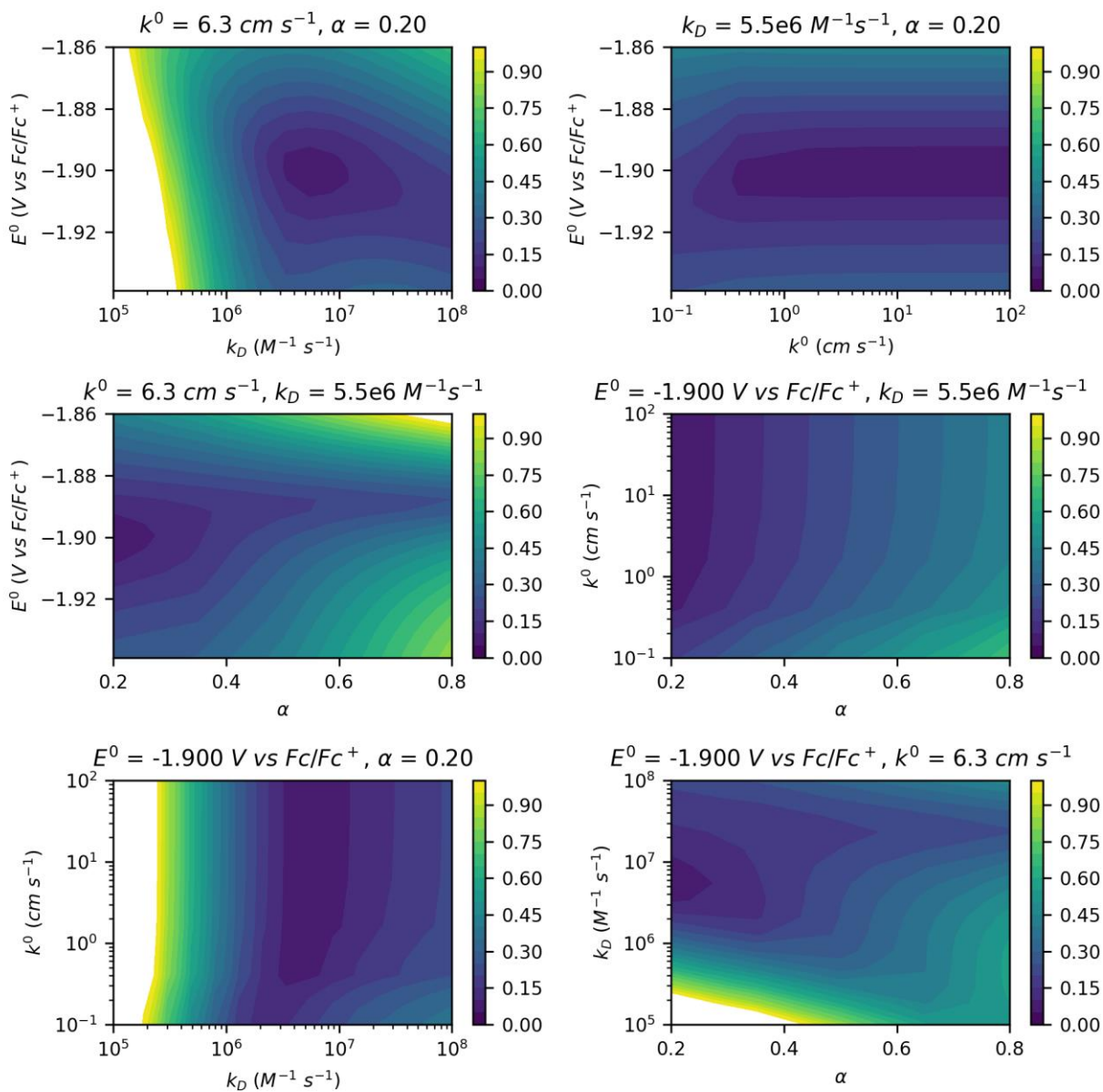


Figure 2.S37. Contour plot of error in ACV fit for 1-methyl-4-*tert*-butyl pyridinium perchlorate (MP).

OPTIMIZED MOLECULAR COORDINATES

Computations were carried out with Gaussian 16, Revision C.01. The following input was used:

```
opt freq=noraman b3lyp/6-31+g(d,p) scrf=(cpcm,solvent=acetonitrile)
pop=nbo geom=connectivity
```

The redox potential was computed as the difference between the summed electronic and thermal energies of the cationic and neutral species.

1⁺				1[·]			
Atom	X	Y	Z	Atom	X	Y	Z
C	0.232059	-0.558299	0.299642	C	0.239064	-0.534619	0.283813
C	-1.104145	1.371103	0.099148	C	-1.104215	1.452562	0.144038
C	0.004971	2.139066	-0.211525	C	0.027966	2.192119	-0.134390
C	1.260066	1.534968	-0.259329	C	1.293402	1.600035	-0.217410
C	1.377739	0.161601	-0.016706	C	1.384830	0.167688	-0.010492
H	0.245433	-1.613425	0.539723	H	0.244837	-1.596776	0.498846
H	-2.106324	1.776120	0.155532	H	-2.101983	1.861211	0.214277
H	-0.120741	3.196955	-0.405320	H	-0.088150	3.260651	-0.290650
H	2.149924	2.112877	-0.481557	H	2.184842	2.172811	-0.433885
C	2.751932	-0.467773	-0.038276	C	2.707828	-0.494439	-0.064526
O	3.734276	0.211233	0.267971	O	3.760594	0.163690	0.021405
N	2.823484	-1.772230	-0.380009	N	2.751698	-1.860316	-0.184150
H	2.058405	-2.271569	-0.809585	H	1.980066	-2.378473	-0.577013
H	3.737699	-2.203361	-0.421253	H	3.668143	-2.269861	-0.303151
N	-0.973518	0.049072	0.358099	N	-0.985239	0.062940	0.370249
C	-2.199643	-0.744193	0.720243	C	-2.189495	-0.707213	0.712643
H	-1.843164	-1.730664	1.022243	H	-1.856678	-1.691213	1.056979
H	-2.650861	-0.259817	1.588498	H	-2.693828	-0.215236	1.552702
C	-3.161076	-0.834309	-0.431228	C	-3.134913	-0.854032	-0.453762
H	-2.781739	-1.301360	-1.338163	H	-2.715764	-1.312067	-1.349230
C	-4.425734	-0.411671	-0.358961	C	-4.415864	-0.475960	-0.428336
H	-4.825250	0.052280	0.539503	H	-4.855623	-0.012841	0.452449
H	-5.104363	-0.528752	-1.198061	H	-5.067444	-0.622932	-1.284716

Table 2.S1. Optimized coordinates for the 1-allyl nicotinamide cation (**1⁺**) and neutral radical (**1[·]**) (units of Å).

2⁺				2[·]			
Atom	X	Y	Z	Atom	X	Y	Z
C	0.638301	-0.253733	0.440519	C	0.688749	-0.304692	0.412040
C	-0.094781	1.942943	0.014587	C	-0.149528	1.924312	0.112408
C	1.154757	2.294641	-0.469251	C	1.093517	2.326878	-0.335692
C	2.170288	1.341783	-0.488126	C	2.167676	1.435306	-0.427303
C	1.906674	0.040746	-0.041546	C	1.936998	0.055289	-0.043162
H	0.367131	-1.222540	0.840713	H	0.460693	-1.306676	0.757236
H	-0.922777	2.638202	0.065107	H	-1.005103	2.577260	0.211940
H	1.321556	3.306671	-0.816338	H	1.220093	3.368048	-0.617937
H	3.164156	1.590980	-0.842242	H	3.143907	1.743327	-0.776197
C	3.028016	-0.972515	-0.037471	C	3.053120	-0.913865	-0.093182
O	4.189671	-0.593963	0.126805	O	4.236247	-0.532121	-0.162545
N	2.678839	-2.266577	-0.201651	N	2.760180	-2.254315	-0.033793
H	1.763931	-2.551793	-0.519609	H	1.857112	-2.604369	-0.317511
H	3.414658	-2.960433	-0.224356	H	3.538732	-2.885812	-0.164016
N	-0.331095	0.689466	0.465082	N	-0.342374	0.582307	0.508880
C	-1.696201	0.330159	0.956437	C	-1.671093	0.150697	0.958014
H	-1.565778	-0.454799	1.702816	H	-1.541522	-0.745062	1.572467
H	-2.093586	1.213898	1.458872	H	-2.074467	0.935576	1.608040
C	-2.608992	-0.126890	-0.185406	C	-2.637872	-0.132114	-0.200137
H	-2.692895	0.676190	-0.927886	H	-2.721325	0.764168	-0.828365
H	-2.155507	-0.988523	-0.690476	H	-2.214674	-0.924459	-0.831565
C	-4.004396	-0.503193	0.333357	C	-4.029750	-0.547470	0.293705
H	-3.910140	-1.296893	1.085662	H	-3.938759	-1.439138	0.928734
H	-4.447519	0.361330	0.844109	H	-4.439369	0.246430	0.932712
C	-4.937301	-0.969395	-0.789957	C	-5.006365	-0.834762	-0.852522
H	-5.924073	-1.230808	-0.394493	H	-5.989975	-1.127833	-0.470225
H	-5.074580	-0.183959	-1.541850	H	-5.143342	0.049761	-1.485588
H	-4.534333	-1.853315	-1.297347	H	-4.639332	-1.647670	-1.489984

Table 2.S2. Optimized coordinates for the 1-butyl nicotinamide cation (**2⁺**) and neutral radical (**2[·]**) (units of Å).

3⁺				3[·]			
Atom	X	Y	Z	Atom	X	Y	Z
C	-1.753619	-0.252526	-0.302383	C	1.795531	-0.269511	0.329078
C	-1.262272	2.043435	-0.113142	C	1.235456	2.058504	0.130815
C	-2.586501	2.329521	0.176658	C	2.551443	2.345023	-0.168429
C	-3.513960	1.291401	0.216538	C	3.528527	1.342945	-0.230203
C	-3.091482	-0.024477	-0.011432	C	3.112076	-0.022166	0.019465
H	-1.356645	-1.233267	-0.530893	H	1.426865	-1.259811	0.570333
H	-0.495386	2.805273	-0.170980	H	0.450861	2.798467	0.205808
H	-2.878426	3.356603	0.356713	H	2.816767	3.381364	-0.355963
H	-4.561427	1.485055	0.417831	H	4.561951	1.559330	-0.463865
C	-4.119689	-1.132528	-0.006383	C	4.119789	-1.109040	-0.011148
O	-5.277369	-0.886439	-0.351161	O	5.336702	-0.859050	0.055023
N	-3.695564	-2.359965	0.364324	N	3.680971	-2.405110	-0.090899
H	-2.812689	-2.520780	0.827145	H	2.767918	-2.631848	-0.455491
H	-4.375848	-3.108139	0.394743	H	4.392367	-3.115618	-0.194297
N	-0.870030	0.771027	-0.353678	N	0.859750	0.724931	0.407237
C	0.568073	0.484894	-0.638387	C	-0.547840	0.410563	0.656090
H	0.597232	-0.374744	-1.309040	H	-0.593458	-0.509176	1.245665
H	0.965396	1.348561	-1.172499	H	-0.971241	1.213984	1.267230
C	2.814494	-0.064740	0.352418	C	-2.821364	-0.043562	-0.367276
C	3.744214	0.983910	0.281943	C	-3.745993	1.001075	-0.207887
C	3.256760	-1.375459	0.117520	C	-3.275357	-1.364758	-0.227004
C	5.085785	0.729264	-0.017233	C	-5.087226	0.734308	0.083336
H	3.419054	2.004291	0.469512	H	-3.414660	2.030765	-0.319666
C	4.597733	-1.633358	-0.181861	C	-4.615707	-1.636295	0.064112
H	2.550292	-2.199794	0.176386	H	-2.575265	-2.187232	-0.353374
C	5.516100	-0.580847	-0.250820	C	-5.526744	-0.586524	0.220890
H	5.793471	1.551963	-0.062622	H	-5.788088	1.556480	0.197729
H	4.924432	-2.654491	-0.355829	H	-4.948106	-2.665784	0.163707
H	6.558802	-0.780272	-0.479837	H	-6.569029	-0.795653	0.443619
C	1.356274	0.215631	0.656764	C	-1.363335	0.248514	-0.647387
H	0.909163	-0.637139	1.177907	H	-0.921494	-0.563354	-1.235861
H	1.269228	1.086224	1.315038	H	-1.269585	1.167291	-1.236833

Table 2.S3. Optimized coordinates for the 1-phenethyl nicotinamide cation (**3⁺**) and neutral radical (**3[·]**) (units of Å).

4⁺				4[·]			
Atom	X	Y	Z	Atom	X	Y	Z
C	0.159026	-0.560977	0.059910	C	-0.003971	-0.358722	-0.073099
C	-1.149350	1.377025	-0.179723	C	-1.044014	1.789479	-0.280584
C	-0.014125	2.164355	-0.277299	C	0.196340	2.392782	-0.239730
C	1.240471	1.564941	-0.192041	C	1.375727	1.646980	-0.121609
C	1.332178	0.177155	-0.036697	C	1.251127	0.204659	-0.047717
H	0.149065	-1.631608	0.218290	H	-0.153167	-1.424917	0.037359
H	-2.146558	1.792221	-0.229654	H	-1.977093	2.326192	-0.380009
H	-0.121968	3.233323	-0.412005	H	0.236563	3.476278	-0.305297
H	2.147642	2.156005	-0.245602	H	2.351799	2.110997	-0.082639
C	2.698848	-0.456164	0.085594	C	2.465473	-0.627697	0.107176
O	3.621932	0.183756	0.593883	O	3.539726	-0.135458	0.498287
N	2.826425	-1.723592	-0.362986	N	2.375821	-1.969831	-0.165590
H	2.133641	-2.171856	-0.944693	H	1.664879	-2.330989	-0.784093
H	3.738749	-2.157620	-0.311503	H	3.240988	-2.491524	-0.131184
N	-1.050639	0.038945	-0.006296	N	-1.144480	0.381765	-0.205494
C	-2.305534	-0.801711	0.126248	C	-2.488623	-0.232109	-0.060437
H	-1.931043	-1.819102	0.249697	H	-3.177931	0.520388	-0.454547
C	-3.129008	-0.727047	-1.160308	C	-2.823413	-0.474405	1.418266
H	-3.956895	-1.436413	-1.079427	H	-3.851920	-0.836264	1.515222
H	-3.557096	0.267203	-1.317893	H	-2.155507	-1.226535	1.852544
H	-2.528225	-0.997953	-2.032365	H	-2.727899	0.449570	1.996700
C	-3.078963	-0.399502	1.382962	C	-2.643555	-1.495322	-0.913921
H	-3.909997	-1.097727	1.513431	H	-3.691634	-1.808056	-0.897674
H	-2.445324	-0.449532	2.272418	H	-2.357091	-1.306907	-1.952847
H	-3.499212	0.607099	1.301340	H	-2.049722	-2.331970	-0.532327

Table 2.S4. Optimized coordinates for the 1-isopropyl nicotinamide cation (**4⁺**) and neutral radical (**4[·]**) (units of Å).

5⁺				5[•]			
Atom	X	Y	Z	Atom	X	Y	Z
C	-1.644042	-0.211066	0.487205	C	-1.700290	-0.247378	0.493693
C	-1.140534	2.054306	0.086968	C	-1.088451	2.050906	0.171632
C	-2.378422	2.252715	-0.502636	C	-2.301345	2.282619	-0.447267
C	-3.263078	1.181822	-0.604474	C	-3.248026	1.266345	-0.616416
C	-2.899411	-0.068578	-0.088736	C	-2.926996	-0.050788	-0.099145
H	-1.274652	-1.150652	0.877878	H	-1.374849	-1.216760	0.853903
H	-0.406384	2.842843	0.192809	H	-0.330317	2.804041	0.334388
H	-2.635294	3.236472	-0.875304	H	-2.507705	3.288148	-0.802351
H	-4.233010	1.300820	-1.073819	H	-4.196356	1.438733	-1.106955
C	-3.861184	-1.225335	-0.233988	C	-3.895136	-1.156768	-0.261853
O	-4.622329	-1.262677	-1.203124	O	-4.829711	-1.080466	-1.081052
N	-3.815663	-2.183218	0.716950	N	-3.725606	-2.292549	0.491411
H	-3.340605	-2.060637	1.599401	H	-3.228305	-2.267371	1.369215
H	-4.468730	-2.952696	0.647154	H	-4.456668	-2.986956	0.418455
N	-0.791934	0.836684	0.562546	N	-0.786977	0.754028	0.643600
C	0.575657	0.633583	1.130384	C	0.555505	0.475940	1.167600
H	0.491230	-0.147223	1.887927	H	0.485411	-0.403814	1.814021
C	1.591507	0.260546	0.046847	C	1.601290	0.249386	0.067048
H	1.274448	-0.667531	-0.444019	H	1.290963	-0.605795	-0.547587
H	1.606000	1.043783	-0.720726	H	1.622762	1.124992	-0.594410
C	2.997942	0.085576	0.637030	C	3.001945	-0.001193	0.640413
H	3.300698	1.015316	1.137760	H	3.298776	0.855361	1.262262
H	2.975168	-0.693830	1.410759	H	2.971189	-0.873052	1.309400
C	4.041767	-0.282342	-0.426181	C	4.064479	-0.231780	-0.442530
H	3.736939	-1.211944	-0.927492	H	3.767120	-1.087507	-1.065778
H	4.058567	0.496369	-1.201929	H	4.094746	0.640424	-1.111496
C	5.454948	-0.456161	0.145722	C	5.468979	-0.483115	0.122029
H	5.757553	0.472767	0.648329	H	5.764880	0.371074	0.746720
H	5.437368	-1.233979	0.921443	H	5.438750	-1.355507	0.789437
C	6.494559	-0.821577	-0.920139	C	6.525767	-0.709468	-0.965449
H	7.491328	-0.938228	-0.481023	H	7.515488	-0.886292	-0.530179
H	6.236343	-1.764238	-1.417335	H	6.274243	-1.577833	-1.586216
H	6.558595	-0.045412	-1.692146	H	6.603314	0.160899	-1.628112
H	0.848004	1.564226	1.630832	H	0.846009	1.322358	1.800093

Table 2.S5. Optimized coordinates for the 1-hexyl nicotinamide cation (**5⁺**) and neutral radical (**5[•]**) (units of Å).

6⁺				6[·]			
Atom	X	Y	Z	Atom	X	Y	Z
C	1.428573	-0.384023	0.557620	C	1.347367	-0.221053	0.614040
C	0.089555	1.453276	-0.051018	C	0.197562	1.766057	-0.093972
C	1.156706	2.047939	-0.703128	C	1.322977	2.163328	-0.788519
C	2.393229	1.406436	-0.714191	C	2.486706	1.386898	-0.812510
C	2.530458	0.161799	-0.088593	C	2.478688	0.133758	-0.083666
H	1.467040	-1.322602	1.095309	H	1.294674	-1.115741	1.223173
H	-0.894454	1.900702	-0.005934	H	-0.724390	2.327769	-0.048721
H	1.011601	3.004622	-1.189263	H	1.283247	3.107521	-1.323830
H	3.251233	1.854218	-1.202696	H	3.372670	1.692298	-1.352387
C	3.884136	-0.509870	-0.084871	C	3.698160	-0.705161	-0.059209
O	4.904788	0.181475	-0.087027	O	4.807691	-0.237408	-0.373580
N	3.895179	-1.860031	-0.059255	N	3.584049	-2.011278	0.344714
H	3.076878	-2.418855	-0.252853	H	2.705707	-2.504231	0.282100
H	4.791268	-2.329165	-0.079815	H	4.417642	-2.577915	0.268274
N	0.240565	0.261330	0.570595	N	0.220240	0.549248	0.624472
C	-0.915500	-0.329006	1.344376	C	-0.953242	0.176282	1.424106
H	-0.615240	-1.345565	1.598718	H	-0.675600	-0.700010	2.015943
H	-0.994387	0.248998	2.267435	H	-1.169608	0.989635	2.126425
C	-2.212378	-0.315631	0.572532	C	-2.187610	-0.120087	0.588058
C	-2.412564	-1.205934	-0.494439	C	-2.167558	-1.129481	-0.387018
C	-3.237587	0.570166	0.931520	C	-3.372518	0.595995	0.798331
C	-3.617730	-1.200042	-1.197858	C	-3.310820	-1.415053	-1.135897
H	-1.628763	-1.905422	-0.772524	H	-1.255281	-1.693557	-0.562593
C	-4.447072	0.571937	0.229085	C	-4.521409	0.309568	0.051702
H	-3.095164	1.255132	1.763140	H	-3.399171	1.381589	1.549379
C	-4.636844	-0.310415	-0.837232	C	-4.492497	-0.695957	-0.917597
H	-3.764948	-1.892681	-2.020827	H	-3.281934	-2.199544	-1.886583
H	-5.236014	1.260091	0.516439	H	-5.432695	0.874244	0.225986
H	-5.575455	-0.310159	-1.383122	H	-5.381653	-0.919157	-1.499922

Table 2.S6. Optimized coordinates for the 1-benzyl nicotinamide cation (**6⁺**) and neutral radical (**6[·]**) (units of Å).

7⁺				7[·]			
Atom	X	Y	Z	Atom	X	Y	Z
C	-0.176155	-0.509762	0.310932	C	0.128983	-0.537975	-0.273347
C	-1.480618	1.430839	0.033915	C	1.512773	1.415074	-0.100499
C	-0.354747	2.174422	-0.281443	C	0.391998	2.180850	0.157425
C	0.891075	1.552378	-0.289427	C	-0.887493	1.618758	0.210917
C	0.984429	0.184288	-0.003892	C	-1.008891	0.188508	-0.003415
H	-0.184445	-1.558092	0.581184	H	0.104872	-1.600178	-0.488036
H	-2.475211	1.856344	0.068681	H	2.519044	1.804494	-0.163174
H	-0.462620	3.227978	-0.506915	H	0.529522	3.246181	0.318293
H	1.793061	2.111156	-0.511675	H	-1.769526	2.211427	0.411833
C	2.349230	-0.464836	0.017081	C	-2.345535	-0.442659	0.019697
O	3.335275	0.204675	0.332240	O	-3.382604	0.240756	-0.069274
N	2.406977	-1.775994	-0.300820	N	-2.424607	-1.810992	0.114360
H	1.642400	-2.269168	-0.738353	H	-1.675910	-2.350166	0.523596
H	3.314447	-2.222824	-0.315444	H	-3.353625	-2.194218	0.224016
N	-1.375459	0.115401	0.329855	N	1.366089	0.030249	-0.336627
C	-2.610140	-0.672214	0.640994	C	2.561730	-0.784517	-0.589907
H	-2.317972	-1.444706	1.352985	H	2.240394	-1.693220	-1.105240
H	-3.297270	0.009650	1.143027	H	3.202249	-0.227146	-1.281721
C	-3.226442	-1.269752	-0.620550	C	3.328717	-1.134435	0.688130
H	-3.518734	-0.489395	-1.328429	H	3.659132	-0.232111	1.211839
H	-2.534280	-1.956989	-1.114884	H	2.705642	-1.722356	1.369489
H	-4.121998	-1.829387	-0.336992	H	4.214974	-1.725174	0.435161

Table 2.S7. Optimized coordinates for the 1-ethyl nicotinamide cation (**7⁺**) and neutral radical (**7[·]**) (units of Å).

COMPUTED REDUCTION POTENTIALS

The potentials computed from Gaussian were uniformly lowered until all were within the ranges of lowest error from ACV experiments. Compound **3** was used as the reference for both X = Br and X = Cl, as once the reduction potential for Compound **3** was in this range all of the remaining reduction potentials were also in the range of lowest error. The dimerization rate constants that give the lowest error at these potentials are also reported in the table.

mNAD ⁺	R =	Comp. <i>E</i> ⁰ (V)	X = Br			X = Cl		
			ACV Upper Limit <i>E</i> ⁰ (V vs Fc/Fc ⁺)	Corrected <i>E</i> ⁰ (V vs Fc/Fc ⁺)	Best-Fit <i>k_D</i> (M ⁻¹ s ⁻¹)	ACV Upper Limit <i>E</i> ⁰ (V vs Fc/Fc ⁺)	Corrected <i>E</i> ⁰ (V vs Fc/Fc ⁺)	Best-Fit <i>k_D</i> (M ⁻¹ s ⁻¹)
1	allyl	3.484	-1.510	-1.515	1.0E+08	-1.511	-1.538	7.5E+08
2	butyl	3.435	-1.542	-1.564	3.8E+08	-1.561	-1.587	1.6E+09
3	phenethyl	3.465	-1.534	-1.534	8.2E+07	-1.557	-1.557	2.9E+08
4	isopropyl	3.407	-1.559	-1.591	1.7E+09	-1.594	-1.614	4.3E+09
5	hexyl	3.408	-1.566	-1.591	4.2E+09	-1.575	-1.614	2.3E+10
6	benzyl	3.494	-1.517	-1.505	3.5E+08	-	-	-
7	ethyl	3.431	-1.548	-1.567	2.6E+08	-	-	-

Table 2.S8. Computed reduction potentials and corresponding best-fit *k_D* values for all twelve mNAD⁺X⁻.

LINEAR REGRESSION DATA

Once the reduction potentials were found, they were used along with Sterimol B5 parameters to predict the dimerization rate constants. The datasets were normalized by first subtracting the average of the dataset from each point, then dividing each point by the standard deviation of the dataset. The equation used to predict the normalized $\log_{10}(k_D)$ was:

$$0.4564 * B5_{norm} - 0.7492 * E_{norm}^0 = \log_{10}(k_D)_{norm}$$

mNAD ⁺	R =	X =	Calculated			Normalized			Predicted $\log_{10}(k_D)$	
			$\log_{10}(k_D)$	E^0	B5	$\log_{10}(k_D)$	E^0	B5	Normalized	Full
1	allyl	Br	8.0	-1.515	4.090	-1.219	1.374	-0.049	-1.051	8.1
2	butyl	Br	8.6	-1.564	4.600	-0.448	0.020	0.331	0.137	9.0
3	phenethyl	Br	7.9	-1.534	2.314	-1.363	0.846	-1.374	-1.261	8.0
4	isopropyl	Br	9.2	-1.591	3.290	0.440	-0.729	-0.646	0.251	9.1
5	hexyl	Br	9.6	-1.591	5.990	0.990	-0.714	1.368	1.159	9.7
6	benzyl	Br	8.6	-1.505	6.040	-0.489	1.646	1.406	-0.592	8.5
7	ethyl	Br	8.4	-1.567	3.260	-0.675	-0.072	-0.668	-0.251	8.7
1	allyl	Cl	8.9	-1.538	4.090	-0.042	0.740	-0.049	-0.577	8.5
2	butyl	Cl	9.2	-1.587	4.600	0.399	-0.614	0.331	0.611	9.3
3	phenethyl	Cl	8.5	-1.557	2.314	-0.606	0.213	-1.374	-0.786	8.3
4	isopropyl	Cl	9.6	-1.614	3.290	0.997	-1.362	-0.646	0.726	9.4
5	hexyl	Cl	10.4	-1.614	5.990	2.016	-1.347	1.368	1.634	10.1

Table 2.S9. Computed and normalized values of E^0 and B5 used to predict $\log_{10}(k_D)$.

APPENDIX FOR CHAPTER 3

CONVOLUTION VOLTAMMETRY

Convolution Voltammetry, also called semiintegral electroanalysis, combines Faraday's law and Fick's second law to describe the concentration of a redox-active material at the electrode surface. One particular advantage of the technique is that it is signal-independent; that is, regardless of the shape of the current function, convolution voltammetry will describe the concentration (on the timescale of cyclic voltammetry). The principles of convolution voltammetry have been known since at least the 1950s,^{78,45} although its relevance for cyclic voltammetry was better recognized in the early 1970s.^{46,79,80} To help the reader understand the essence of convolution voltammetry, two derivations will be provided below. The first is heuristic, and the second is more rigorous, invoking Laplace techniques. Both describe the equation $ox + ne^- \rightarrow red$.

Heuristic Derivation

We start with Faraday's law:

$$\frac{-I}{nFAD} = \frac{\partial}{\partial x} c_{ox}$$

where I is the faradaic current ($I < 0$ for reduction), n is the number of electrons transferred ($n > 0$ for reduction), F is Faraday's constant, A is the electrode surface area, D is the diffusion coefficient of the substrate, and c_{ox} is the concentration of the oxidized substrate. We also write Fick's second law:

$$D \frac{\partial^2}{\partial x^2} c_{ox} = \frac{\partial}{\partial t} c_{ox}$$

The key transformation is to observe that, if $D \frac{\partial^2}{\partial x^2}$ and $\frac{\partial}{\partial t}$ are equivalent operators, they are equivalent at any power. That is, if an operation returns $D \frac{\partial^2}{\partial x^2}$ when performed twice, it would also return $\frac{\partial}{\partial t}$ when performed twice. We can write:

$$\sqrt{D} \frac{\partial}{\partial x} c_{ox} = \pm \frac{\partial^{1/2}}{\partial t^{1/2}} c_{ox}$$

where $\frac{\partial^{1/2}}{\partial t^{1/2}}$ is the semiderivative with respect to time. Plugging this result into Faraday's law above, we find:

$$\frac{-I}{nFA\sqrt{D}} = \pm \frac{\partial^{1/2}}{\partial t^{1/2}} c_{ox}$$

Taking the semiintegral of both sides affords the expression:

$$c_{ox} - c^0 = \mp \frac{\partial^{-1/2}}{\partial t^{-1/2}} \frac{I}{nFA\sqrt{D}}$$

where c^0 is the initial bulk concentration of the substrate. Because the expression being semiintegrated is always negative (I and n have opposite signs), and because $c^0 \geq c_{ox}$, we find that the plus sign is needed. Thus, the concentration is given by:

$$c_{ox} = c^0 + \frac{\partial^{-1/2}}{\partial t^{-1/2}} \frac{I}{nFA\sqrt{D}}$$

Reference ⁴⁶ provides a thorough explanation of how to find derivatives/integrals of any order.

Formal Derivation

We first define the deviation variable $C = c_{ox} - c^0$. Taking the Laplace transform of Fick's second law converts the equation from a partial differential equation to an ordinary differential equation:

$$D \frac{\partial^2}{\partial x^2} \bar{C} = s\bar{C}$$

where an overbar denotes a function in Laplace space. This differential equation has the solution:

$$\bar{C} = a_1 e^{x\sqrt{s/D}} + a_2 e^{-x\sqrt{s/D}}$$

where a_1 and a_2 are unknown constants. Observing that the concentration is finite at large x , we must have $a_1 = 0$, and so

$$\bar{C} = a_2 e^{-x\sqrt{s/D}}$$

If we plug this expression into Faraday's law, we find:

$$\frac{-\bar{I}}{nFAD} = -\sqrt{\frac{s}{D}} \bar{C}$$

which upon rearrangement yields:

$$\bar{C} = \frac{\bar{I}}{nFA\sqrt{Ds}}$$

According to the convolution theorem, the inverse Laplace transform of the product of two functions in Laplace space, equals the convolution of the two functions in the time domain. As the inverse transform of $\frac{1}{\sqrt{s}}$ is $\frac{1}{\sqrt{\pi t}}$, we have:

$$c_{ox} = c^0 + \frac{1}{nFA\sqrt{D}} \int_0^t \frac{I(t-\tau)}{\sqrt{\pi\tau}} d\tau$$

One of the benefits of the convolution technique is that the integral may be adapted to more complicated electrochemical systems. For example, if, upon reduction, the species c_{red} decayed by a first-order reaction (with rate constant k), we should add a chemical reaction term to Fick's second law, namely:

$$\frac{\partial}{\partial t} c_{red} = D \frac{\partial^2}{\partial x^2} c_{red} - k c_{red}$$

After the same transformations as above, we find the following expression for the concentration in the Laplace domain:

$$\bar{c}_{red} = \frac{-\bar{I}}{nFA\sqrt{D}(s+k)}$$

observing that $\frac{I}{nFAD} = \frac{\partial}{\partial x} c_{red}$. Upon returning from Laplace space, the concentration of the reduced intermediate is described by the following convolution integral:

$$c_{red} = \frac{-1}{nFA\sqrt{D}} \int_0^t \frac{I(t-\tau)e^{-k\tau}}{\sqrt{\pi\tau}} d\tau$$

Electrochemical systems with pre- or post- equilibria may be treated in an analogous way.

NMR SPECTRA

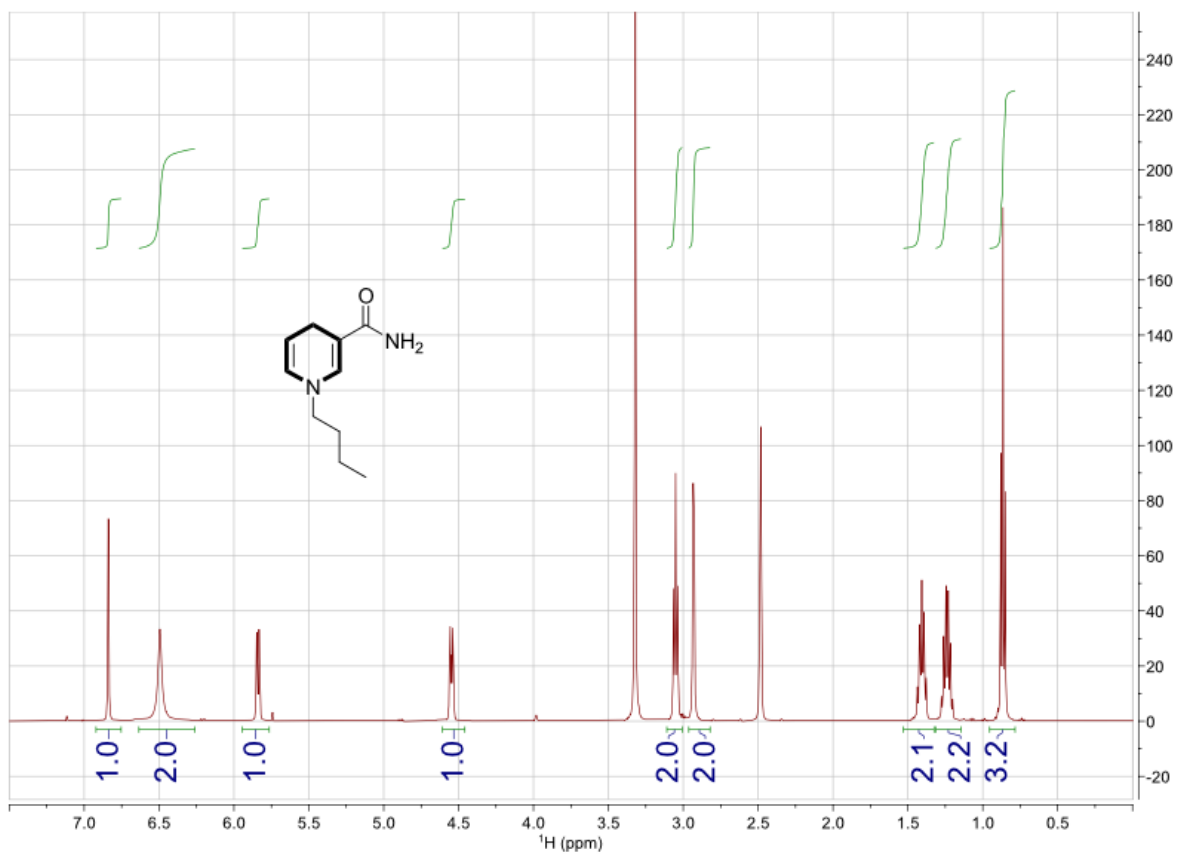


Figure 3.S1: ¹H-NMR spectrum for 1-*n*-butyl-1,4-dihydro nicotinamide.

¹H NMR (500 MHz, dmsO) δ 6.84 (d, $J = 1.5$ Hz, 1H), 6.49 (s, 1H), 5.84 (dd, $J = 8.0, 1.6$ Hz, 1H), 4.55 (dt, $J = 8.1, 3.4$ Hz, 1H), 3.05 (t, $J = 7.0$ Hz, 2H), 2.93 (d, $J = 2.0$ Hz, 2H), 1.41 (p, $J = 7.5$ Hz, 2H), 1.24 (h, $J = 7.4$ Hz, 2H), 0.87 (t, $J = 7.4$ Hz, 3H).

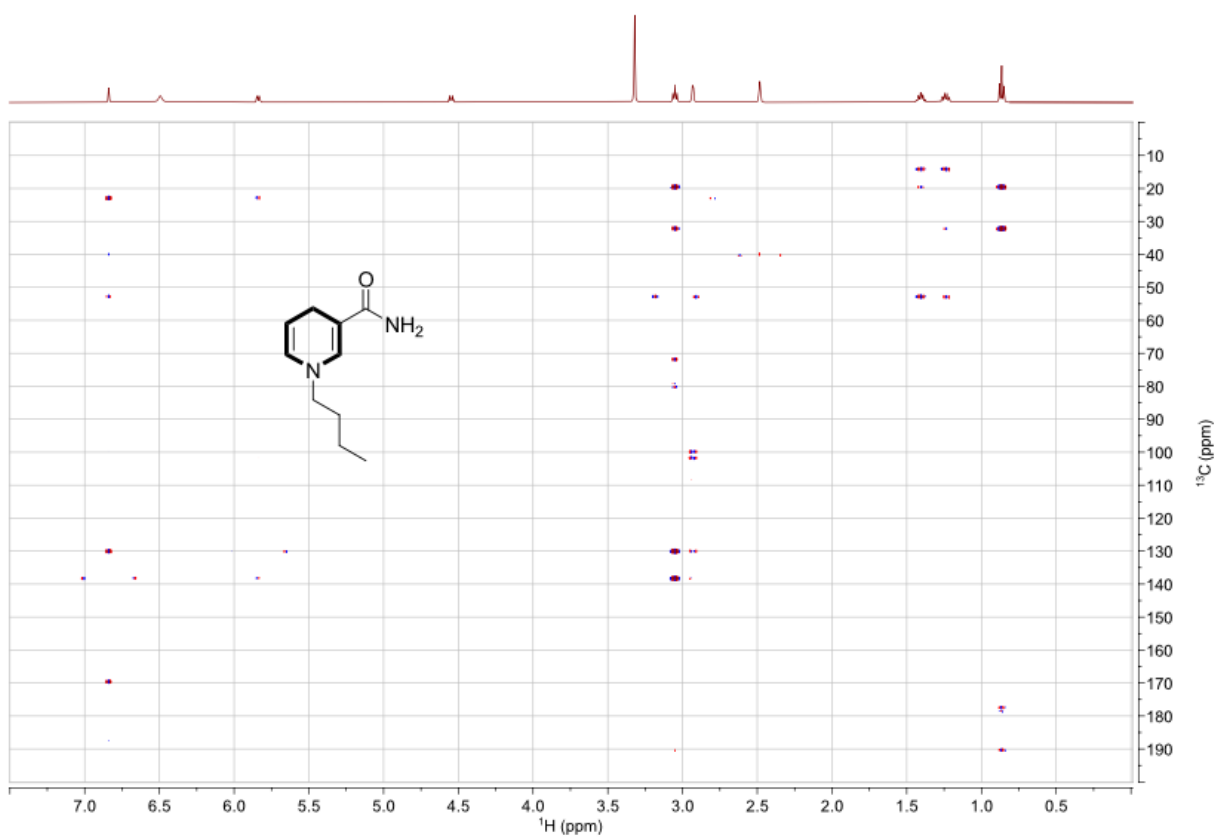


Figure 3.S2: HMBC spectrum for 1-*n*-butyl-1,4-dihydro nicotinamide.

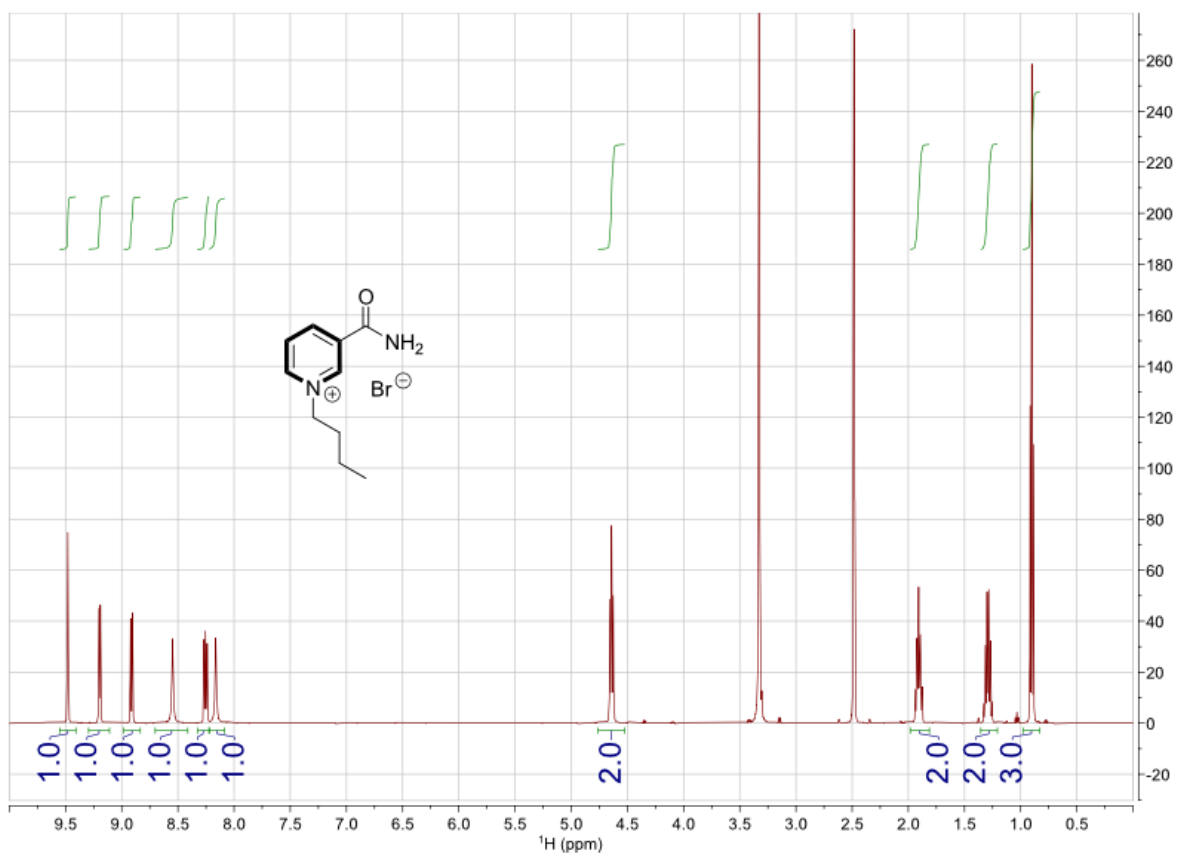


Figure 3.S3: ¹H-NMR spectrum for 1-*n*-butyl nicotinamide bromide.

¹H NMR (500 MHz, dms_o) δ 9.48 (t, $J = 1.5$ Hz, 1H), 9.20 (d, $J = 6.0$ Hz, 1H), 8.91 (d, $J = 8.3$ Hz, 1H), 8.55 (s, 1H), 8.25 (dd, $J = 8.1, 6.1$ Hz, 1H), 8.16 (s, 1H), 4.64 (t, $J = 7.5$ Hz, 2H), 1.91 (p, $J = 7.5$ Hz, 2H), 1.29 (h, $J = 7.4$ Hz, 2H), 0.90 (t, $J = 7.4$ Hz, 3H).

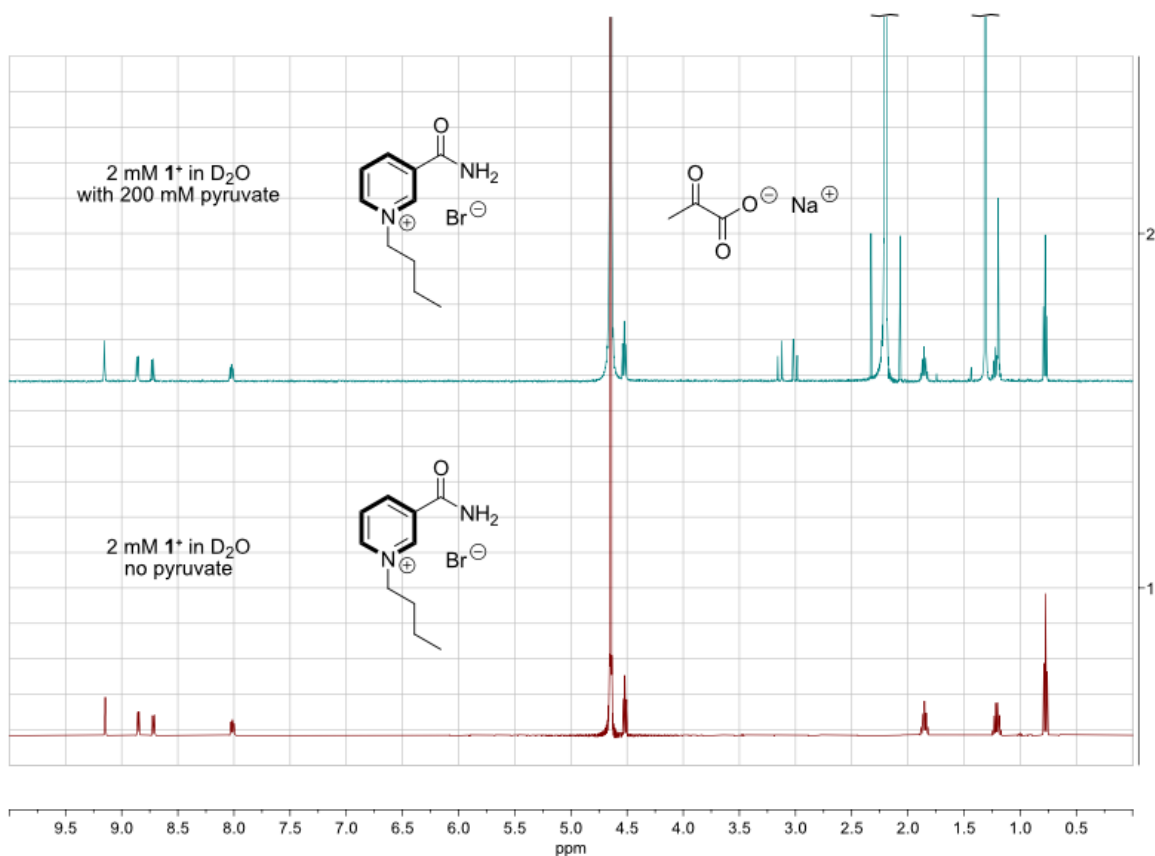


Figure 3.S4: ¹H-NMR spectrum for 1-*n*-butyl nicotinamide bromide in D₂O, with and without 200 mM sodium pyruvate.

¹H NMR (500 MHz, D₂O) δ 9.15 (s, 1H), 8.85 (dd, *J* = 6.0, 1.5 Hz, 2H), 8.72 (dt, *J* = 8.2, 1.6 Hz, 1H), 8.01 (dd, *J* = 8.1, 6.1 Hz, 2H), 4.52 (t, *J* = 7.5 Hz, 4H), 1.85 (p, *J* = 7.6 Hz, 4H), 1.21 (h, *J* = 7.4 Hz, 4H), 0.77 (t, *J* = 7.4 Hz, 5H).

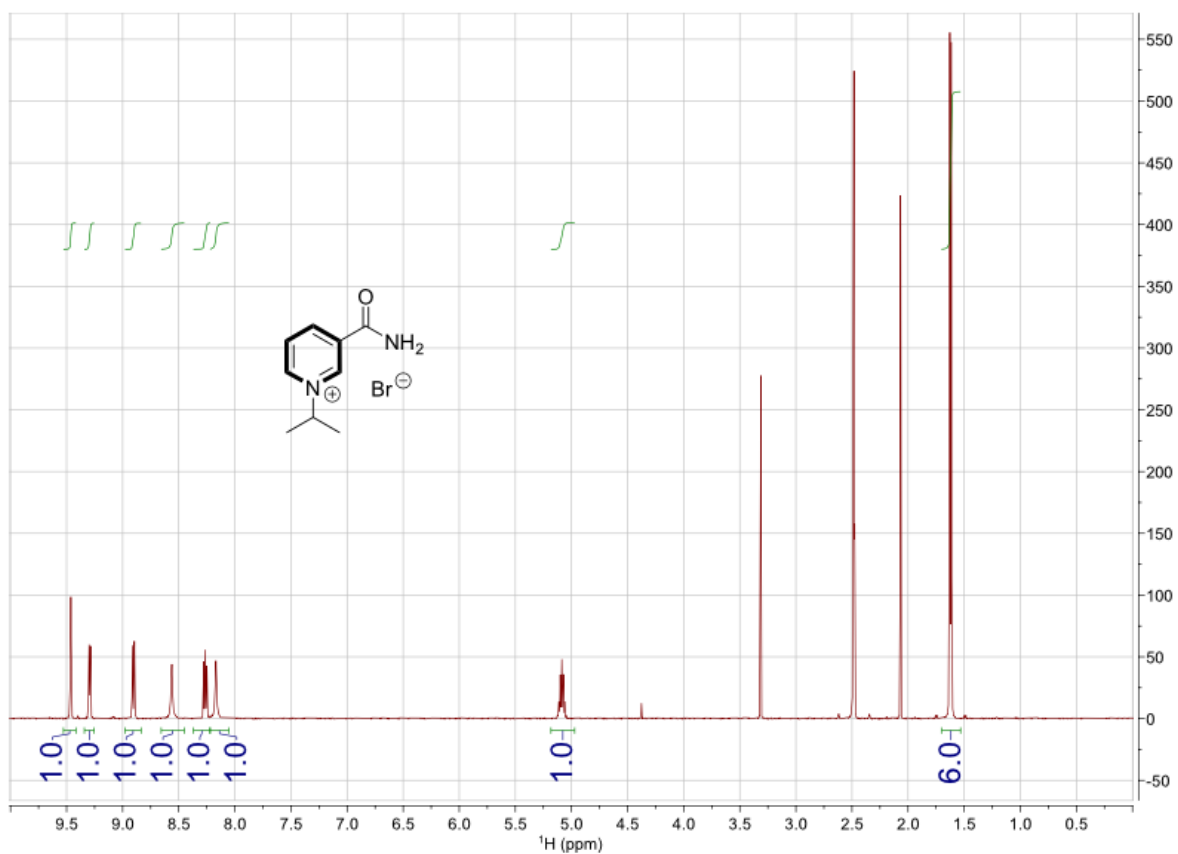


Figure 3.S5: ¹H-NMR spectrum for 1-*iso*-propyl nicotinamide bromide.
¹H NMR (500 MHz, dms_o) δ 9.46 (t, *J* = 1.6 Hz, 1H), 9.29 (d, *J* = 5.8 Hz, 1H), 8.90 (dt, *J* = 8.1, 1.4 Hz, 1H), 8.56 (s, 1H), 8.26 (dd, *J* = 8.0, 6.1 Hz, 1H), 8.17 (s, 1H), 5.08 (hept, *J* = 6.7 Hz, 1H), 1.62 (d, *J* = 6.7 Hz, 6H).

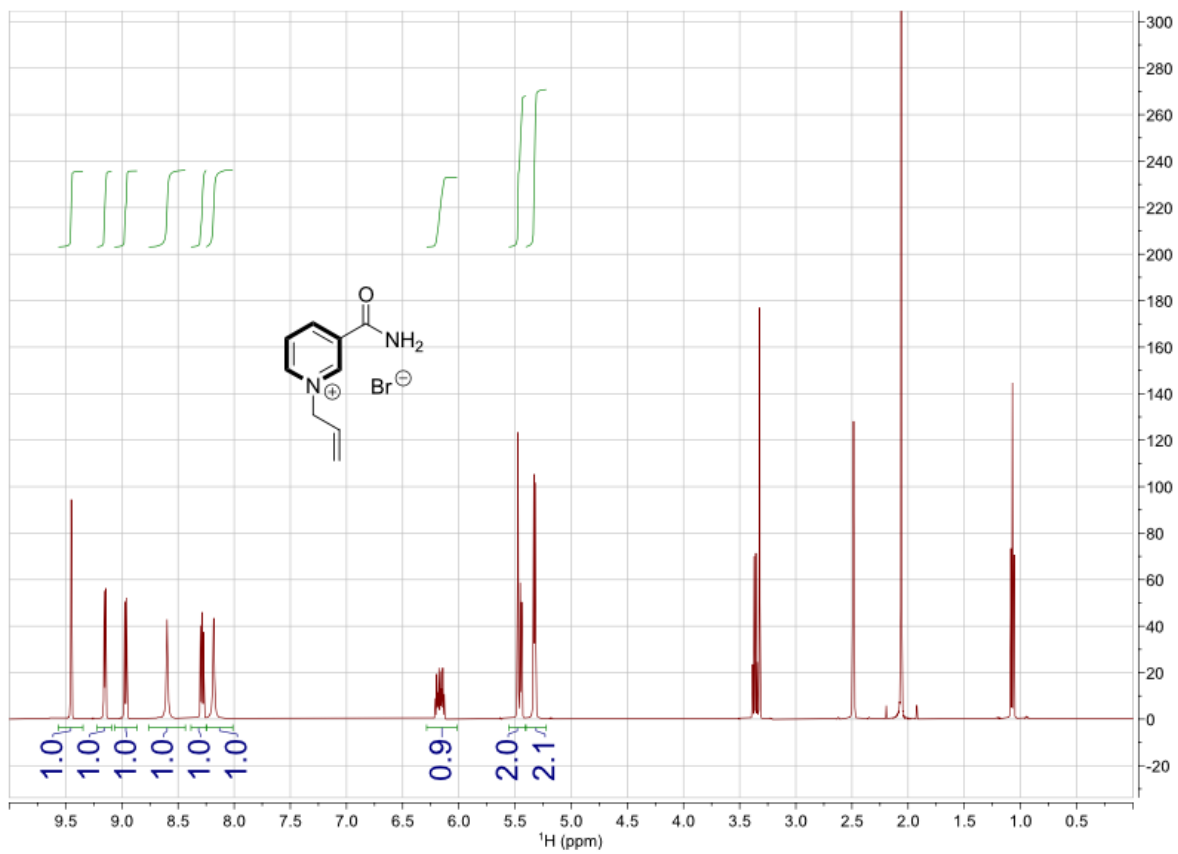


Figure 3.S6: ^1H -NMR spectrum for 1-allyl nicotinamide bromide.

^1H NMR (500 MHz, dmsO) δ 9.45 (t, $J = 1.6$ Hz, 1H), 9.15 (d, $J = 5.6$ Hz, 1H), 8.97 (dt, $J = 8.0$, 1.3 Hz, 1H), 8.60 (s, 1H), 8.29 (dd, $J = 8.1$, 6.1 Hz, 1H), 8.18 (s, 1H), 6.22 – 6.12 (m, 1H), 5.47 (s, 1H), 5.45 (dt, $J = 6.4$, 1.0 Hz, 1H), 5.33 (d, $J = 6.3$ Hz, 2H).

APPENDIX FOR CHAPTER 4

Experimental:

Electrochemistry measurements were taken on a Biologic VSP potentiostat, with a 2 mm boron doped diamond working electrode, Pt wire counter electrode, and SCE reference electrode. All samples were purged with nitrogen before scanning. Unless otherwise noted, cyclic voltammetry (CV) scans were taken at 800 mV s^{-1} , and alternating current voltammetry (ACV) scans were taken at 100 mV s^{-1} with an alternating potential of 8 mV amplitude and 20 Hz frequency.

Bulk electrolysis experiments were run with a BK Precision 9110 power supply. Unless otherwise noted, the following conditions were constant for all electrolyses: anode chamber: 1 mL sat. aq. NaHCO_3 , 4.95 mL H_2O , 50 μL sat. aq. NaI , Pt mesh electrode; cathode chamber: 1 mL sat. aq. NaHCO_3 , 1 mL sat. aq. NaCl , 4 mL H_2O , boron doped diamond plate electrode, and substrate. For the three electrolyses, the substrates were (A) 1-ethyl nicotinamide bromide (14.2 mg, 0.061 mmol, 10 mM), (B) N,N-dimethylpyruvamide (13.9 mg, 0.12 mmol, 20 mM), and (C) a combination of these two substrates (14.2 mg and 13.9 mg, respectively). The two chambers were separated with a dialysis membrane that had been soaked in brine (sat. aq. NaCl). After preparing the solutions, the cathode chamber was purged with nitrogen for 5-10 minutes, the cell was blocked from sunlight, and the power source was switched on. The electrolyses were run at constant potential (-3.50 V vs counter electrode) for two hours under nitrogen, at which point 1 mL of CDCl_3 was added to the cathode chamber to extract the products. The CDCl_3 was removed and dried through a plug of Na_2SO_4 directly into an NMR tube, and the extracts were characterized with ^1H , COSY, HSQC, HMBC, and ^{13}C NMR. For the electrolyses monitored by a flow NMR setup, electrolysis (D) was identical to electrolysis (C) except the concentration of **DMP** was 50 mM, and electrolysis (E) was identical to electrolysis (C) except the H_2O was replaced with D_2O .

NMR spectra were gathered on an Agilent 500 MHz or on Bruker Avance 500 MHz or 600 MHz NMR machines.



Figure 4.S1. Bulk Electrolysis setup.

Synthesis:

1-Butyl nicotinamide bromide:

Prepared according the method described in Chapter 3.

1-Ethyl nicotinamide bromide:

Prepared according the method described in Chapter 3.

Diacetyltartaric anhydride:

Adapted from a previous procedure.⁸⁶ Tartaric acid (7.51 g, 50.0 mmol) and acetic anhydride (16.85 g, 165 mmol, 3.3 eq) were added to a 125 mL Erlenmeyer flask. Sulfuric acid (0.25 g, 5 mol%) was added, and then a stir bar was added to the mixture. The mixture was heated to a gentle boil with mixing (the tartaric acid will dissolve once the mixture has warmed above room temperature). After boiling for 1 hr, the clear brown fluid was allowed to cool to room temperature, during which a solid mass crystallized from solution. The precipitate was vacuum filtered and

rinsed with diethyl ether to afford the title product as fluffy whitish crystals (9.71g, 90%). ¹H NMR (500 MHz, cdcl₃) δ 5.69 (s, 2H), 2.25 (s, 6H).

Pyridinium oxomaleic anhydride:

Modified from a previous procedure.⁸⁷ Glacial acetic acid (2.60 g, 43 mmol) was added to diacetyltartaric anhydride (1.08 g, 5 mmol) in a 50 mL round bottom flask to create a slurry. Pyridine (1.215 mL, 15 mmol) was added, and the flask was immediately stoppered and swirled gently by hand while being heated in a 60 °C water bath. Once a deep clear red-orange color had developed (3-5 minutes), the flask was removed from the heat and the stopper removed, and 30 mL of a 4:1 v/v Et₂O/THF solution was added. The flask was immediately stoppered again and immersed in an ice bath. Once an orange precipitate had separated from a clear orange solution, the solution was decanted, and the precipitate was rinsed with 4:1 v/v Et₂O/THF (1 x 10 mL) and with Et₂O (1 x 10 mL). The solid was dried under vacuum and collected as a buff-colored powder (635 mg, 3.3 mmol, 66%). ¹H NMR (500 MHz, dmsO) δ 8.78 (dt, *J* = 6.3, 1.7 Hz, 2H), 8.26 (tdd, *J* = 7.7, 4.2, 1.8 Hz, 1 H), 7.79 (ddq, *J* = 7.9, 4.6, 1.5 Hz, 2H), 4.90 (s, 1H).

Note: Pyridinium oxomaleic anhydride should be used immediately upon preparation. It decomposes within days at room temperature.

Note: The acetic acid buffers the reactivity of the pyridine, allowing the reaction rate to be controlled by the temperature.

Note: An alternative synthesis that produces good crystals at a slight cost in yield is as follows: Diacetyltartaric anhydride (1.08 g, 5 mmol) was dissolved in 2.25 g THF (filtered immediately beforehand through a plug of silica gel) in a 20 mL scintillation vial. Then, pyridine (1.62 mL, 20 mmol) was added, and the vial was capped and shaken 2-3x over the course of 4 minutes, during which time a clear deep green color developed. The cap was removed shortly before 4 minutes, and at 4 minutes exactly, acetic acid (0.575 mL, 10 mmol) was added. The vial was capped and shaken again, and allowed to stand until orange needlelike crystals had stopped growing in solution (the fluid slowly turns dark red during crystal growth, which may take anywhere from 30 minutes to three hours). After this time, the fluid was removed from the crystals with a glass pipette, and the crystals were washed with 3:1 v/v Et₂O/THF mixture (3 x 1 mL), and then with Et₂O (3 x 1 mL). The crystals were finally dried under vacuum to afford the title product (45-55% yield). ¹H NMR (500 MHz, cdcl₃) δ 7.64 (s, 2H), 2.25 (s, 6H).

Pyruvanilide:

Adapted from a previous procedure.⁸⁶ Aniline (0.30 mL, 3.3 mmol) was added to pyridinium oxomaleic anhydride (99 mg, 0.51 mmol) in a scintillation vial. The contents of the vial became warm and released CO₂ as the powder dissolved. When bubbling had stopped (~5 minutes), the contents were diluted with Et₂O and EtOAc, and the organic layer was washed with 3 M HCl. The aqueous layer was extracted 3x with EtOAc, and the combined organic layers were concentrated *in vacuo* and purified with a silica column (10% → 15% EtOAc/hexanes). The desired fractions (R_f = 0.35 in 15% EtOAc/hexanes) were concentrated *in vacuo* to an ivory-colored crystalline solid (35 mg, 43%). ¹H NMR (500 MHz, cdcl₃) δ 7.64 (dd, *J* = 8.4, 1.1 Hz, 2H), 7.38 (m, 2H), 7.19 (dt, *J* = 7.5, 1.1 Hz, 1H), 2.58 (s, 3H).

Pyruvanilide-4-carboxylic acid:

Pyridinium oxomaleic anhydride (445 mg, 2.3 mmol) and *p*-aminobenzoic acid (315 mg, 2.3 mmol) were dissolved in acetonitrile (6 mL) with THF (2 mL) in a 20 mL scintillation vial containing a stir bar. The contents were mixed overnight at 70 °C, and then the solvent was removed *in vacuo* to give a solid orange residue. The residue was combined with EtOAc (20 mL) in a separatory funnel and washed with HCl (10 mL of 3 M solution). The organic layer was collected, dried through a MgSO₄ plug, and concentrated *in vacuo* to afford an orange powder.* The crude powder was purified with column chromatography (20% → 50% EtOAc/hexanes) and dried under vacuum to afford the title product as a fluffy white powder (92 mg, 19%).

*Note: Another extract was performed here, where the crude powder was dissolved in 15 mL hot acetonitrile, and then added to a separatory funnel with EtOAc (20 mL), Et₂O (20 mL), and HCl (20 mL of 3 M solution). After extracting, the organic layer was dried through a MgSO₄ plug and concentrated *in vacuo* to afford an ivory-colored powder. The ¹H NMR spectra before and after this second extraction were nearly identical, however.

¹H NMR (500 MHz, dmsO) δ 12.73 (s, 1H), 10.63 (s, 1H), 7.86 (m, 4H), 2.37 (s, 3H).

N,N-Dimethylpyruvamide:

Pyridinium oxomaleic anhydride (193 mg, 1 mmol) was dissolved in acetonitrile (10 mL) in a 50 mL round bottom flask. Dimethylamine (0.7 mL of a 2.0 M solution in THF, 1.4 mmol) was added, and the solution was stoppered, swirled gently, and left to stand overnight at room temperature. The following day, 0.3 g silica gel was added to the clear yellowish solution, and the contents of the flask were concentrated on a rotovap to give a well-behaved orange powder. A silica column

was prepared (silica gel loaded as a slurry in 10% EtOAc/hexanes), the top of the column was covered with a small amount of sand, and the orange powder from the flask was charged on top in an even layer, and then covered with more sand. The column was eluted with 10% → 100% EtOAc/hexanes, and the product collected in fractions 3-5 ($R_f = 0.21$ in 33% EtOAc/hexanes). The target fractions were concentrated *in vacuo* to afford the title product as a pale yellowish oil (55 mg, 48%). $^1\text{H NMR}$ (500 MHz, cdCl_3) δ 3.03 (s, 3H), 2.99 (s, 3H), 2.43 (s, 3H).

NMR SPECTRA

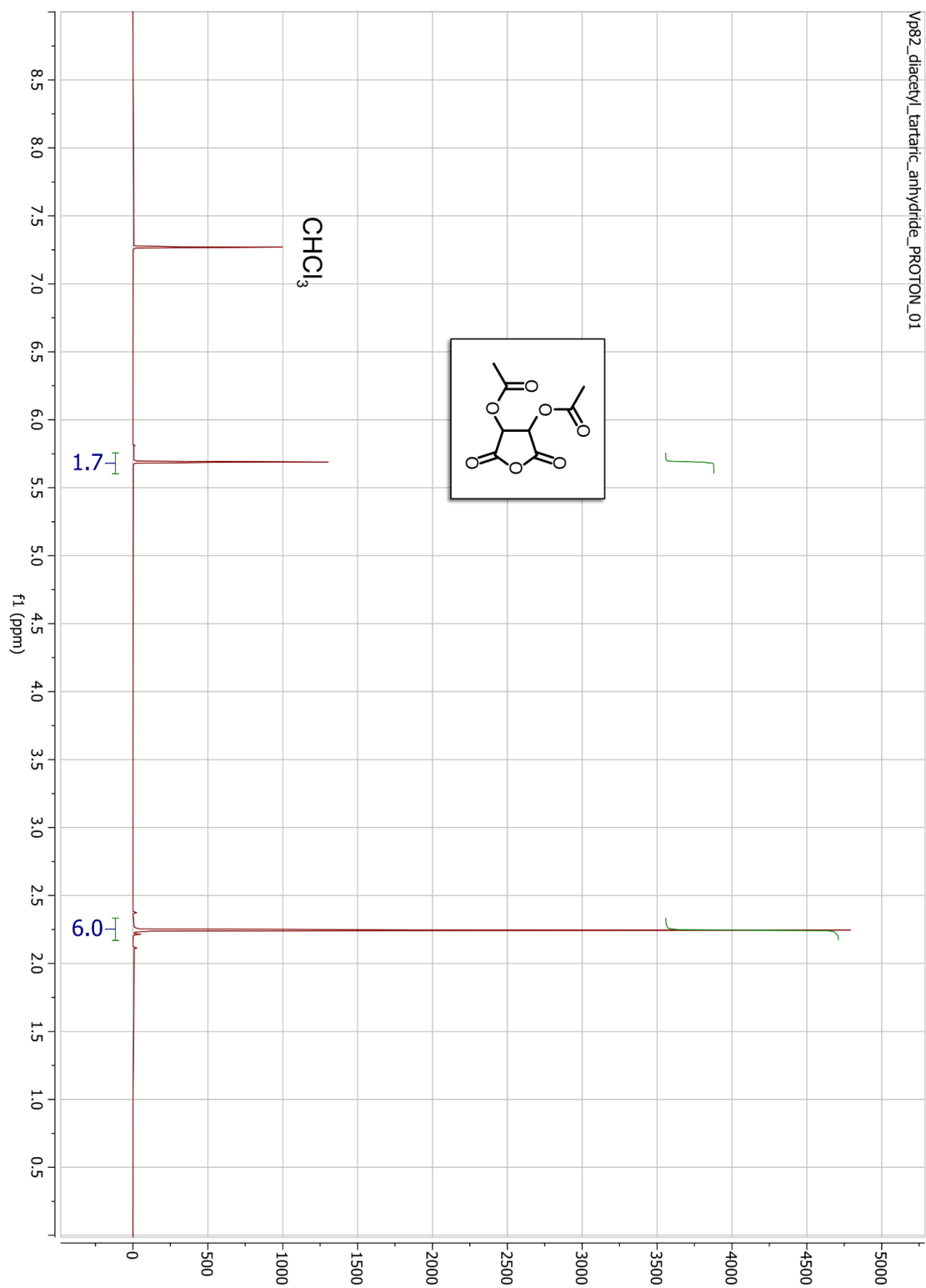


Figure 4.S2. ¹H NMR spectrum of diacetyltartaric anhydride.

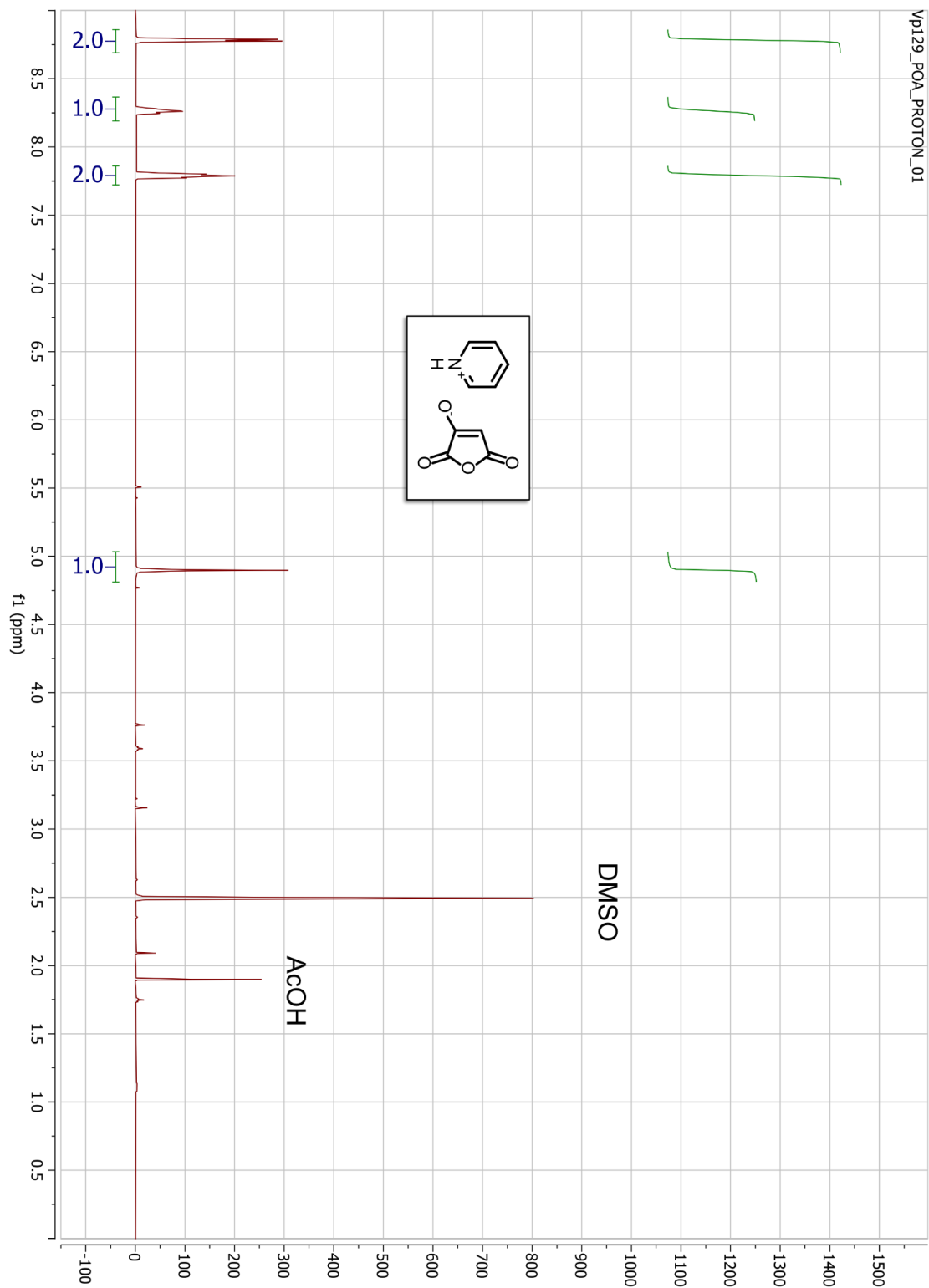


Figure 4.S3. ^1H NMR spectrum of pyridinium oxomaleic anhydride.

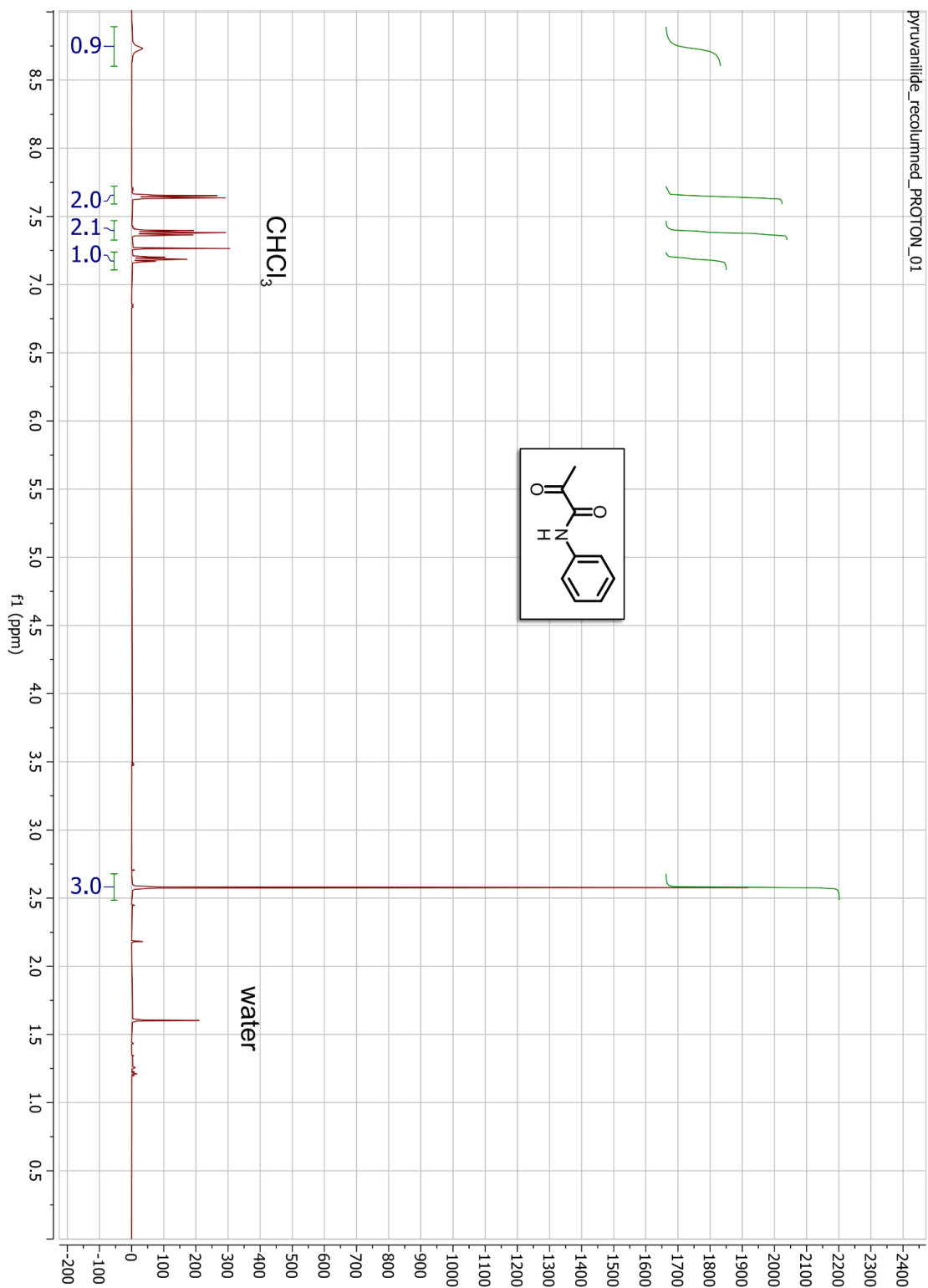


Figure 4.S4. ¹H NMR spectrum of pyruvanilide.

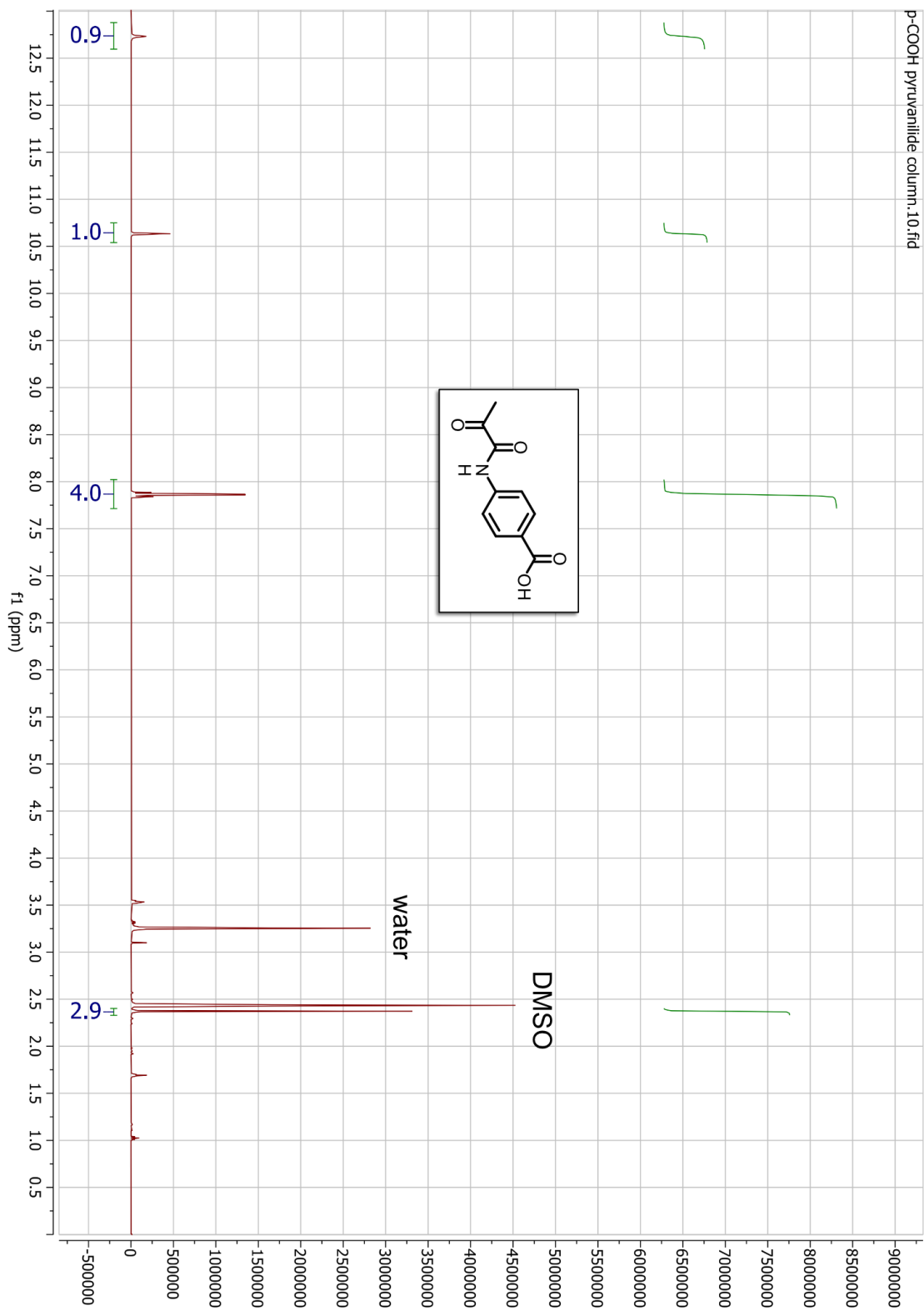


Figure 4.S5. ^1H NMR spectrum of pyruvanilide-4-carboxylic acid.

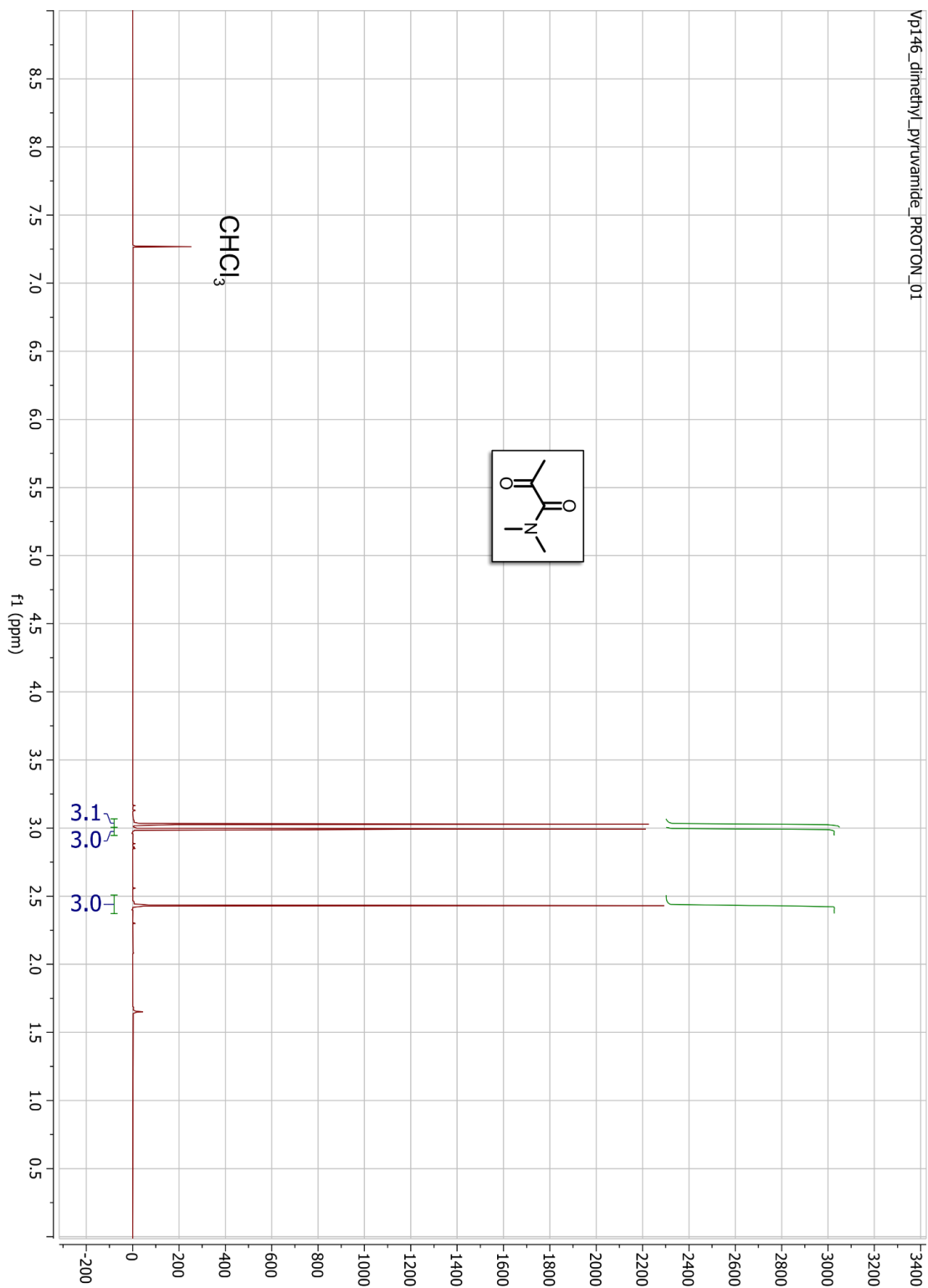


Figure 4.S6. ¹H NMR spectrum of N,N-dimethylpyruvamide.

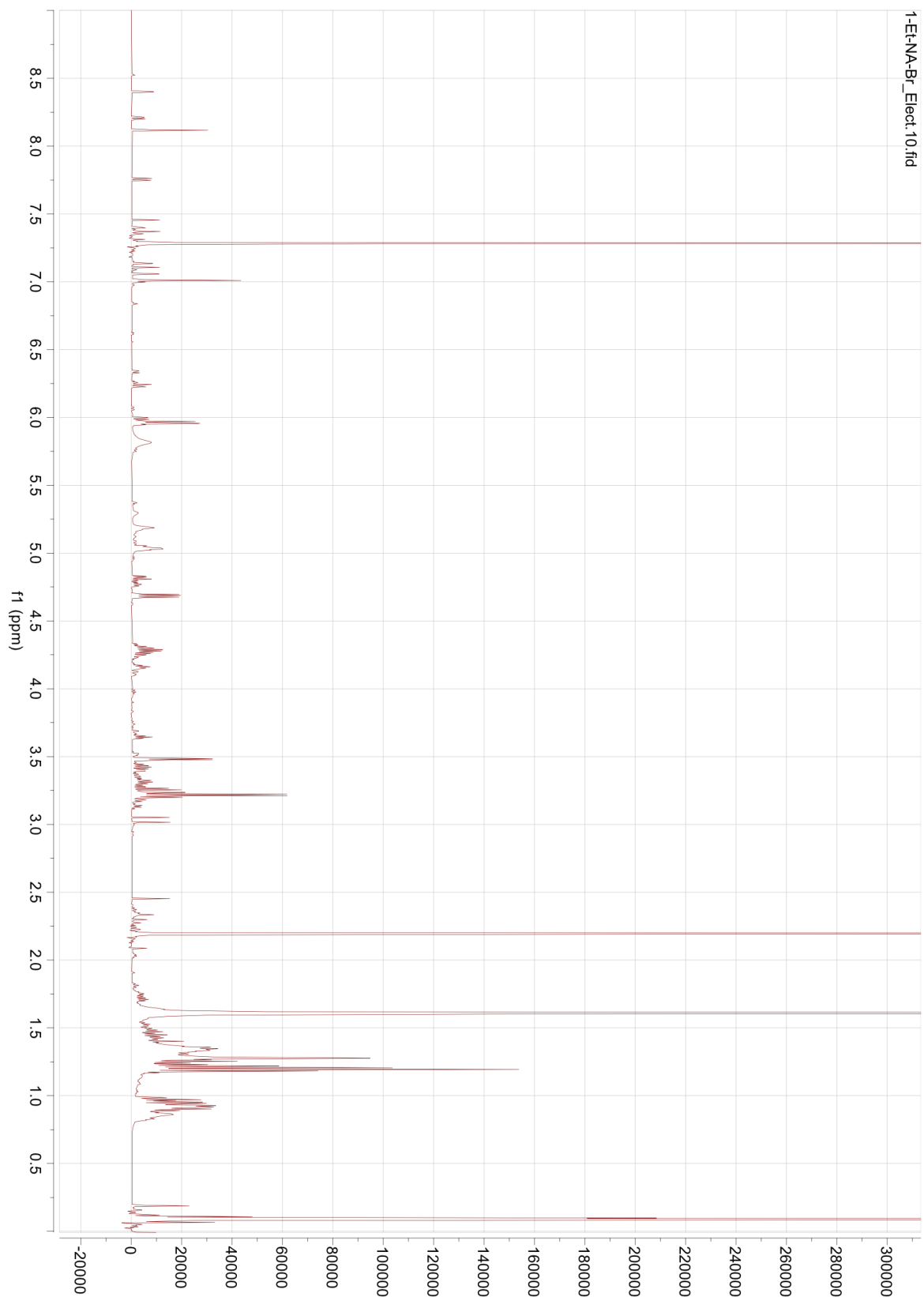


Figure 4.S7. ¹H NMR spectrum of CDCl₃ extract of Electrolysis (A) (10 mM 1-ethyl nicotinamide bromide).

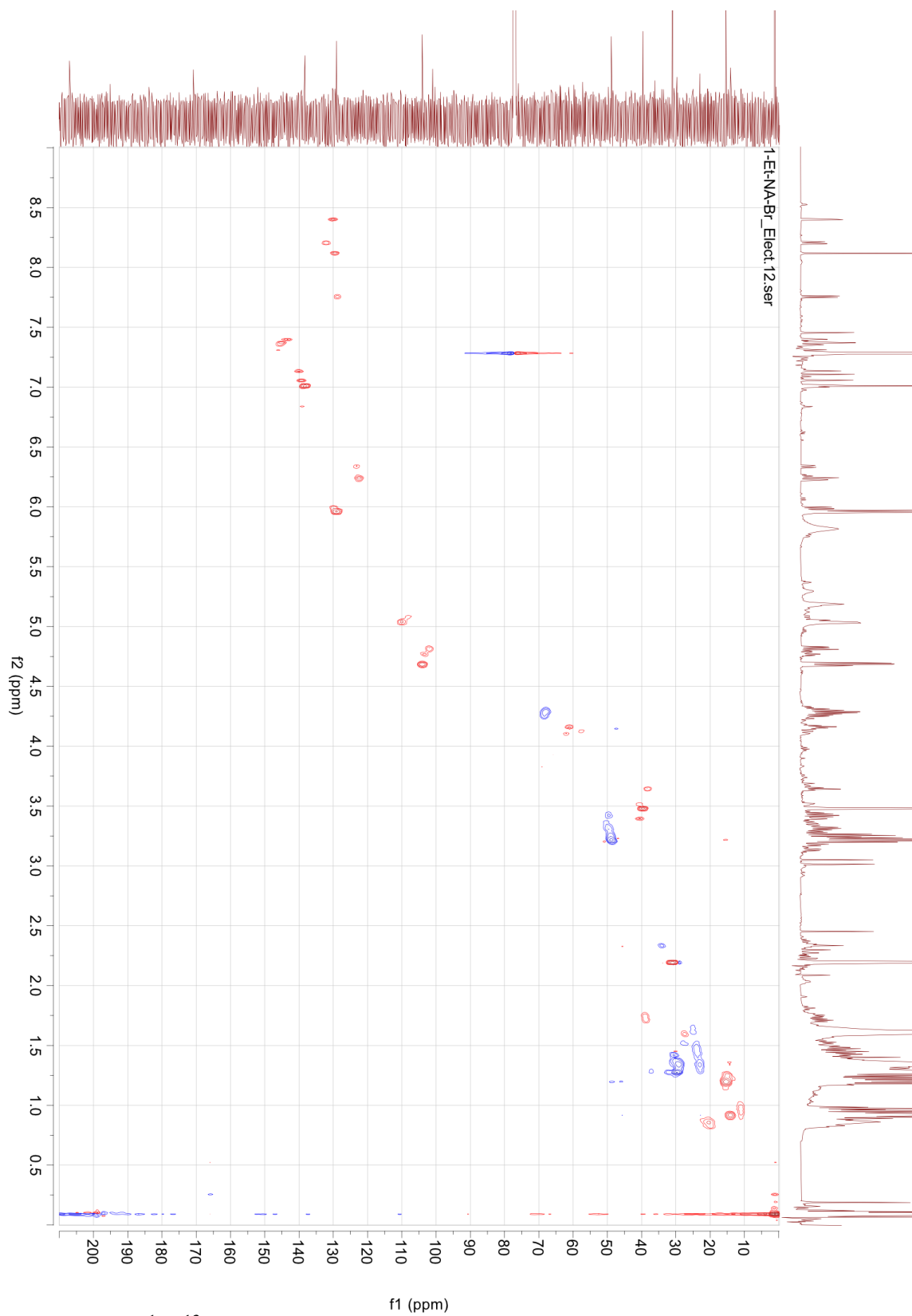


Figure 4.S8. ^1H - ^{13}C HSQC NMR spectrum of CDCl_3 extract of Electrolysis (A) (10 mM 1-ethyl nicotinamide bromide).

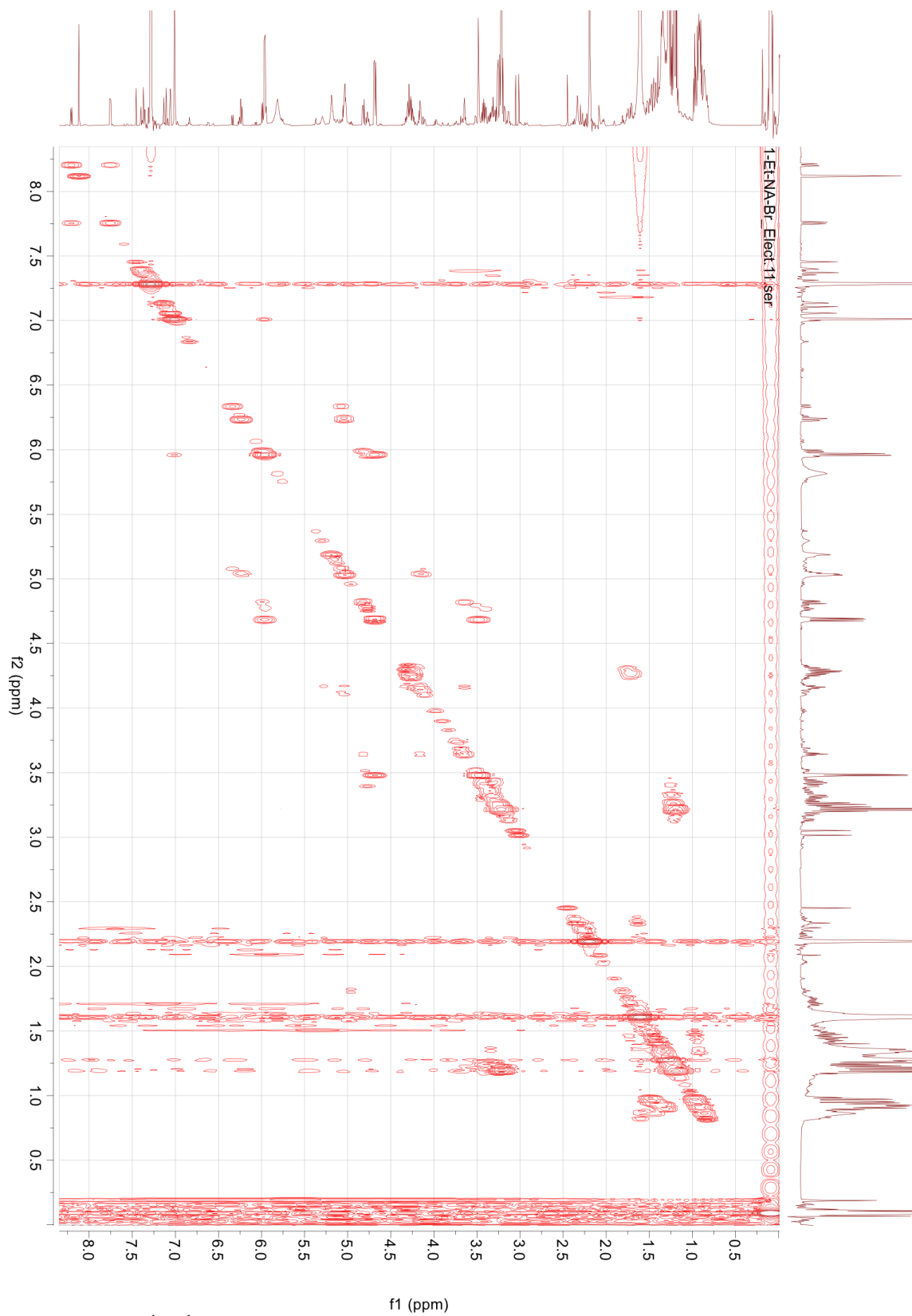


Figure 4.S9. ^1H - ^1H COSY NMR spectrum of CDCl_3 extract of Electrolysis (A) (10 mM 1-ethyl nicotinamide bromide).

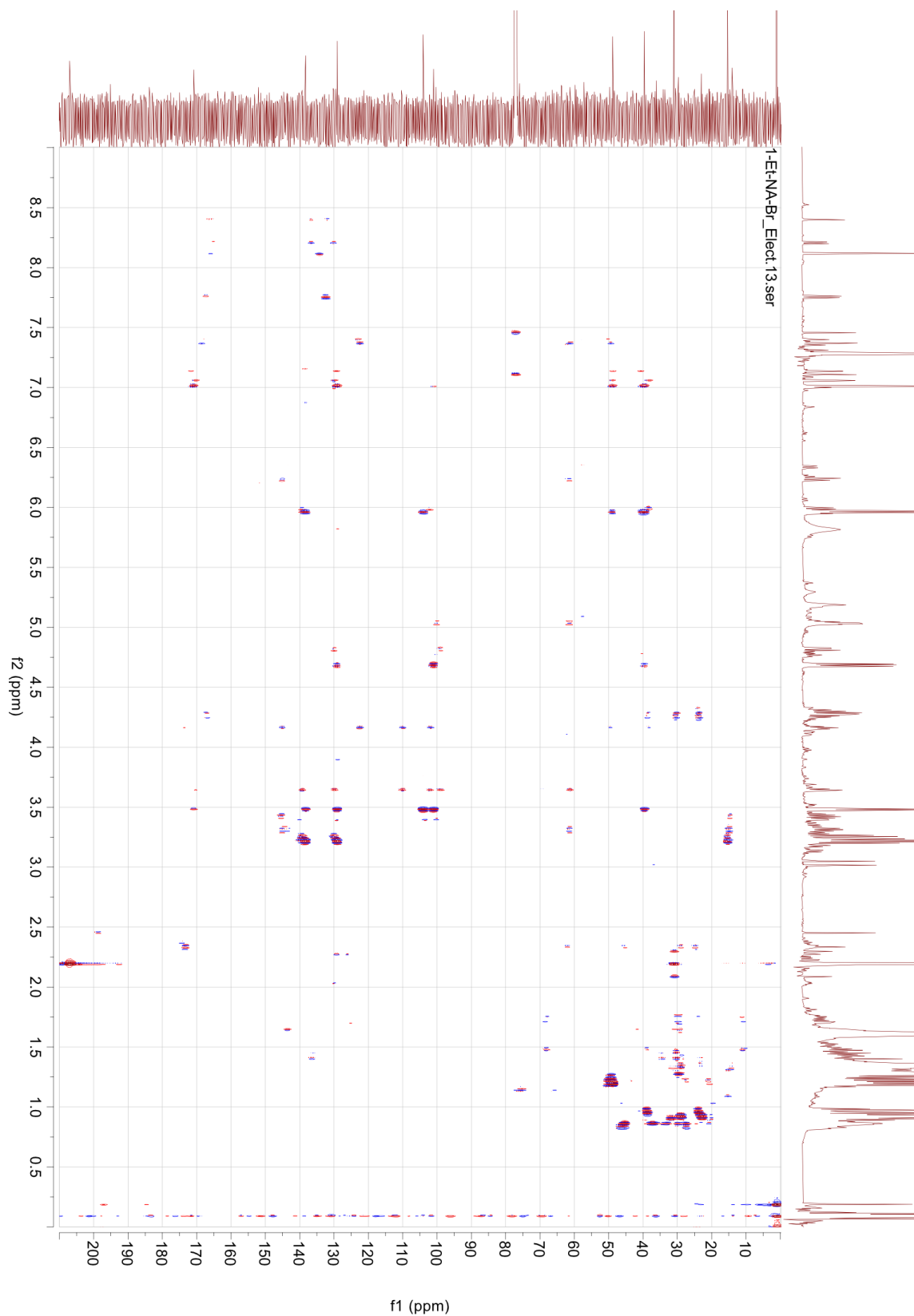


Figure 4.S10. ^1H - ^{13}C HMBC NMR spectrum of CDCl_3 extract of Electrolysis (A) (10 mM 1-ethyl nicotinamide bromide).

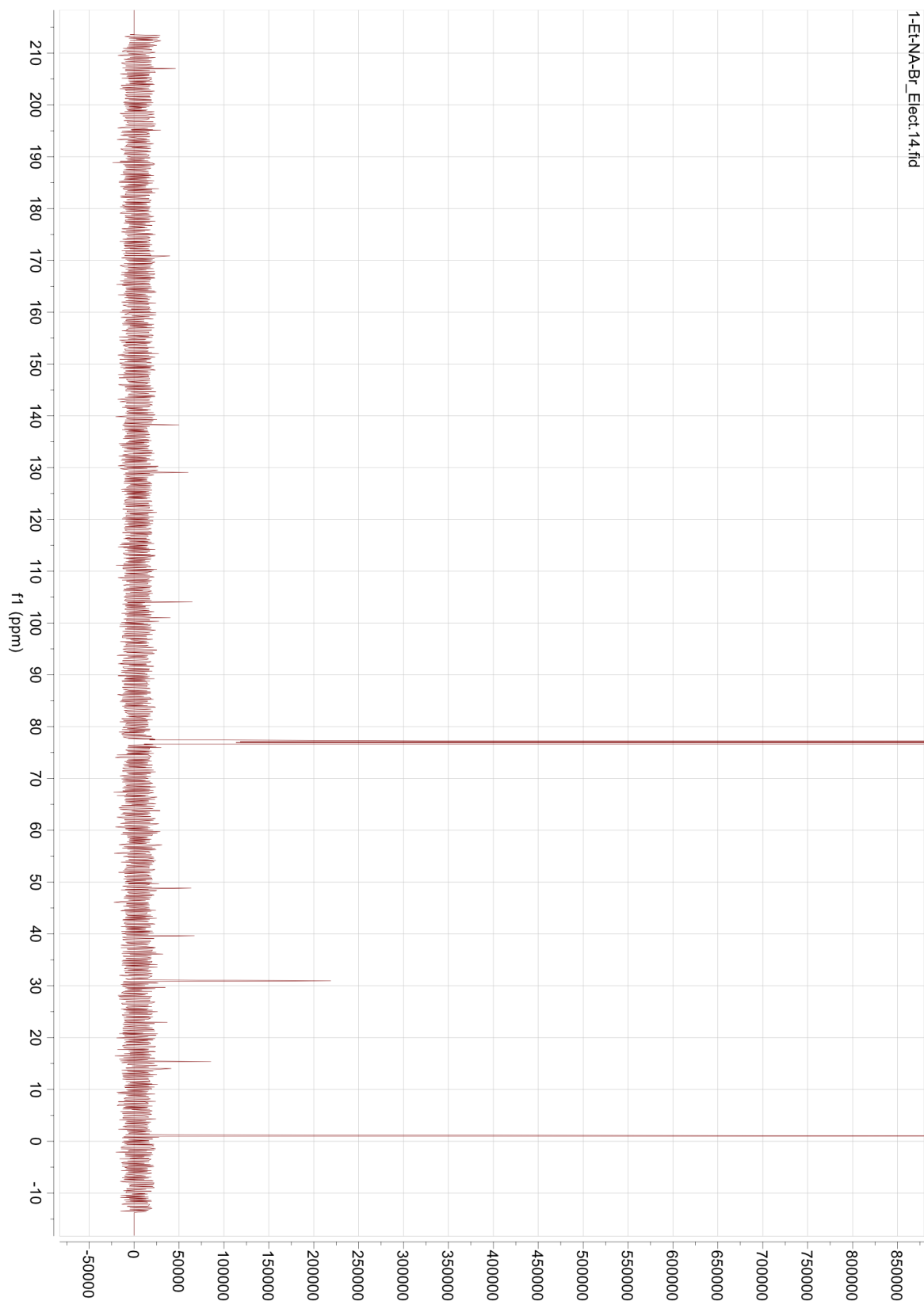


Figure 4.S11. ^{13}C NMR spectrum of CDCl_3 extract of Electrolysis (A) (10 mM 1-ethyl nicotinamide bromide).

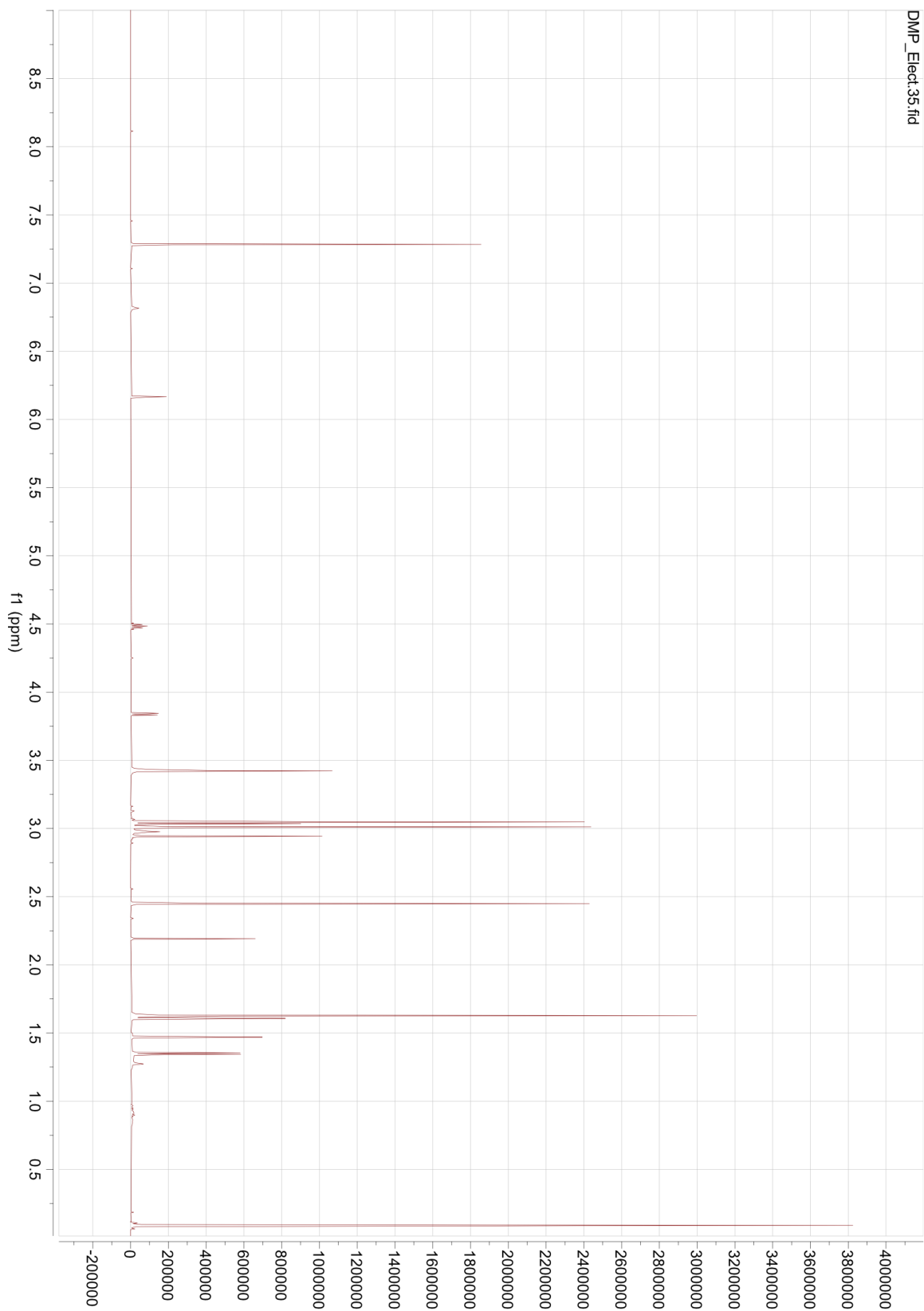


Figure 4.S12. ^1H NMR spectrum of CDCl_3 extract of Electrolysis (B) (20 mM N,N-dimethylpyruvamide).

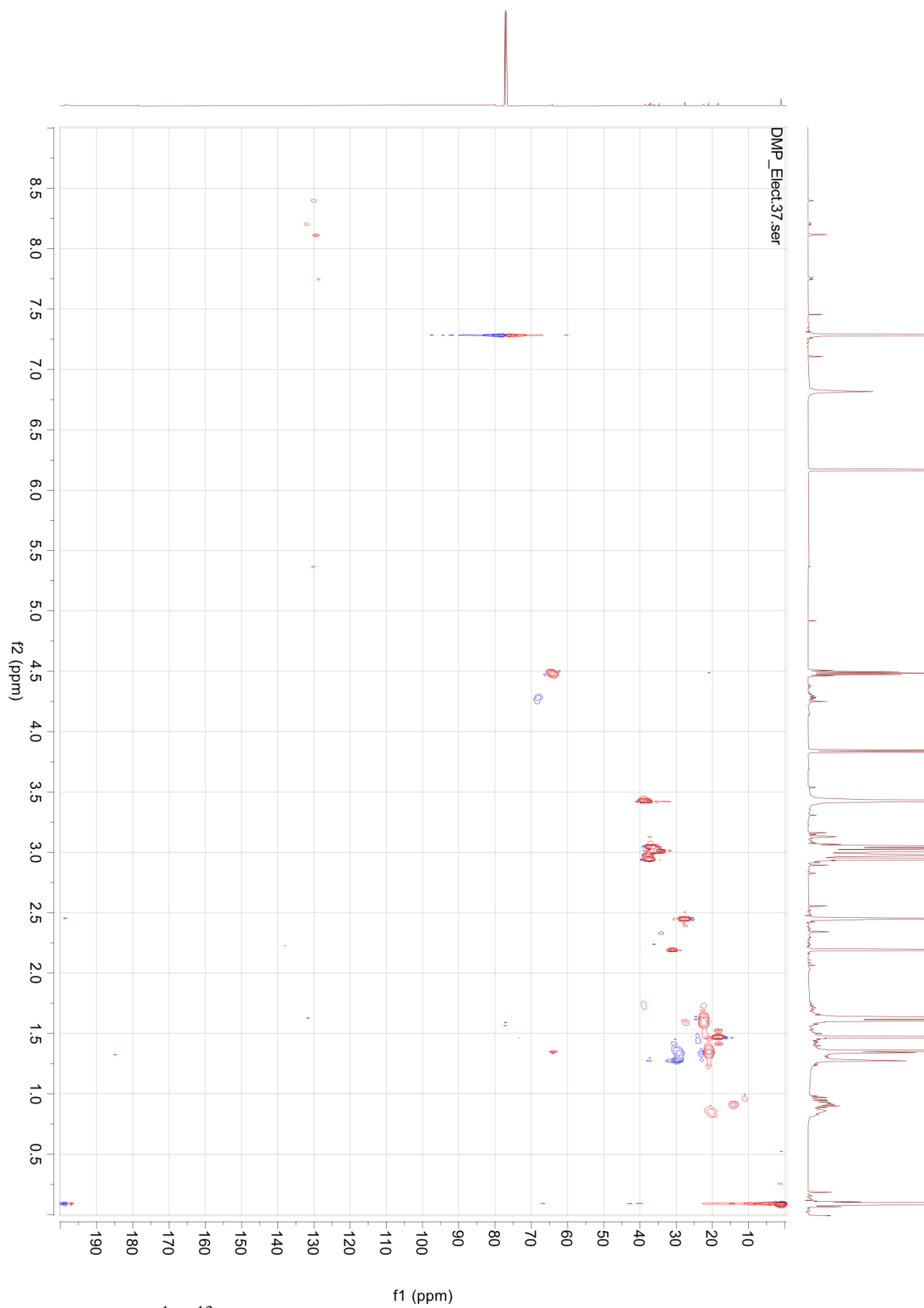


Figure 4.S13. ^1H - ^{13}C HSQC NMR spectrum of CDCl_3 extract of Electrolysis (B) (20 mM N,N-dimethylpyruvamide).

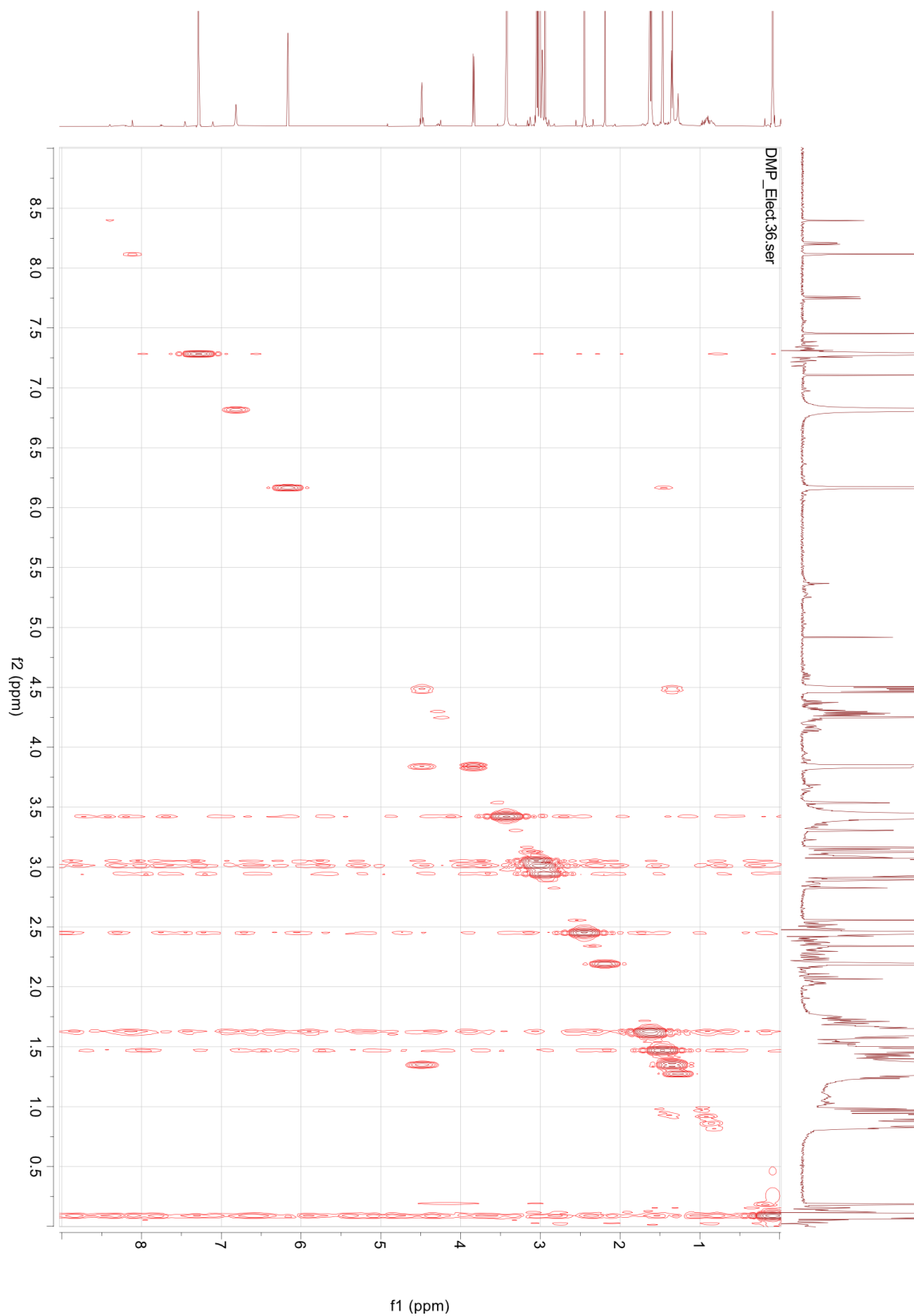


Figure 4.S14. ^1H - ^1H COSY NMR spectrum of CDCl_3 extract of Electrolysis (B) (20 mM N,N-dimethylpyruvamide).

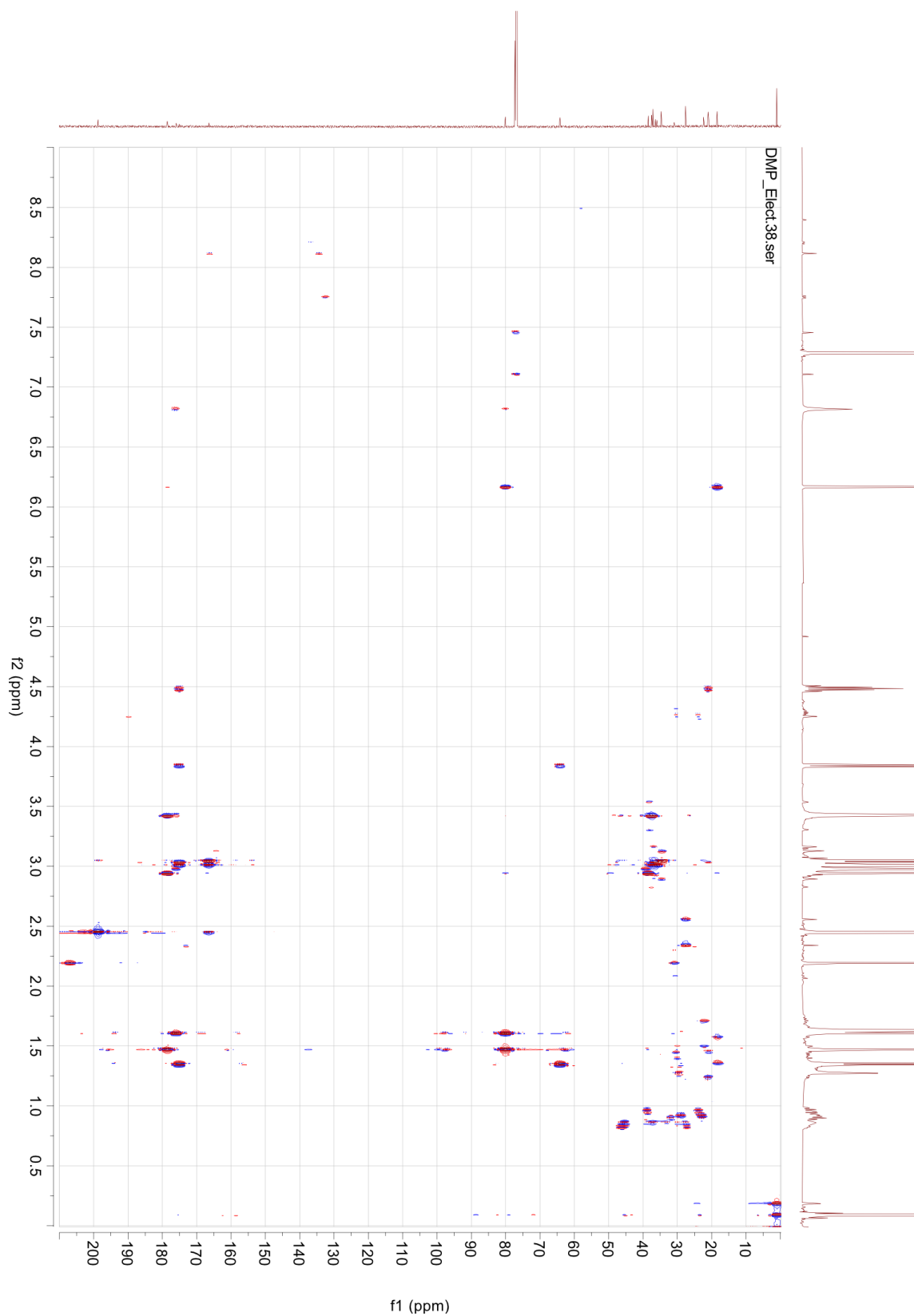


Figure 4.S15. ^1H - ^{13}C HMBC NMR spectrum of CDCl_3 extract of Electrolysis (B) (20 mM N,N-dimethylpyruvamide).

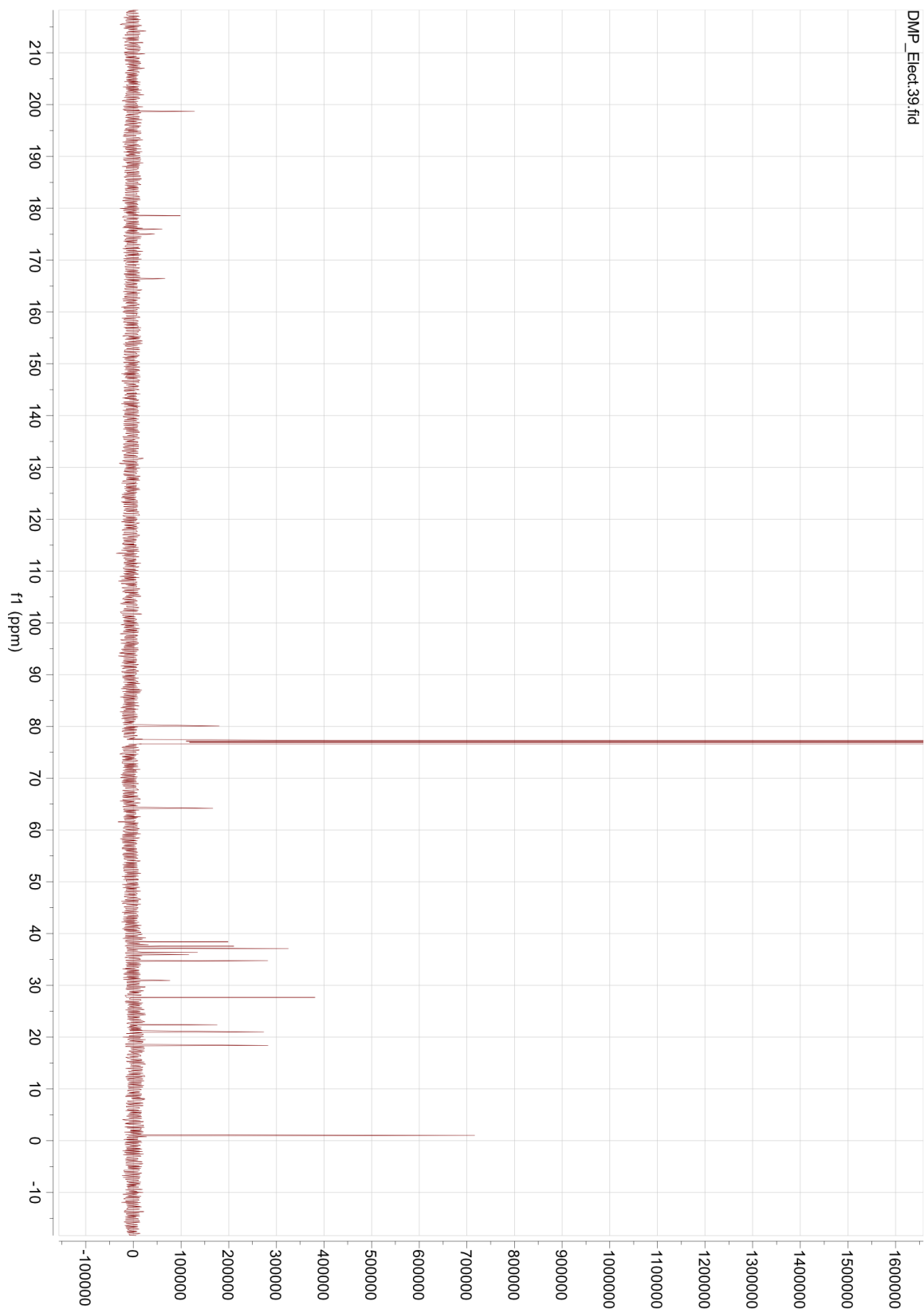


Figure 4.S16. ^{13}C NMR spectrum of CDCl_3 extract of Electrolysis (B) (20 mM N,N-dimethylpyruvamide).

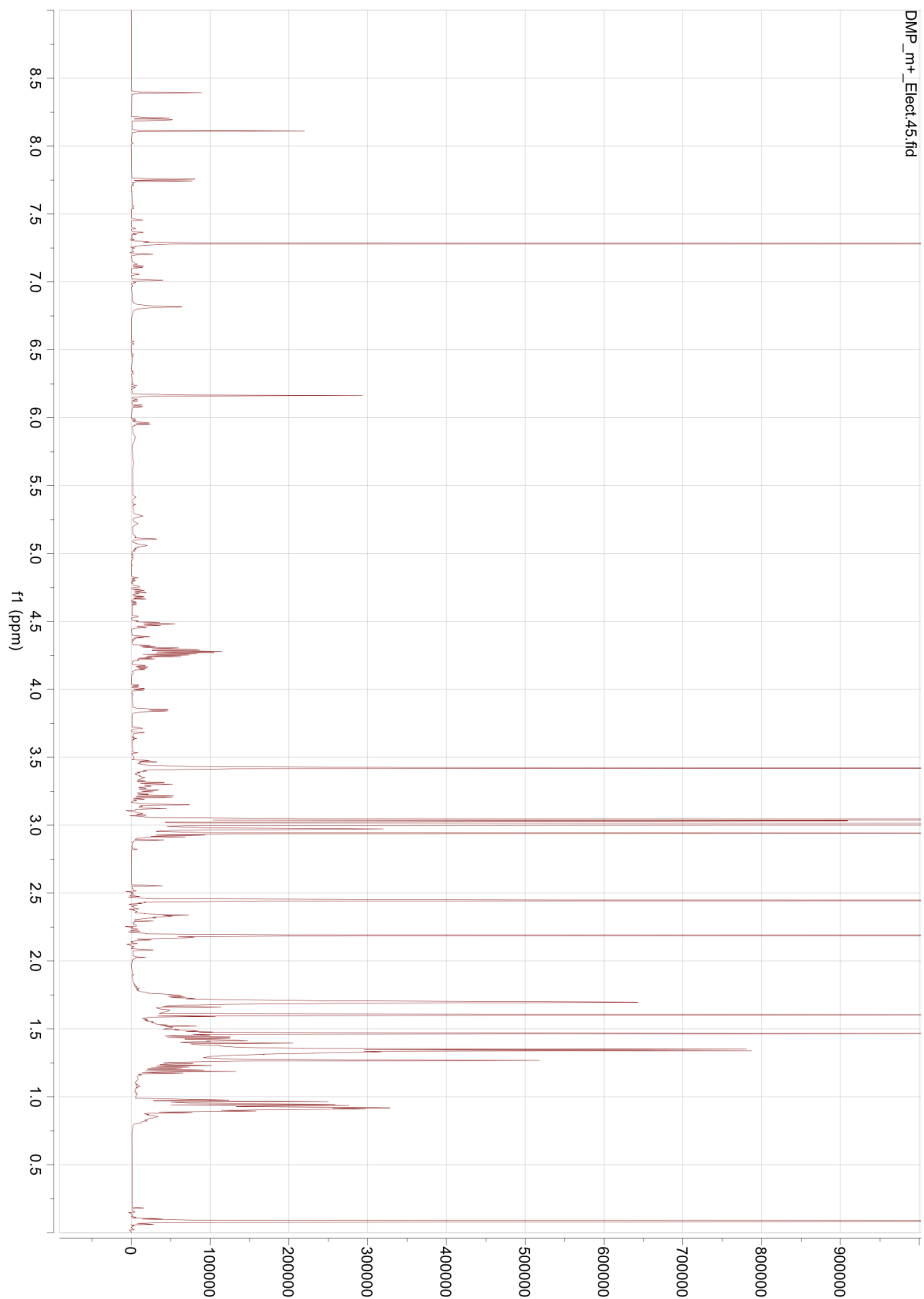


Figure 4.S17. ¹H NMR spectrum of CDCl₃ extract of Electrolysis (C) (10 mM 1-ethyl nicotinamide bromide + 20 mM N,N-dimethylpyruvamide).



Figure 4.S18. ^1H - ^{13}C HSQC NMR spectrum of CDCl_3 extract of Electrolysis (C) (10 mM 1-ethyl nicotinamide bromide + 20 mM N,N-dimethylpyruvamide).



Figure 4.S19. ^1H - ^1H COSY NMR spectrum of CDCl_3 extract of Electrolysis (C) (10 mM 1-ethyl nicotinamide bromide + 20 mM N,N-dimethylpyruvamide).

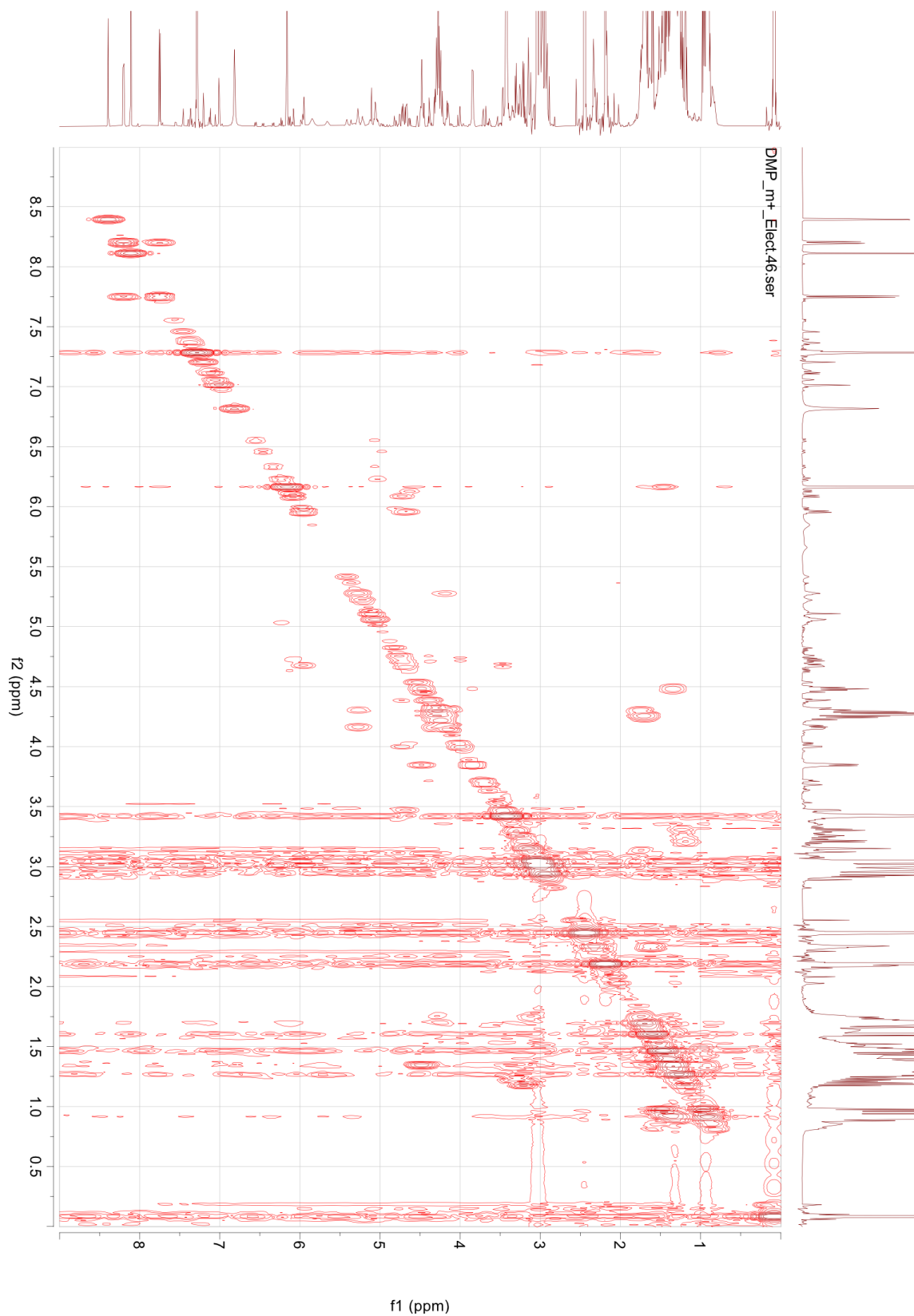


Figure 4.S20. Closeup of ^1H - ^1H COSY NMR spectrum of CDCl_3 extract of Electrolysis (C) (10 mM 1-ethyl nicotinamide bromide + 20 mM N,N-dimethylpyruvamide).

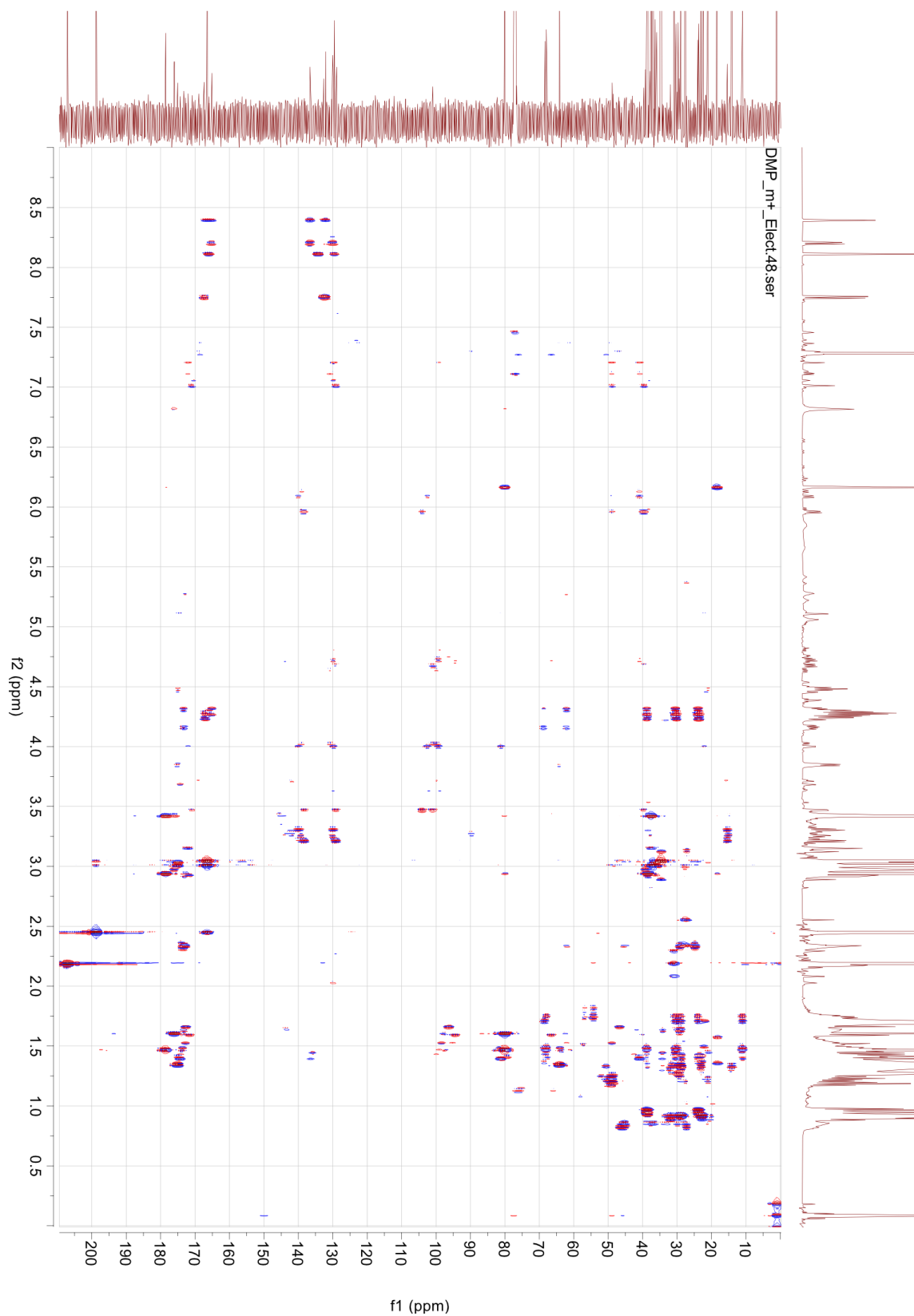


Figure 4.S21. ^1H - ^{13}C HMBC NMR spectrum of CDCl_3 extract of Electrolysis (C) (10 mM 1-ethyl nicotinamide bromide + 20 mM N,N-dimethylpyruvamide).

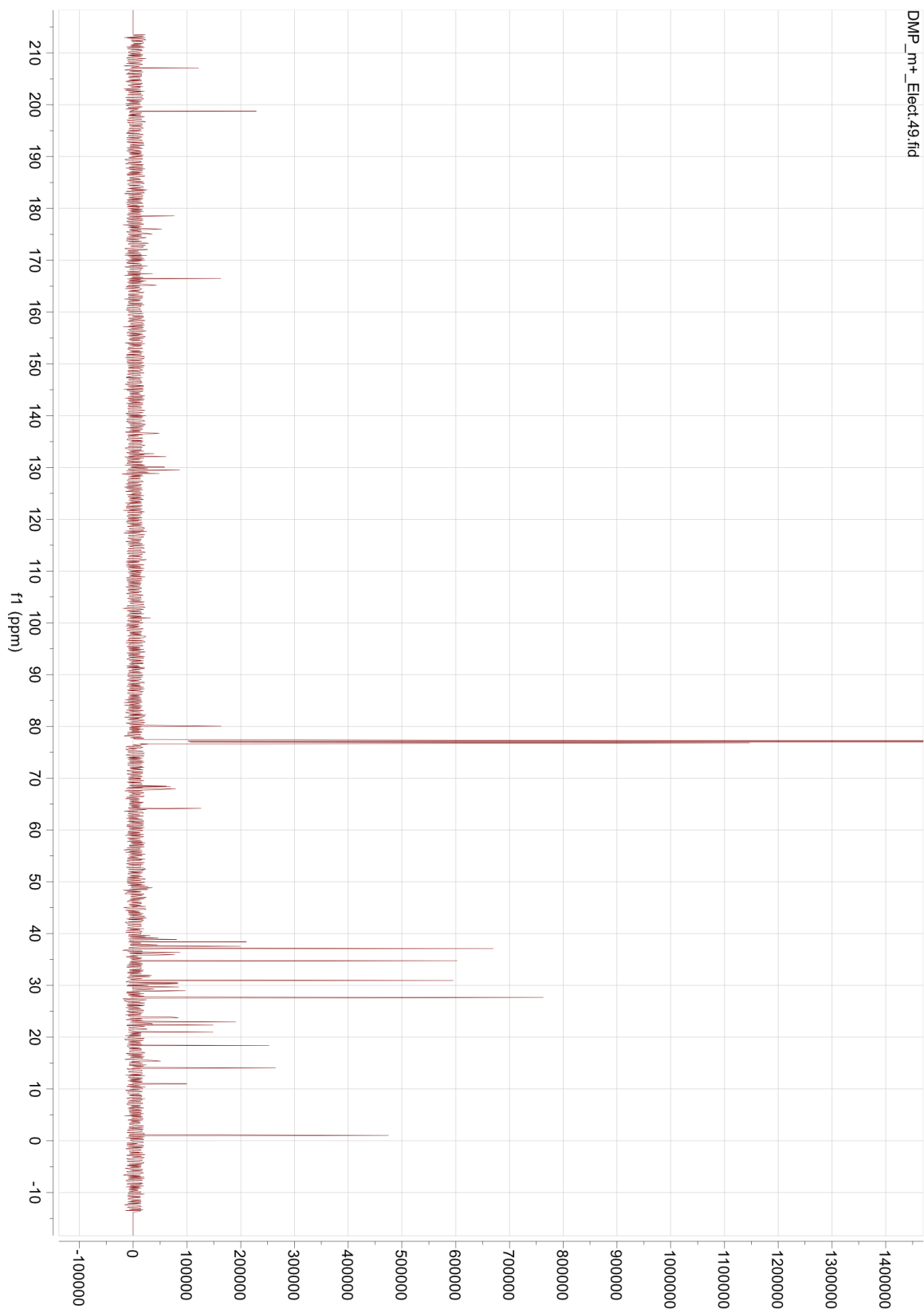


Figure 4.S22. ^{13}C NMR spectrum of CDCl_3 extract of Electrolysis (C) (10 mM 1-ethyl nicotinamide bromide + 20 mM N,N-dimethylpyruvamide).

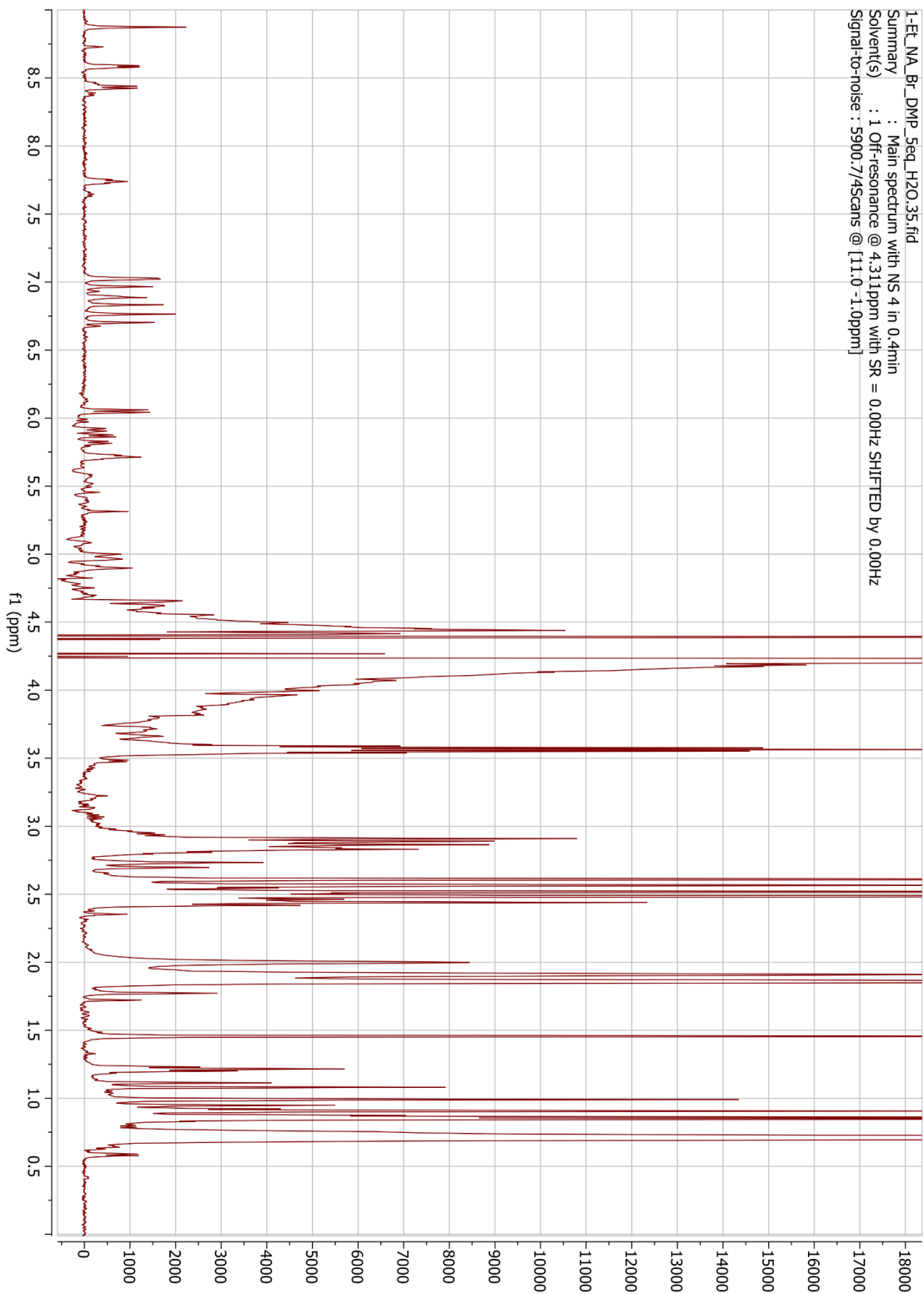


Figure 4.S23. ¹H NMR spectrum of Electrolysis (D) (10 mM 1-ethyl nicotinamide bromide + 50 mM N,N-dimethylpyruvamide in H₂O).

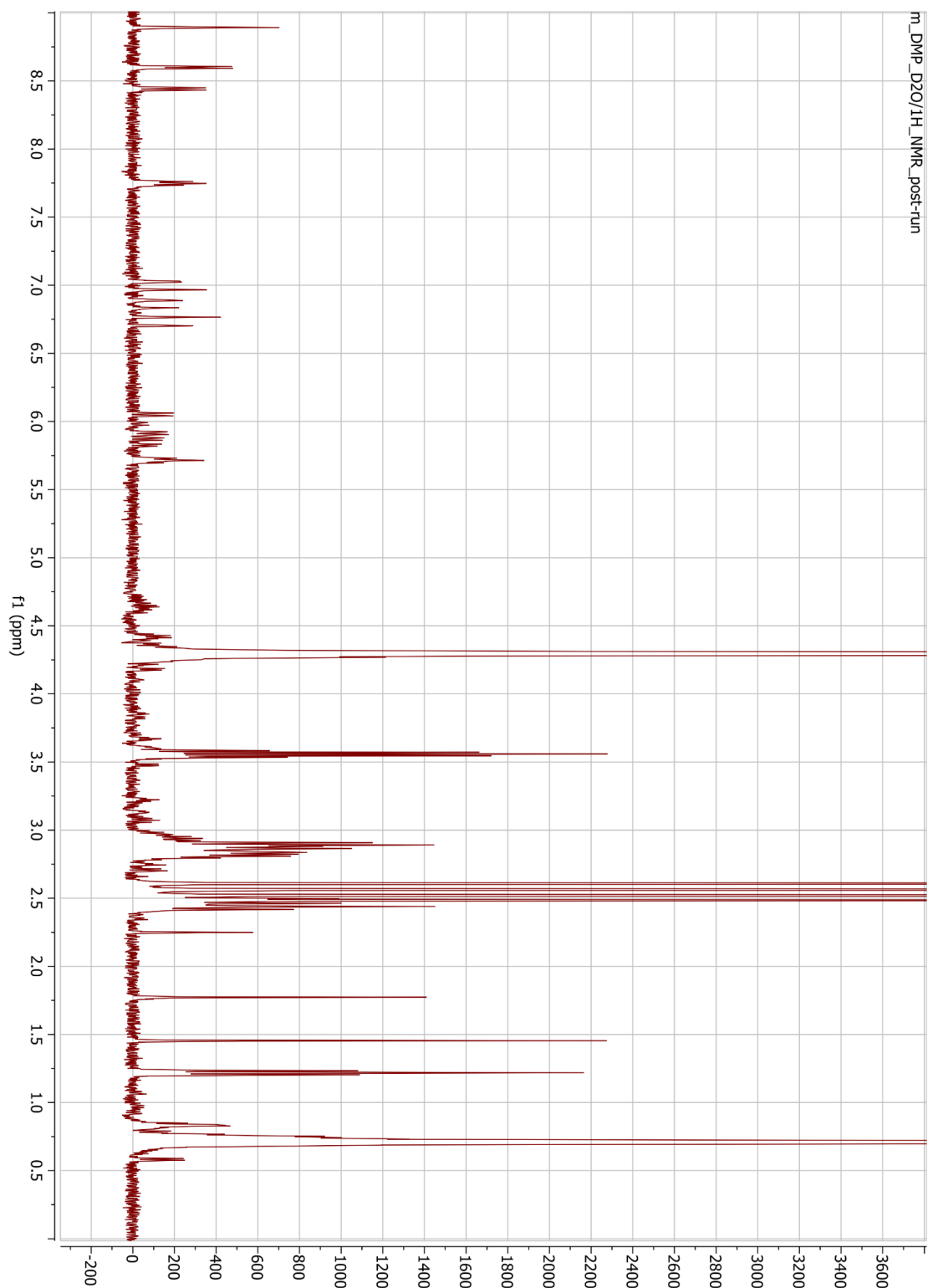


Figure 4.S24. ¹H NMR spectrum of Electrolysis (E) (10 mM 1-ethyl nicotinamide bromide + 20 mM N,N-dimethylpyruvamide in D₂O).

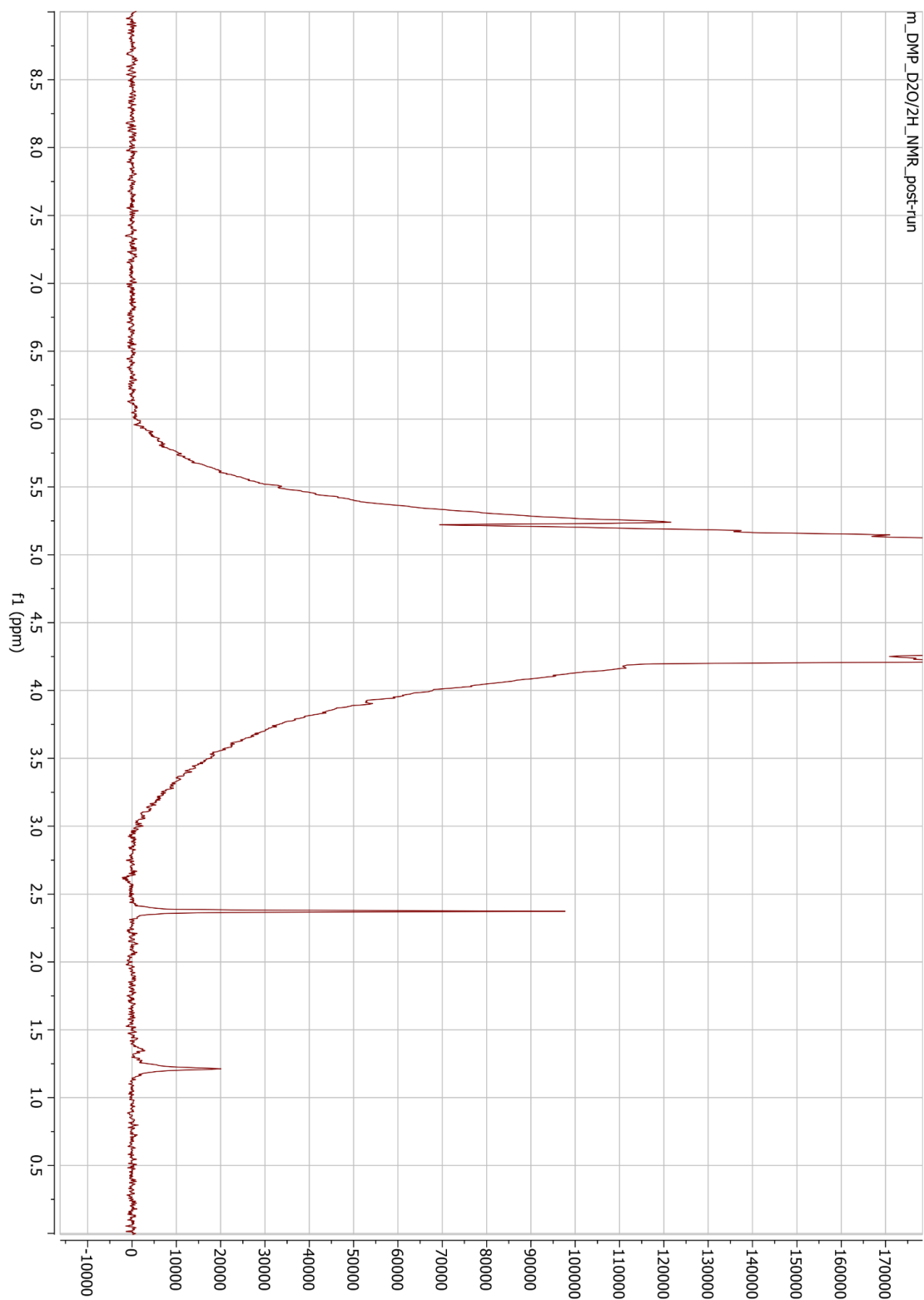


Figure 4.S25. ^2H NMR spectrum of Electrolysis (E) (10 mM 1-ethyl nicotinamide bromide + 20 mM N,N-dimethylpyruvamide in D_2O).

OPTIMIZED MOLECULAR COORDINATES

Computations were carried out with Gaussian 16, Revision C.01. The following input was used:

```
opt freq=noraman b3lyp/6-31+g(d,p) scrf=(cpcm,solvent=acetonitrile)
pop=nbo geom=connectivity
```

Atom	m^+		
	X	Y	Z
C	-0.176089	-0.509546	0.311412
C	-1.480684	1.430902	0.034119
C	-0.354895	2.174575	-0.281232
C	0.890954	1.552648	-0.289140
C	0.984433	0.184639	-0.003339
H	-0.184381	-1.557920	0.581418
H	-2.475315	1.856274	0.068713
H	-0.462907	3.228039	-0.506970
H	1.792737	2.111519	-0.511862
C	2.348967	-0.464881	0.016881
O	3.335897	0.204092	0.331259
N	2.405847	-1.775941	-0.300934
H	1.640393	-2.268806	-0.737343
H	3.312939	-2.223488	-0.316277
N	-1.375373	0.115508	0.330126
C	-2.609972	-0.672248	0.640950
H	-2.317890	-1.444594	1.353095
H	-3.297397	0.009597	1.142562
C	-3.225545	-1.270030	-0.620785
H	-3.517620	-0.489746	-1.328829
H	-2.532957	-1.957157	-1.114663
H	-4.121110	-1.829780	-0.337464
Energy (Hartree)	-495.959485		
Energy (kJ/mol)	-1302142		
Energy (kcal/mol)	-311219		

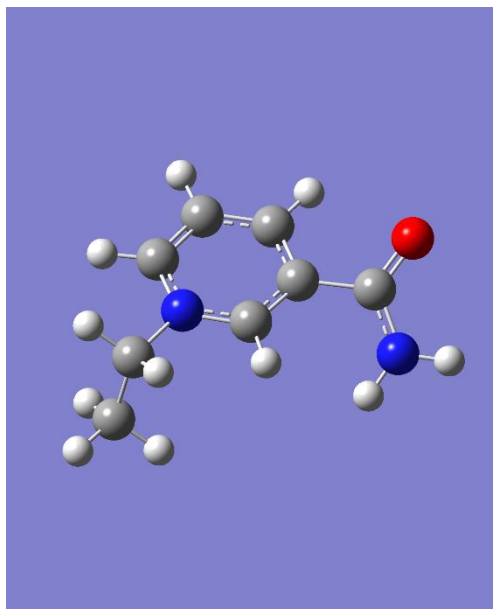


Figure 4.S26. Optimized structure for 1-ethyl nicotinamide cation (m^+).

Table 4.S1. Optimized coordinates and energy for 1-ethyl nicotinamide cation (m^+).

$\dot{\mathbf{m}}$			
Atom	X	Y	Z
C	-0.129200	-0.538290	0.272834
C	-1.512890	1.414681	0.100874
C	-0.391929	2.180844	-0.155911
C	0.887464	1.618914	-0.209102
C	1.009160	0.188258	0.003933
H	-0.105517	-1.600726	0.486408
H	-2.519314	1.803739	0.162917
H	-0.529470	3.246274	-0.316129
H	1.769451	2.211930	-0.409241
C	2.345428	-0.442746	-0.020204
O	3.382822	0.241471	0.065376
N	2.425406	-1.810961	-0.112025
H	1.675860	-2.352560	-0.516475
H	3.354276	-2.194316	-0.222352
N	-1.365874	0.029742	0.335929
C	-2.561756	-0.785090	0.589215
H	-2.240252	-1.694485	1.103120
H	-3.201462	-0.228183	1.282085
C	-3.329576	-1.133231	-0.688757
H	-3.660077	-0.230299	-1.211348
H	-2.707150	-1.720816	-1.370980
H	-4.215853	-1.723845	-0.435630
Energy (Hartree)		-496.084559	
Energy (kJ/mol)		-1302470	
Energy (kcal/mol)		-311298	

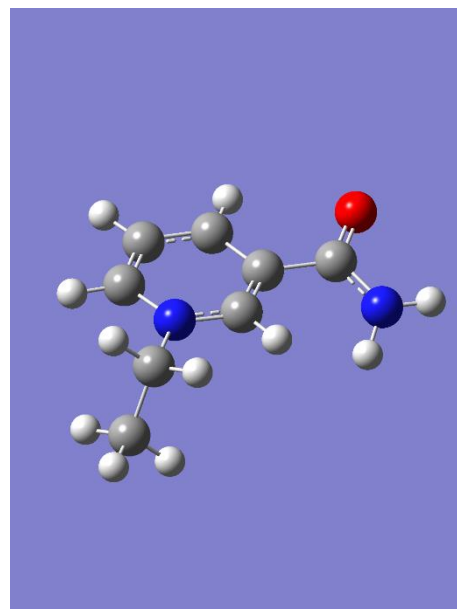


Figure 4.S27. Optimized structure for 1-ethyl nicotinamide radical ($\dot{\mathbf{m}}$).

Table 4.S2. Optimized structure and energy for 1-ethyl nicotinamide radical ($\dot{\mathbf{m}}$).

m^-			
Atom	X	Y	Z
C	0.116904	-0.597570	-0.145655
C	1.548621	1.346572	-0.513493
C	0.443880	2.138134	-0.015028
C	-0.797919	1.635130	0.229765
C	-1.043991	0.180452	0.004757
H	0.083756	-1.684011	-0.152550
H	2.536224	1.640379	-0.160190
H	0.633918	3.199881	0.145151
H	-1.614119	2.258321	0.576647
C	-2.351834	-0.372357	0.047010
O	-3.398964	0.327952	0.235755
N	-2.558367	-1.760103	-0.184589
H	-1.804783	-2.386336	0.074426
H	-3.434033	-2.063754	0.227195
N	1.333555	-0.084256	-0.306544
C	2.495735	-0.964180	-0.438936
H	2.135296	-1.986454	-0.585944
H	3.029318	-0.659621	-1.350128
C	3.444303	-0.915780	0.762996
H	3.836515	0.091975	0.927422
H	2.934712	-1.242627	1.675303
H	4.294403	-1.583263	0.586057
Energy (Hartree)		-496.157655	
Energy (kJ/mol)		-1302662	
Energy (kcal/mol)		-311344	

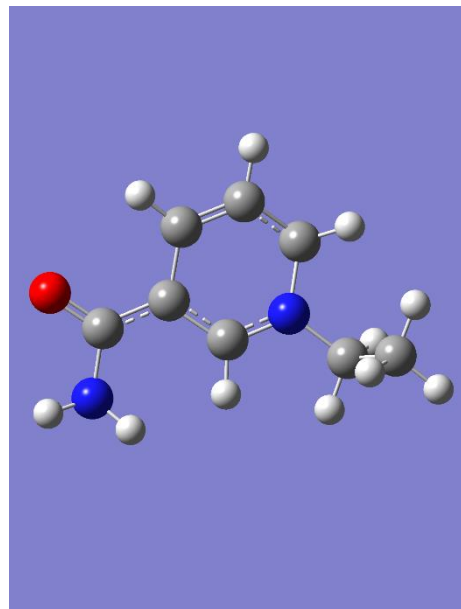


Figure 4.S28. Optimized structure for 1-ethyl nicotinamide anion (m^-).

Table 4.S3. Optimized structure and energy for 1-ethyl nicotinamide anion (m^-).

mH⁺			
Atom	X	Y	Z
C	0.169509	-0.529077	-0.307239
C	1.516739	1.431536	-0.060205
C	0.428046	2.185911	0.258662
C	-0.972140	0.146337	0.015480
H	0.177183	-1.576678	-0.580640
H	2.518489	1.837310	-0.114954
H	0.563793	3.239875	0.471609
C	-2.322109	-0.512786	-0.025018
O	-3.306045	0.144997	-0.380032
N	-2.383664	-1.818514	0.317598
H	-1.624697	-2.298216	0.779178
H	-3.287458	-2.272801	0.311765
N	1.393814	0.093681	-0.345055
C	2.607668	-0.705882	-0.644758
H	2.311446	-1.487420	-1.346190
H	3.310079	-0.041371	-1.150192
C	3.218659	-1.300821	0.626069
H	3.519083	-0.516094	1.325487
H	2.516667	-1.973496	1.126342
H	4.107019	-1.874104	0.347166
C	-0.935668	1.606465	0.321858
H	-1.380964	1.802810	1.313447
H	-1.617556	2.143951	-0.359665
Energy (Hartree)		-495.959485	
Energy (kJ/mol)		-1302142	
Energy (kcal/mol)		-311219	

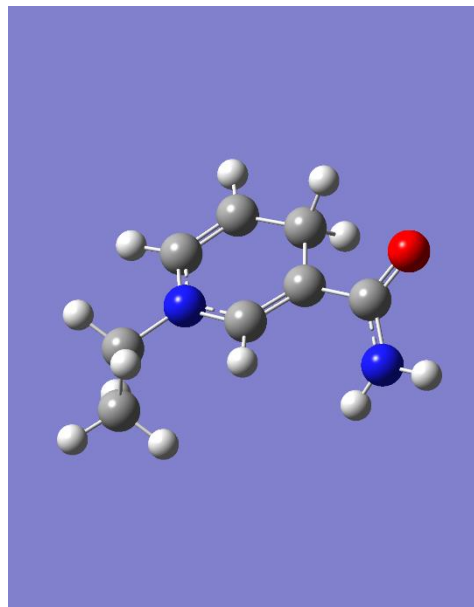


Figure 4.S29. Optimized structure for protonated 1-ethyl nicotinamide radical (**mH⁺**).

Table 4.S4. Optimized structure and energy for protonated 1-ethyl nicotinamide radical (**mH⁺**).

Atom	mH		
	X	Y	Z
C	0.158801	-0.534311	-0.300327
C	1.508519	1.414212	-0.107189
C	0.443730	2.188004	0.151236
C	-0.987915	0.154195	-0.030632
H	0.153725	-1.601810	-0.493719
H	2.520954	1.801573	-0.127996
H	0.607719	3.243916	0.343124
C	-2.297359	-0.506850	0.028320
O	-3.350179	0.162924	0.053770
N	-2.368123	-1.883058	0.020772
H	-1.596450	-2.441310	0.355111
H	-3.285827	-2.269468	0.196369
N	1.395317	0.042232	-0.382955
C	2.603448	-0.770713	-0.570001
H	2.321930	-1.650722	-1.155038
H	3.302886	-0.191250	-1.181018
C	3.265653	-1.192177	0.744939
H	3.564473	-0.319695	1.334823
H	2.585123	-1.800838	1.349138
H	4.162620	-1.784757	0.536159
C	-0.974557	1.664744	0.161726
H	-1.477541	1.935692	1.101903
H	-1.570455	2.158431	-0.622173
Energy (Hartree)		-496.693273	
Energy (kJ/mol)		-1304068	
Energy (kcal/mol)		-311680	

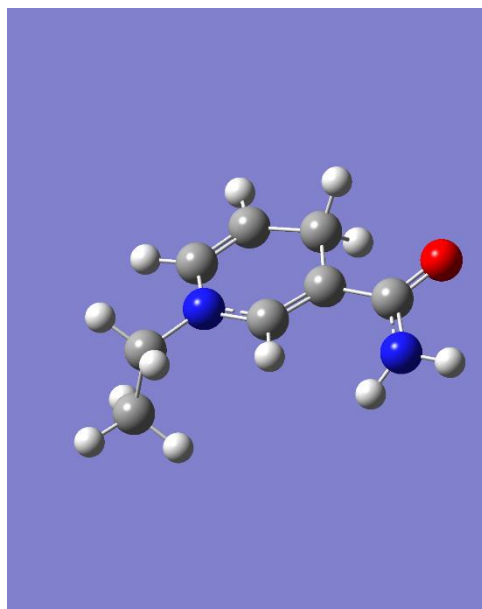


Figure 4.S30. Optimized structure for 1-ethyl-1,4-dihydro nicotinamide (mH).

Table 4.S5. Optimized structure and energy for 1-ethyl-1,4-dihydro nicotinamide (mH).

DMP			
Atom	X	Y	Z
C	-0.046029	-0.541015	0.113245
O	-0.046046	-1.771084	0.298530
N	-1.156639	0.190407	-0.070995
C	1.330824	0.142931	0.170940
O	1.604627	0.862518	1.120939
C	2.310470	-0.232094	-0.905340
H	2.386985	-1.321396	-0.976789
H	1.941952	0.126915	-1.874304
H	3.287594	0.205639	-0.695704
C	-1.168878	1.628912	-0.342542
H	-1.702377	2.157830	0.453390
H	-0.154859	2.019901	-0.399256
H	-1.671783	1.819986	-1.295267
C	-2.447758	-0.505431	-0.034909
H	-2.493297	-1.273351	-0.812589
H	-2.598564	-0.983687	0.936740
H	-3.239595	0.224025	-0.203375
Energy (Hartree)	-401.086579		
Energy (kJ/mol)	-1053053		
Energy (kcal/mol)	-251686		

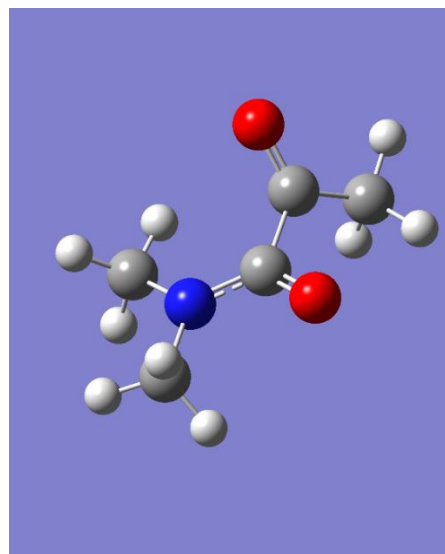


Figure 4.S31. Optimized structure for N,N-dimethylpyruvamide (DMP).

Table 4.S6. Optimized structure and energy for N,N-dimethylpyruvamide (DMP).

DMP⁻			
Atom	X	Y	Z
C	0.054342	-0.492016	-0.022972
O	0.054914	-1.761356	0.120584
N	-1.184208	0.175732	-0.208610
C	1.286586	0.265251	-0.102174
O	1.359573	1.489761	-0.504806
C	2.574692	-0.464089	0.242297
H	3.277071	0.242374	0.699885
H	2.412946	-1.305885	0.921085
H	3.063068	-0.863628	-0.660500
C	-1.425469	1.421544	0.521333
H	-1.707945	1.226341	1.571498
H	-0.530583	2.040169	0.495670
H	-2.249390	1.969275	0.049609
C	-2.364620	-0.677007	-0.257750
H	-2.189621	-1.529557	-0.915021
H	-2.651223	-1.067728	0.733995
H	-3.203949	-0.090819	-0.646573
Energy (Hartree)	-401.186398		
Energy (kJ/mol)	-1053315		
Energy (kcal/mol)	-251748		

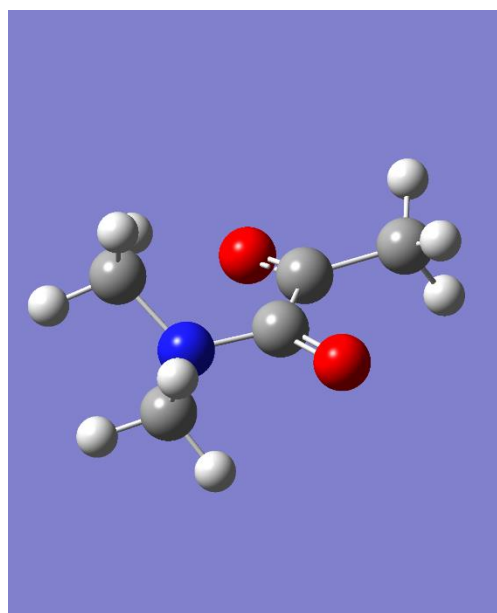


Figure 4.S32. Optimized structure for N,N-dimethylpyruvamide radical anion (**DMP⁻**).

Table 4.S7. Optimized structure and energy for N,N-dimethylpyruvamide radical anion (**DMP⁻**).

DMPH⁺			
Atom	X	Y	Z
C	-0.104244	-0.531204	-0.076993
O	0.036510	-1.753522	-0.242664
N	-1.213953	0.179312	0.059851
C	2.172491	-0.071676	1.086161
H	1.928708	0.741682	1.786910
H	1.963424	-1.009049	1.605446
H	3.226365	0.002599	0.812165
C	-1.231069	1.635581	0.227044
H	-0.219486	2.041752	0.234956
H	-1.784690	2.089395	-0.598810
H	-1.717492	1.885239	1.173089
C	-2.513701	-0.500144	0.033995
H	-3.077764	-0.174340	-0.844344
H	-2.357926	-1.576764	-0.009004
H	-3.069065	-0.241190	0.938799
O	1.640320	0.571219	-1.191666
H	2.593224	0.796521	-1.241213
C	1.276145	0.075342	-0.070592
Energy (Hartree)		-401.47059	
Energy (kJ/mol)		-1054061	
Energy (kcal/mol)		-251927	

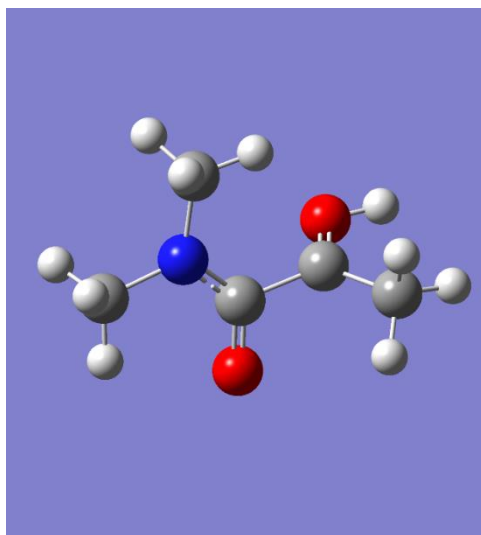


Figure 4.S33. Optimized structure for protonated N,N-dimethylpyruvamide (**DMPH⁺**).

Table 4.S8. Optimized structure and energy for protonated N,N-dimethylpyruvamide (**DMPH⁺**).

DMPH·			
Atom	X	Y	Z
C	-0.011828	-0.553045	-0.002376
O	-0.006360	-1.810691	0.031808
N	-1.197473	0.147003	-0.087792
C	2.553488	-0.528716	0.277671
H	2.375154	-1.467160	0.802458
H	3.121788	-0.753382	-0.637331
H	3.185384	0.113859	0.905007
C	-1.409161	1.476305	0.490421
H	-0.464574	1.958187	0.723334
H	-1.960988	2.108938	-0.212887
H	-2.000230	1.389080	1.412323
C	-2.422014	-0.631341	-0.248229
H	-2.243290	-1.478318	-0.910150
H	-2.792821	-1.013182	0.713841
H	-3.189292	0.014990	-0.683311
O	1.295239	1.419965	-0.519937
H	2.200403	1.765352	-0.493409
C	1.262806	0.146533	-0.034204
Energy (Hartree)		-401.642373	
Energy (kJ/mol)		-1054512	
Energy (kcal/mol)		-252034	

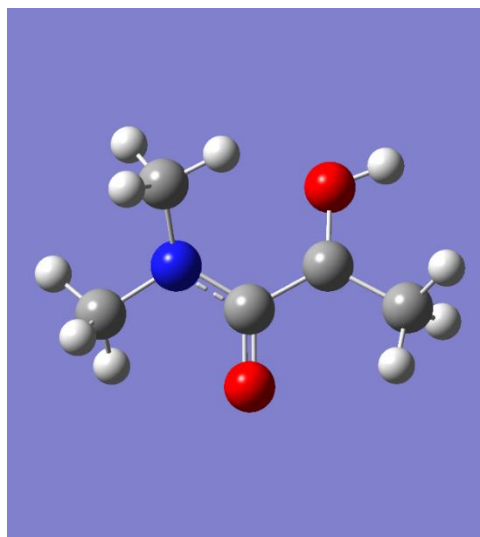


Figure 4.S34. Optimized structure for protonated N,N-dimethylpyruvamide radical (**DMPH·**).

Table 4.S9. Optimized structure and energy for protonated N,N-dimethylpyruvamide radical (**DMPH·**).

m-DMP-1			
Atom	X	Y	Z
C	2.463250	0.475384	0.008585
C	1.591961	-1.158260	1.477819
C	0.415236	-0.502785	1.578972
C	1.309656	1.207501	0.053221
H	3.356977	0.837291	-0.486957
H	1.821377	-2.036789	2.070244
H	-0.321178	-0.851572	2.294372
C	1.224139	2.573103	-0.519647
O	0.387836	3.394049	-0.105371
N	2.117700	2.919313	-1.493759
H	2.594442	2.223347	-2.047621
H	2.007656	3.832718	-1.912530
N	2.614796	-0.716611	0.654848
C	3.863455	-1.491968	0.537367
H	4.666277	-0.787537	0.305318
H	4.080392	-1.919890	1.520269
C	3.784712	-2.589545	-0.524230
H	2.990955	-3.306715	-0.293074
H	3.591783	-2.164991	-1.514334
H	4.734563	-3.132498	-0.562008
C	0.090563	0.652030	0.704027
H	-0.486885	1.423195	1.209910
O	-0.820136	0.202187	-0.465182
C	-2.044577	-0.313692	-0.190778
O	-4.061835	-0.106122	1.039469
C	-3.043904	0.443281	0.515343
N	-2.240877	-1.592252	-0.643002
C	-3.558133	-2.075445	-1.067556
H	-3.635649	-2.026161	-2.162847
H	-3.676177	-3.119155	-0.760897
H	-4.342945	-1.481582	-0.609482
C	-1.129820	-2.346900	-1.221687
H	-1.348077	-3.412711	-1.113141
H	-1.010702	-2.124921	-2.291551
H	-0.200301	-2.116314	-0.707720
C	-2.903338	1.952756	0.607389
H	-2.743058	2.260257	1.648630
H	-2.095494	2.357946	-0.003803
H	-3.851420	2.399246	0.286339
Energy (Hartree)		-897.115617	
Energy (kJ/mol)		-2355377	
Energy (kcal/mol)		-562949	

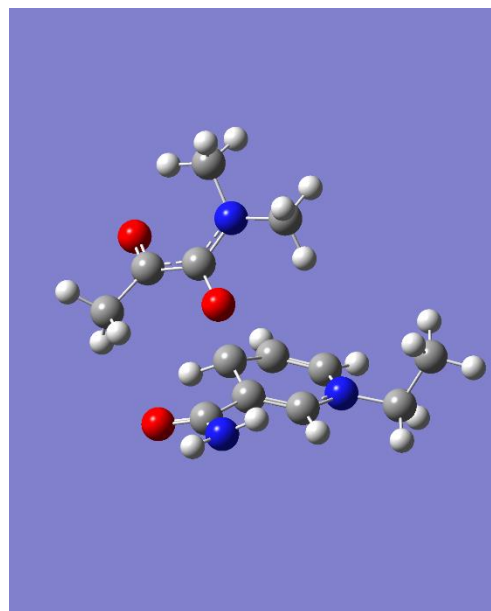


Figure 4.S35. Optimized structure for an adduct of **m** and **DMP** (**[m-DMP-1]**).

Table 4.S10. Optimized structure and energy for an adduct of **m** and **DMP** (**[m-DMP-1]**).

m-DMP-2			
Atom	X	Y	Z
C	2.364368	0.184110	-0.590122
C	1.951287	-1.390232	1.124237
C	0.973209	-0.626203	1.654851
C	1.386494	1.021672	-0.131716
H	3.034138	0.466798	-1.394414
H	2.288044	-2.308456	1.591779
H	0.511548	-0.934743	2.586286
C	1.195367	2.388889	-0.670280
O	0.599650	3.260748	-0.013052
N	1.725475	2.683535	-1.895106
H	1.945801	1.961879	-2.565143
H	1.524758	3.600445	-2.270176
N	2.624480	-1.034534	-0.034860
C	3.762243	-1.847791	-0.505987
H	3.485903	-2.898203	-0.381501
H	3.868485	-1.668270	-1.578542
C	5.068216	-1.539811	0.228188
H	5.362570	-0.495067	0.087118
H	4.974689	-1.731848	1.301622
H	5.867899	-2.176724	-0.163149
C	0.458206	0.579781	0.950563
H	0.207227	1.402899	1.617058
O	-4.345212	0.215337	0.528284
C	-3.206110	-0.198861	0.185623
O	-0.843190	0.223222	0.248284
C	-2.028654	0.289167	0.894451
N	-3.068560	-1.037005	-0.907577
C	-2.061116	-2.096931	-0.991911
H	-2.513803	-3.065878	-0.736437
H	-1.670697	-2.160722	-2.013294
H	-1.234141	-1.902880	-0.316269
C	-4.272681	-1.311488	-1.685230
H	-3.972211	-1.664246	-2.675946
H	-4.899110	-2.084848	-1.216673
H	-4.867161	-0.404022	-1.789426
C	-2.175345	0.990475	2.207239
H	-1.944839	2.062597	2.129437
H	-3.206397	0.894234	2.546224
H	-1.515357	0.571971	2.976686
Energy (Hartree)	-897.123053		
Energy (kJ/mol)	-2355397		
Energy (kcal/mol)	-562953		

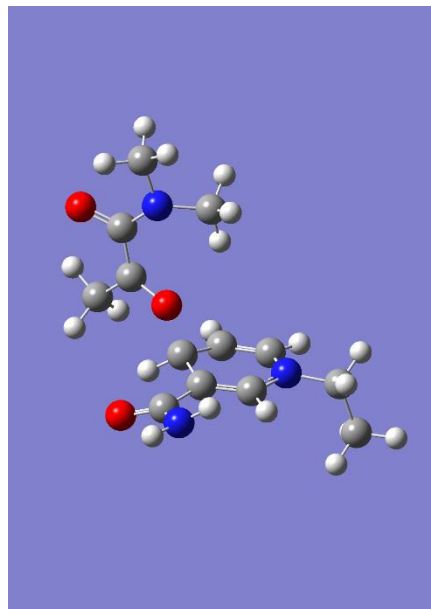


Figure 4.S36. Optimized structure for an adduct of $m\cdot$ and DMP (**m-DMP-2**).

Table 4.S11. Optimized structure and energy for an adduct of $m\cdot$ and DMP (**m-DMP-2**).

[m-DMP-1] ⁻			
Atom	X	Y	Z
C	-2.403664	0.639046	-0.022040
C	-1.724667	-1.216575	-1.324735
C	-0.498683	-0.687685	-1.513137
C	-1.191471	1.251300	-0.172236
H	-3.247391	1.138327	0.442537
H	-2.055417	-2.123772	-1.819073
H	0.177045	-1.176235	-2.205073
C	-1.009107	2.665030	0.225998
O	-0.197849	3.412779	-0.349007
N	-1.802714	3.151671	1.232158
H	-2.225140	2.532694	1.908134
H	-1.629929	4.101110	1.532973
N	-2.682054	-0.600179	-0.525995
C	-3.982437	-1.243495	-0.290228
H	-4.720421	-0.451942	-0.132664
H	-4.264516	-1.770997	-1.206694
C	-3.969073	-2.206457	0.898829
H	-3.243567	-3.011783	0.745867
H	-3.713568	-1.681441	1.824788
H	-4.959150	-2.657899	1.021653
C	-0.016202	0.506699	-0.749826
H	0.588272	1.161707	-1.384121
O	0.841444	0.144958	0.403385
C	2.138037	-0.414672	0.174129
O	4.457666	-0.041553	-0.260707
C	3.229332	0.382768	-0.114384
N	2.285439	-1.791887	0.510274
C	1.836409	-2.157944	1.849434
H	0.735865	-2.198419	1.950664
H	2.226593	-3.149665	2.114644
H	2.214931	-1.433170	2.577044
C	1.906624	-2.795735	-0.479713
H	2.351299	-3.764027	-0.211059
H	0.814859	-2.943730	-0.565753
H	2.288665	-2.505899	-1.462449
C	3.043550	1.887220	-0.303674
H	3.315331	2.175448	-1.328781
H	2.034625	2.247625	-0.099601
H	3.744931	2.408356	0.362023
Energy (Hartree)	-897.224474		
Energy (kJ/mol)	-2355663		
Energy (kcal/mol)	-563017		

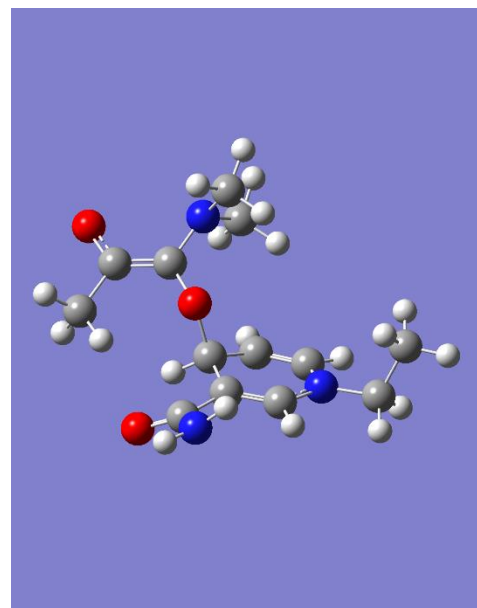


Figure 4.S37. Optimized structure for an adduct of **m**[•] and **DMP**^{•-} ([**m-DMP-1**]⁻).

Table 4.S12. Optimized structure and energy for an adduct of **m**[•] and **DMP**^{•-} ([**m-DMP-1**]⁻).

[m-DMP-2] ⁻			
Atom	X	Y	Z
C	-2.357036	0.040577	0.514021
C	-1.497349	-1.476450	-1.089348
C	-0.599755	-0.573428	-1.528631
C	-1.486098	1.020472	0.133979
H	-3.155349	0.226489	1.224591
H	-1.627512	-2.447294	-1.555410
H	0.013960	-0.823507	-2.387379
C	-1.621105	2.403689	0.641000
O	-1.216465	3.385440	-0.008891
N	-2.256009	2.588257	1.842270
H	-2.307405	1.845212	2.523413
H	-2.279381	3.532091	2.203481
N	-2.347956	-1.220083	-0.016352
C	-3.400667	-2.187901	0.333080
H	-2.959314	-3.187268	0.278101
H	-3.671502	-2.014940	1.377952
C	-4.636442	-2.096548	-0.565625
H	-5.101004	-1.107648	-0.496683
H	-4.379530	-2.285569	-1.612748
H	-5.374598	-2.843723	-0.256188
C	-0.357412	0.728113	-0.819584
H	-0.250167	1.548473	-1.536484
O	4.363453	-0.089942	-0.613824
C	3.137603	-0.123442	-0.178112
O	0.864859	0.707283	-0.010734
C	2.100360	0.614423	-0.714287
N	2.872136	-0.957398	0.994338
C	1.961645	-2.076715	0.766925
H	2.402816	-2.850008	0.105890
H	1.721897	-2.559081	1.723268
H	1.036449	-1.721978	0.316738
C	4.068030	-1.394815	1.704175
H	3.765317	-1.819325	2.669192
H	4.648344	-2.164722	1.164158
H	4.732379	-0.548655	1.888688
C	2.303770	1.584321	-1.842318
H	2.107893	2.627925	-1.538919
H	3.343190	1.523255	-2.172852
H	1.668284	1.398825	-2.724661
Energy (Hartree)	-897.227954		
Energy (kJ/mol)	-2355672		
Energy (kcal/mol)	-563019		

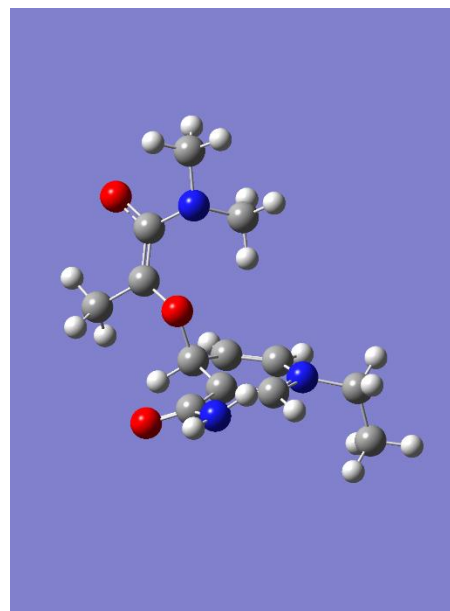


Figure 4.S38. Optimized structure for an adduct of $m\cdot$ and $DMP\cdot^-$ ($[m-DMP-2]\cdot^-$).

Table 4.S13. Optimized structure and energy for an adduct of $m\cdot$ and $DMP\cdot^-$ ($[m-DMP-2]\cdot^-$).

[m-DMP-3] ⁻			
Atom	X	Y	Z
C	-2.352852	0.126316	0.383221
C	-1.413962	-1.876503	-0.464200
C	-0.373056	-1.210204	-0.990580
C	-1.331391	0.878002	-0.119366
H	-3.258000	0.580231	0.773984
H	-1.597511	-2.929089	-0.653514
H	0.307851	-1.749137	-1.641324
C	-1.539681	2.332556	-0.277661
O	-1.053804	2.978838	-1.226281
N	-2.349926	2.968233	0.634492
H	-2.482253	2.583383	1.558172
H	-2.427478	3.972446	0.549382
N	-2.373193	-1.245811	0.344888
C	-3.579449	-1.978960	0.744075
H	-3.265498	-2.973030	1.078716
H	-4.002300	-1.470056	1.615434
C	-4.632460	-2.100894	-0.363028
H	-4.977710	-1.113694	-0.687577
H	-4.231393	-2.628871	-1.234219
H	-5.498464	-2.661428	0.005167
C	-0.065488	0.231996	-0.665987
H	0.231732	0.753949	-1.579501
O	2.448323	-0.143803	-1.720068
C	2.429522	-0.207566	-0.470776
O	0.947437	-0.307625	1.526465
C	1.183213	0.333914	0.353590
N	3.510380	-0.742978	0.177216
C	4.644881	-1.189505	-0.628692
H	5.312842	-0.355293	-0.887369
H	5.215923	-1.922462	-0.052431
H	4.294398	-1.646318	-1.553961
C	3.793635	-0.593672	1.605158
H	4.179232	-1.541180	2.000288
H	4.562030	0.177162	1.763890
H	2.863769	-0.335189	2.112016
C	1.522998	1.844500	0.580120
H	2.421335	1.925385	1.202142
H	1.687171	2.400140	-0.350826
H	0.702380	2.317779	1.129190
Energy (Hartree)	-897.257112		
Energy (kJ/mol)	-2355749		
Energy (kcal/mol)	-563037		

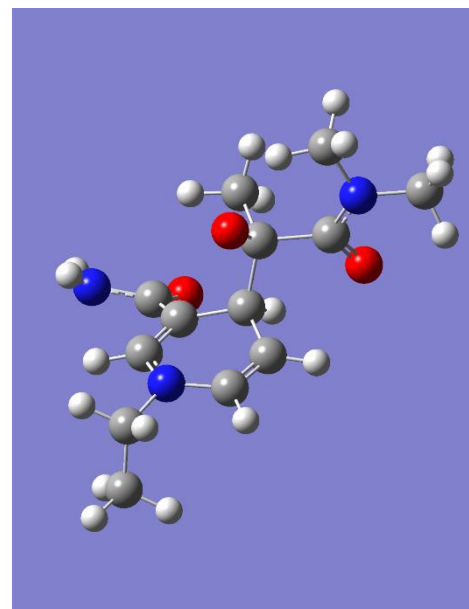


Figure 4.S39. Optimized structure for an adduct of $m\cdot$ and $DMP\cdot^-$ ([m-DMP-3]⁻).

Table 4.S14. Optimized structure and energy for an adduct of $m\cdot$ and $DMP\cdot^-$ ([m-DMP-3]⁻).

[m-DMP-1-enol]H			
Atom	X	Y	Z
C	-2.478602	0.616851	0.004310
C	-1.836441	-1.222715	-1.334814
C	-0.605125	-0.705631	-1.528892
C	-1.258883	1.216475	-0.143646
H	-3.310717	1.114708	0.489874
H	-2.180241	-2.119006	-1.839195
H	0.058390	-1.187843	-2.237149
C	-1.028853	2.613385	0.291903
O	-0.148312	3.320452	-0.230120
N	-1.842352	3.126705	1.264297
H	-2.344095	2.527200	1.902358
H	-1.633204	4.060377	1.590174
N	-2.776797	-0.606416	-0.521605
C	-4.083962	-1.239847	-0.280870
H	-4.810354	-0.441603	-0.106602
H	-4.378694	-1.751468	-1.201777
C	-4.065968	-2.216677	0.895936
H	-3.350720	-3.027464	0.725127
H	-3.795675	-1.705515	1.825311
H	-5.059310	-2.659096	1.023395
C	-0.114406	0.473395	-0.760302
H	0.509643	1.129777	-1.368711
O	0.764764	0.054033	0.396347
O	4.346424	-0.043781	-0.349387
C	3.073023	0.473872	-0.214824
N	2.431696	-1.696716	0.498018
C	2.231144	-2.013418	1.920091
H	1.166177	-2.076340	2.192971
H	2.700919	-2.976683	2.143614
H	2.704496	-1.243813	2.535660
C	1.882999	-2.741504	-0.375082
H	2.357046	-3.696563	-0.126082
H	0.793509	-2.856426	-0.269766
H	2.109901	-2.505377	-1.417956
C	3.010563	1.936204	-0.509960
H	3.268585	2.133722	-1.558247
H	2.023050	2.352544	-0.309095
H	3.748754	2.463973	0.106775
C	2.071597	-0.351141	0.161863
H	4.249192	-0.981235	-0.074647
Energy (Hartree)		-897.71017	
Energy (kJ/mol)		-2356938	
Energy (kcal/mol)		-563322	

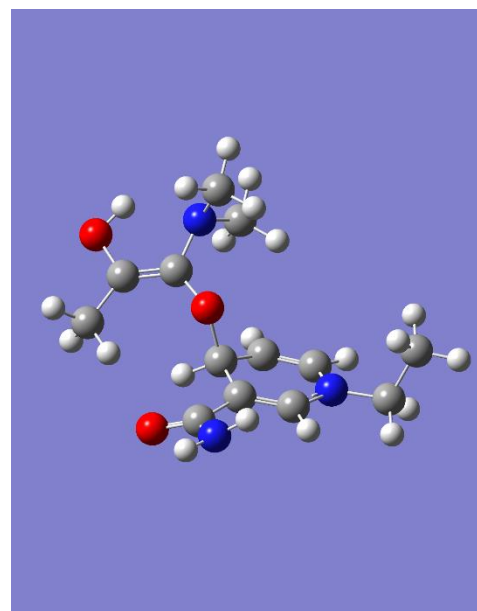


Figure 4.S40. Optimized structure for a protonated adduct of **m**[•] and **DMP**^{•-} (**[m-DMP-1-enol]H**).

Table 4.S15. Optimized structure and energy for a protonated adduct of **m**[•] and **DMP**^{•-} (**[m-DMP-1-enol]H**).

[m-DMP-1]H			
Atom	X	Y	Z
C	-2.443932	0.692060	-0.114304
C	-1.978087	-1.447670	-1.006316
C	-0.677100	-1.139702	-1.184356
C	-1.146808	1.094980	-0.267533
H	-3.227707	1.376763	0.190748
H	-2.409952	-2.379638	-1.354226
H	-0.036459	-1.839264	-1.707722
C	-0.753487	2.512612	-0.098080
O	0.250778	2.979404	-0.663347
N	-1.551648	3.316710	0.670412
H	-2.169965	2.931761	1.368895
H	-1.231875	4.263328	0.823547
N	-2.875543	-0.566450	-0.416982
C	-4.268187	-0.973934	-0.171545
H	-4.885759	-0.072349	-0.204832
H	-4.579406	-1.611445	-1.004533
C	-4.452801	-1.702622	1.160708
H	-3.848938	-2.614813	1.198673
H	-4.166670	-1.062024	2.000856
H	-5.503623	-1.983887	1.285114
C	-0.073813	0.108175	-0.624910
H	0.657119	0.547791	-1.303997
O	0.654021	-0.177477	0.656075
O	3.088710	0.752236	-1.189358
C	2.806533	0.702098	-0.001011
N	2.322637	-1.772224	-0.028833
C	3.762335	-2.065091	-0.066113
H	4.208434	-2.111870	0.944737
H	3.909853	-3.038383	-0.541685
H	4.296263	-1.317172	-0.652623
C	1.621016	-2.866193	0.655265
H	1.797091	-3.797201	0.108955
H	1.976330	-3.001995	1.693752
H	0.549210	-2.672603	0.677614
C	3.136976	1.817083	0.956971
H	2.274641	2.052906	1.587601
H	3.942291	1.482060	1.623671
H	3.462326	2.704756	0.413113
C	2.043360	-0.498045	0.621230
H	2.314576	-0.538790	1.693172
Energy (Hartree)	-897.718422		
Energy (kJ/mol)	-2356960		
Energy (kcal/mol)	-563327		

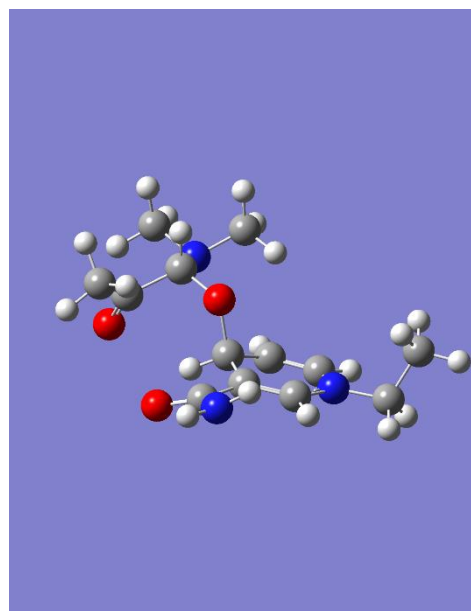


Figure 4.S41. Optimized structure for a protonated adduct of **m·** and **DMP·** (**[m-DMP-1]H**).

Table 4.S16. Optimized structure and energy for a protonated adduct of **m·** and **DMP·** (**[m-DMP-1]H**).

[m-DMP-2]H			
Atom	X	Y	Z
C	2.379077	0.113114	-0.571108
C	1.722295	-1.530477	0.998771
C	0.818601	-0.699861	1.559110
C	1.492721	1.022778	-0.070152
H	3.116259	0.378892	-1.320859
H	1.947675	-2.508640	1.409172
H	0.319260	-1.012710	2.469674
C	1.516203	2.445734	-0.480625
O	1.067185	3.341309	0.256810
N	2.087336	2.759807	-1.683368
H	2.182331	2.072597	-2.416136
H	2.039366	3.726752	-1.973905
N	2.464607	-1.174306	-0.119219
C	3.520100	-2.074075	-0.619417
H	3.127563	-3.093657	-0.576121
H	3.678920	-1.836091	-1.674208
C	4.830778	-1.965649	0.162696
H	5.242870	-0.953276	0.102844
H	4.685161	-2.218634	1.217618
H	5.567086	-2.659744	-0.255167
C	0.447413	0.602854	0.920574
H	0.283108	1.389777	1.660088
O	-3.876691	0.845360	-0.600594
O	-3.108160	-0.010767	-0.130114
C	-0.811547	0.481035	0.141852
N	-3.172571	-1.316714	-0.496809
C	-2.281049	-2.371400	-0.014949
H	-2.764405	-2.967316	0.769100
H	-2.042207	-3.035042	-0.851630
H	-1.347066	-1.959452	0.358484
C	-4.208264	-1.761038	-1.427643
H	-3.763186	-2.052816	-2.386392
H	-4.728145	-2.628851	-1.007990
H	-4.919267	-0.954035	-1.591607
C	-2.405902	1.717074	1.580058
H	-2.490111	2.522710	0.847623
H	-3.368704	1.612368	2.090094
H	-1.660718	1.990860	2.331308
C	-2.031871	0.402190	0.900036
H	-1.944641	-0.379709	1.665825
Energy (Hartree)		-897.752019	
Energy (kJ/mol)		-2357048	
Energy (kcal/mol)		-563348	

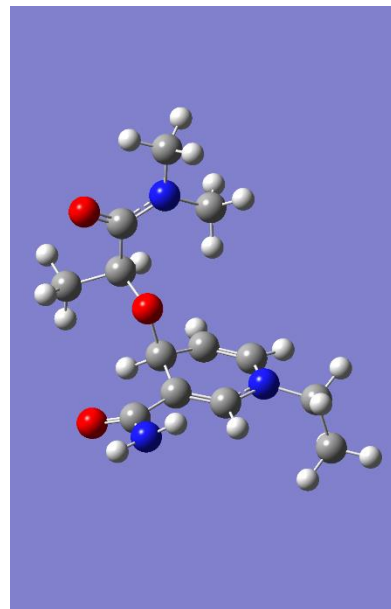


Figure 4.S42. Optimized structure for a protonated adduct of $m\cdot$ and $DMP\cdot$ ($[m-DMP-2]H$).

Table 4.S17. Optimized structure and energy for a protonated adduct of $m\cdot$ and $DMP\cdot$ ($[m-DMP-2]H$).

[m-DMP-3]H			
Atom	X	Y	Z
C	-2.340629	0.115783	0.347542
C	-1.363969	-1.830729	-0.578458
C	-0.342445	-1.124044	-1.099721
C	-1.341405	0.912049	-0.126434
H	-3.255112	0.527406	0.761126
H	-1.527892	-2.876670	-0.814288
H	0.329996	-1.614457	-1.795159
C	-1.547569	2.374529	-0.232840
O	-0.978411	3.052400	-1.107917
N	-2.426100	2.968229	0.635709
H	-2.656985	2.539849	1.519924
H	-2.502897	3.974913	0.587988
N	-2.322465	-1.253794	0.257073
C	-3.485794	-2.044366	0.689613
H	-3.119110	-3.032841	0.981303
H	-3.884056	-1.573608	1.592436
C	-4.576032	-2.169857	-0.378116
H	-4.966557	-1.186712	-0.660087
H	-4.194104	-2.660803	-1.278904
H	-5.406584	-2.768932	0.009406
C	-0.065795	0.310346	-0.700046
H	0.247201	0.890063	-1.569650
O	2.492048	0.158552	-1.697727
C	2.435769	-0.086822	-0.479216
C	1.155310	0.351235	0.308205
N	3.469753	-0.717395	0.143525
C	4.610982	-1.110720	-0.687408
H	5.301531	-0.271292	-0.840066
H	5.145633	-1.917300	-0.180880
H	4.264400	-1.456719	-1.660458
C	3.740339	-0.764745	1.584160
H	3.982227	-1.792321	1.875309
H	4.604640	-0.129231	1.814497
H	2.880015	-0.437307	2.155288
C	1.407169	1.752979	0.876050
H	2.270559	1.750406	1.546920
H	1.592037	2.465371	0.069188
H	0.537714	2.085270	1.448689
O	0.867724	-0.494230	1.426023
H	0.542550	-1.341959	1.080259
Energy (Hartree)		-897.750479	
Energy (kJ/mol)		-2357044	
Energy (kcal/mol)		-563347	

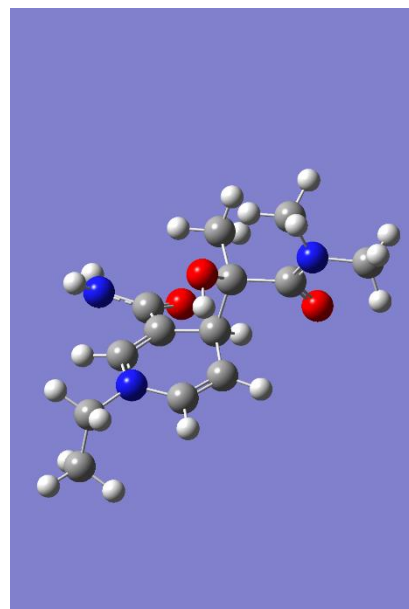


Figure 4.S43. Optimized structure for a protonated adduct of $m\cdot$ and $DMP\cdot^-$ (**[m-DMP-3]H**).

Table 4.S18. Optimized structure and energy for a protonated adduct of $m\cdot$ and $DMP\cdot^-$ (**[m-DMP-3]H**).